Inaugural dissertation

for

obtaining the doctoral degree

of the

Combined Faculty of Mathematics, Engineering and Natural Sciences

of the

Ruprecht - Karls - University

Heidelberg

Presented by

M.Sc. Nadja Lehmann

born in: Berlin

Oral examination: 18.10.2023

Development of axon-carrying dendrite cells in murine hippocampus and primary somatosensory cortex

Referees:

Prof. Dr. Hilmar Bading

Prof. Dr. Andreas Draguhn

List of Figures

List of Tables

Contents

List of Abbreviations

AcD	**A**xon - **c**arrying **D**endrite: axon branches off a dendrite
aCSF	**a**rtificial **c**erebro**s**pinal**f**luid
AIS	**A**xon **I**nitial **S**egment
ank-G	**ank**yrin-**G**
AP	**A**ction **P**otential
bicuculline	(-) - Bicuculline methiodide
Cs-MeSO$_3$	**C**e**s**ium **Me**than**s**ulf**o**nate
DIV	**D**ay **I**n **V**itro
EGTA	**E**thylene **G**lycol-bis(β-aminoethylether)-N,N,N,N-**t**etraacetic**a**cid
GABA	**G**amma - **A**mino**b**uytric **A**cid
GFP	**G**reen **F**luorescent **P**rotein
IgG	**I**mmuno**g**lobulin**G**
Mg-ATP	**A**denosine 5'-**t**ri**p**hosphate magnesium salt
MgSO$_4$	Magnesium sulfate
Na$_2$-GTP	**G**uanosine 5'-**t**ri**p**hosphoate sodium salt
Na$_v$	voltage - gated sodium channel
nonAcD	**nonA**xon - **c**arrying **D**endrite: Dendrite does **not** carry an axon
Na$_2$Phosphocreatine	Phosphocreatine disodium salt hydrate

OTC	**O**rgano**t**ypic Slice **C**ulture
PBS	**P**hosphate **B**uffered **S**aline
PFA	**P**ara**f**orm**a**ldehyde
S1	Primary **S**omatosensory Cortex
vGAT	**v**esicular **GA**BA **T**ransporter
vHC	**v**entral **H**ippo**c**ampus

1 Abstract - Zusammenfassung

In some neurons, axons originate from a basal dendrite, resulting in an axon-carrying dendrite (AcD) branch with unique functional features. Initial observations showed that the AcD has a privileged position, allowing circumvention of somatic inhibition and providing a highly efficient synaptic input channel, resulting in potentially distinct functional implications for overall network activity. Although AcD neurons have been described in numerous anatomical regions across species, their developmental profile and putative ability to remodel their axonal onset throughout their lifetime remains largely unknown. Therefore, this project investigated the early maturation profile of AcD neurons in comparison to nonAcD neurons in the murine ventral hippocampus (vHC) and primary somatosensory (S1) cortex, using a transgenic mouse line (Thy1-GFP-M). Additionally, to investigate large-scale morphological plasticity, I used immunofluorescence and live-cell imaging of neurons from the mouse primary somatosensory cortex in organotypic slice cultures. In a second approach, I employed an established *in vivo* paradigm to manipulate sensory input to layer V pyramidal cells in the barrel cortex. This study demonstrates that the proportion of AcD neurons peaks in juvenile mice and that $Na_v1.6$ is clustered more distally in the axon initial segment of AcD neurons than in nonAcD neurons. Furthermore, neurons are indeed capable of changing the onset of their axon origin from somatic to dendritic and *vice versa* within a few days *in vitro*. Furthermore, the manipulation of sensory input drives large-scale morphological plasticity especially with regard to the axon onset *in vivo*. Altogether, the study contributes to the understanding of developmental and activity-dependent plasticity of a functionally important variant of mammalian pyramidal neurons.

Zusammenfassung

In einigen Neuronen entspringen die Axone aus dem basalen Dendriten, was zu einem axontragenden Dendritenast (AcD) mit einzigartigen funktionellen Merkmalen führt. Erste Beobachtungen haben gezeigt, dass der AcD eine privilegierte Position innehat, die es ermöglicht somatische Inhibition zu umgehen und einen besonders effizienten synaptischen Eingangskanal schafft, was sich möglicherweise auf die gesamte Netzwerkaktivität auswirkt. Obwohl AcD-Neurone in zahlreichen kortikalen Regionen bei verschiedenen Spezies beschrieben wurden, sind ihr Entwicklungsprofil und ihre Fähigkeit, den axonalen Ursprung im Laufe ihres Lebens als Reaktion auf Veränderungen der Netzwerkaktivität umzugestalten, noch weitgehend unbekannt. Daher untersuchte ich in diesem Projekt das frühe Reifungsprofil von AcD-Neuronen im Vergleich zu Nicht-AcD-Neuronen im ventralen Hippocampus (vHC) und primären somatosensorischen (S1) Kortex der Maus unter Verwendung einer transgenen Mauslinie (Thy1-GFP-M). Um die morphologische Plastizität im großen Maßstab zu untersuchen, verwendete ich außerdem Immunfluoreszenz und Live-Cell-Imaging von Neuronen aus dem primären somatosensorischen Kortex der Maus in organotypischen Schnittkulturen. In einem zweiten experimentellen Ansatz habe ich ein etabliertes *in vivo*-Paradigma angewandt, um den sensorischen Input in die Schicht-V-Pyramidenzellen im Barrel-Cortex zu manipulieren. Diese Studie zeigt, dass der Anteil an der AcD-Neuronen in jungen Mäusen ihren Höhepunkt erreicht und dass $Na_v1.6$ im Axoninitialsegment von AcD-Neuronen weiter distal angesammelt ist als in Nicht-AcD-Neuronen. Außerdem sind Neurone tatsächlich in der Lage, innerhalb weniger Tage *in vitro* den Beginn ihres Axonursprungs von somatisch zu dendritisch und umgekehrt zu ändern, und dass die Manipulation des sensorischen Inputs eine umfangreiche morphologische Plastizität *in vivo* bewirkt. Insgesamt trägt die Studie zum Verständnis der entwicklungs- und aktivitätsabhängigen Plastizität einer funktionell wichtigen Variante von Pyramidenneuronen in Säugetieren bei.

2 Introduction

The classic view of neuron morphology centers on the observation that in most cortical principal neurons, the axon emerges from the soma. In some neurons, however, the axon emerges from a basal dendrite, a morphology termed axon-carrying dendrite (AcD). Recent evidence indicates that a dendritic origin of the axon leads to distinct functional properties with a direct impact on neuronal network activity. Here, I will introduce recent knowledge about AcD neurons and will summarize current knowledge about the influence of axonal origin, with special respect to the axon initial segment (AIS). Finally, I will introduce the brain regions used in this study as model systems to investigate AcD development and function.

2.1 Axon-carrying dendrite cells

Information processing in the central nervous system (CNS) occurs at all structural levels, ranging from macromolecules to population dynamics (reviewed in (Tozzi 2015)). One fundamental signal for communication is the action potential (AP). APs enable neurons to establish neuronal interactions at various levels from global communication between brain regions to functional microcircuits. Thus, they mediate and regulate information processing. At the cellular level, neurons receive information via synaptic inputs to their dendrites (with some inhibitory input targeted to the soma or axon), which act like 'antennae' and pick up information from thousands of presynaptic terminals (reviewed in (Stuart and Spruston 2015). This input is then integrated within the somatodendritic compartment, and upon reaching a sufficient threshold, axonal output (AP) is generated at the axon initial segment (AIS). Subsequently, the AP propagates along the axon to the presynaptic terminals, exciting or inhibiting neurons further downstream. Usually, axons originate from the somatic envelope. However, they can also emerge from dendrites, as already observed by Ramón y Cajal (1937). Since then, such non-somatic axon origins have been described in numerous brain regions and neuronal subpopulations within several species (Häusser et al. 1995; Martina 2000; Peters, Proskauer, and Kaiserman-Abramof 1968; Thome, Kelly, et al. 2014, (reviewed in (Triarhou 2014)).

In the late 19^{th} century, Ramón y Cajal observed dendrite-derived axons in unipolar neurons of invertebrate abdominal ganglia cells, but also in the optical lobes of birds, reptiles, amphibians, and fish (reviewed in (Triarhou 2014)). A recent study

by Wahle et al. (2022) showed that 10–21% of pyramidal neurons in the gray matter of the sensory cortex of non-primates (including mice, rats, cats, ferrets, and pigs) had an AcD. In these animals, AcD neurons were more abundant in the supragranular layer than in the infragranular layer (Wahle et al. 2022). However, another study showed that in the somatosensory cortex of rats approximately 30% of thick-tufted layer V neurons emerge from a dendrite (Hamada et al. 2016). In organotypic slice cultures (OTC) from the visual cortex of rats, approximately 46% of pyramidal neurons with dendritic axon origin were observed (Höfflin et al. 2017). Thus, the number of AcD neurons observed in non-primates strongly depends on the cortical layer and subregion. In contrast, in primates, the number of AcD neurons ranged between 4-7% in cortical areas, and in humans, it was approximately 1-9% (Wahle et al. 2022). Interestingly, this study observed that in macaques and humans, AcD cells were more abundant in the infragranular layer than in the supragranular layer, in contrast to non-primates. This observation might be linked to the fact that the infragranular layers are thicker in non-human primates and humans, which may be associated with higher cortical functions and complex behavior (Rockland 2022).

In contrast to observations made in the sensory cortices of non-primates and primates, the number of AcD neurons was higher in the CA1 of humans than in mice (Benavides-Piccione et al. 2020). They observed 20% of AcD neurons in the hippocampal CA1 region in mice and 44% of axons emerging from a basal dendrite in humans. However, in other studies obtained from the rodent hippocampal CA1 region, the number of AcD neurons ranged from approximately 50% to 83% (Tamamaki et al. 1987; Thome, Kelly, et al. 2014). Interestingly, the number of AcD neurons varies among the subregions of the hippocampus. The highest percentage of AcD neurons (~50%) occurs in the central CA1 portion, while in subregion CA3 only 28% and in subiculum only 21% of AcD neurons were observed (Thome, Kelly, et al. 2014). In most cases, the axon emerges from a basal dendrite, but it can also emerge from an apical dendrite with lower frequency between 2% and 5% (Thome, Kelly, et al. 2014; Lorincz and Nusser 2010).

Different somatic or dendritic axon onsets were observed in several brain regions, with tremendous discrepancies in the reported numbers. In dopaminergic neurons in the substantia nigra of the midbrain, the axon predominantly emerges from a dendrite, reaching the highest percentage of this structural feature in all brain regions studied so far (76%) (Häusser et al. 1995). These neurons have a

sparse dendritic tree with few unbranched dendrites (Häusser et al. 1995). The distance from the axon to the soma ranged from a few micrometers to 240 µm in extreme cases (Häusser et al. 1995). The axons were observed to originate most frequently from dendrites that were located medially (35%), with lower percentages in basal (23%), apical (19%), and lateral (23%) dendrites (Häusser et al. 1995). Furthermore, axon-bearing dendritic cells have been observed in retinal ganglion cells of Dogiel, cerebellar granule cells, and spinal motor neurons (reviewed in (Triarhou 2014)). In addition to excitatory neurons, axons can emanate from dendrites of inhibitory neurons as well. In the midbrain, approximately 54% of GABAergic interneurons exhibit axon-bearing dendrites (Häusser et al. 1995). Approximately 44% of interneurons in the visual cortex have an axon-carrying dendrite, in basket cells 37% and in Martinotti cells approximately 60% (Höfflin et al. 2017). In the sensory cortex, approximately 30% of all interneurons have an AcD (Wahle et al. 2022). Parvalbumin-positive neurons (fast-spiking GABAergic basket and Chandelier cells) showed AcD morphology in approximately 22%, whereas somatostatin-positive neurons (non-fast-spiking interneurons) showed approximately 45-50% AcDs (Wahle et al. 2022).

Neurons with an AcD showed further morphological differences from those with an axon of somatic origin. Thick-tufted layer V neurons with an AcD in rat somatosensory cortex have fewer basal and apical dendritic sections and lower complexity (Hamada et al. 2016). In the hippocampus, the basal dendrite from which the axon emanates is longer than basal dendrites that do not carry an axon (Hodapp et al. 2022). In addition, axons that emerge from dendrites are thinner than somatic axons (Benavides-Piccione et al. 2020). Electron microscopy revealed that in layer II/III pyramidal neurons of the cerebral cortex, axons emanating from dendrites have less prominent axonal hillocks (Peters, Proskauer, and Kaiserman-Abramof 1968). When the axon and a dendrite emerge simultaneously, the common stem shares features of both processes, i.e. the morphological fine structure of a dendrite, but also characteristics of an axon, indicated by a low number of ribosomes and the presence of fasciculate microtubules, which are characteristic for the axon hillock (Peters, Proskauer, and Kaiserman-Abramof 1968).

These observations indicate that AcD neurons appear in numerous brain regions, as well as in many species, such as primates and humans. Thus, they appear to be evolutionarily conserved, indicating that they serve some important functions. What functional implications can be assumed when an axon emerges from a den-

drite instead of the soma?
Neuronal morphology has a strong impact on biophysical properties, such as (passive) integration of synaptic inputs, membrane time constants and others. Several studies have described the role of AP initiation sites using computational modeling. Brette (2013) introduced the resistive coupling theory, an application of the cable theory (Hermann 1905; Hodgkin and Rushton 1946). The resistive coupling theory applies when the soma acts as a current sink for the initiation site, because of the size differences between the large soma and thin axon and the short distance between these two sites (Telenczuk et al. 2017). This implies that the sodium current generated at the AIS flows primarily towards the large somatodendritic membrane, where it can be measured as a capacitive current (I_{cap}). This is mostly the case in pyramidal neurons because of the location of the AP initiation site in a thin axon, which is located close to the much larger somatodendritic compartment (Peters, Proskauer, and Kaiserman-Abramof 1968; Kole and Brette 2018). This phenomenon results in a voltage gradient between the soma (V_s) and axonal site (V_a) because the intracellular medium is resistive, and the axial current follows Ohm's law (Figure 1, left illustration). The gradient between these two sites is equal to the product of the input current and the axial coupling resistance (R_a) (dV = R_a × I, Kole and Brette 2018). The geometry of the axonal and dendritic branches connecting the soma and AIS determines the axial resistance (R_a). R_a is inversely proportional to the somatodendritic cross-sectional area and proportional to the AIS distance from the soma (reviewed in (Kole and Brette 2018)). According to this simplified model, AP generation is significantly influenced by the geometry of the AIS and nearby dendritic sites. To produce APs, it is assumed that neurons with a distal AIS or with thin axons are more excitable (reviewed in (Kole and Brette 2018)). This prediction is consistent with the fact that spike initiation occurs at the distal end of the AIS owing to its larger electronic isolation (Baranauskas et al. 2013; Eyal et al. 2014).

However, some studies have shown that a distal location of the AIS is assumed to reduce neuronal excitability (Grubb and Burrone 2010; Lezmy et al. 2017). Subsequent to chronic depolarization, the AIS clustered more distally, including voltage-gated sodium channels, and its relocation correlated with an increased current threshold for AP initiation (Grubb and Burrone 2010). In addition, a distal relocation of the spike initiation zone, specifically of Na_v and K_v7 channels, resulted in a reduction of intrinsic excitability (Lezmy et al. 2017). Furthermore, according to the resistive coupling theory, the current delivered to the soma by the AIS spike

is inversely proportional to the AIS distance (Kole and Brette 2018). Thus, it can be assumed that the soma receives less current from a dendritic axon than from a somatic axon.

Some experimental studies have described the unique functions of the dendrites that carry the axon. Interestingly, this dendrite, where the axon branches off, has been observed to have a privileged position. First, multiphoton glutamate uncaging revealed that synaptic input onto this AcD generates APs with a lower activation threshold than input to regular dendrites (Thome, Kelly, et al. 2014). Second, axon-bearing dendrites are intrinsically more excitable and generate dendritic spikes with a higher probability and greater strength (Thome, Kelly, et al. 2014). Third, owing to its distal location, the AcD can circumvent somatic inhibition, thereby being able to fire APs even with strong perisomatic inhibition (Hodapp et al. 2022). Perisomatic inhibition is assumed to play a crucial role in network function. Sharp wave ripple oscillations, which are important for memory consolidation (Girardeau et al. 2009; Fernández-Ruiz et al. 2019), exhibit particularly strong perisomatic inhibition (Schlingloff et al. 2014). During this network state, AcD neurons are able to fire, whereas nonAcD neurons are much less prone to generate action potentials (Hodapp et al. 2022). Hence, AcDs constitute a privileged synaptic input channel with tremendous power over AP generation. Insight into the abundance, structure, and function of AcD neurons in neural networks would be incomplete without examining the role of a critical subcomponent, the AIS.

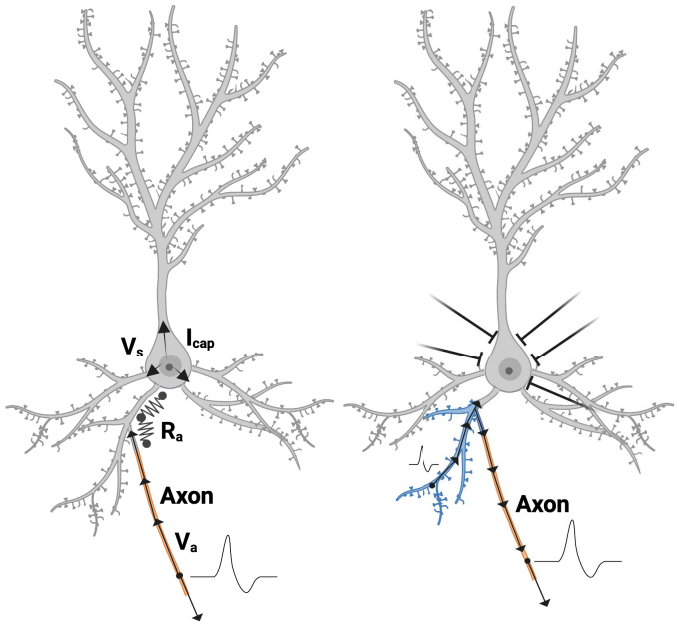

Figure 1: Schematic overview of theoretical and practical functions assigned to AcD neurons. The illustration on the left shows the biophysical impacts that influence the current flow entering the axon emerging from a dendrite. The current flows mainly to the soma along the path of axial resistance (R_a). The soma acts as a current sink because at the large somatodendritic membrane, the current exists as a capacitive current (I_{cap}). The current flow direction to the soma is due to the size differences of the large soma and thin axon, and the short distance between these two sites. These large size differences result in a voltage gradient between the soma (V_s) and axon (V_a). Illustration adapted from Kole and Brette (2018). The illustration on the right depicts the current experimental functions assigned to AcD neurons. The AcD (blue) generates dendritic spikes that can flow directly to the axon (orange). In addition, when somatic inhibition occurs, the axon is still able to generate APs because it can circumvent perisomatic inhibition owing to its distal location.

2.2 The AIS and its role in neuronal polarity

AcD neurons are defined by the remarkable feature that axons branch off dendrites. To understand the functional implications of such an axon onset, it is necessary to introduce the AIS. The AIS is the primary location for AP initiation and maintenance of neuronal polarity (reviewed in (Rasband 2010)).

Directional information processing in a neuron relies on its asymmetrical morphology (reviewed in (Rasband 2010; Kapitein and Hoogenraad 2011)). Neurons consist of two different compartments: the somatodendritic compartment (soma and dendrites) and the axonal compartment (axon), with different functions (reviewed in (Leterrier and Dargent 2014)). As previously described, neurons receive and

integrate excitatory and inhibitory synaptic inputs at their dendrites and somata. APs are generated at the AIS upon surpassing a voltage threshold and travel to downstream synaptic sites. This process relies on the polarized structure of the somatodendritic and axonal compartments (reviewed in (Leterrier and Dargent 2014; Leterrier, Clerc, et al. 2017; Rasband 2010)).

The AIS was already described in 1968 by Palay et al., and since then its molecular composition, organization, and role in network activity have been elucidated (reviewed in (Jamann, Jordan, et al. 2018; Leterrier 2018; Leterrier 2021; Rasband 2010)). The AIS is located at the proximal axon with an average length of 20 to 40 µm, depending on cell type, and is highly enriched with voltage-gated ion channels (reviewed in (Leterrier, Potier, et al. 2015; Rasband 2010)). Its location underlines the main functions of the AIS: maintaining axonal polarity and initiating APs (reviewed in (Leterrier and Dargent 2014)). The molecular composition of the AIS is defined by three morphological features: (i) closely apposed microtubules, (ii) a ~50 nm-thick undercoat lining of the axolemma, and (iii) an almost complete absence of ribosomes (Figure 2, (Palay et al. 1968; Peters, Proskauer, and Kaiserman-Abramof 1968), reviewed in (Leterrier 2018)). Microtubules and actin filaments are polar structures that play important roles in cell division, transport, and movement of cell organelles (reviewed in (Leterrier, Dubey, et al. 2017)). AIS proteins form a layered scaffold that extends from microtubules to the axolemma (Figure 2, (Leterrier, Potier, et al. 2015); reviewed in (Leterrier 2018)). Ankyrin-G (ank-G) is the central component of this scaffold and organizes AIS proteins, due to its membrane-binding domain, and its spectrin-binding, serine-rich tail and carboxy-terminal domain (reviewed in (Leterrier 2018)). The amino-terminal side of ank-G is embedded into the actin/spectrin submembrane scaffold, which anchors voltage-gated ion channels and cell adhesion molecules (CAM), such as neurofascin 186 (NF-186) and NrCAM (Neuronal Cell Adhesion Molecules) ((Davis et al. 1996), reviewed in (Leterrier 2018)). NF-186 plays a crucial role in recruiting components of the extracellular matrix and is important for GABAergic innervation at the AIS (Ango et al. 2004; Hedstrom et al. 2007). By interacting with microtubule-associated proteins (e.g., EB1/3), the carboxy-terminal of ank-G links this submembrane scaffold to microtubules (Leterrier, Vacher, et al. 2011). The actin/spectrin submembrane complex is periodically organized with actin rings connected by spectrin tetramers of αII-spectrin and βIV-spectrin (Xu, Zhong, et al. 2013; Huang et al. 2017). These actin rings are evenly spaced along the axon at a distance of ~190 nm (Xu, Zhong, et al. 2013). This periodic scaf-

fold is assumed to be crucial for the resilience of the axon (Dubey et al. 2020). This scaffold can buffer axonal extensions by unfolding its spectrin tetramers in a reversible manner to alleviate any mechanical stress (Dubey et al. 2020). The molecular specialization of the AIS leads to restricted lateral mobility of membrane proteins (Winckler et al. 1999). Channels and CAMs bound to ank-G are highly immobilized and lipid movement is suppressed in regions where ank-G is expressed (Nakada et al. 2003; Boiko, Vakulenko, et al. 2007). Therefore, the specific and enriched assembly of proteins at the AIS functions as a diffusion barrier that is constituted by the dense membrane skeleton meshwork in the AIS. Immobilization of protein movement at the AIS supports the maintenance of neuronal polarity between somatodendritic and axonal compartments.

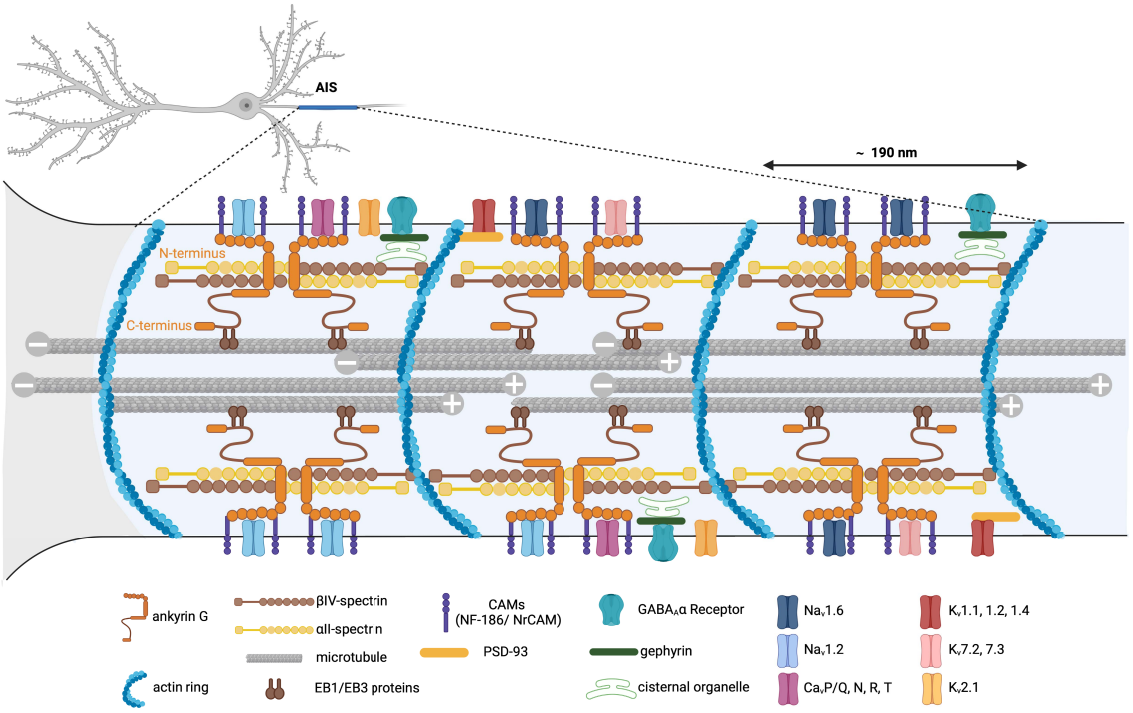

Figure 2: The AIS and its molecular composition. This illustration depicts the molecular composition of the axolemma and the submembrane cytoskeleton. This illustration highlights protein interactions, anchoring of voltage-gated ion channels, interaction of $GABA_A$ α receptors, and polarization of the AIS (see text for details). This illustration was adapted from the work of Engelhardt et al. 2019.

2.2.1 Channels at the AIS

The main feature of the AIS is the high density of voltage-gated ion channels. Voltage-gated ion channels are integral membrane proteins that play pivotal roles in the generation and propagation of APs, which are essential for neuronal com-

munication. Voltage-gated sodium (Na_v) and potassium (K_v) channels are densely clustered in the AIS and nodes of Ranvier in mammalian neurons (Figure 2). Additionally, the geometry of the AIS, such as the diameter, position, length, and properties of Na_v channels, influences AP initiation and backpropagation to the soma (Hu, Tian, et al. 2009; Mainen et al. 1995; Moore et al. 1983), reviewed in (Kole and Stuart 2012)).

Na_v channels are concentrated at the AIS, anchored by ank-G (reviewed by (Leterrier 2018)), and are primarily responsible for AP initiation. When neurons are stimulated, these channels open rapidly, allowing a rapid influx of sodium ions into neurons, which initiates the depolarization phase of the AP (Hodgkin and Huxley 1952). In general, three subtypes of Na_v channels (Na_v1.1, 1.2, and 1.6) are localized in the AIS with developmental, regional, and cell-type specific differences ((Lorincz and Nusser 2008), reviewed in (Kole and Stuart 2012)). The main Na_v channel isoform in mature excitatory neurons of the CNS is Na_v1.6, which is located in the distal part of the AIS in pyramidal neurons (Hu, Tian, et al. 2009; Lorincz and Nusser 2008). Na_v1.6 channels have the striking feature of hyperpolarized voltage dependence of activation at the AIS, thereby facilitating the generation of APs and shaping the repetitive discharge properties (Figure 3A, (Royeck et al. 2008)). In contrast, Na_v1.2 is expressed in the proximal part of the AIS in cortical pyramidal neurons and does not seem to colocalize with Na_v1.6 (Hu, Tian, et al. 2009). The expression of Na_v isoforms undergoes a shift in retinal ganglion cells during development. In early developmental stages around P2-P14, Na_v1.2 is the dominant isoform located at the AIS (Boiko, Van Wart, et al. 2003). During maturation, Na_v1.6 starts to cluster within the AIS (first detected around P9) and becomes the dominant isoform in retinal ganglion cells in adult rats (Boiko, Van Wart, et al. 2003).

Na_v1.2 has a high voltage threshold and promotes AP propagation to the soma (Figure 3, Hu, Tian, et al. 2009). Therefore, this channel subtype is involved in defining the threshold for AP propagation into the somatodendritic region of a neuron (Hu, Tian, et al. 2009). Na_v1.1 is located in the proximal part of the AIS in GABAergic interneurons, retinal ganglion cells, and spinal cord neurons (Ogiwara et al. 2007; Van Wart et al. 2007; Duflocq et al. 2008; Lorincz and Nusser 2008; Lorincz and Nusser 2010). Interestingly, in the nucleus laminaris neurons in birds, Na_v channels are located more distally in the AIS of neurons that have high characteristic frequencies (>2kHz) compared to neurons that are tuned to

have low characteristic frequencies (<1kHz) (Kuba, Ishii, et al. 2006; Kuba and Ohmori 2009). This indicates that the location of Na_v channels is related to the speed of input processing in neurons, with distal locations favoring rapid input-output coupling (Kuba and Ohmori 2009). It is assumed that the number of Na_v channels in the AIS of pyramidal neurons is 3-fold to 50-fold higher in the AIS than in the soma (Lorincz and Nusser 2010; Fleidervish et al. 2010; Kole, Ilschner, et al. 2008). Thus, this high density of Na_v channels defines the AP initiation site and is crucial for AP initiation.

K_v channels repolarize the membrane potential by allowing the efflux of potassium ions out of neurons, thus terminating the AP (reviewed in (Kole and Stuart 2012)). They influence the frequency of APs because their rate of opening and closing directly impacts the refractory period of neurons (reviewed in (Kole and Stuart 2012)). The low-threshold K_v1 subtype is the predominant K_v channel at the AIS in most neuronal types and densely clusters at the distal end of the AIS (Lorincz and Nusser 2008; Inda et al. 2006; Van Wart et al. 2007); reviewed by (Kole and Stuart 2012)). Three subtypes of K_v1 have been observed in the AIS ($K_v1.1$, 1.2, 1.4) (Ogawa et al. 2008). The K_v1 channel density increases 10-fold with a proximal-distal gradient (Kole, Letzkus, et al. 2007). K_v1 channels are fast-activating, but slowly inactivated voltage-gated ion channels that are active at rest (Figure 3B, Kole, Letzkus, et al. 2007). Blocking K_v1 channels located in the AIS resulted in an increase in the AP half-width, thereby possibly playing a crucial role in influencing the firing frequency, which further affects the transmitter release at the presynaptic terminal (Kole, Letzkus, et al. 2007; Dodson et al. 2002; Connor and Stevens 1971). K_v1 channels are in contrary to Na_v channels not anchored by ank-G but are clustered by postsynaptic density-93 (PSD-93) (Ogawa et al. 2008). In contrast, K_v7 ($K_v7.2$, 7.3) channels have a similar binding motif as Na_v channels, and are thus anchored by ank-G and localized distally within the AIS (Figure 2, Pan 2006). K_v7 channels stabilize the neuronal resting potential and are clustered near Na_v channels, thereby preventing repetitive firing of APs and dampening AP initiation (Figure 3B, Battefeld et al. 2014). The approximate location of K_v7 to Na_v channels can also enhance the conduction of the AP by accelerating the spike upstroke (Battefeld et al. 2014). $K_v2.1$ is located proximally in the AIS of pyramidal neurons in the hippocampus and cortex (Sarmiere et al. 2008), and clusters at ank-G-deficient sites (King et al. 2014). K_v2 channels have a high activation threshold and are activated by APs (Johnston et al. 2008). Functionally, they promote repetitive firing by accelerating the repolarization phase by

hyperpolarizing the membrane (Johnston et al. 2008). Because of its location, K_v2.1 channels might regulate the backpropagation of APs from the AIS to the soma (Sarmiere et al. 2008). These results are controversial, because most studies only observed K_v2.1 in the somatodendritic compartment and not in the axonal compartment (Scannevin et al. 1996; Du et al. 2000).

Although less abundant, Ca_v channels contribute to the modulation of the AP frequency (Bender and Trussell 2009). An influx of calcium ions can activate various intracellular pathways, potentially modifying the activity of other ion channels, thus altering the waveform and frequency of APs (Bender and Trussell 2009). Calcium (Ca^{2+}), which enters the AIS via voltage-gated Ca_v channels, can be sequestered by organelles that are localized to the AIS of pyramidal neurons in the hippocampus and neocortex (Peters, Proskauer, and Kaiserman-Abramof 1968). The AIS of neocortical pyramidal neurons contains P/Q-type (Ca_v2.1), N-type (Ca_v2.2) as well as R- and T-type Ca_v channels (Bender and Trussell 2009; Yu et al. 2010). Ca_v2.1 and Ca_v2.2 are clustered at the AIS and control AP generation and waveform (Yu et al. 2010). These channels have a high activation threshold and suppress AP generation by facilitating AP repolarization through the activation of Ca^{2+}-activated K_v channels in pyramidal neurons of the prefrontal cortex (Figure 3C, Yu et al. 2010). T-type (Ca_v3.1/Ca_v3.2) and R-type (Ca_v2.3) Ca_v channels influence AP generation and spike burst shape (Figure 3C, Bender and Trussell 2009). Low voltage-activated calcium channels trigger burst firing, and blocking these channels results in broadening of the AP (Bender and Trussell 2009). Interestingly, Ca^{2+} influx occurs in two distinct domains depending on the Ca_v subtype (Lipkin et al. 2021). Ca_v3 localizes to hotspot regions that are coupled to calcium stores, whereas Ca_v2 channels localize to non-hotspot regions, assuming that these different subtypes contribute to different regulations of cellular processes (Lipkin et al. 2021). In addition, there is also evidence that Ca^{2+} can also enter the AIS through Na_v channels (Hanemaaijer et al. 2020).

Another aspect of electrogenesis in the AIS are GABAergic neurons that form axo-axonic synapses along the AIS in principal neurons. These synapses are present in numerous cortical areas and species such as rats, cats, and monkeys (Somogyi, Freund, et al. 1982; Somogyi, Nunzi, et al. 1983). GABAergic axo-axonic synapses at the AIS are located predominantly close to intra-axonal Ca^{2+}-stores, the cisternal organelles, thereby influencing the excitability of pyramidal neurons by increasing the intra-axonal calcium which furthermore regulates $GABA_A$ re-

ceptors which are associated with axo-axonic synapses (Figure 2, Benedeczky et al. 1994). Interestingly, whether axo-axonic synapses depolarize or hyperpolarize the membrane depends strongly on the resting membrane potential and the reversal potential of $GABA_A$ receptors of the postsynaptic neuron (Woodruff et al. 2011). When pyramidal neurons of layers II/III have a more hyperpolarized membrane than the reversal potential of GABA (E_{GABA}), axo-axonic synapses are depolarizing, whereas they have a hyperpolarizing effect when the postsynaptic membrane is more depolarized than E_{GABA} (reviewed in (Inan and Anderson 2014). During development, GABA undergoes a postnatal shift. During early developmental stages, GABA signals induce outward Cl^- currents and thereby depolarize, whereas in the mature brain, it induces the inflow of Cl^- and thereby hyperpolarizes the membrane (reviewed in (Peerboom and Wierenga 2021)). Hence, each GABA stage during development ensures that its role matches that of the developing network.

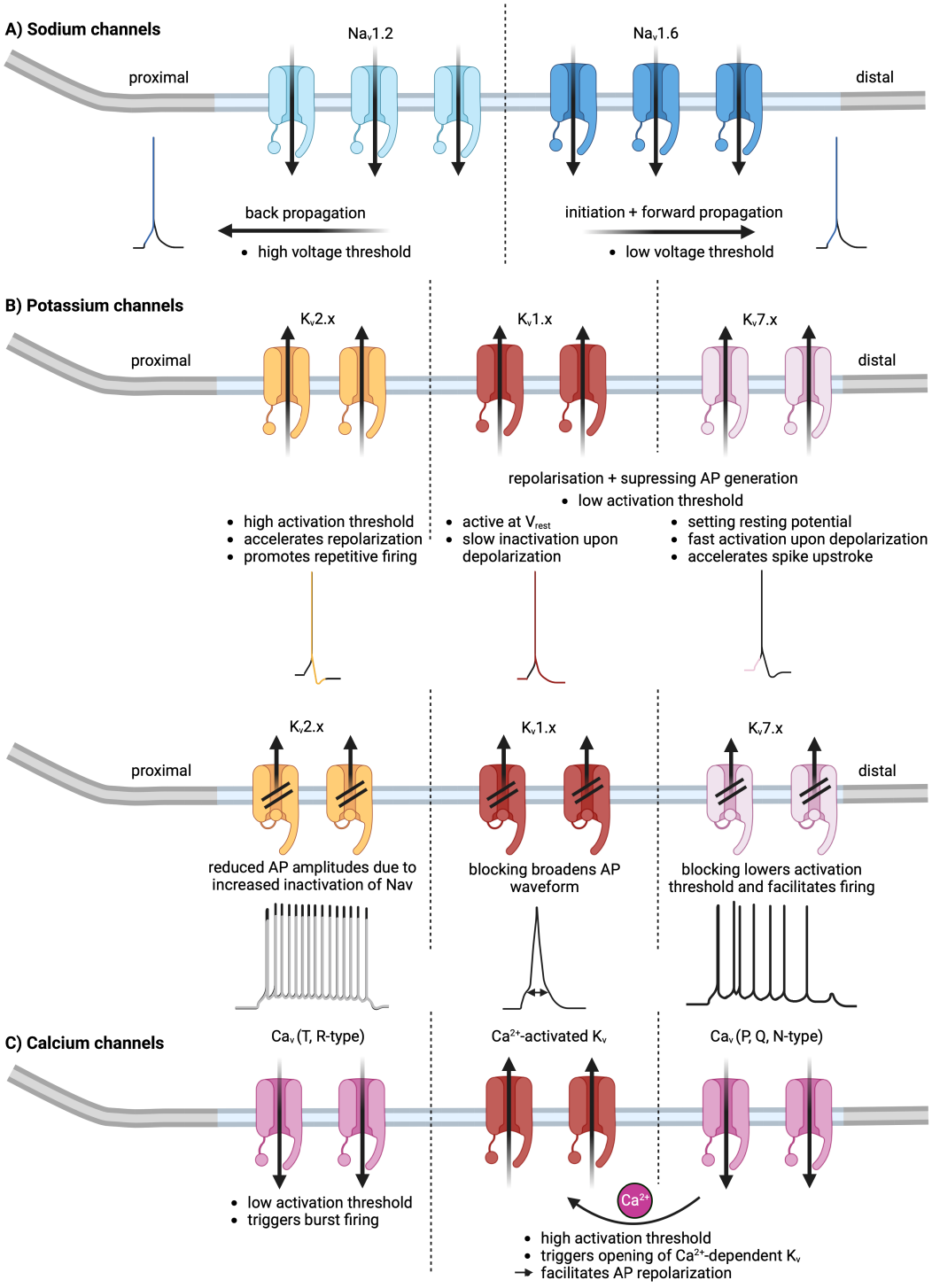

Figure 3: Voltage-gated ion channels clustered in the AIS and their regulation of action potentials. Action potential (AP) illustrations show when channels are active (indicated by color) and the influence of the specific channel on the AP. **A** $Na_v1.6$ is the Na_v main subtype responsible for AP initiations. $Na_v1.2$ is expressed proximally in the AIS and influences the backpropagation of APs to the somatodendritic membrane.

Figure 3 continued:

B K_v7 channels cluster distally within the AIS and are activated upon depolarization, thereby restricting repetitive firing and dampening AP initiation. K_v1 channels, also cluster distally, are fast-activating but slowly inactivated voltage-gated ion channels that are active at rest, influencing AP duration. K_v2 channels cluster proximally and are activated upon depolarization. They accelerate the repolarisation phase, thereby promoting repetitive firing. Owing to their location, they may regulate the backpropagation of APs to the soma. **C** Ca_v (P/Q, N-type) channels have high activation thresholds. When activated, they suppress AP generation by activating the calcium-activated K_v channels. Ca_v (T, R-type) channels have a low activation threshold and trigger burst firing, blocking those channels also resulted in increased AP duration. This illustration was adapted from the work of Engelhardt et al. 2019.

2.2.2 AIS plasticity

The AIS can adapt to physiological or pathophysiological changes in network activity or signaling pathways by fine-regulating its morphology despite its complex architecture (reviewed in (Yamada and Kuba 2016; Jamann, Jordan, et al. 2018)). Morphological alterations in the AIS and changes in neuronal excitability both occur in the time range from seconds to days (reviewed in (Petersen et al. 2017)). This interdependence suggests a potential regulatory mechanism for maintaining homeostasis. AIS plasticity can be subdivided into developmental plasticity and plasticity evoked by activity-dependent processes in mature neurons.

Developmental plasticity During the development phase, specific time windows known as critical periods (CP) occur (reviewed in (Jamann, Jordan, et al. 2018; Reh et al. 2020; Hensch 2005)). In these periods, experience-dependent plasticity forms new connections in sensory networks (reviewed in (Jamann, Jordan, et al. 2018)). The timing for opening and closing of a CP is influenced by several factors, including the sensory modality of a particular cortical region (reviewed in (Jamann, Jordan, et al. 2018)). One particular aspect of neuronal development is the AIS specialization, which can be first detected in motor neurons at embryonic day (E) 9.5 in mice (Le Bras et al. 2014), in cortical neurons at E14.5 in mice in Cajal-Retzius cells in layer I, and at E20.5 in neurons in presumed layer V neurons (Gutzmann et al. 2014). AIS scaffold proteins, particularly ank-G, recruit ion channels and CAMs (Zhou et al. 1998; Jenkins and Bennett 2001; Hedstrom et al. 2007). To date, in the primary visual and somatosensory cortex, AIS maturation has been observed in a triphasic manner, with maximal AIS length at juvenile stages (~P13), and a minimal AIS length in early postnatal day (P3) and adult mice (P28 and >P180) (Figure 4A, Gutzmann et al. 2014; Jamann, Dannehl, et

al. 2021). However, the cingulate cortex, a non-sensory cortex, showed an increase in AIS length during postnatal development, but remained stable throughout adulthood (Gutzmann et al. 2014). A pivotal principle of neuronal plasticity is the morphological adaptation in response to altered network activity. Local network activity or cell-intrinsic programs induce alterations in neuronal connections by forming and/or retracing neurites and synapses (reviewed in (Hensch 2005)). To maintain homeostasis, neuronal subcellular compartments respond to altered networks by adjusting their morphological structures.

Activity-dependent plasticity Plasticity is not restricted to CPs during development but can also occur in response to changes in network activity. Several studies have described AIS-specific parameters that contribute to neuronal excitability, such as length, position at the axon, and ion channel expression (reviewed in (Petersen et al. 2017; Jamann, Jordan, et al. 2018)). Global and chronic depolarization (2 days *in vitro*) by increased extracellular K^+ levels in dissociated hippocampal neurons induced relocation of the AIS (Figure 4B, Grubb and Burrone 2010). Additionally, increased extracellular K^+ levels were also observed to reduce AIS length in a time frame of only 3h in hippocampal dentate granule cells, which also resulted in Na_v channel reduction (Figure 4B, Evans, Dumitrescu, et al. 2015). This depolarization, elicited by elevated K^+ concentrations, increases intracellular Ca^{2+} concentration by activating L-type (Evans, Dumitrescu, et al. 2015) and T-type Ca_v channels (Grubb and Burrone 2010). Increasing the extracellular concentration of glutamate to unphysiologically high levels and thereby activating NMDA receptors leads to rapid endocytosis of Na_v and $K_v7.2/7.3$ ion channels within 10 minutes (Benned-Jensen et al. 2016). Furthermore, increased activity in pyramidal neurons of the barrel field cortex results in a decrease in AIS length *in vivo* (Jamann, Dannehl, et al. 2021). These changes were accompanied by a reduction in the intrinsic excitability by decreasing the repetitive firing rate and increasing the current required to reach the threshold to initiate APs (Jamann, Dannehl, et al. 2021). Depriving neurons of sensory input also affects the AIS. Removing sensory input *in vivo* resulted in increased AIS length and increased Na_v channel expression in the nucleus magnocellularis neurons and pyramidal neurons of the barrel cortex (Kuba, Oichi, et al. 2010; Jamann, Dannehl, et al. 2021). Functionally, this deprivation results in an increased excitability of these neurons. The removal of afferent inputs also showed changes in different K_v channels. One week after cochlear removal, $K_v1.1$ channels were replaced by slowly activating $K_v7.2$ channels (Kuba, Adachi, et al. 2014). This switch in ion channel expression

also increases excitability.

What mechanisms induce these alterations in the AIS length, position, and clustering of voltage-gated ion channels? One mechanism that has been described in response to chronic depolarization and ischemia is endocytosis of voltage-gated ion channels (Schafer et al. 2009; Benned-Jensen et al. 2016). The reduction of Na_v and K_v channels is triggered by an increased influx of Ca^{2+} through NMDA receptors, which in turn activates calpain, a protease involved in cytoskeleton proteolysis (Schafer et al. 2009). Furthermore, phosphorylation can strengthen or loosen numerous interactions within the AIS scaffold (Bréchet et al. 2008; Vacher et al. 2011; Evans, Sammons, et al. 2013; Evans, Dumitrescu, et al. 2015; Liu and Devaux 2014; Xu and Cooper 2015). Protein kinase CK2 regulates the interaction between ank-G and Na_v and K_v7 channels (Bréchet et al. 2008; Xu and Cooper 2015). AIS shortening and relocation are regulated by the Ca^{2+}- activated phosphatase calcineurin (Evans, Sammons, et al. 2013; Evans, Dumitrescu, et al. 2015). Cyclin-dependent kinase 5 (CDK5) protects AIS length by phosphorylating Na_v channels and promoting K_v1 channel clustering (Vacher et al. 2011). Therefore, it has an opposing effect compared to calcineurin (Evans, Dumitrescu, et al. 2015). Calmodulin regulates the assembly and clustering of K_v7 channels in the AIS (Liu and Devaux 2014). Other factors such as myosin light chain and myosin II contractile activity play a crucial role in regulating the assembly and distribution of AIS components along the axon (Berger et al. 2018). In addition, the AIS position can also be regulated by extrinsic factors, such as BDNF/NT3 (Guo et al. 2017). Changes in the AIS position, but not in the innervation pattern of GABAergic synapses, result in a mismatch between AIS and its synapses (Wefelmeyer et al. 2015; Benned-Jensen et al. 2016). This mismatch downregulates neuronal excitability (Wefelmeyer et al. 2015).

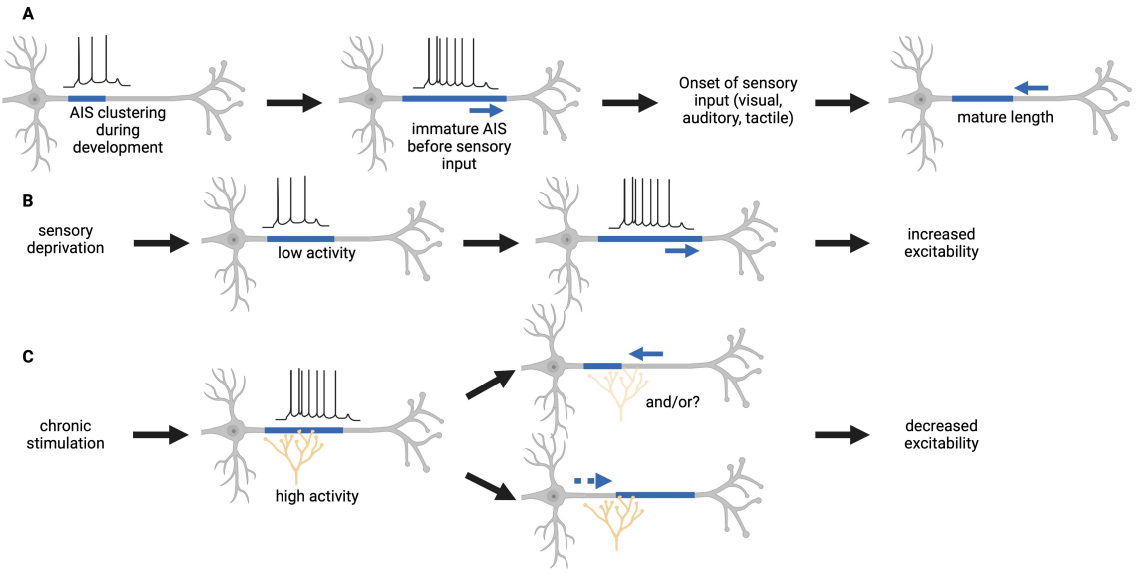

Figure 4: AIS plasticity. **A** The AIS of cortical pyramidal neurons increases in length until the onset of sensory input during development. **B** Sensory deprivation reduces the synaptic input and leads to AIS elongation, which is assumed to result in increased cellular excitability. **C** Chronic network stimulation leads to AIS length reduction and distal relocation. Axo-axonic synapses remain in place, further reducing cellular excitability. This illustration was adapted from the work of Engelhardt et al. 2019.

2.3 Pyramidal neurons in sensory processing and memory

Pyramidal neurons, named for their characteristic pyramidal-shaped cell bodies, are the primary excitatory neurons in the mammalian brain, particularly in the cerebral cortex and hippocampus, where they play crucial roles in many cognitive processes (reviewed in (Bekkers 2011)). Pyramidal neurons extend their axons over long distances and act as projection neurons. A subset of pyramidal neurons shows AcD characteristics instead of the canonical somatic axon origin. Although most pyramidal neurons share a similar morphology, with a dominant apical dendrite and several short-branched basal dendrites, their appearance varies across different cortical regions, even within a species (see Introduction 2.1). In this section, I describe the fact that even if neurons share a similar morphological shape, their functions can vary significantly depending on their location, inputs, and specific circuits they are part of.

2.3.1 Hippocampus

The hippocampus is a phylogenetically older cortical region and is critical for a wide range of functions, including spatial and declarative learning (Holmes and

Adey 1960), memory storage (Scoville and Milner 1957), and consolidation (reviewed in (McGaugh 2000)). Beyond these functions, it is also crucially involved in the regulation of emotions, fear, anxiety, stress (reviewed in (Bartsch and Wulff 2015)), and attention control (Green and Arduini 1954). The hippocampus consists of five subfields: dentate gyrus, and cornu ammonis (CA) which is usually subdivided into CA3, CA2, and CA1, and subiculum (Figure 5). Each subfield has its own functional characteristics that are particularly prominent in the way information is represented (Lee, Yoganarasimha, et al. 2004; Leutgeb et al. 2004). In this circuit, the dentate gyrus is the subfield most associated with receiving input from the upper layers of the entorhinal cortex (EC) via the perforant path. These signals are further projected via mossy fibers to CA3, and further propagated to CA1 via Schaffer collaterals and the subiculum by excitatory connections through the trisynaptic pathway (Figure 5, reviewed in (Cembrowski and Spruston 2019)). The second circuit, which is known in the hippocampus, is the monosynaptic pathway that bypasses the dentate gyrus and CA3 and directly projects information from the EC to CA1, via another branch of the perforant path, called the alvear pathway. CA1 and subiculum represent the outbound of these pathways and project to deep layers of the EC (Figure 5). Pyramidal neurons are found in CA3, CA1, and subiculum and are densely packed in these regions with a classic orientation. Their cell bodies are densely packed in the stratum pyramidale, the apical dendrite and its branches are located in the stratum radiatum and lacunosum-moleculare, while the basal dendrites are in stratum oriens. Apical and basal dendrites receive associative and commissural input (Draguhn et al. 2000).

Furthermore, the hippocampus consists of three distinct axes: the proximal-distal ‘transverse’ axis, the superficial-deep ‘radial’ axis, and the dorso-ventral ‘long’ axis. Subregions and axes have been described to exhibit extensive heterogeneity in their contribution to the different roles of the hippocampus (Figure 5, reviewed in (Cembrowski and Spruston 2019)). The pyramidal neurons in the CA3 region are essential for encoding, storing, and retrieving declarative memory (reviewed in (Cherubini and Miles 2015)), while CA1 mostly represents features of the environment (reviewed in (Igarashi et al. 2014)). Hippocampal pyramidal cells are one of the most studied neuronal subtypes in the mammalian brain and show marked heterogeneity along the axes. The proximal-distal axis is mainly responsible for encoding contextual information and is activated during spatial exploration (reviewed in (Cembrowski and Spruston 2019)). CA3 cells, located closer to the dentate gyrus, are strongly innervated by neurons of the EC and are most ex-

citable, while the most robust reactivation of memory retrieval was observed in the central CA3 region (Sun et al. 2017). Especially the CA1 region was found to have a heterogeneity along the transverse axis and may have distinct coding properties (reviewed by (Igarashi et al. 2014)). Overall, neurons in the CA1 region represent spatial information by specific place cells that fire specifically when the animal is at a certain location (O'Keefe and Dostrovsky 1971), as reviewed in (Igarashi et al. 2014)). Neurons that are located closer to the CA3 region represent spatial information more accurately, whereas neurons located closer to the subiculum process information about objects or odor identity, as well as associations with spatial locations (reviewed in (Igarashi et al. 2014)). The radial axis processes spatial learning and navigation. Superficial neurons border the stratum radiatum, whereas deep neurons are located closer to stratum oriens. The superficial layer is much more populated than the deep layer and cells are moderately smaller in the superficial CA1 region (reviewed in (Geiller et al. 2017)). Furthermore, early-born neurons are located in the superficial layer, whereas later-born neurons are positioned in the deep layer (reviewed by (Hayashi et al. 2015)). Pyramidal neurons located in the superficial layer fire earlier and at a higher probability than deep-layer neurons, but deep-layer neurons fire more bursts of action potentials (reviewed in (Geiller et al. 2017)). Additionally, deep-layer neurons have a higher probability to exhibit place fields during behavioral tasks ((Danielson et al. 2016), reviewed in (Geiller et al. 2017)), hypothesizing that the deep layer is important for spatial learning, while the superficial layer is involved in spatial navigation and foraging (Danielson et al. 2016). The dorsal-ventral axis is associated with emotional processing and spatial memory. The dorsal hippocampus is mostly associated with spatial information, whereas the ventral hippocampal connectivity is associated with areas involved in anxiety and emotional components ((Padilla-Coreano et al. 2016), reviewed in (Petrovich et al. 2001)). Furthermore, electrophysiological differences between the dorsal and ventral CA1 regions have been characterized in pyramidal neurons, which augment circuit differences (Dougherty et al. 2012; Malik et al. 2016). Neurons in the ventral hippocampus are intrinsically more excitable than those in the dorsal hippocampus, which changes linearly along this axis (Dougherty et al. 2012; Malik et al. 2016). Furthermore, the dendritic surface and branching of neurons in the dorsal hippocampus are greater than those in the ventral hippocampus (Dougherty et al. 2012). Interestingly, the birthdate of pyramidal neurons also contributes to heterogeneity. Neurons with the same birthdate exhibit strong coactivity across brain states and have a stronger preservation of overlapping place fields across different environments, in contrast to neurons born

on different days (Huszár et al. 2022). Overall, the presence, distribution, morphological differences, and date of birth of pyramidal cells in the hippocampus contribute differently to the crucial functions of the hippocampus.

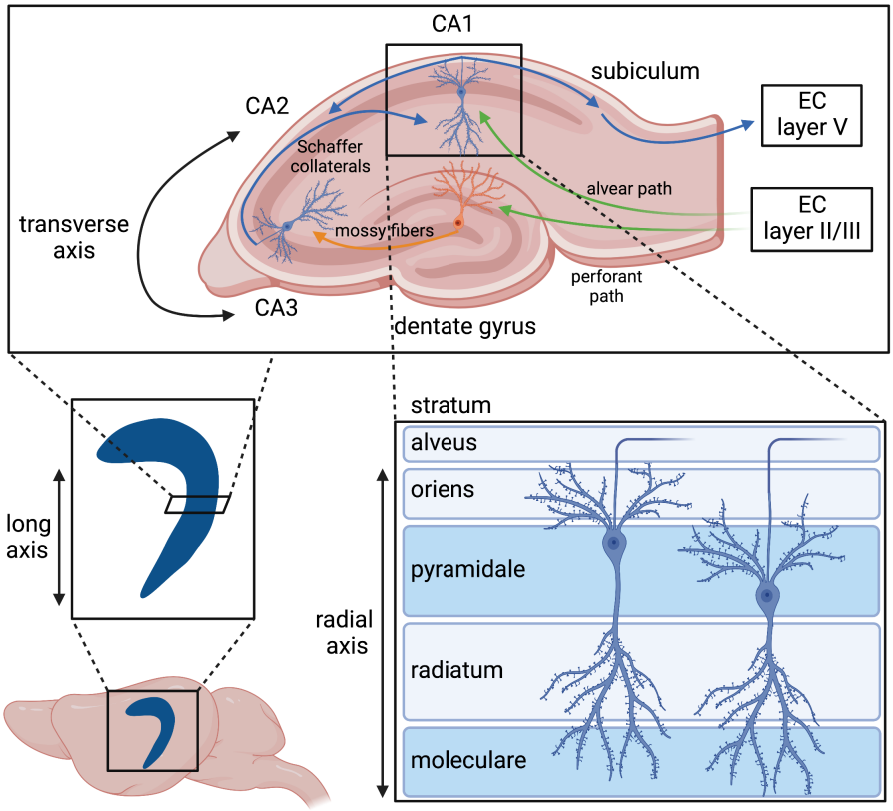

Figure 5: Hippocampal projections sites and functional distinct axes in the hippocampus. The long axis describes the axis from the ventral to dorsal hippocampus. The transverse axis describes the axis between the subregions of the hippocampus (dentate gyrus, CA3, CA2, CA1, and the subiculum). The radial axis describes the axis from the superficial to the deep layer. The upper illustration also depicts the different input and output sites of the hippocampus with monosynaptic (alvear) and trisynaptic (perforant) pathways. The illustration in the lower right depicts pyramidal neurons and their morphological orientation within the radial axis.

2.3.2 Primary somatosensory cortex

Pyramidal neurons are the most common type of neurons in the neocortex and play a key role in transmitting information between cortical areas and subcortical nuclei. These cells can be found in all cortical layers, except layer I, and are categorized according to their projection site (reviewed in (DeFelipe and Fariñas 1992)). Typical pyramidal neurons contain a prominent apical dendrite that is directed towards the pia mater and generally reaches layer I, where it forms a

tuft of branches; exceptions are most pyramidal neurons of layer VI and some of layer V (Figure 6, reviewed in (DeFelipe and Fariñas 1992)). From the base of the cell or its basal dendrite, the axon is directed downwards to the white matter and leaves the cortex to terminate in other cortical or subcortical regions (reviewed in (DeFelipe and Fariñas 1992)). Pyramidal neurons of the supragranular layer show smaller cell bodies and dendritic size compared to the infragranular layer and have a greater cell density, where the smallest cell bodies and dendritic size were found in layer IV followed by layer II (Rojo et al. 2016). The number of branches per dendritic order increased with the depth of the layer, excluding layer IV (Rojo et al. 2016).

This heterogeneity may stem from their afferent input and/or projection site. Therefore, I will describe the projection pathway of sensory information processing, using the whisker–barrel system as an example (Figure 6). When a whisker is stimulated, sensory receptors in the whisker follicle, originating from somata in the trigeminal ganglion, are activated and relay information along the trigeminal nerve to corresponding nuclei in the brain stem. This signal is transmitted to specific thalamic nuclei, which serve as relay stations before sending information to the primary whisker-related somatosensory cortex (S1) for conscious sensory perception (reviewed in (Staiger and Petersen 2021)). Single whiskers (also known as mystacial vibrissae) on the snout of a mouse are individually represented by an anatomically defined unit, which are called “barrelettes” in the trigeminal nuclei (Ma 1991), “barreloids” in the ventral posteromedial nucleus (VPM) of the thalamus (Van Der Loos 1976; Sugitani et al. 1990) and “barrels” in the whisker-related S1, which is also termed barrel cortex (Woolsey and Van der Loos 1970). These barrels are arranged in a pattern that precisely matches the positioning of the whiskers on the snout. It is assumed that two major parallel pathways of ascending sensory information processing occur in mice: 1) the lemniscal pathway from the principal trigeminal nucleus to the VPM and then to layer IV of barrels in S1, which relays information on touch and whisker position, and 2) the paralemniscal pathway from the spinal trigeminal interpolaris nucleus to the first-order division of the posterior medial thalamic nucleus (POm) and further to layer IV of whisker-related secondary somatosensory cortex (S2) (El-Boustani et al. 2020). The higher-order POm innverates layer I and layer Va of both S1 and S2 in mice and was found to not receive sensory input from the brainstem (El-Boustani et al. 2020), implying that this pathway might be entirely driven by cortical feedback pathways ((Theyel et al. 2010), reviewed in (Staiger and Petersen 2021)). Barrels

are located in S1, with the strongest specialization in layer IV. They do not only represent whiskers in the barrel cortex, but also forepaw inputs in their respective S1 projection regions (Woolsey and Van der Loos 1970). Pyramidal neurons of layer IV and spiny stellate cells receive input from thalamic afferents, the first-order nucleus (VPM) (Benshalom and White 1986). In particular, spiny stellate cells receive a large proportion of thalamo-cortical axons (10 to 23%, (Benshalom and White 1986)). Pyramidal neurons in layer IV extend their apical dendrite into layer I. Spiny stellate cells, on the other hand, lack apical dendrites and are confined to layer IV. Both cell types project to layer III and to upper layer V, but also provide horizontal projections within layer IV. Layer II/III receives a major input from layer III of the contralateral hemisphere but also from ascending layer IV (lemniscal pathway) and layer Va (paralemnisical pathway) (reviewed in (Staiger and Petersen 2021)). These signals are integrated, and these neurons send their axons to layer V, where they ramify (reviewed in (Thomson 2007)), but also send long-range axonal projections to the motor cortex, whisker-related S2, dysgranualar zone, perirhinal temporal association cortex, and striatum (Yamashita et al. 2018). These layers (II/III/IV) process whisker inputs arriving via different whiskers within the mystacial array, which is important for associative information processing (reviewed in (Staiger and Petersen 2021)).

The predominant inputs to layer V neurons and their dendrites in layer III come from short- and long-range cortio-cortical projections, as well as the higher-order POm (reviewed in (Staiger and Petersen 2021)). Pyramidal neurons in layer V can be distinguished according to their receiving and projection sites as well as their firing characteristics, which can be intrinsically bursting or regular. The intrinsically bursting neurons are large pyramidal neurons (thick-tufted) with long apical dendrites, whose axons project to superior colliculus and/or pons. Regular spiking pyramidal neurons are smaller, shorter, and slender-tufted and project mostly to the contralateral hemisphere. Slender-tufted neurons dominate layer Va, whereas thick-tufted are dominant in layer Vb (Oberlaender, Boudewijns, et al. 2011). Pyramidal neurons in layer Va extend their apical dendrites up to layer I, and both layers are strongly innervated by the POm (Petreanu, Mao, et al. 2009) and have been observed to increase their activity in response to whisker movement (De Kock and Sakmann 2009). Layer Va neurons are also innervated by layer VI corticothalamic neurons (Kim et al. 2014) and innervate the apical dendrite of thick-tufted neurons in layer Vb (Oberlaender, Boudewijns, et al. 2011). Thick-tufted layer Vb pyramidal cells integrate information from all other layers

and display a major output node of the barrel cortex that contributes to sensory information processing and feeds forward this information to cortico-thalamic loops by projecting their axons to the striatum, superior colliculus, pons, and trigeminal nuclei (reviewed in (Staiger and Petersen 2021)). In the barrel cortex, thick-tufted layer V neurons in the deep layer, Vb, respond strongly to single whisker deflections (De Kock, Bruno, et al. 2007) and project strong, giant boutons to the POm (Groh et al. 2008). Interestingly, the large pyramidal layer V neurons are the major recipient of the excitation from layer III pyramidals while the smaller, slender-tufted layer V cells receive little or none of this input (Thomson and Bannister 1998).

Layer VI neurons, like layer V neurons, can also be distinguished according to their projection sites: 1) pyramidal neurons with cortio-thalamic (CT) projections and 2) cortico-cortical (CC) projections. The latter often have a non-pyramidal or inverted appearance (Kumar and Ohana 2008; Petrof et al. 2012; Pichon et al. 2012). CT pyramidal cells extend their apical dendrite in layer Va to III and their axonal collaterals remain to a large extent in layer VI and arborize throughout layer VI to layer IV. These neurons receive input from VPM and POm and mostly connect to cortico-cortical (CC) cells, local inhibitory neurons, nucleus reticularis (NRT) thalami and/or primary sensory core thalamic nuclei such as ventroposterior-medial (VPM) nuclei, which enables them to activate but also inhibit lemniscal relay cells ((Lam and Sherman 2010), reviewed in (Staiger and Petersen 2021)). CC cells grow an axon that reaches most layers of the barrel cortex and projects to S2 and motor cortex (Zhang and Deschênes 1997; Pichon et al. 2012). They are robustly activated after passive whisker touch (Oberlaender, De Kock, et al. 2012). These cells are assumed to form depressing synapses with CT cells (Mercer et al. 2005) and respond with a very short latency to whisker stimulation (Egger et al. 2020). It is assumed that their activity may potentially supply a rapid and robust input to certain layer Vb neurons, thereby assuring that sensory-evoked input is reliably transformed into cortical output (Egger et al. 2020).

Manipulation of the barrel cortex Early sensory experience influences the development of brain circuits, which affects both the morphological and functional organization of the brain, thus strongly influencing behavioral maturation. During the development of the sensory system, the wiring of the brain is influenced by various factors such as the competition between synaptic inputs and maintaining a balance between excitation and inhibition (reviewed in (Hensch 2005)). The time windows in early postnatal development where neuronal circuits are most

vulnerable to alterations are called “critical periods” and are necessary for normal development. Sensory deprivation during critical periods leads to irreversible alterations in cortex organization and later cognitive-behavioral abilities (reviewed in (Erzurumlu and Gaspar 2012)). To investigate the influence of neuronal activity on neural circuits, the barrel cortex is a widely used model system for studying these neuronal structure-function relationships (reviewed in (Erzurumlu and Gaspar 2012; Staiger and Petersen 2021)). Manipulation of the sensory periphery in various ways during a critical developmental period can result in plastic changes in the size and patterns of pre- and postsynaptic elements within the barrel cortex (reviewed in (Erzurumlu and Gaspar 2012)). At birth, rodent pups have already a complete set of fine whisker hairs that are immobile and curved backward. Shortly before their eyes open, these pups start displaying active “whisking” behavior at P14 (reviewed in (Erzurumlu and Gaspar 2012)). Whisker follicle cauterization or lesions of the infraorbital nerve before P4 permanently alter the central neural patterns’ organization and behavior. Cauterizing follicles of one row of whiskers on the day of birth caused the barrels, which correspond to this whisker row, to shrink in size; the barrels from the remaining whiskers, on the other hand, expanded in size (Van Der Loos and Woolsey 1973). Denervation of the sensory input by infraorbital nerve transection or vibrissa follicle damage leads to an aberration or complete absence of barrels in the cortex, respectively (Belford and Killackey 1980; Jensen and Killackey 1987). Whisker trimming or plucking in rodent pups does not lead to a complete absence of barrels because it does not completely block peripheral evoked activity and only reduces sensory activity (reviewed in (Kaas et al. 1983; Erzurumlu and Gaspar 2012). These moderate manipulations in P0 to P3 old rodent pups have been reported to reduce dendritic complexity and spines of barrel neurons and lead to behavioral deficits in the animal (Lee, Chen, et al. 2009). Furthermore, barrel cells in layer IV synapse onto neurons in layers II/III. The critical period for this projection appears between P10 and P14 (Maravall et al. 2004; Maravall 2004). For horizontal intralayer connections between layer II/III neurons, the critical period appears between P13-P16 (Wen and Barth 2011). These types of inputs have a discrete onset, induced by single whisker experience-induced plasticity, and cannot be induced before or after these time windows (Wen and Barth 2011). These findings indicate that sensory experience plays a crucial role in the development of the barrels and connectivity, which can be strongly influenced during critical periods of postnatal development.

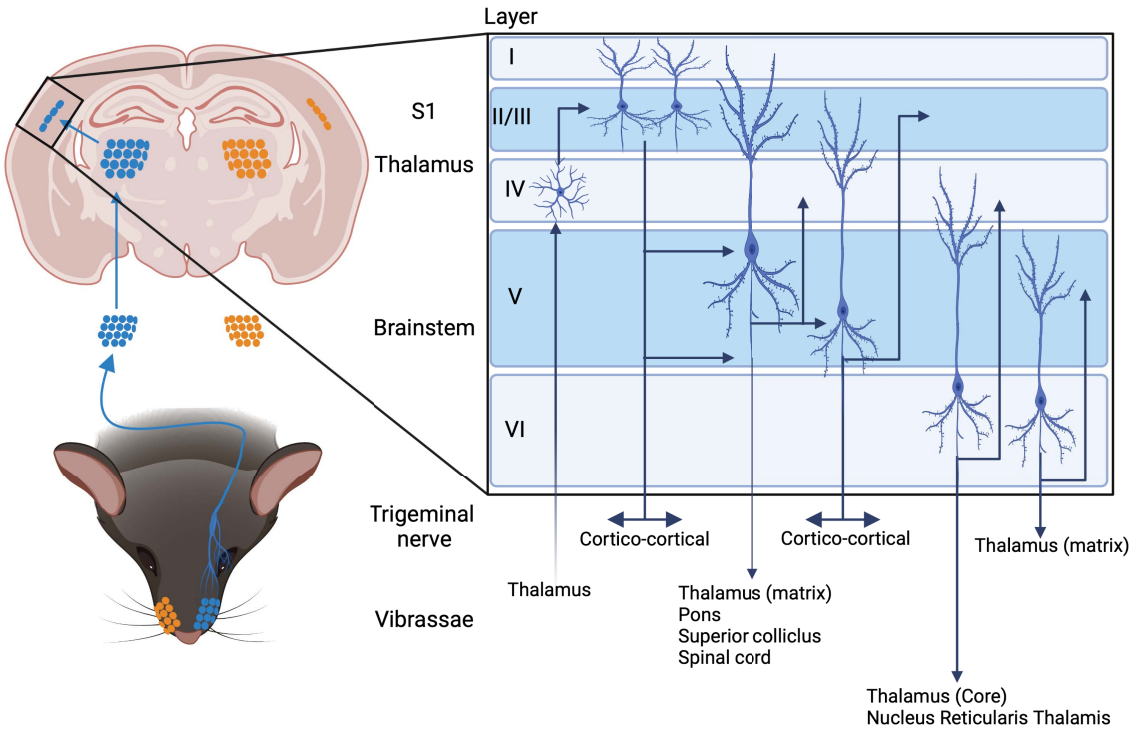

Figure 6: Whisker-related projection pathway. Whisker stimulation activates sensory receptors in the whisker follicle stemming from the trigeminal ganglion. The trigeminal nerve relays a signal to the contralateral brainstem. This signal is transmitted to specific thalamic nuclei before information is sent to the whisker-related somatosensory cortex. The illustration on the right depicts the input, intracortical, and output pathways (for details, see the text). This illustration was inspired by the work of Thomson 2007.

2.4 Objectives

As outlined in the introduction, dendritic, rather than somatic, axon origins in various neuronal populations have been described in several brain regions and species. It is also clear that different sites of axon origins lead to different functional properties of neurons within their respective networks. However, it is still largely unknown what drives the development of AcD cells. Previous studies carried out in the hippocampus showed that the dendrite from which the axon branches off, functions as a privileged synaptic input channel (Thome, Kelly, et al. 2014) and enables the axon to circumvent somatic inhibition (Hodapp et al. 2022). Furthermore, in previous studies, the AIS was observed to adapt in its length and/or position in an activity-dependent manner (Grubb and Burrone 2010; Evans, Dumitrescu, et al. 2015; Jamann, Dannehl, et al. 2021).

Therefore, this study aimed to investigate the development of axon onset and AIS in principal neurons of the hippocampus and the primary somatosensory cortex. These brain regions were selected to investigate putative differences between a sensory and a memory-processing network. Additionally, I aimed to elucidate whether the development of axon onset is influenced in an activity-dependent manner as has been observed for the AIS.

The following questions were addressed in this thesis:

• What are the morphological differences between AcD and nonAcD neurons with respect to the length and sodium channel distribution of their AIS and axo-axonic synapses?

• Does the ratio of AcD neurons change during development in murine hippocampus and primary somatosensory cortex (S1)?

• Does neuronal activity influence the emergence of an axon/AIS at the basal dendrite versus the soma?

Based on these questions, the presented results reveal new insights into the distribution of sodium channels along the AIS of AcD and nonAcD cells and that the number of AcD neurons varies during development, especially in the hippocampus. Live-cell imaging *in vitro* revealed that the axon origin can be dynamically regulated by transforming from AcD and nonAcD state and *vice versa* over a few

days. Finally, this work demonstrates that increased network activity promotes AcD development, both *in vitro* and *in vivo*.

3 Material and Methods

Parts of the text of the following section have been taken from Lehmann et al. 2023 and were originally written by myself.

3.1 Animals

All animal procedures were performed in accordance with the guidelines of the Animal Care and Use Committee of Mannheim Medical Faculty, Heidelberg University, and were approved by the state of Baden-Württemberg under EU guidelines (35-9185/G-119/20). Mice of both sexes from a transgenic mouse line expressing green fluorescent protein (GFP) under the Thy1 promoter (Tg/Thy1-EGFP) MJrs/J, provided by Jackson Laboratory Maine, USA (Feng et al. 2000) were used in this study. Mice were kept in the animal house under regular supervision and were maintained with water and food *ad libitum* on a regular 12/12 h light/dark cycle at a temperature of 22 ± 2°C and relative humidity of 45-65%. The offspring were separated from their mothers at P28.

Sparse intrinsic EGFP labeling of excitatory cells in the primary somatosensory cortex (S1) and ventral hippocampus (vHC) allowed the analysis of individual cell morphology without prior staining. Most Thy-GFP-positive cells were expressed in the CA1 region of the vHC, and in layers V and VI of the S1 cortex.

3.1.1 Development study

To investigate AcD development in the S1 and vHC, 5-6 brains per age group were analyzed (Figure 7). S1 and vHC from the same mice were investigated. During early maturation up to P8, Thy1-GFP-positive cells were not observed in S1. Therefore, until P8, only Thy1-positive cells from the vHC were analyzed. To further investigate the differences in maturation between AcD and nonAcD cells in each brain region, the AIS length, $Na_v1.6$ channel distribution within the AIS, and its expression length were analyzed by staining against markers for the AIS scaffold protein ank-G and the voltage-activated sodium channel $Na_v1.6$ (for more details, see section for staining procedure 3.3.2 and for analysis 3.4.2). Furthermore, axo-axonic synapses located at the AIS were investigated in P28 old animals by staining against markers for the AIS scaffold (βIV-spectrin), $GABA_A$ receptor α2 subunit (postsynaptic site), and vGAT (presynaptic site).

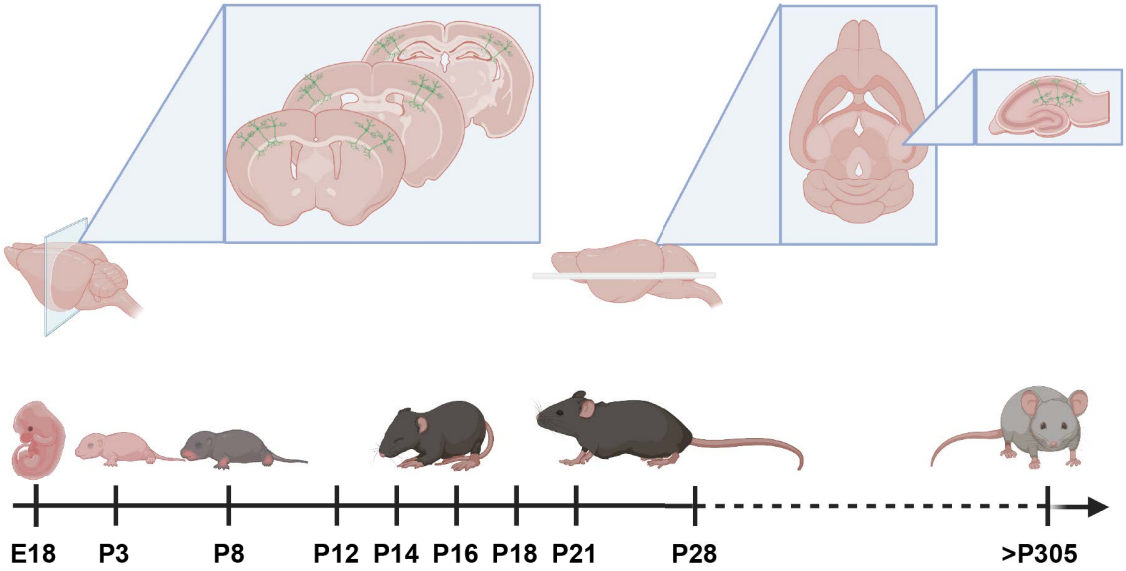

Figure 7: Schematic overview of the experimental design of the developmental study. Brain slices were acquired from transgenic mice (Thy-GFP). For the analysis of the primary somatosensory cortex (S1), the brains were dissected coronally (upper left) and horizontally for the ventral hippocampus (upper right). Green neurons indicate Thy1-GFP positive cells). Selected time points coincided with numerous critical windows of neuronal differentiation and connection (Erzurumlu and Gaspar 2012).

3.1.2 Sensory deprivation and activation paradigm

To manipulate the activity of the barrel field cortex, whiskers were trimmed unilaterally daily either from P0 to P16, P12 to P16, or for five consecutive days in adult mice (>P100, Figure 8). Whisker trimming was performed under a binocular microscope by using a curved scissor. The whiskers of the pups were trimmed without anesthesia because they showed no signs of distress and could be easily handled. Adult mice (>P100) were briefly anesthetized with isoflurane before trimming to minimize stress during the procedure. For the sensory activation study, mice with unilaterally clipped whiskers were placed in an enriched environment (EE) cage for 6h daily over a period of five consecutive days (Figure 8). The EE cage was significantly larger than the home cage (floor space home cage: 542 cm^3 (cage type 1285L, Techniplast Germany GmbH), EE cage: 1500 cm^3 (cage type 1500U, Techniplast Germany GmbH). Furthermore, the EE cage contained different beddings (diverse barks in different sizes, moss, pine cones, different sizes of pebbles, cellulose paper) and objects with different textures (wooden bridge, fabric hammock, cardboard tubes, self-rolled bubble wrap tunnel, wooden sticks, and marbles). Novel objects were added daily to the EE cages, to avoid habituation. The cages were maintained in the dark. One hour prior to the EE cage

exposure, mice were placed in their home cage in a darkened room to adjust to their surroundings. Unilateral whisker trimming allowed to compare the putative effects of sensory manipulations within individual mice; thus, the sensory-deprived hemisphere was compared to the hemisphere of intact whisker projection. For the different paradigms 5-6 brains were analyzed (EE juvenile: 6 brains, EE mature: 5 brains, short-term deprivation: 6 brains, long-term deprivation: 5 brains). For AcD percentage analysis, approximately 100 Thy1-GFP neurons in the barrel field per brain and hemisphere were analyzed. For AIS analysis of layer V neurons, an approximately equal number of AIS in AcD and nonAcD neurons were analyzed, despite the variations in their frequencies within the samples and experiments. Therefore, approximately 25 AIS per hemisphere and brain were analyzed.

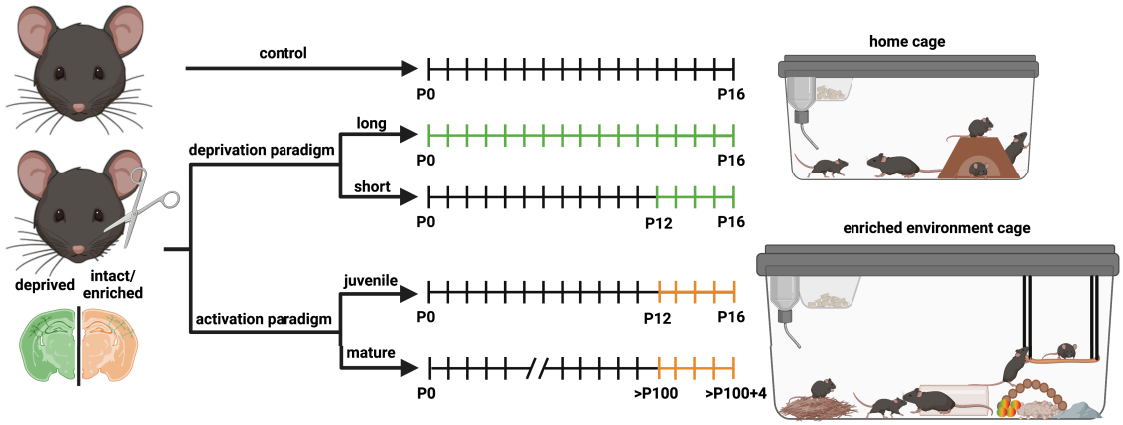

Figure 8: Schematic overview of the experimental design of *in vivo* studies. Unilateral whisker trimming was performed at different time periods indicated by the timelines. The periods ranged from P0-P16 and P12-16 in the deprivation paradigm (green hemisphere and lines). For the activation paradigm, unilateral whisker trimming was performed for five consecutive days and mice were placed in an enriched environment cage (EE) for 6h daily (in young mice: P12-P16) and in adult mice (>P100 + 4 days) (orange hemisphere and lines). In control mice, whiskers remained unaffected bilaterally. Whisker-related projection sites were compared among individual mice (trimmed vs. intact). The EE cage was larger than the home cage (452 cm^3 vs. 1500 cm^3), contained different beddings (diverse barks of different sizes, moss, pine cones, different sizes of pebbles, cellulose paper) and objects with different textures (wooden bridge, fabric hammock, cardboard tubes, self-rolled bubble wrap tunnel, wooden sticks, and marbles). Novel objects were added daily to the EE cages to avoid habituation.

3.2 Organotypic slice culture

3.2.1 Preparation

Animals aged P5 were quickly decapitated and their brains were placed in ice-cold preparation medium (Table 1). For coronal slicing, the cerebellum was removed and the posterior part of the brain was glued onto a vibratome stage. To improve the stability of the brain during slicing, a 1% agarose block dissolved in PBS was placed on the ventral side of the brain. Coronal slices were prepared using a vibratome (Microm HM 650V with a cooling chamber, Microm CU65, Thermo Scientific). The slice thickness was 275 µm to preserve the 3D organization and network connectivity within the slice. The hemispheres were dissected and transferred onto semipermeable Millicell cell culture inserts (Millipore, 0.4 µm pores, diameter 30 mm, hydrophilic PTFE) and placed in a cooled 6-well plate (Sarstedt AG & Co.KG, Nürnbrecht, Germany). Each well contained 1 ml of preparation medium. After dissecting the brain, Millicell inserts were transferred into a new sterile 6-well plate under sterile conditions, and 37°C warm cell culture growth medium was added to each well (Table 2). Freshly created organotypic slice cultures (OTC) were kept in an incubator (Hera cell 150, Thermo Electron Corporation) at 35°C and 5% CO2. The culture medium (1 ml) was exchanged three days after slicing with either fresh, untreated medium or with medium containing one of the following treatments: 15 µM (-)- bicuculline methiodide; 10 mM $MgSO_4$; 6 mM KCl; 1 µM ifenprodil hemitartrate; or 1 µM DMSO; Table 3. The treatment series lasted for seven consecutive days, initiated from day 3 *in vitro* (DIV) to DIV10. One cultured hemisphere was treated with one of the reagents mentioned above and the contralateral hemisphere served as a control (Figure 9). Additionally, to exclude effects of lateralization, hemispheres of cortical OTCs were alternately treated with one of the reagents (Figure 9). Every second day, half of the medium (500 µl) was renewed.

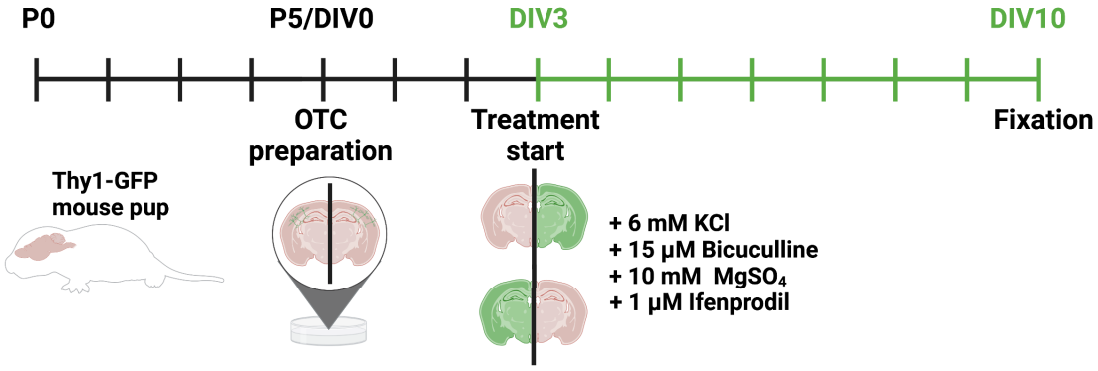

Figure 9: Schematic overview of the experimental design of *in vitro* studies. Cortical OTCs were generated from Thy1-GFP mice at P5 by dissecting the brain coronally. The hemispheres of the cortical slices were separated. The treatment series lasted for seven consecutive days, initiated from DIV3 to DIV10. One hemisphere was treated with one of the reagents, while the contralateral hemisphere served as a control. To avoid hemispherical effects, hemispheres were alternately treated with one of the reagents (indicated by the color of the hemispheres). At DIV10, OTCs were fixed and immunohistochemically stained.

Composition	Volume (500 ml)	Source
Minimum Essential Medium (MEM) (1x)	470.5 ml	Gibco, Life Technologies Corporation, NY, USA
GlutaMAX^{TM}-I (100x)	5 ml	Gibco, Life Technologies Corporation, NY, USA
1 M HEPES in 0.85% NaCl	12 ml	Lonza, Verviers, Belgium
D(+)-Glucose (45%)	5 ml	Sigma-Aldrich, St. Louis, USA
Penicillin/Streptomycin	5 ml	Sigma-Aldrich, St. Louis, USA
1M NaOH	2 ml	

Table 1: Preparation medium

Composition	Volume (50 ml)	Source
Minimum Essential Medium (MEM) (1x)	21 ml	Gibco, Life Technologies Corporation, NY, USA
Basal Medium Eagle (BME)	12.5 ml	Gibco, Life Technologies Corporation, NY, USA
Normal Horse Serum (NHS)	12.5 ml	Gibco, Life Technologies Corporation, NY, USA
GlutaMAX^{TM}-I (100x)	0.5 ml	Gibco, Life Technologies Corporation, NY, USA
1 M HEPES in 0.85% NaCl	1.25 ml	Lonza, Verviers, Belgium
D(+)-Glucose (45%)	0.75 ml	Sigma-Aldrich, St. Louis, USA
Sodium Bicarbonate (7.5%)	1 ml	BioWhittaker, Lonza, Walkersville, USA
Penicillin/Streptomycin	0.5 ml	Sigma-Aldrich, St. Louis, USA
1M NaOH	20 µl	

Table 2: Growth culture medium

Reagent	Composition	Molecular weight	Source
KCl	In growth culture medium: 6 mM KCl	M=74.56 g/mol	Carl Roth, Karlsruhe, Germany
$MgSO_4$	In growth culture medium: 10 mM $MgSO_4$*7H2O	M=246.48 g/mol	AppliChem, Darmstadt, Germany
Bicuculline	In growth culture medium: 15 µM (-)-Bicuculline methiodide	Varies per batch, in experiments: M=518.31 g/mol	Tocris, Bioscience, Bristol, UK
Ifenprodil	In growth culture medium: 1 µM Ifenprodil Hemitartrate	Varies per batch, in experiments: M=414.00 g/mol	Sigma-Aldrich, St. Louis, USA
Dimethyl sulfoxide (DMSO)	used as solvent for ifenprodil and added to culture medium in corresponding control OTCs		Sigma-Aldrich, St. Louis, USA

Table 3: Treatments used in OTCs

3.2.2 Live-cell imaging

OTCs grown on semipermeable membranes have been used as models for long-term live-cell imaging (Gogolla et al. 2006). Thy1-GFP positive cells in treated and control OTCs were live-imaged from DIV3 to DIV10 every 24h. These OTCs were placed in single sterile tissue culture dishes (Falcon, 35 mm, Easy-Grip Style Cell Culture Dish, Cat.No. 353001, Thermo Fisher Scientific, Waltham, USA). For live-image acquisition, a C2 Nikon confocal microscope (Nikon Instruments, laser line: 488 nm) with a 60x objective (water immersion, numerical aperture of 1.0, CFI Apo 60XW NIR) was used. Images were sized 1024 × 1024 pixels, and vertical step size was 0.5 µm. For optimal acquisition, the laser intensity and exposure time were adjusted based on the fluorescence intensity of the labeled cells. To further enhance the intensity, the pinhole was opened, but never exceeded 2 AU (Airy Unit of the pinhole diameter). To image OTC in aqueous solution, sterile PBS (37°C warm) was placed on the slice and immediately removed after image acquisition. After imaging and removing the PBS, the OTC was placed back in the incubator. Image acquisition lasted for a maximum of 30 minutes per OTC. To avoid contamination, the lens was cleaned with 70% ethanol in water before and after imaging the individual OTCs.

3.2.3 Electrophysiology

Whole-cell patch-clamp recordings were performed in treated and control cortical OTCs in the S1 region from DIV6 to DIV10. For recording, OTCs were moved into a chamber perfused with artificial cerebrospinal fluid (aCSF, composition: 125 mM NaCl, 2.5 mM KCl, 1.25 mM NaH_2PO_4, 25 mM $NaHCO_3$, 1 mM $MgCl_2$, 2 mM $CaCl_2$, 25 mM glucose, pH 7.4, oxygen-saturated with 95% O_2, 5% CO_2, Table 4), which had a temperature of 35-37°C (monitored by TC-20, temperature control system, NPI electronic GmbH, Tamm, Germany). OTC slices were imaged using an upright Nikon Eclipse FN1 equipped with a DIC contrast filter (Supplementary Table 10). Neurons were visually identified and selected for whole-cell recordings. The neuronal type was confirmed during recording by the characteristic firing pattern as well as post hoc by the characteristic morphology (biocytin-filling and staining). Patch pipettes (borosilicate glass, outer diameter 1.5 mm, inner diameter 0.8 mm, Science Products GmbH, Hofheim, Germany) were pulled on a Flaming/Brown P-97 Puller (Sutter Instruments, Novato, USA). The tip resistance ranged from 3 to 6 MΩ in bath solution. The patch pipette was connected to an AgCl wire and was filled with an intracellular solution based on potassium glu-

conate (Table 4): 140 mM K-gluconate, 3 mM KCl, 4 mM NaCl, 10 mM HEPES, 0.2 mM EGTA, 2 mM Mg-ATP, 0.1 mM Na_2-GTP. The solution was titrated to pH 7.2 with KOH, and had an osmolarity of 270 mOsmol/l. The liquid junction potential was calculated to be + 15.9 mV (https://swharden.com/LJPcalc/) and corrected in the analysis. For recording excitatory synaptic inputs, I used an intracellular solution based on cesium methanesulfonate which contained: 135 mM Cs-$MeSO_3$, 8 mM NaCl, 10 mM HEPES, 0.3 mM EGTA, 0.1 mM spermine, 7 mM Na_2Phosphocreatine, 2 mM Mg-ATP, 0.3 mM Na_2-GTP. This internal solution was titrated to pH 7.3 with KOH, and had an osmolarity of 300 mOsmol/l. The liquid-junction potential was calculated to be + 16.5 mV (https://swharden.com/LJPcalc/) and corrected in the analysis. Prior to recordings, 3 mg/ml biocytin (Sigma-Aldrich, St. Louis, USA) was added to the intracellular solution for post hoc morphological reconstruction. Recordings were performed using a HEKA EPC10 USB amplifier controlled by the Patchmaster Software (HEKA Electronics, Multi Channel System MCS GmbH, Reutlingen, Germany). The data were low-pass filtered at 10 kHz in the amplifier in combination with an additional Bessel filter at 2.9 kHz. They were digitized and sampled at 50 kHz. Fast and slow capacitances were compensated with the included auto-function of the Patchmaster Software in cell-attached and whole-cell configurations, respectively. To ensure the quality of recordings, the series resistance (R_s) was repeatedly measured by giving a negative 10 mV test pulse for 100 ms, and neurons exceeding 25 MΩ of R_s were excluded from the analysis. Additionally, during post hoc analysis, the measured voltage values obtained from neurons in the current-clamp mode during step protocols were corrected by subtracting the steep voltage transients. Cells were also excluded from analysis if they required more than -200 pA holding current to remain at -70 mV resting potential. The resting membrane potential (RMP) was measured upon entering the whole-cell configuration in current-clamp mode at I=0 as soon as the measured membrane potential had stabilized. (APs) were elicited with a step protocol of 20 ms pulses, with an increment of 10 pA per step. For the analysis of firing patterns, 500 ms long current pulses were injected with an increment of 50 pA per step. This protocol was used to construct input-output (AP frequency) curves. Spontaneous postsynaptic currents (PSCs) were recorded for 120 seconds at -70 mV. For the examination of voltage-dependent conductances, the neuron was clamped stepwise for 500 ms to different voltages ranging from -90 mV to +30 mV, with an increment of 10 mV per step. At each voltage step, the maximal inward current was observed. Early and delayed rectifier potassium currents were measured at a voltage step of +30 mV.

Solution	Composition	Source
aCSF Solution	In ddH_2O:	
	125 mM NaCl	Carl Roth, Karlsruhe, Germany
	2.5 mM KCl	Carl Roth, Karlsruhe, Germany
	1.25 mM Na_2PO_4 * $2H_2O$	Carl Roth, Karlsruhe, Germany
	25 mM $NaHCO_3$	Merck, Darmstadt, Germany
	1 mM $MgCl_2$ * H_2O	Merck, Darmstadt, Germany
	2 mM $CaCl_2$	AppliChem, Darmstadt, Germany
	25 mM D(+)-Glucose	Carl Roth, Karlsruhe, Germany
	Osmolarity: 300mOsmol/l	
Intracellular Solution based on K-Gluconate	In ddH_2O:	
	140 mM Potassium D-Gluconate	Sigma-Aldrich, St. Louis, USA
	3 mM KCl	Carl Roth, Karlsruhe, Germany
	4 mM NaCl	Carl Roth, Karlsruhe, Germany
	10 mM HEPES Buffer grade	AppliChem, Darmstadt, Germany
	0.2 mM EGTA	Sigma-Aldrich, St. Louis, USA
	2 mM Mg-ATP	Sigma-Aldrich, St. Louis, USA
	0.1 mM Na_2-GTP	Sigma-Aldrich, St. Louis, USA
	pH: 7.2 with 1M KOH	
	Osmolarity: 270 mOsmol/l	
	3 mg/ml Biocytin	Sigma-Aldrich, St. Louis, USA
Intracellular Solution based on Cs-$MeSO_3$	In ddH_2O:	
	135 mM Cs-$MeSO_3$	Sigma-Aldrich, St. Louis, USA
	8 mM NaCl	Laborchem International neoFroxx GmbH, Einhausen, Germany
	10 mM HEPES Buffer grade	Carl Roth, Karlsruhe, Germany
	0.3 mM EGTA	Sigma-Aldrich, St. Louis, USA
	0.1 mM Spermine	Sigma-Aldrich, St. Louis, USA
	7 mM Na_2Phosphocreatine	Sigma-Aldrich, St. Louis, USA
	2 mM Mg-ATP	Sigma-Aldrich, St. Louis, USA
	0.3 mM Na_2-GTP	Sigma-Aldrich, St. Louis, USA

Solution	Composition	Source
	pH: 7.3 with KOH Osmolarity: 300 mOsmol/l 3 mg/ml Biocytin	 Sigma-Aldrich, St. Louis, USA

Table 4: Solutions for electrophysiology

3.3 Immunofluorescence

3.3.1 Tissue fixation

For the developmental study, E18–P8 animals were decapitated, and their brains were immediately dissected and fixed by immersion in 2% paraformaldehyde (PFA, 100 mM PBS, pH 7.4, Table6) at 4°C. The fixation duration depended on the diameter of the brain, according to the 'rule of thumb' predicting 1 mm tissue penetration per hour. Therefore, fixation time ranged from 1.5h to 2.5h. Following this, the brains were cryoprotected with 30% sucrose solution overnight at 4°C. Animals aging P12 and older were transcardially perfused under deep anesthesia with ketamine (120 mg/kg per body weight) and xylazine (16 mg/kg per body weight) (Table 5). First, mice were exsanguinated with ice-cold 0.9% NaCl (B.Braun Melsungen AG, Melsungen, Germany) and subsequently fixed with 2% PFA at room temperature for 5 minutes. The brains were removed from the skull and cryoprotected in 30% sucrose solution overnight at 4°C. On the following day, the cerebellum was removed, and the brain was placed in a Tissue-Tek Cryomold (Sakura Finetek Europe, aan den Rjin, Netherlands) filled with the cryoprotectant Tissue-Tek (Sakura Finetek Europe, aan den Rjin, Netherlands). A container filled with isopentane was pre-cooled in liquid nitrogen. Once the isopentane reached the desired low temperature, the cryomold with the brain was carefully placed in this container and snap-frozen. These samples were stored at -20°C until sectioning. Sectioning was performed using a cryostat (Microm, HM 550, Thermo Scientific, Waltham, USA). The tissue block was first trimmed to the desired region. Brain slices for the S1 cortex were coronally orientated, and slices for vHC horizontally. Slices from the region of interest were cut at 80 µm thickness and post-fixed in 2% PFA for 15 min under free-floating conditions. After post-fixation, the slices were placed in 1x PBS and kept in the dark until multichannel immunofluorescence staining was performed. OTC slices were fixed in 2% PFA for 20 minutes at 4°C and stored in 1x PBS at 4°C for up to two days until staining was performed.

Solution	Target	Concentration	Source
Isoflurane	analgetic and muscle relaxant		CP Pharma, Burgdorf, Germany
Ketamine (10%)	analgetic and hypnotic	120 mg/kg per body weight	bela-pharm GmbH & Co.KG, Vechta, Germany
Xylazine (2%)	sedative, analgetic, and muscle relaxant	26 mg/kg per body weight	Serumwerk Bernburg AG, Bernburg, Germany
NaCl (0.9%)			B. Braun Melsungen AG, Melsungen, Germany

Table 5: Anesthetics and its utilization

Solution	Composition	Source
NaCl	0.9% NaCl	B. Braun Melsungen AG, Melsungen, Germany
PFA	In 1x PBS: 2% PFA pH: 7.4	Merck, Darmstadt, Germany
Sucrose	In 1x PBS: 30 % Sucrose	Carl Roth, Karlsruhe, Germany
Isopentan (2-Methylbutan)		Carl Roth, Karlsruhe, Germany

Table 6: Solutions for tissue fixation

3.3.2 Staining

Brain slices from the Thy1-EGFP transgenic mouse line were protected from light during storage to avoid fading of the EGFP signal. For multichannel immunofluorescence staining, slices were incubated in blocking buffer solution (1% BSA, 0.2% fish skin gelatin, 0.1% Triton, or 1% Triton in 1x PBS, Table 7) for at least 1h in the dark to block non-specific binding sites and remove background staining. Subsequently, sections were incubated overnight with the primary antibody solution at 4°C (Table 8). Slices were then washed 3 times with 1x PBS for 10 minutes to remove any remaining unbound primary antibodies. After washing, the slices were incubated in the secondary antibody solution for at least 2h (Table 9). This was followed by another washing step of 3 times 10 minutes with 1x PBS to remove the redundant antibodies. The slices were then moved onto a cover slide (Epredia, Breda, Netherlands) and dried for approximately 10 minutes. Finally, the slices were immersed in a mountain medium (Roti-Mount FluroCare, Carl Roth) with an antifading effect and covered with a coverslip (Carl Roth GmbH & Co. KG). The covered slides were dried overnight before confocal microscopy to avoid movement during the image acquisition.

Solution	Composition	Source
Blocking & Dilution buffer for standard IHC	In 1x PBS: 1% normal fish skin gelatine 0.1% Triton X-100	Sigma-Aldrich, St.Louis, USA Carl Roth, Karlsruhe, Germany
Blocking & Dilution buffer for sodium channel IHC	In 1x PBS: 1% normal fish skin gelatine 1% Triton X-100	Sigma-Aldrich, St.Louis, USA Carl Roth, Karlsruhe, Germany
PBS (1x)	In ddH_2O: 10 mM Na_2PO_4*H_2O 1.47 mM KH_2PO_4 130 mM NaCl 2.68 mM KCl pH: 7.4	All chemicals: Carl Roth, Karlsruhe, Germany

Table 7: Solutions for immunofluorescence staining

Antibody (host species)	Dilution	Target	Immunogene	Type	Source
Ankyrin-G (guinea pig)	1:1000	AIS scaffold	Recombinant protein corresponding to AA 1784 to 1961 from mouse Ankyrin-G	Poly-clonal	Synaptic Systems, Göttingen, Germany, Cat.No. 386 005
βIV-spectrin (rabbit)	1:1000	AIS scaffold	Recombinant proteins corresponding to Human βIV-spectrin, amino acids 2237-2256	Poly-clonal	selfmade, Biotrend Chemicals GmbH, Cologne, Germany
$GABA_A$ α2 receptor (guinea pig)	1:250	$GABA_A$ α2 receptor (postsynaptic site)	Synthetic peptide corresponding to AA 29 to 37 from rat GABA-A receptor α2	Poly-clonal	Synaptic Systems, Göttingen, Germany, Cat.No. 224 104
GFP (chicken)	1:2000	Green fluoresent proteins	Recombinant full length protein corresponding to GFP	Poly-clonal	Abcam, Cambridge, United Kingdom, Cat.No.ab13970
$Na_v1.6$ (rabbit)	1:2000	$Na_v1.6$ sodium channel	Peptide CIANHT-GVDIHRNGDFQKNG, corresponding to amino acid residues 1042-1061 of rat $Na_v1.6$. Intracellular loop between domains II and III	Poly-clonal	Alomone Labs, Jerusalem, Israel, Cat.No. ASC-009
vGAT (chicken)	1:1000	vGAT (presynaptic site)	Recombinant protein corresponding to residues near the amino terminus of rat VGAT	Poly-clonal	Synaptic Systems, Göttingen, Germany, Cat.No. 131 006

Table 8: Primary antibodies

Antibody (host species)	Dilution	Fluorophore	Source
anti-chicken IgG (goat)	1:1000	Alexa Fluor ® 488	Life Technologies, Carlsbad, USA, Cat.No. A-11039
anti-chicken IgG (goat)	1:500	Alexa Fluor ® 647	Life Technologies, Carlsbad, USA, Cat.No. A32933
anti-guinea pig IgG (goat)	1:1000	Alexa Fluor ® 568	Life Technologies, Carlsbad, USA, Cat.No. A-11075
anti-rabbit IgG (goat)	1:1000	Alexa Fluor ® 514	Life Technologies, Carlsbad, USA, Cat.No. A31558
anti-rabbit IgG (goat)	1:1000	Alexa Fluor ® 568	Life Technologies, Carlsbad, USA, Cat.No. A-11011
anti-rabbit IgG (goat)	1:500	Alexa Fluor ® 647	Life Technologies, Carlsbad, USA, Cat.No. A32733
Streptavidin	1:500	Alexa Fluor ® 568	Life Technologies, Carlsbad, USA, Cat.No. S11226

Table 9: Secondary antibodies, IgG = Immunoglobulin G

3.3.3 Confocal laser scanning microscopy in fixed tissue

Confocal imaging was carried out using a C2 Nikon confocal microscope (Nikon Instruments, laser lines: 488, 543, and 642nm) with a 60x objective (oil immersion, numerical aperture of 1.4) and a SP5 confocal microscope (Leica, LiMA Core Facility Mannheim; laser lines: Ar 488 nm /20 mW, 514 nm /20 mW, DPSS 561 nm /20 mW, HeNe 633 nm / 10 mW), with a 63x objective (oil immersion, numerical aperture 1.4). The image size was 1024 × 1024 pixels, with a confocal x-y-resolution of 0.21 µm per pixel. The thickness of the single optical sections

was 0.5 µm. Image stacks were taken over a thickness of up to 40 µm in size. For optimal acquisition, the exposure intensity was monitored and laser settings were initially set such that the exposure intensity for each laser was normally distributed, and too many oversaturated pixels were avoided.

3.4 Analysis and statistics

3.4.1 Cell classification criteria

NonAcD cells were identified when the axon branched off directly from the cell body (Figure 10, middle panel). AcD neurons were defined as cells in which the axon with its AIS branched off from a dendrite (Figure 10, left image). Specifically, the stem dendrite, where the axon branches off, had to exhibit a maximal diameter of 20% of the soma diameter, and its branching axon had to be at least 2.5 µm away from the cell body; otherwise, it was defined as a nonAcD neuron. Shared root neurons, where the axon and dendrite branch off simultaneously, were grouped into nonAcD neurons if not mentioned otherwise (Figure 10, right image). This subtype was defined when not only the axon and dendrite branched off simultaneously but also when the soma narrowed towards the region where the axon and dendrite branched off. This narrowing of the somatic membrane exceeded 20% of the maximal somatic diameter.

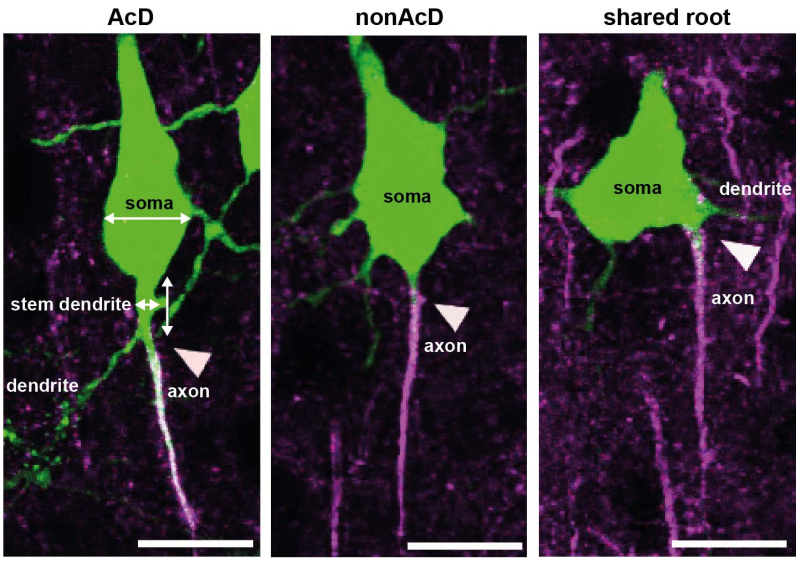

Figure 10: Representative examples of classified cells. Classification criteria for an AcD neuron needed to fulfill the following criteria: 1) the diameter of the stem dendrite did not exceed 20% from the somatic diameter (each diameter is indicated by the double-sided arrow), 2) the stem dendrite was at least 2.5 µm long before the axon branched off. A nonAcD neuron was classified when the axon originated from the soma. A shared root cell was classified when an axon and dendrite branched off simultaneously, which is frequently observed in combination with somatic membrane narrowing. Arrows indicate axonal origin. Scale bar = 15 µm.

3.4.2 Morphological measurements

For the classification of neurons, each neuron with its full morphology was cropped in Fiji (ImageJ) (Schindelin et al. 2012) and the classification name was entered into the file name of the cropped file. This procedure was assisted by Stefan Markovic, Institute of Anatomy and Cell Biology, Johannes Kepler University Linz, Austria, and completely conducted for all neurons stained after *in vivo* experiments. Stefan Markovic was blinded to the treatment groups for the classification process of the neurons in the *in vivo* experiments. In addition, the classification of each neuron underwent a double-verification process according to the 4-eyes principle. Afterwards, a self-written Python script counted all cells per cell type, age, brain region, or condition and calculated the percentage of the observed cell types. For each neuron, I analyzed the AIS length (based on the expression length of a scaffold marker (βIV-spectrin or ank-G), expression length of sodium channel stainings (based on $Na_v1.6$ channel), and the distance between the beginning of the AIS and the sodium channel staining. For this, a combination of a Fiji plugin called simple neurite tracer (SNT) (Ferreira et al.

2021) with a self-written Python script was used. In brief, SNT enables the measurement of distances in three dimensions by following the maximum pixel intensity between the manually selected start and end points of a selected channel (in my case the AIS) using the A*-search algorithm. The start point was manually selected at the soma, and the end point was manually selected after AIS staining had disappeared (Figure 11A). These data were exported and used for further analyses. To minimize the error due to the personal perception of AIS start and end points, I wrote a Python script to determine those boundaries (published on Github: `https://github.com/NadjaLe/ChannelAnalysis/blob/main/Channel_analysis_SNT_GitHub.py`). Briefly, for each measured AIS, the pixel intensity was normalized. The start and end points of an AIS were defined when the pixel intensity of a local average (five pixels) reached more than 40% of the maximum intensity of local averages within the AIS, searching from the manually selected start point for the AIS start and from the selected endpoint for the AIS end (Figure 11C). AIS lengths shorter than 10 µm were excluded from further analysis. The sodium channel distribution was analyzed in the same way. Here, the pixel intensity threshold was set at 30% of the maximum intensity (Figure 11D). Additionally, the distance from the soma to the AIS start point was calculated according to previously calculated values, as well as the distance from the AIS starting point to the sodium channel starting point. To analyze the colocalization of synaptic puncta at the AIS in Thy-GFP-positive cells, a Fiji plugin for spot localization (ComDet) in three dimensions was used (published on Github: `https://github.com/ekatrukha/ComDet`). Cropped images from the classification task, in which the AIS, $GABA_A$ receptor $\alpha 2$ subunit (postsynaptic neuron), and vGAT (presynaptic terminal) were stained, were used for this analysis. In each image, the AIS was manually marked and selected as the region of interest to search for colocalizations. A ‘macro’ (custom-defined routine) in Fiji was created to automate this procedure. In brief, the background was subtracted using the rolling ball method with a selected radius of 25.0 pixels to increase the signal quality and reduce the background. The maximum distance between colocalized spots was set at 3 pixels (~0.74 µm), and the approximated particle size and its intensity threshold were defined (for GABAergic receptors and vGAT: approximated particle size 3 pixels (~0.74 µm)). Afterwards, all colocalizations found by the plugin were displayed in the image and manually verified. Finally, all verified colocalizations were counted for each AIS.

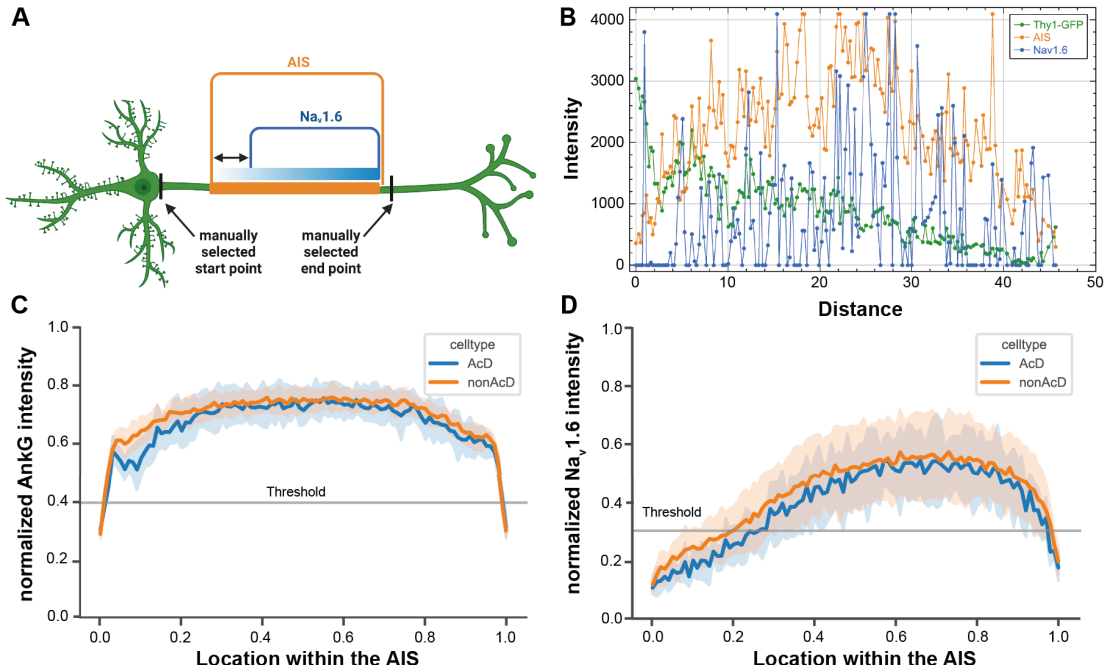

Figure 11: Analysis of AIS, length of Na$_v$1.6 distribution, and distance between AIS start and Na$_v$1.6 expression start. **A** Illustration of AIS, length of Na$_v$1.6 distribution, and distance between AIS start and Na$_v$1.6 expression start. Black lines at the neuron indicate manually selected start and end points in SNT. **B** Example of a raw data trace and its distribution between manually selected points for each measured channel (Thy1-GFP, AIS, and Na$_v$1.6 exported from SNT. **C** Normalized ank-G intensity distribution from measurements acquired in the S1 to indicate the selection for the threshold for the AIS start and end point (40%). **D** Normalized Na$_v$1.6 intensity distribution from measurements acquired in the S1 to indicate the selection for the threshold for the Na$_v$1.6 start and end point (30%).

3.4.3 Electrophysiological data analysis

Analyses were performed offline using the AxoGraph software (AxoGraph Scientific, USA). Passive cell property values, such as R$_s$ (series resistance), R$_{mem}$ (membrane resistance), τ (membrane time constant), and C$_{mem}$ (membrane capacitance), were calculated using the functions implemented in AxoGraph, where a test pulse of 10 mV was applied for 100 ms. Resting membrane potential (RMP) was determined by averaging the recorded traces. The current threshold was defined at the first current step of a 20 ms current pulse, where an AP was reliably elicited. The voltage threshold was measured at the point where the first derivative of the phase plot exceeded 50 mV/ms. The AP amplitude was measured from the voltage threshold to the AP voltage peak. The AP half-width was defined as the width from the middle voltage of the rising phase between the AP threshold and peak voltage. For the analysis of the input-output curve, the APs elicited by the

current step protocol were counted manually. Spontaneous EPSC events were automatically detected using an implemented event-detection function from AxoGraph. An EPSC template was created and compared to the recorded events. The template had the following parameters: template length 20 ms, amplitude -10 pA, rise-time 1 ms, decay-time 3 ms. After detection, the EPSC amplitudes exceeding 60 pA were excluded. The mean amplitude, rise-time, and frequency of EPSCs were calculated for each neuron, and the average values were compared between groups.

3.4.4 Statistical analysis

Statistical tests were performed and graphs were plotted using GraphPad Prism 9 (GraphPad Software, Inc.). Prior analysis, data were tested for normal distribution by Shapiro-Wilk or Kolmogorov-Smirnov test. For parametric comparisons between two groups, an unpaired or paired *t*-test was applied. One-way ANOVA was used to compare one group over several time points or multiple groups, followed by Tukey's multiple comparisons test. Two-way ANOVA followed by Tukey's Multiple Comparisons test or Sidák's Multiple Comparison test was used to compare the two groups over several time points. If an unequal number of data points occurred within groups, two-way ANOVA with a mixed-effects model (REML) was performed. For nonparametric distributed data, Kruskal-Wallis ANOVA followed by Dunn's Multiple Comparisons post hoc test was applied to compare more than two groups. In all graphs, boxplots indicate the median, 25% and 75% percentiles (boxes) with minimum and maximum values (whiskers). Violin plots show the median (middle dashed line), 25% and 75% percentiles (small dashed lines at the top and bottom) with minimum and maximum values. The shape of the violin plot represents the data distribution. Graphs of the measured peak inward currents and firing patterns represent the mean values and standard deviations (SD). Bar plots show the mean values and SD. P-values and number of samples are stated in each figure legend as well as in Supplementary Tables for Multiple Comparison results.

3.4.5 Data illustration

Schematic illustrations were created using the BioRender.com software. Representative electrophysiological traces were exported using the AxoGraph software (AxoGraph Scientific, USA) or PatchView (Hu and Jiang 2022). To reduce the noise in electrophysiological traces for EPSC illus-

trations, these traces were imported using the 'load-heka-python' library (https://github.com/easy-electrophysiology/load-heka-python), and subsequently processed with a 2 kHz low-pass Bessel filter (as described in: (https://spikesandbursts.wordpress.com/2022/07/03/patch-clamp-data-analysis-in-python-postsynaptic-currents-and-potentials/). Their presentation was improved using Adobe Illustrator (Adobe Inc. San José, CA, USA). The presentation of microscopic images was improved using Adobe Photoshop and Adobe Illustrator (Adobe Inc., San José, CA, USA). For 3D reconstruction of cell morphology, the surface rendering function of Imaris V9.9 (Oxford Instruments) was used, thus revealing intricate details about the axonal onset.

4 Results

4.1 Structural characteristics of AcD neurons

Neurons with different axon origins have been described in several brain regions with tremendous discrepancies in the percentage and distance of axon onset (see Introduction 2.1). Neurons in which dendrites carry an axon are called “AcD” (axon-carrying dendrite) neurons (Thome, Kelly, et al. 2014). Usually, a thin dendrite and axon bifurcate from a thicker dendrite, which is called stem dendrite (Figure 12, left panel). In this study, neurons, where the axon emanated from the soma, were named “nonAcD” (non-axon-carrying dendrite) (Thome, Kelly, et al. 2014, examples in Figure 12). The axon branching off a dendrite is typically located more distally from the soma compared to nonAcD neurons. This distal location, in combination with the axon-dendrite bifurcation, is a criterion in this study for AcD classification (for details, see Materials and Methods 3.4.1). The specific location of axon onset in AcD neurons is essential to their functions. This is because, as explained in the introduction (Section 2.1), it allows the neuron to bypass somatic inhibition, which usually limits neuronal output (Hodapp et al. 2022). Furthermore, it enables the AcD to act as a preferential channel for synaptic input (Thome, Kelly, et al. 2014). As a result of these characteristics, AcD neurons are believed to have a significant influence on the overall network activity. Despite these features, there is still much unknown about the morphological differences between AcD and nonAcD neurons and their possible resulting differences in signal integration and propagation.

In this study, S1 and vHC of mice were examined regarding AcD and nonAcD cells. Structural differences between AcD and nonAcD neurons were investigated in terms of axo-axonic synapses, AIS length, length of $Na_v1.6$ clustering, and the location of $Na_v1.6$ within the AIS. To address these questions, immunofluorescence was applied to investigate putative morphological differences. To examine the morphological structure and percentage of AcD neurons in these brain regions, a transgenic mouse line (Thy1-GFP M) was used, which intrinsically expresses green fluorescent protein in excitatory neurons. This intrinsic labeling allowed for the reconstruction of neuronal morphology. To investigate putative differences in the number of AcD neurons between the sexes, mice aged between P18 and P21 were included in this study. For morphological analysis, a mean of approximately 120 cells in S1 and approximately 138 cells in vHC Thy-GFP-positive cells per

mouse were analyzed. Female mice were observed to have an average of 12.83 ± 4.2% AcD neurons and male mice showed an average of 14.99 ± 6.1% AcD neurons in the S1 brain region (Figure 12, P=0.4159, unpaired *t*-test, female mice n = 8, male mice n = 9). In the vHC group, more AcD neurons were observed. In female mice, 34.95 ± 6.1% of AcD neurons were observed, and in male mice, 39.20 ± 13.67% were observed (P=0.5728, unpaired *t*-test, female mice n=4, male mice n=8). Together, these data show that there is no significant difference between female and male mice in the percentage of AcD neurons in either brain region.

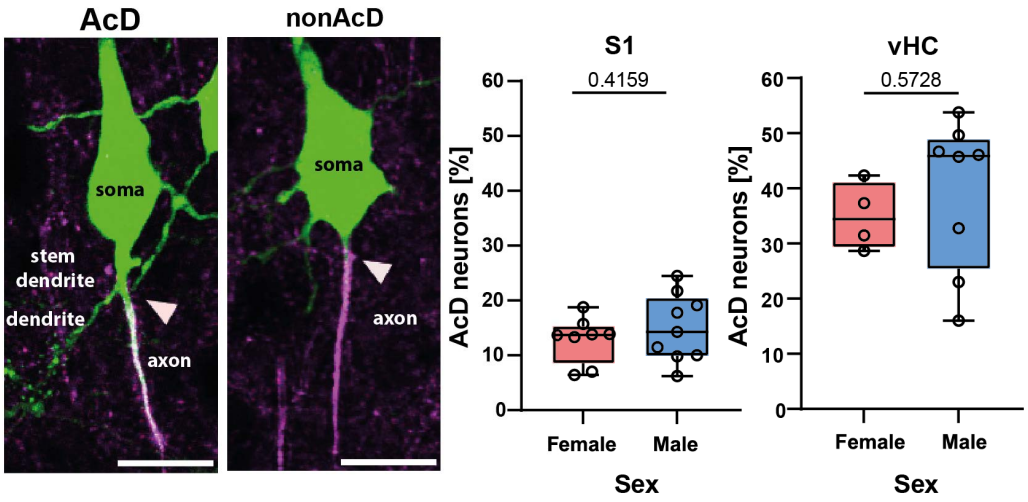

Figure 12: No sex-specific differences in the number of AcD neurons in S1 and vHC. Representative examples of an AcD neuron (left) and nonAcD neuron (right). Arrows indicate the origin of the axon. The axon is labeled against the scaffold protein βIV-spectrin for the axon initial segment (magenta). Scale bar = 15 µm. Data on the number of AcD neurons in S1 and vHC in female and male mice. Each dot represents a single mouse. Mice used in this study were between P18 and P21. The number of AcD neurons in either brain region was not significantly different between male and female mice (unpaired *t*-test, S1 female n=8, male n=9; vHC female n=4, male n=8). Boxplots indicate the median with 25–75% intervals, and error bars indicate min. to max. values.

4.1.1 Similar abundance of axo-axonic Synapses

Pyramidal neurons in the cortex and hippocampus, including the subregions S1 and vHC, are sites of interaction with GABAergic interneurons. These interneurons target various parts of those neurons, including their soma and dendrites, but can also specifically target their AIS (Peters, Proskauer, and Ribak 1982). Some interneurons, such as Chandelier neurons, specialize in forming axo-axonic synapses exclusively, contacting pyramidal neuron AIS with a high propensity (Peters, Proskauer, and Ribak 1982). Ramified Chandelier axons densely innervate hundreds of neighboring pyramidal neurons and thus exert significant influ-

ence on neuronal excitability due to their unique positioning and direct modulation of pyramidal cell output (Inan and Anderson 2014). In early postnatal development between the second and third postnatal weeks, substantial changes occur in GABA neurotransmission (Romo-Parra et al. 2008, reviewed in (Peerboom and Wierenga 2021)) and the innervation of GABAergic interneurons (Pan-Vazquez et al. 2020). This period is marked by a shift in the polarity of GABA action (Owens et al. 1996; Rivera et al. 1999), and Chandelier cells begin to strongly target the AIS of pyramidal neurons (Pan-Vazquez et al. 2020). This period coincides with the appearance of most AcD neurons during the second and third postnatal week in mice (see Results Section 4.2). Owing to this complicating relationship between GABAs developmental shift and the timing of AcD neuron emergence, this study focused on the GABAergic innervation pattern of the AIS in juvenile, but more mature mice (P28) in AcD and nonAcD neurons.

To investigate putative differences in the number of axo-axonic GABAergic synapses between AcD and nonAcD neurons in S1 and vHC, immunofluorescence was performed against βIV-spectrin (a scaffold marker of the axon initial segment (AIS)), vesicular GABA transporter ((vGAT) expressed in the presynaptic neuron), and GABA$_A\alpha$2 receptor (expressed in the postsynaptic neuron; Figure13A and B). Only when the Thy1-GFP signal, together with the AIS, GABA$_A$Rα2, and vGAT signals appeared in a defined range of three pixels (approximately 0.75 µm), they were counted as putative GABAergic synapses. Colocalization was determined using the Fiji plugin “ComDet” and manually verified (Figure 13B, squares in merged image). Approximately 52 cells in S1 and 73 in vHC were analyzed per animal. Both GABA$_A$Rα2 and vGAT appeared along the somato-dendritic and axonal membranes (Figure 13B), with the strongest expression along the soma. The mean number of putative axo-axonic synapses in the vHC group was lower than that observed in S1. In S1, the mean number of putative GABAergic synapses at the AIS in AcD neurons averaged 2.1 ± 0.83 and in nonAcD neurons 2.3 ± 0.76, showing no significant difference between these cell types (Figure 13C, P=0.5022, paired *t*-test, n=6). Similarly, in the vHC group, the number of putative axo-axonic synapses in AcD neurons averaged 1.1 ± 0.93 and in nonAcD neurons 1.5 ± 1.4, with no significant differences between these cell types (P=0.1143, paired *t*-test, n=6). In summary, the number of putative axo-axonic synapses in mice aged P28 was not significantly different between AcD and nonAcD neurons in both brain regions in S1 and vHC.

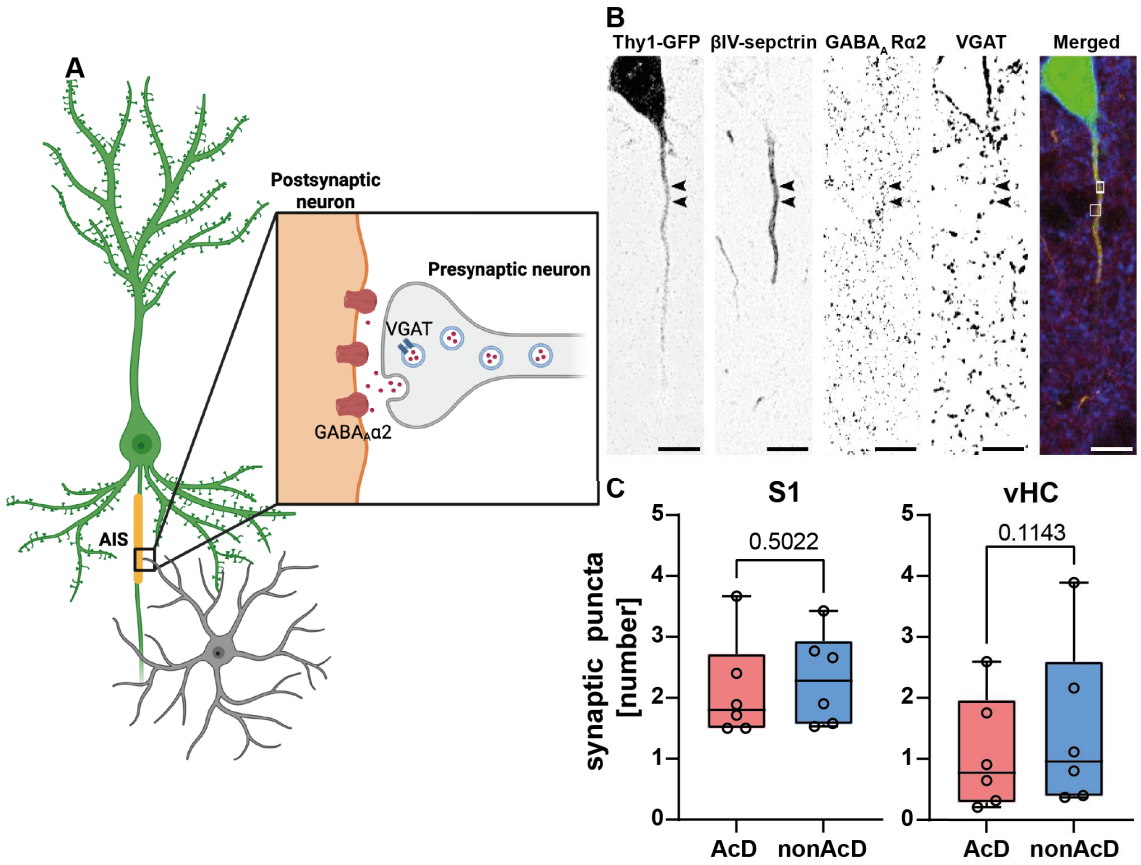

Figure 13: AcD and nonAcD cells exhibit similar amounts of GABAergic synapses at the AIS. A Schematic overview of the experimental design. The green neuron represents a Thy1-GFP positive cell and the gray neuron represents a GABAergic interneuron. This interneuron innervates the AIS of the Thy1-GFP positive cell. The close-up depicts the presynaptic terminal of the interneuron with vGAT as a vesicular GABA transporter, and the postsynaptic site at the AIS with the GABA$_A\alpha$2 receptor. **B** Representative confocal images of synaptic puncta at the AIS with colocalization. Immunostaining against βIV spectrin as an AIS marker, GABA$_A\alpha$2 receptor for the postsynaptic site, and vGAT for the presynaptic site. The merged image shows the co-localization of AIS (yellow), GABA$_A\alpha$2 receptor (red), and vGAT (blue). Squares and arrows indicate the colocalization found by the Fiji plugin ComDet. Scale bar = 15µm. **C** Data on the number of synaptic puncta at the AIS of AcD and nonAcD neurons in mature mice (P28) in the brain regions S1 and vHC. The number of putative GABAergic synapses at the AIS in AcD and nonAcD neurons was similar in the S1 and vHC groups. Each dot represents a single mouse (paired *t*-test, S1 and vHC n=6).

4.1.2 $Na_v1.6$ clusters more distally within the AIS in AcD neurons

The AIS is a highly specialized membrane domain located proximally at the axon and functions as the main regulator of input integration and generation of action potentials ((Coombs et al. 1957), reviewed in (Leterrier 2018)). To execute this function, it clusters several scaffold proteins, such as βIV-spectrin and ankyrin-G (ank-G), and is highly enriched with voltage-gated ion channels, (Komada and Soriano 2002; Inda et al. 2006; McCormick et al. 2007), reviewed in (Leterrier, 2018)). This study focused on $Na_v1.6$, which is known to play an important role in action potential initiation (Royeck et al., 2008). Therefore, it has the strongest putative effect on network activity.

In this study, ank-G was used as a scaffold marker for the AIS to identify axon onset in Thy1-GFP positive cells and stained against $Na_v1.6$ for sodium channel distribution within the AIS (Figure 14B). I investigated whether the distal location of the AIS in AcD neurons leads to differences in the molecular composition of the AIS by measuring its length, the length of $Na_v1.6$ clustering, and the location of $Na_v1.6$ within the AIS (Figure 14A). The AIS length, $Na_v1.6$ expression length, and $Na_v1.6$ distance to the AIS start were measured using a Fiji plugin called SNT in combination with a self-written Python script to minimize the error of subjective selection of the start and end points of the AIS (see Materials and Methods Section 3.4.2). To investigate putative morphological differences between AcD and nonAcD neurons in Thy1-GFP positive cells, mice aged from P12 to >P305 (>10 months) were included in this study. Therefore, parameters of the AIS were compared in AcD and nonAcDs derived from the same mouse and approximately 50 AIS in S1 and 69 AIS in vHC per mouse were analyzed.

The measured AIS length of Thy1-GFP neurons was slightly shorter (~2 µm) in the vHC group than in the S1 group. However, within each brain region, the AIS length was not significantly different between AcD and nonAcD neurons. In S1, the AIS length of AcD neurons averaged 39.1 ± 5.7 µm and in nonAcD neurons 38.6 ± 5.2 µm (Figure 14C left panel, P=0.3998, paired *t*-test, n=38 mice). In the vHC group, the AIS length of AcD neurons averaged 37.3 ± 4.1 µm and that in nonAcD neurons was 37.0 ± 4.5 µm (Figure 14D left panel, P=0.3903, paired *t*-test, n=35 mice).

The length of $Na_v1.6$ clustering was shorter than the AIS length (~10 µm). The length of $Na_v1.6$ clustering was very similar in S1 and vHC, but was not signif-

icantly different between AcD and nonAcD neurons. However, a slightly longer $Na_v1.6$ expression length was observed in nonAcD neurons than in AcD neurons. In S1, the $Na_v1.6$ length was observed to be on average 29.6 ± 6.0 µm long in AcD neurons and in nonAcD neurons 31.0 ± 4.5 µm (Figure 14C middle panel, P=0.0824, paired *t*-test, n=38). In vHC, the $Na_v1.6$ length averaged in AcD neurons 29.6 ± 5.2 µm and that in nonAcD neurons 30.4 ± 5.0 µm (Figure 14D middle panel, P=0.0627, paired *t*-test, vHC n=35 mice). However, there was a significant difference between AcD and nonAcD neurons regarding the distance between the start of the AIS and the onset of the dense $Na_v1.6$ expression. Overall, the $Na_v1.6$ expression was more distally located within the AIS in S1 than in vHC. In S1, the distance between AIS onset and $Na_v1.6$ clustering onset was on average 7.6 ± 4.2 µm in AcD neurons and in nonAcD neurons 6.0 ± 3.0 µm (Figure 14C right panel, ***P=0.0008, paired *t*-test, n=38 mice). In vHC, this distance averaged in AcD neurons 6.0 ± 2.5 µm and in nonAcD neurons 4.9 ± 2.1 µm (Figure 14D right panel, ***P=0.0001, paired *t*-test, n=35 mice).

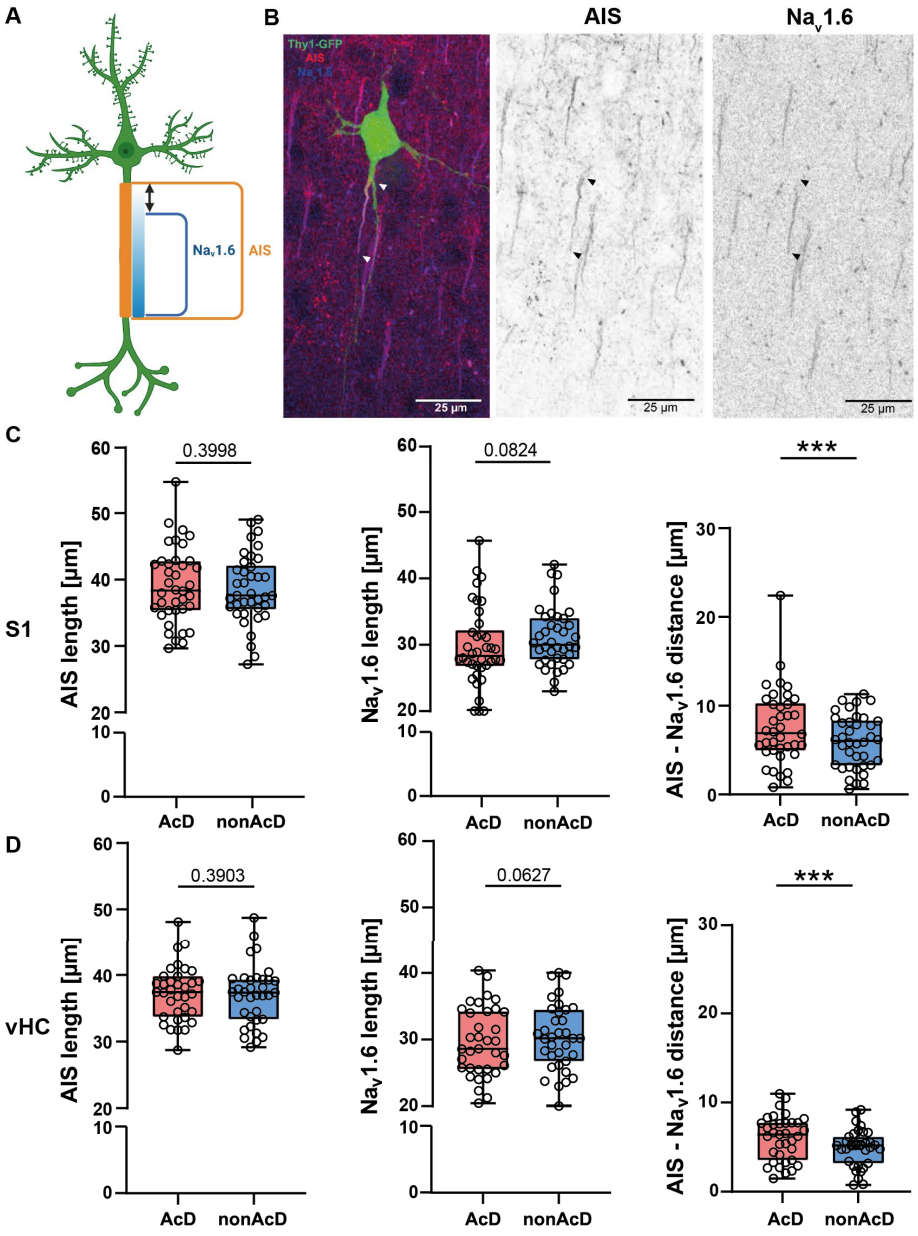

Figure 14: Na$_v$1.6 channels cluster more distally within the AIS in AcD neurons than in nonAcD neurons. A Schematic overview of the experimental design. The green cell represents a Thy1-GFP positive neuron, the orange bar depicts the AIS, and the blue bar represents Na$_v$1.6 channel clustering within the AIS. The AIS - Na$_v$1.6 distance was measured between the calculated starting point of the AIS and the calculated starting point of the Na$_v$1.6 distribution. **B** Representative confocal images of AIS length and Na$_v$1.6 length. Immunostaining against ank-G (red) and Na$_v$1.6 (blue). Arrows indicate the starting and end points of the AIS. **C** and **D** Data on AIS length, Na$_v$1.6 expression length, and the distance of AIS - Na$_v$1.6 within the AIS of AcD and nonAcD neurons in the S1 and vHC. The AIS length and Na$_v$1.6 expression length were not significantly different in AcD and nonAcD cells, whereas in AcD neurons, the Na$_v$1.6 channels started to cluster more distally within the AIS in both brain regions. Each dot represents a single mouse (paired *t*-test, S1 n=38; vHC n=35).

Conclusion on structural characteristics of AcD neurons

The structural characteristics of AcD and nonAcD neurons in S1 and vHC were largely similar. Their AIS features, such as length and $Na_v1.6$ channel clustering, exhibited substantial similarities. Furthermore, both neuron types seem to have comparable numbers of putative GABAergic synapses clustered at the AIS. However, a notable difference was observed in the positioning of the $Na_v1.6$ channel cluster within the AIS. $Na_v1.6$ channel clustered more distally in AcD neurons than in nonAcD neurons across both brain regions. This distinctive location may affect the likelihood of these neurons initiating APs (see Discussion Section 5.1).

4.2 Development of AcD neurons

In previous studies (Gutzmann et al. 2014; Jamann, Dannehl, et al. 2021), AIS length was observed to change in an activity-dependent manner during development in different cortical areas (S1 and visual cortex). Based on this observation, the question remained whether this developmental plasticity is a unique feature of the AIS or applies to the whole axon onset. This section investigates the structural morphology and percentage of AcD neurons during the development in S1 and vHC. Interestingly, secondary observation showed that in both brain regions and increasing age, the soma of Thy1-GFP positive neurons increased in its size and became more spherical (Figure 15).

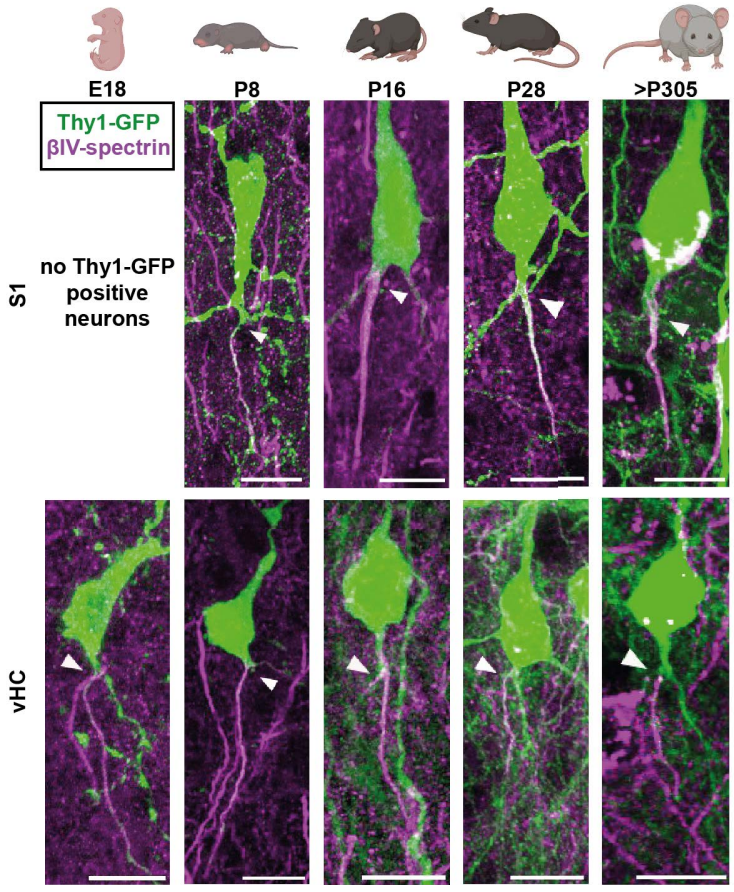

Figure 15: Representative examples of Thy1-GFP positive AcD neurons during development in S1 and vHC. Illustration depicts AcD neurons at different time points during development, which shows the morphological alteration of the entire cell body. Notably, the soma of Thy1-GFP neurons increased in size and became more spherical during development. Immunostaining against βIV-spectrin for labeling the AIS. Arrows indicate the origin of the axons. Scale bar = 15 µm.

4.2.1 The number of AcD neurons changes during development

The percentage of AcD neurons during development was investigated in S1 and vHC, starting from late embryonic age until maturity (Figure 16A). The chosen time points for the developmental study coincided with numerous critical windows of neuronal differentiation and connection (reviewed in (Erzurumlu and Gaspar 2012). These are periods when significant changes in structural plasticity occur (Erzurumlu and Gaspar 2012). They begin to appear from the embryonic age until maturation (for more details about critical periods, see Introduction Sections 2.2.2 and 2.3.2). The aim of this study was to thoroughly describe the percentage of AcD neurons during development. Therefore, the different cellular architectures were quantified. As a complicating factor, I had to consider a third cell type, in addition to AcD and nonAcD neurons. In this cell type, the axon and dendrite branched off simultaneously. This cell type is referred to as a shared root cell in this study (Figure 16B). In further experiments, these cells were classified as nonAcD neurons. A total of 5 to 8 animals per group at 8 time points in S1 and 10 time points in vHC were included in this study (E18, P3, P8, P12, P14, P16, P18, P21, P28, older than 10 months (>P305); in S1: Thy1-positive neurons appeared at P8). Coronal sections containing S1 and horizontal sections containing vHC were immunohistochemically labeled using antibodies against AIS markers βIV-spectrin or ank-G. Using confocal microscopy, approximately 100 Thy1-positive cells per animal and per brain region were imaged, classified, and subjected to morphometric analysis.

In S1 and vHC regions, the number of AcD neurons changed during development. However, the effect was more prominent in the vHC, which contained more AcD neurons than S1. In the vHC group, the number of AcD neurons ranged from 14.9% at P8 to 42.3% at P28 (Figure 16C). In contrast, in S1, the number of AcD neurons ranged from 8.7% in >P305 mice to 19.2% in P12 mice.

More specifically, in S1, the number of AcD neurons varied just slightly during development, with the highest average number of AcD neurons occurring at P12 (19.2 ± 5.0%). However, it decreased significantly in mature (>P305) mice (8.7± 4.4%) (Figure 16C, *P=0.0177 for age, ordinary one-way ANOVA, Tukey's multiple comparisons test, P8 n=5, P12 n=5, P14 n=5, P16 n=6, P18 n=18, P21 n=8, P28 n=6, >P305 n=6). A similar developmental process was observed in the number of shared root cells. In S1, most shared root cells were observed in juvenile mice (P18-P28) with a peak at P28 (7.1 ± 3.3%). Although not significant, the number of

shared root cells increased slightly during development (3% at P14 to 7% at P28), but decreased again in mature mice (>P305) (2.3%) (Figure 16D, P=0.1187 for age, ordinary one-way ANOVA, Tukey's multiple comparisons test, P8 n=5, P12 n=5, P14 n=5, P16 n=6, P18 n=18, P21 n=8, P28 n=6, >P305 n=6). These results show that the number of AcD neurons changes during development, whereas no significant effect was observed for the shared root cells.

However, a striking pattern in the percentage of AcD neurons during development was observed in the vHC. While the highest number of AcD neurons was observed in P28 mice (42.3 ± 4.9%), the lowest number was observed in P8 mice (14.9 ± 2.0%). Interestingly, during development, the highest increase in AcD neurons occurred from P8 (14.9 ± 2.0%) to P12 mice (34.2 ± 3.1%). In general, the number of AcD neurons was significantly lower in the early developmental stages (E18, P3, and P8) than in juvenile mice (P12-P28) but decreased again in mature mice (>P305) (Figure 16B, ****P<0.0001 for age, ordinary one-way ANOVA, Tukey's multiple comparisons test, E18 n=6, P3 n=5, P8 n=6, P12 n=5; P14 n=5; P16 n=5, P18 n=6; P21 n=6; P28 n=6, >P305 n=6). While in S1, the percentage of shared root cells remained largely unchanged during development, the number of shared root cells changed significantly in the vHC. The lowest number of shared root cells was observed in E18 and P3 mice (2.2 ± 2.7%, 2.8 ± 1.9%, respectively) and increased continuously to the highest average in P28 mice (9.8 ± 1.7%), but decreased again in mature mice (>P305, 3.4 ± 1.4%) (****P<0.0001 for age, ordinary one-way ANOVA, Tukey's multiple comparisons test, E18 n=6, P3 n=5, P8 n=6, P12: n=5; P14 n=5; P16 n=5, P18 n=6; P21 n=6; P28 n=6, >P305 n=6). Taken together, the developmental profile of shared root cells is similar to that of the AcD neurons. However, in contrast to AcD development, the number of shared root cells increased more continuously from young to juvenile age rather than rapidly between specific time points.

In summary, the number of AcD neurons developed differently in the S1 and vHC groups. Especially in the vHC, the increase in the number of AcD neurons was prominent from young (E18 to P8) to juvenile (P12-P28) mice, followed by a decrease in the number in mature mice (>P305), indicating an age-dependent AcD development. In S1, the number of AcD neurons changed during development, although not as prominently as in the vHC. Interestingly, shared root cells exhibit a developmental profile similar that to of AcD neurons in the vHC; however, there are differences in their incline.

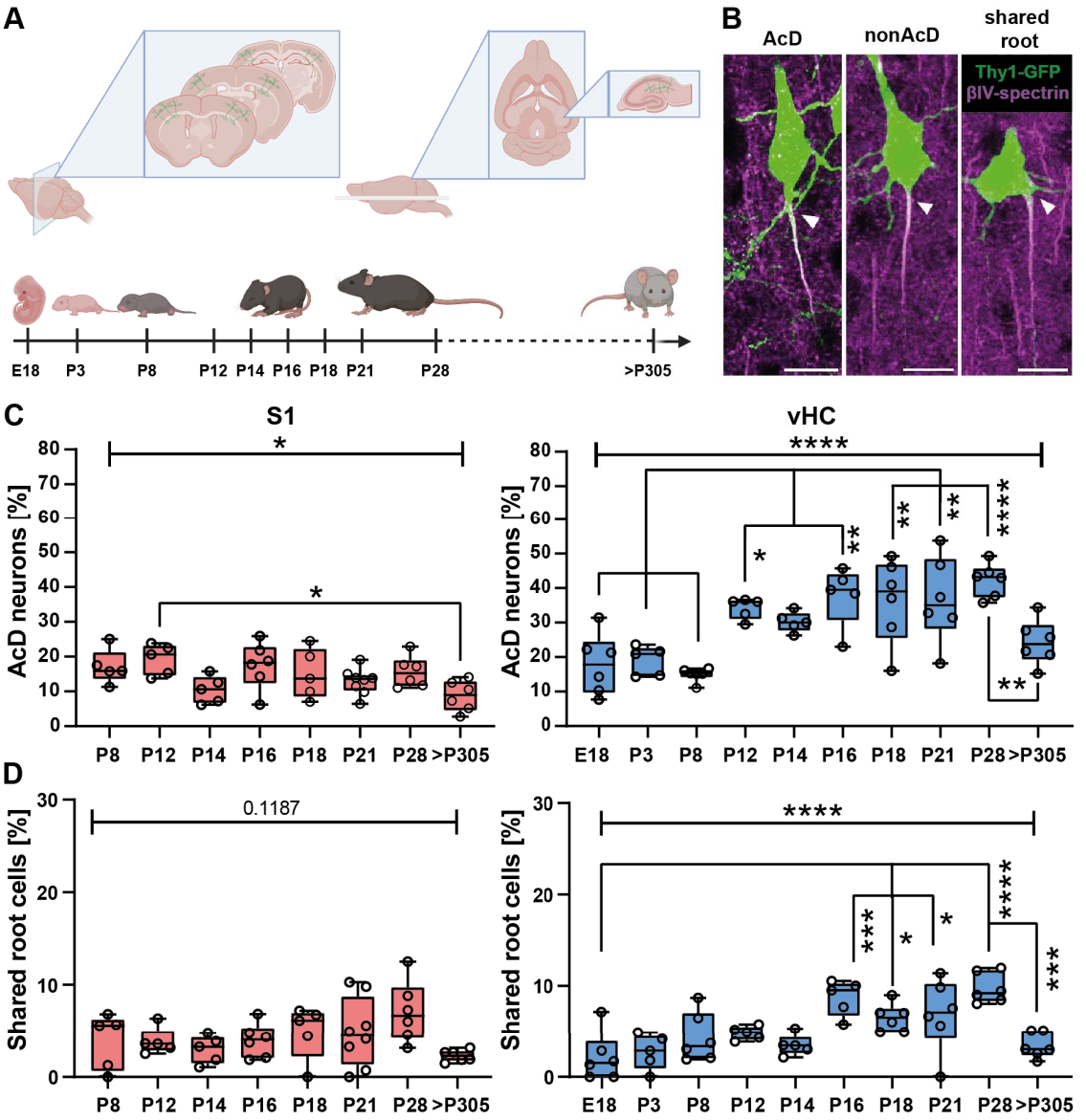

Figure 16: The number of AcD neurons changes during development. A Schematic overview of the experimental design. Most Thy1-GFP positive cells were expressed in layers V and VI of S1 and in the CA1 region of vHC. **B** Representative confocal images of AcD, nonAcD, and shared root cells. Thy1-GFP neuron (green) and immunostaining against βIV-spectrin (magenta) for AIS labeling. Arrows indicate the origin of the axons. Scale bar = 15 µm. **C** Population data on the number of AcD neurons in the S1 and vHC. In S1, the number of AcD neurons changed significantly during development (P=0.0177 for age, ordinary one-way ANOVA, Tukey's multiple comparisons test). However, at P12, there were significantly more AcD neurons than in mature (>P305) mice. In the vHC, the number of AcD neurons increased drastically to P12 compared to earlier time points (E18-P8) and remained stable during maturation (P12-P28) (P<0.0001 for age, ordinary one-way ANOVA, Tukey's multiple comparisons test). However, in mature mice, the number of AcD neurons decreased significantly.

Figure 16 continued:

D Population data on the number of shared root cells in the S1 and vHC groups. The number of shared root cells remained unchanged during development, however, the number of shared root cells was the lowest in mature mice (>P305) (P=0.1187 for age, ordinary one-way ANOVA, Tukey's multiple comparisons test). In vHC group, the number of shared root cells increased from P16 to P28 and decreased significantly in >P305 (P<0.0001 for age, ordinary one-way ANOVA, Tukey's multiple comparisons test), each dot represents a single mouse, S1 n=5-8 per group, vHC n=5-6 per group, * P>0.05, ** P<0.01, *** P<0.001, **** P<0.0001). Only representative statistical results are shown in the graphs. Significant bars at the top of each graph represent the p-value of the ANOVA. All results of multiple comparisons are shown in Supplementary Table for S1: 12 and for vHC: 13.

4.2.2 Similar development profile of AIS and $Na_v1.6$ expression length

Previous studies have thoroughly characterized the changes in AIS length during development in the S1 barrel field (BF) and visual cortex (Gutzmann et al. 2014; Jamann, Dannehl, et al. 2021). However, there remains a knowledge gap regarding the developmental profile of the AIS in the vHC and entire S1, particularly in relation to AcD and nonAcD neurons. In addition, the development of voltage-gated sodium channels, primarily responsible for AP initiation at the AIS (Royeck et al. 2008), remained largely unexplored. Notably, an existing patch-clamp study indicated that pyramidal neurons in the cerebral cortex increase their Na_v conductance by 10-fold in relation to their membrane area between the second and third postnatal weeks (Hamill et al. 1991). However, whether this increase in sodium conductance applies specifically to the AIS or to the entire somato-dendritic membrane is unknown. For voltage-gated sodium channel analysis, this study focused on $Na_v1.6$, a subtype mainly responsible for AP initiation (Royeck et al. 2008). In more detail, the present study investigated the AIS length, length of $Na_v1.6$ clustering within the AIS, and its distance from the AIS starting point in AcD and nonAcD neurons in S1 and vHC. Hence, immunofluorescence was performed and antibodies against ank-G and $Na_v1.6$ were used. AIS length, $Na_v1.6$ expression length along the AIS, and $Na_v1.6$ distance to the AIS start were measured using a Fiji plugin called SNT in combination with a self-written Python script (Figure 17A, for more details see Materials and Methods Section 3.4.2). The number of AIS analyzed per animal strongly depended on the number of Thy1-positive AcD neurons in the respective brain regions. The number of Thy1-positive cells increased steadily during development, but started to appear at P8 in S1. Sufficient and reliable labeling of $Na_v1.6$ within the AIS was only possible in mice aged at least P12. Therefore, this study investigated the AIS-dependent parameters from P12 onward. At P12, approximately 30 Thy1-positive cells with AIS per brain region and animal were analyzed. During the later stages of development, approximately 100 Thy1-positive cells were analyzed per brain region and animal.

Similar development profile of AIS length in S1 and vHC In the study by Jamann, Dannehl, et al. (2021), which investigated AIS length during development in S1BF, a phasic development profile of AIS length changes was observed. In the present study, I was able to confirm this developmental profile for the entire S1 brain region and the vHC for the time interval between juvenile and mature mice (Figure 17D). In both brain regions, the developmental profile of the AIS length

can be distinguished into two phases: juvenile (P12-P16) and mature mice (P28 ->P305). In S1, AIS length peaked in AcD neurons at P14 (mean AIS length 45.3 ± 6.2 µm) and in nonAcD neurons at P12 (45.6 ± 3.1 µm), and decreased during further maturation to an average AIS length of 31.1 ± 1.1 µm in AcD neurons and in nonAcD neurons to 29.3 ± 1.8 µm in fully mature mice (>P305) (Figure 17D, ****P<0.0001 for age, P=0.5223 for cell type, P=0.1750 for age × cell type interaction; two-way ANOVA with mixed-effects model (REML), P12 n=5; P14 n=5; P16 n=5, P18 n=6; P21 n=6; P28 n=6,>P305 n=4). Interestingly, the AIS length further decreased between early matured mice (P28) (mean AIS length AcD: 35.0 ± 2.4 µm, nonAcD: 35.3 ± 1.6 µm) and fully matured mice (>P305, mean AIS length AcD: 31.1 ± 1.1 µm, nonAcD: 29.3 ± 1.8 µm). However, the decrease was not statistically significant. At no specific time point during development, significant differences between AcD and nonAcD cells were observed (Two-way ANOVA with mixed-effects model, Sidák's multiple comparisons test; details in Supplementary Table for S1 15). In the vHC group, AIS length peaked in both AcD and nonAcD neurons at P16 (40.5 ± 5.6 µm, 40.7 ± 3.8 µm, respectively) but decreased during further maturation to an average length of 31.9 ± 2.3 µm in AcD neurons and in nonAcD neurons to 30.9 ± 1.4 µm (****P<0.0001 for age, P=0.7379 for cell type, P=0.9855 for age × cell type interaction; two-way ANOVA with mixed-effects model (REML), P12 n=5; P14 n=5; P16 n=5, P18 n=5; P21 n=5; P28 n=6,>P305 n=4). In contrast to S1, AIS length remained stable in vHC between early matured mice (P28) to fully matured mice (>P305) (AIS length P28: AcD 32.9 ± 1.3 µm, nonAcD 32.02 ± 1.6 µm, >P305: AcD 31.9 ± 2.6 µm, nonAcD 31.0 ± 1.4 µm). Similar to S1, no significant difference between AcD and nonAcD neurons was observed at any time point during development (Two-way ANOVA with mixed-effects model, Sidák's multiple comparisons test; details in Supplementary Table for vHC 16) In conclusion, the AIS of juvenile mice was longer than that of mature mice in both brain regions. Although AIS length changes during development, there were no significant differences between AcD and nonAcD at specific time points during development.

Similar development profile of Na_v1.6 expression length along the AIS in S1 and vHC The Na_v1.6 channels are anchored by ank-G (reviewed by (Leterrier 2018)) and begin to cluster at the AIS during postnatal development (Boiko, Van Wart, et al. 2003; Akin, Solé, Dib-Hajj, et al. 2015). However, during early postnatal development, they do not cluster preferentially at the AIS, but also at the somatic membrane in pyramidal neurons (Figure 17C), which was also observed by

Akin, Solé, Johnson, et al. (2016). However, staining for $Na_v1.6$ channels within the AIS in animals younger than P12 was not reliable. This observation might be caused by a development switch of $Na_v1.2$ to $Na_v1.6$ during development, as observed in retinal ganglion cells (Boiko, Van Wart, et al. 2003). Therefore, this study focused on the investigation of $Na_v1.6$ parameters at the AIS in mice from P12 onward.

A developmental profile similar to that of AIS length was observed in $Na_v1.6$ length in both brain regions. In S1, the $Na_v1.6$ expression length developmental profile, like the AIS length developmental profile, can be distinguished between juvenile (P12-P16) and mature mice (P28 - >P305). $Na_v1.6$ expression on average covered the most distance in P18 mice (AcD: 33.3 ± 6.0 µm, nonAcD: 34.3 ± 5.2 µm) and the least in AcD neurons in P28 mice (25.3 ± 3.8 µm) and in nonAcD neurons in >P305 mice (26.7 ± 2.7 µm). Thus, $Na_v1.6$ expression length decreased significantly during development between juvenile and mature mice (Figure 17E, *P=0.0307 for age, P=0.3242 for cell type, P=0.6926 for age × cell type interaction; two-way ANOVA with mixed-effects model (REML), P12 n=5; P14 n=5; P16 n=5, P18 n=6; P21 n=6; P28 n=6,>P305 n=4). No significant differences between AcD and nonAcD neurons were observed at any specific time point in the course of this developmental study (Two-way ANOVA with mixed-effects model, Sidák's multiple comparisons test; details in Supplementary Table for S1 15). In vHC, $Na_v1.6$ expression length changes were more prominent than in S1, with a phasic profile similar to the AIS length, where juvenile and mature mice can be distinguished. The $Na_v1.6$ length peaked, similar to S1, at P18 in both cell types (AcD: 33.3 ± 3.0 µm, nonAcD: 34.3 ± 1.8 µm). Interestingly, the lowest $Na_v1.6$ was observed in P28 mice ($Na_v1.6$ length AcD: 23.3 ± 2.6 µm, nonAcD: 24.1 ± 2.3 µm). A significant decrease in $Na_v1.6$ expression length was observed between P18 (AcD: 33.3 ± 3.1 µm, nonAcD: 34.3 ± 1.8 µm) and P28 (AcD: 23.2 ± 2.6 µm, nonAcD: 24.1 ± 2.3 µm) but the length of $Na_v1.6$ clustering increased again in fully matured mice (P>305) ($Na_v1.6$ AcD: 26.9 ± 1.5 µm, nonAcD: 25.7 ± 2.6 µm) (Figure 17E, **P=0.0026 for age, P=0.5165 for cell type, P=0.9561 for age × cell type interaction; two-way ANOVA with mixed-effects model (REML), P12 n=5; P14 n=5; P16 n=5, P18 n=5; P21 n=5; P28 n=6,>P305 n=4). No significant differences between AcD and nonAcD cells were observed (Two-way ANOVA with mixed-effects model, Sidák's multiple comparisons test; details in Supplementary Table for vHC 16). Taken together, the developmental profile of $Na_v1.6$ expression length is similar to that of the AIS length and can be distinguished with the longest length in

juvenile mice and the shortest length in mature mice. However, while the length of $Na_v1.6$ clustering remained stable in mature mice in S1, it increased from early mature (P28) to fully mature (>P305) mice in the vHC group.

The position of $Na_v1.6$ within the AIS changes during development Interestingly, while the AIS length and $Na_v1.6$ expression length exhibited a similar developmental profile in both brain regions, the location of $Na_v1.6$ within the AIS fluctuated more strongly in S1 than in vHC. Similar to AIS and $Na_v1.6$ expression length in S1, juvenile mice (P12-P16) showed differences in the location of $Na_v1.6$ within the AIS. While the distal location of $Na_v1.6$ peaked at P12 in nonAcD neurons (mean distance: 8.7 ± 2.6 µm) and in AcD neurons at P16 (11.6 ± 6.0 µm), the most proximal location of $Na_v1.6$ within the AIS occurred in >P305 mice (AcD: 2.4 ± 1.5 µm, nonAcD: 1.9 ± 0.9 µm). However, in contrast to the AIS length and $Na_v1.6$ expression length in S1, the decrease to the most proximal $Na_v1.6$ location in fully mature mice (>P305) was not monotonic but changed between P21, P28, and fully mature mice (Figure 17F, ***P=0.0002 for age, P=0.0578 for cell type, P=0.8770 for age × cell type interaction; two-way ANOVA with mixed-effects model (REML), P12 n=5; P14 n=5; P16 n=5, P18 n=6; P21 n=6; P28 n=6,>P305 n=4). Overall, $Na_v1.6$ clustering within the AIS was more distal in AcD neurons than in nonAcD neurons (see Section 4.1.2). However, no significant differences between AcD and nonAcD cells were observed at any specific time point during development (Two-way ANOVA with mixed-effects model, Sidák's multiple comparisons test; details in Supplementary Table 15). In contrast to prominent changes in AIS and $Na_v1.6$ length during development in vHC, the location of $Na_v1.6$ changed slightly during development. The vHC displayed a similar developmental profile of $Na_v1.6$ location within the AIS as observed in S1, however, it was not as prominent. The distance of $Na_v1.6$ within the AIS peaked in AcD and nonAcD neurons at P16 (AcD: 8.1 ± 2.6 µm, nonAcD: 5.8 ± 2.4 µm). However, on average, the $Na_v1.6$ distance decreased significantly from P16 to P18 (AcD: 4.3 ± 2.1, nonAcD: 3.3 ± 1.8 µm) (Figure 17E, P=0.0534 for age, *P=0.0403 for cell type, P=0.9311 for age × cell type interaction; two-way ANOVA with mixed-effects model (REML), P12 n=5; P14 n=5; P16 n=5, P18 n=5; P21 n=5; P28 n=6,>P305 n=4). Overall, $Na_v1.6$ clustering within the AIS was more distal in AcD neurons than in nonAcD neurons (see Section 4.1.2). However, no significant difference at any specific time point was observed during development in AcD and nonAcD neurons in either brain region (two-way ANOVA with mixed-effects model (REML), Sidák's multiple comparisons test; details in Supplementary Table 16).

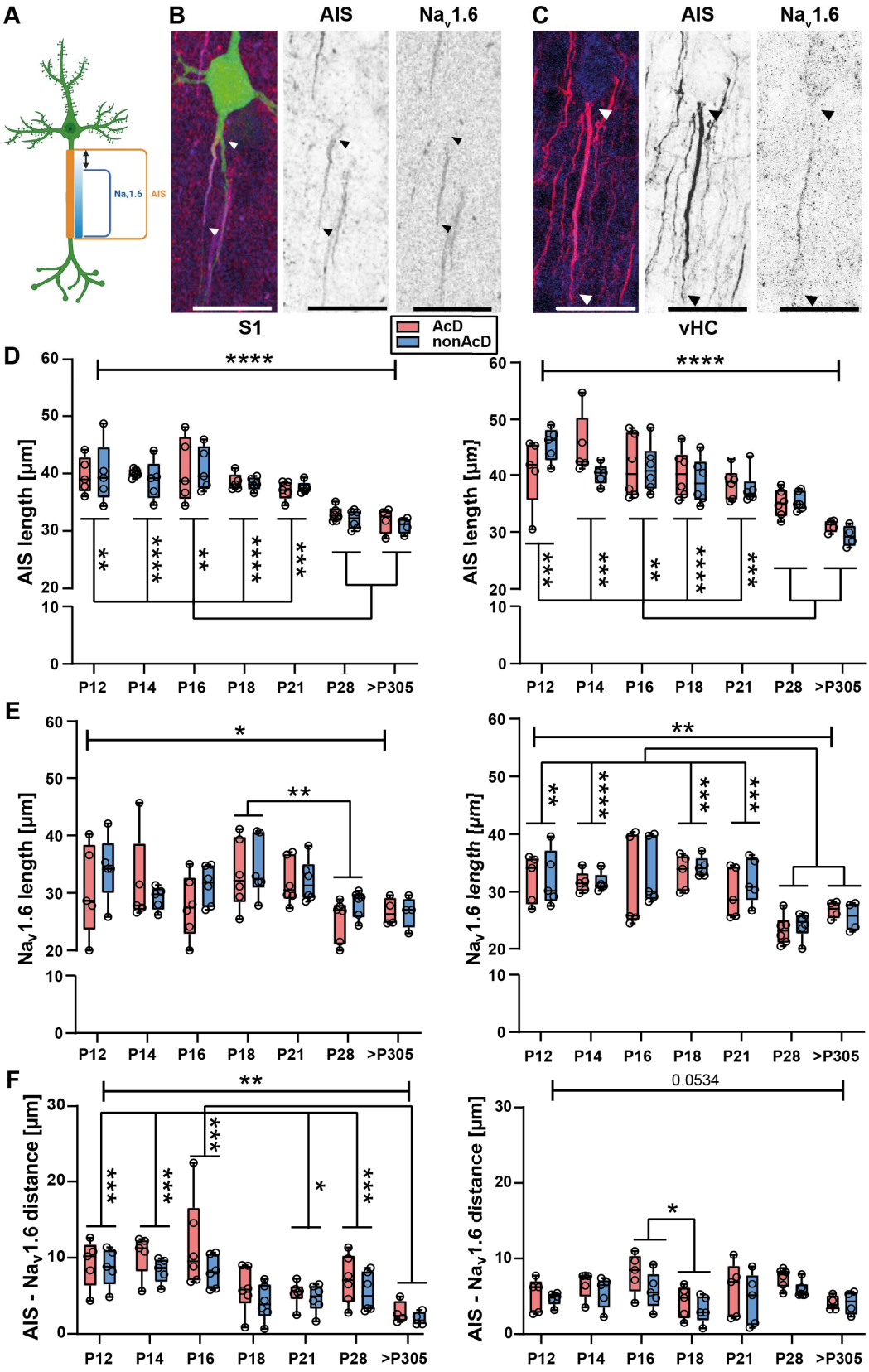

Figure 17: AIS length, Na$_v$1.6 length, and AIS-Na$_v$1.6 distance change during development.

Figure 17 continued:

A Schematic illustration of analyzed parameters for AIS length, Na$_v$1.6 expression length, and the position of Nav$_v$1.6 clustering within the AIS. **B** Representative examples of immunohistochemical staining for ank-G (as AIS marker) and Nav$_v$1.6 channel. **C** Representative examples of immunohistochemical staining of the AIS and Nav1.6 channel in P8 mice. Notably, Nav1.6 is also expressed at the soma. **D-F** The left panels show data from the S1 region and the right panels show data from the vHC. **D** The AIS length increased slightly from P12 to P16 but decreased during further maturation, especially compared to mature mice (P28 and >P305 mice). In vHC, AIS length peaked at P14 but also decreased during further maturation, especially compared to mature mice (P28 and >P305). **E** The Na$_v$1.6 expression length shows the same phenomenon as the AIS length in the brain regions, but the effect is not as prominent. **F** The AIS-Na$_v$1.6 distance increased from P12 to P16 in S1 and decreased from P18 to P21. At P28, it slightly increased again, but reached a minimum in mice aged >P305. In vHC, the AIS-Na$_v$1.6 distance was generally less than that in S1, and only significantly decreased from P16 to P18 (for all graphs: upper bar indicates p-value of two-way ANOVA with mixed-effects model (REML), Tukey's multiple comparisons test, S1 and vHC P<0.0001, where each dot represents a single mouse, S1 and vHC n=4-6 per group, *P>0.05, ** P<0.01, *** P<0.001, **** P<0.0001). Only representative statistical results are shown in the graphs. All results of multiple comparisons are shown in Supplementary Table for S1 14, 15 and for vHC 16, 17.

Conclusion on development of AcD neurons

In summary, the population of AcD neurons underwent significant changes throughout the developmental stages, especially in the vHC group. A noticeable increase in the number of AcD neurons was observed in juvenile mice (P12 to P28), surpassing the numbers observed in both younger (E18 to P3) and adult mice (>P305). Moreover, the AIS underwent adaptive modifications in its length during development, with a similar profile across both brain regions. Similar trends were also identified in Na$_v$1.6 channel clustering length and its positioning within the AIS. However, while developmental changes in the Na$_v$1.6 channel expression length were more apparent in the vHC, the S1 region showed a more pronounced shift in the positioning of the Na$_v$1.6 channels within the AIS.

4.3 Activity-dependent AcD development *in vitro*

After investigating the development profile of AcD neurons, I aimed to determine the potential mechanisms driving the development of AcD neurons. Therefore, this study investigated whether axonal morphology is predetermined or whether it forms in an adaptive, activity-dependent process. To address this, cortical organotypic slice cultures (OTCs) from the same transgenic mouse line (Thy1-GFP M) from P5 pups were created, and two different sets of experiments were performed. One experimental set consisted of live-cell imaging in which these intrinsically labeled Thy1-GFP neurons were imaged every 24h from day 3 *in vitro* (DIV) to DIV10. In the other set of experiments, cortical OTCs were treated with different reagents that are known to influence network activity. The treatment started on DIV3 and lasted for seven days. Half of the culture medium was exchanged every two days after the start of treatment. Subsequently, OTCs were fixed and immunofluorescence was performed against βIV-spectrin and the GFP signal was boosted with an antibody against GFP. Using confocal microscopy, Thy1-positive cells in cortical OTCs of S1 were imaged, classified, and subjected to morphometric analysis. AIS labelling simplified the identification process to separate the axonal branch from dendritic processes. However, in live-cell imaging, axonal and dendritic processes were distinguished according to the absence of dendritic spines on the axon.

4.3.1 Pharmocological treatment

In this study, pharmacological treatments were used to modulate network activity in cortical OTCs. Two reagents (KCl and bicuculline) were selected to increase the network activity, while two other reagents ($MgSO_4$ and ifenprodil) were chosen to decrease it. As mentioned above, those OTCs were treated for seven consecutive days from DIV3 to DIV10. To exclude a hemispherical effect, treated and untreated cultures were derived from the same brain slice and alternately treated. Elevated extracellular KCl concentrations have been widely used to study neuronal activity in the network (Grubb and Burrone 2010; Golbs et al. 2011). Previous studies have applied KCl with varying durations and concentrations, ranging from seconds to days and up to 150 mM (reviewed in (Rienecker et al. 2020)). While Grubb and Burrone (2010) used 15 mM KCl, a reduction to 6 mM KCl has also been proven to be effective in the same context (Jamann, Dannehl, et al. 2021). Therefore, in the present study, 6 mM KCl was added to the culture medium. Bicuculline methiodide is a widely used GABA-antagonist of the $GABA_A$ recep-

tors (Olsen et al. 1976). Blocking GABAergic synapses leads to an increase in neuronal and network activity, as shown in, e.g., hippocampal OTCs (Samoilova et al. 2003), cortical cultures (Caeser et al. 1989), and dopamine neurons in acute slices (Johnson and Seutin 1997). AIS length adaptations were observed after treatment with 15 µM bicuculline in acute slices (Jamann, Dannehl, et al. 2021). Therefore, 15 µM of bicuculline was added to the culture medium. To decrease network activity, magnesium sulfate ($MgSO_4$) and ifenprodil were used to increase the physiological block of NMDA receptors (Dodge and Rahamimoff 1967; Nowak et al. 1984; Dribben et al. 2010). The efficacy of this manipulation has been demonstrated in several brain regions, including the hippocampus and the cortex (Nowak et al. 1984; Hallak et al. 1994). A previous study observed increased AIS length with prolonged $MgSO_4$ treatment (+10 mM) in hippocampal OTCs (Thome, Janssen, et al. 2023), thus the same concentration was employed to the culture medium used in this study. Ifenprodil is known for its ability to block presynaptic NMDA receptors (Woodhall et al. 2001), specifically those that contain the subunit GluNR2B (Williams 1993). These presynaptic NMDA receptors are most abundant in juvenile stages (<P20, reviewed in (Bouvier et al. 2015)) and have been suggested to play a crucial role in axonal guidance and synaptic formation during development (Wang et al. 2011). Notably, prolonged ifenprodil treatment (1 µM) in slice cultures revealed the functional importance of the GluNR2B subunit in the migration of cerebellar granule cells (Mancini and Atchison 2007). Based on these findings, ifenprodil at the same concentration was selected to study its effects on neuronal morphology during development.

4.3.2 Live-cell imaging: transformation of neuronal morphology

The text of the following section has been adapted from Lehmann et al. 2023 and was originally written by myself.

To capture potential morphological changes, Thy1-GFP neurons in cortical OTCs were live-imaged every 24h for up to seven days, starting from DIV3 to DIV10 (Figure 18A). Subsequently, the visual classification of axon origin was verified by immunofluorescence against βIV-spectrin. Most neurons that were observed for at least two consecutive days retained their morphological type (65 nonAcD, 16 AcD of 98 neurons). However, in some neurons, the axon onset shifted between a dendritic and a somatic origin, and *vice versa* in a matter of days (a total of 17 of 98 cells). The transformation from a nonAcD to an AcD neuron was observed

slightly more frequently than the AcD to nonAcD transformation (11 vs. 6 cells). In one example, two transformations of the same neuron within six consecutive days were observed, from nonAcD to AcD, and again back to nonAcD (example given in Figure 18B.1-B.2). Five different transformation types were observed: three for conversion to AcD and two for conversion to the nonAcD morphology. First, an axon sprouted from the axonal shaft within 24 hours, converting a formerly somatic axon onset into a dendritic one and producing AcD morphology (Figure 18B.1; 2 of 11 cases). Second, the dendritic arbor and axon merged into a single branch (Figure 18C; 2 of 11 cases). Third, the axon migrated from the soma towards the dendrite, which was also observed to be linked to a soma protrusion in some cases (Figure 18D and E, 6 of 11 cases). The transition from AcD to nonAcD morphology required the retraction of the AcD stem dendrite until the axonal and dendritic branches emerged from the somatic envelope (Figure 19B and D, 5 of 6 cases). In one case, the dendrite gradually separated from the axon until it was sequestered and enveloped laterally from the soma (Figure 19C).

In conclusion, it appears that axon onset is a dynamic feature, moving over time from AcD to nonAcD state and *vice versa*. Since the proximal anatomy of the examined neurons remained dynamic and at least one neuron changed back to its previous nonAcD morphology, these modifications are probably not permanent.

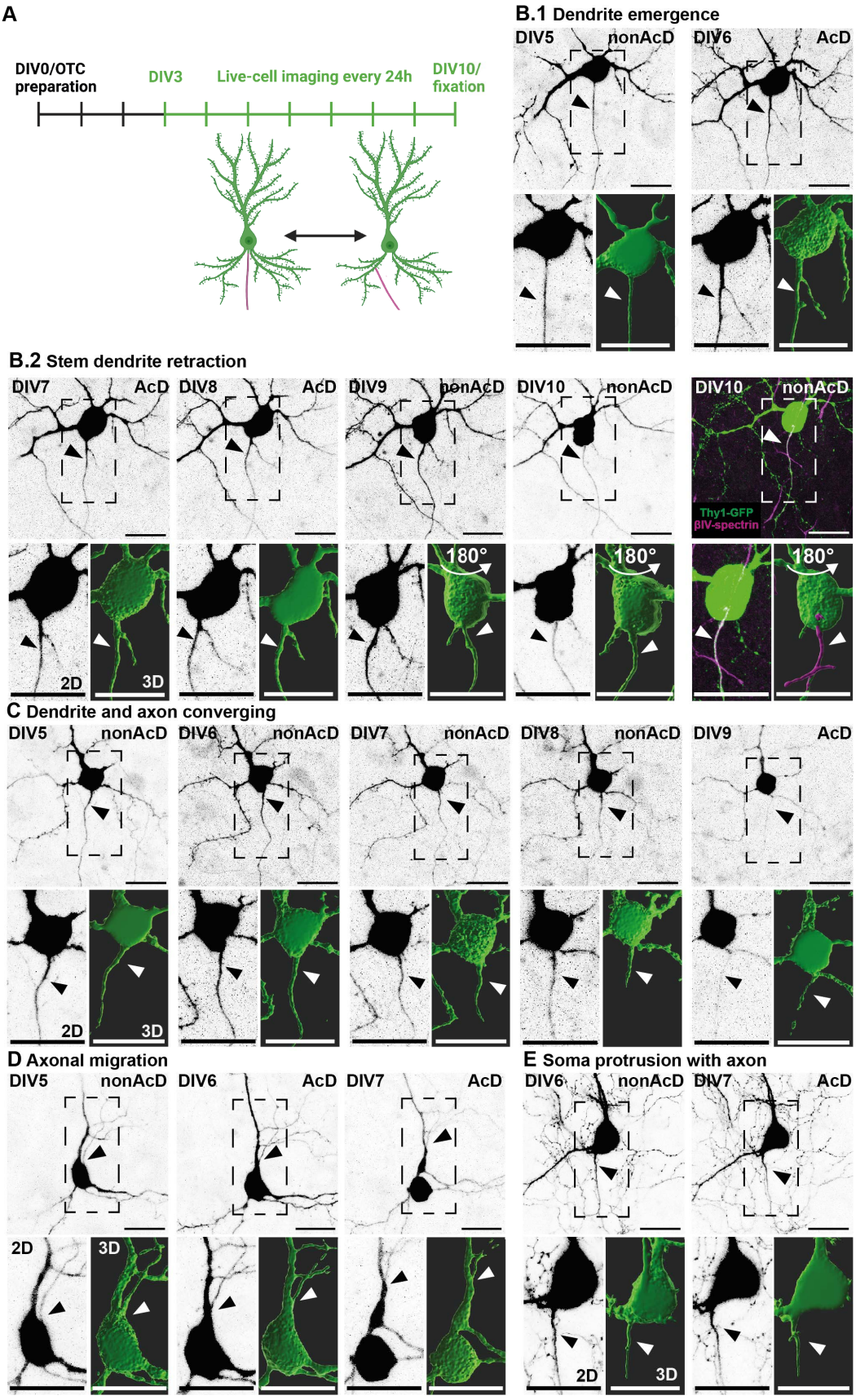

Figure 18: Representative examples for axon onset transformation from nonAcD to an AcD state. Representative examples of different transformation paths of live-imaged Thy1-GFP positive neurons.

Figure 18 continued:

A Schematic overview of experimental design. Live-cell imaging was performed for seven consecutive days (DIV3 to DIV10). Every 24h the same cell was imaged until it was fixed at DIV10. Subsequently, AIS was labeled by staining the scaffold marker βIV-spectrin (magenta). **B** The same cell underwent two transformation processes within six consecutive days. **B.1** shows the dendrite emergence within 24h, **B.2** depicts the stem dendrite retraction of the neuron until the axon emerges from the soma. **C** The pathway of axon and dendrite converging. **D** Transition pathway of axonal migration, in this case along the apical dendrite. **E** Soma sequesters and moves the axons further away from the cell body. The arrows indicate the origin of the axons. Rectangular box indicates the area for the close-up. Scale bar: 25 µm. Examples from this image were also published in Lehmann et al. 2023.

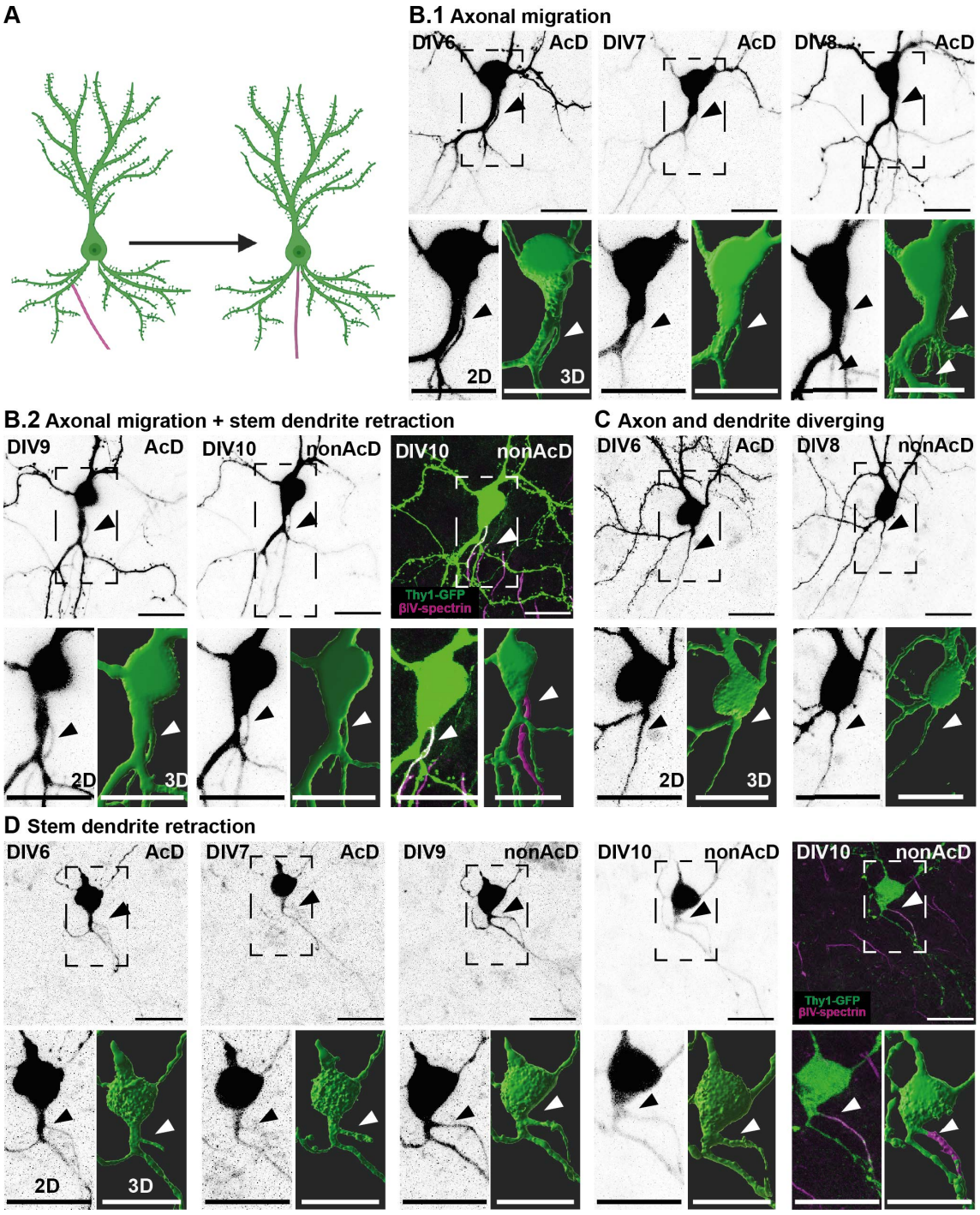

Figure 19: Transformation pathways from an AcD to nonAcD state. Representative example of a Thy1-GFP positive neuron during live-cell imaging. Every 24h the same cell was imaged until it was fixed at DIV10. Subsequently, AIS was labeled by staining the scaffold marker βIV-spectrin (magenta). **A** Schematic illustration of transformation direction. **B** The same neuron underwent two different processes. **B.1** The axon of the neuron migrates along the dendrite. **B.2** In addition to axonal migration, the stem dendrite is retracted until the AIS originates from the soma. **C** The pathway of axon and dendrite diverging. **D** The retraction of the stem dendrite. Rectangular box indicates the area for the close-up. The arrows indicate the origin of the axons. Scale bar: 25 µm. Examples from this image were also published in Lehmann et al. 2023.

4.3.3 Number of AcD neurons depends on network activity

Parts of the text of the following section have been adapted from Lehmann et al. 2023 and were originally written by myself.

Based on previous research demonstrating structural AIS plasticity in response to changes in network activity *in vitro* and *in vivo* (see Introduction Section 2.2.2), this study investigated whether such network changes also affect the transition between AcD and nonAcD morphologies in the utilized OTC system. As previously stated, proven *in vitro* pharmacological paradigms were applied to either boost (bicuculline, KCl) or reduce (ifenprodil, $MgSO_4$) network activity. Cortical OTCs were prepared from P5 animals and treated with one of the above-mentioned reagents for seven days from DIV3 to DIV10 (Figure 20A). OTCs were fixed and immunofluorescently processed at DIV10. To rule out any hemispherical effects, treated and untreated cultures were produced from alternating hemispheres of the same brain slice (Figure 20A).

In this study, the culture medium contained 15 µM bicuculline to increase network activity (Caeser et al. 1989). Data analysis revealed that the number of AcD neurons in the bicuculline-treated hemisphere was significantly higher than that in the control hemisphere (Figure 20D, bicuculline-treated OTC: 32.9 ± 16.4% vs. control: 14.6 ± 10.1%; **P=0.0013, paired *t*-test, n=16). However, when the extracellular KCl concentration was increased (+ 6 mM KCl in medium) to boost network activity (Grubb and Burrone 2010; Golbs et al. 2011), I did not detect any significant changes in the number of AcD cells (Figure 20E, KCl: 16.4 ± 11.0%, CTL: 25.3 ± 22.2%, P=0.2309, paired *t*-test, n=10). By blocking NMDA receptors, two pharmacological approaches were employed to reduce network activity. Data indicated that when 10 mM $MgSO_4$ was added to the culture medium, the number of AcD neurons decreased, however, the difference was not statistically significant (Figure 20F, $MgSO_4$: 9.9 ± 6.9%, CTL: 22.6 ± 12.6%, P=0.0520, paired *t*-test, n=10). When presynaptic NMDA receptors were blocked with 1 µM ifenprodil, no effect was observed on the number of AcD neurons (20G, ifenprodil: 13.0 ± 10.6%, CTL: 14.8 ± 24%, P=0.8750 paired Wilcoxon test, n=6). In summary, bicuculline treatment increased the number of AcD neurons in the treated OTC hemispheres compared to that in the control.

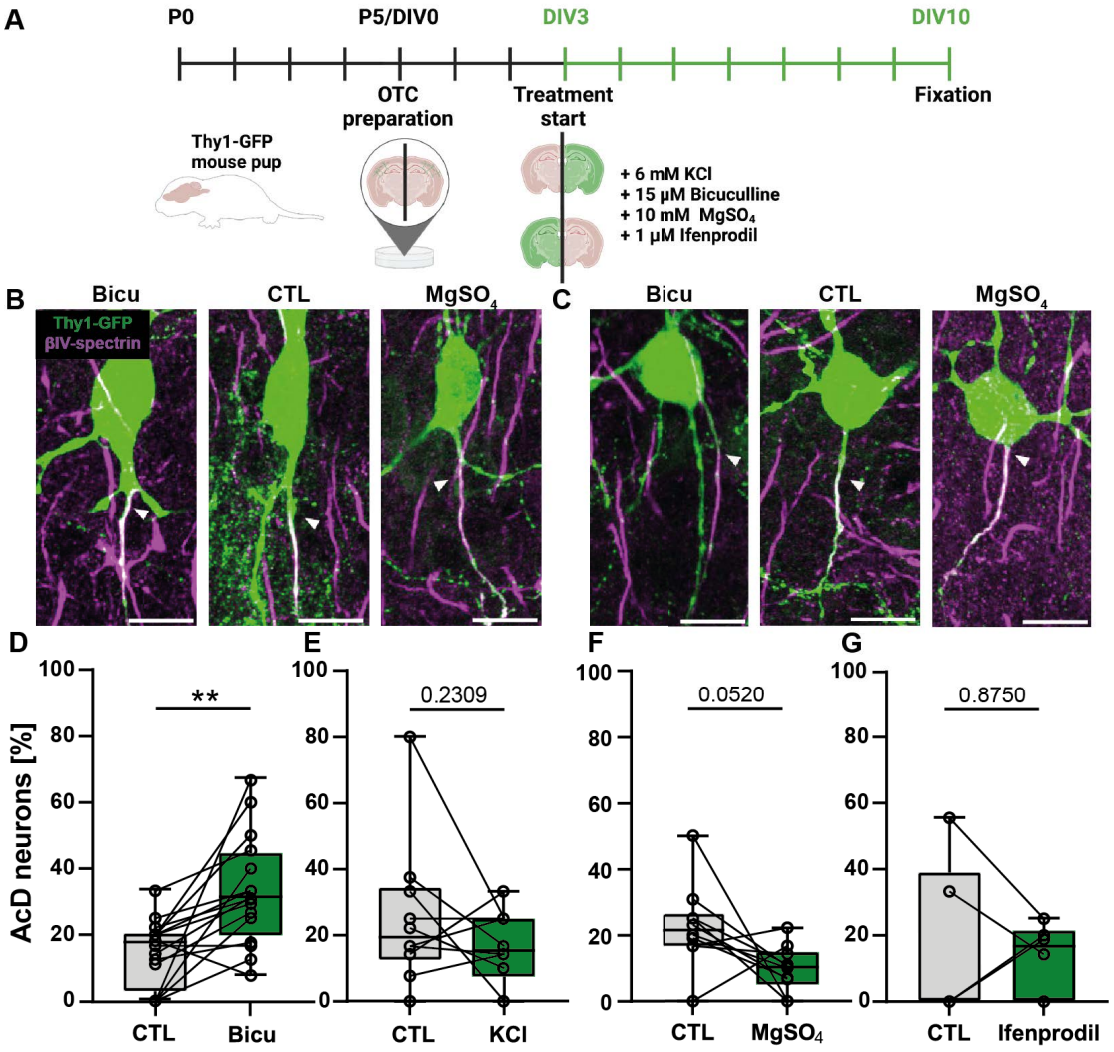

Figure 20: AcD neurons develop in an activity-dependent manner *in vitro*. **A** Experimental design: Hemispheres of cortical OTCs were alternately treated with one reagent (6 mM KCl, 15 µM bicuculline, 1 µM ifenprodil hemitartrate, or 10 mM $MgSO_4$), with the contralateral hemisphere serving as a control (indicated by the colors in the hemispheres). The treatment series lasted for seven days (from DIV3 to DIV10). **B** Representative examples of treated AcD neurons. **C** Representative examples of treated nonAcD neurons. Scale bar = 15 µm. **D** Increasing network activity by treating OTCs with bicuculline, thereby blocking GABAergic synapses, significantly increased the number of AcD neurons in the OTC compared with that in the control hemisphere (paired *t*-test, P=0.0013, n=16). **E** Treatment of OTCs with KCl and increasing network activity did not show any effect (paired *t*-test, n=10). **F** Silencing spontaneous network activity with $MgSO_4$ decreased the number of AcD neurons in OTCs compared with that in their control hemisphere, however not significantly (paired *t*-test, n=10). **G** Blocking presynaptic NMDA receptors with ifenprodil did not affect the number of AcD neurons (paired Wilcoxon test, n=6).

AIS Length remains unaffected by the treatments Previous studies have shown that the AIS adapts in an activity-dependent manner (Evans, Dumitrescu,

et al. 2015; Kuba, Adachi, et al. 2014; Jamann, Dannehl, et al. 2021). Increased activity predominantly has a short-term effect on the AIS length (Jamann, Dannehl, et al. 2021), while AIS length changes following decreased network activity take several days (Thome, Janssen, et al. 2023). To address this observation, I focused on investigating treatments that changed the number of AcD neurons. Therefore, immunofluorescence against βIV-spectrin was performed. AIS length and distance from the AIS to the soma were analyzed (Figure 21A and B). AIS length in bicuculline-treated cells was approximately 3.5 µm in median shorter than the AIS length in control and $MgSO_4$-treated cells, whereas AIS length of $MgSO_4$-treated cells remained mostly unchanged (Bicu: 27.5 µm, CTL: 30.3 µm, $MgSO_4$: 31.0 µm). However, this effect was not significant (Figure 21C, P=0.2767 for cell type, P=0.1463 for treatment, P=0.6038 for cell type × treatment interaction, two-way ANOVA with mixed effects model (REML), Tukey's multiple comparisons test). It is interesting to note that regardless of the treatment, AIS length was slightly longer in AcD than in nonAcD neurons, while in the control group, AIS length was similar in AcD and nonAcD neurons. When increasing network activity with bicuculline, the mean AIS length of AcD neurons was slightly longer (~2.5 µm) than in nonAcD neurons, however, not significantly (mean AIS length: AcD 28.7 ± 8.8 µm, nonAcD 26.2 ± 6.5 µm) (P=0.7477, Sidák's multiple comparisons test, AcD n=26, nonAcD n=29). Similarly, in $MgSO_4$-treated OTCs, the AIS length of AcD neurons was also slightly longer (~3.2 µm) than in nonAcD neurons (mean AIS length: AcD 32.0 ± 11.5 µm, nonAcD 28.7 ± 11.3 µm) (P=0.7292, Sidák's multiple comparisons test, AcD n=11, nonAcD n=37). In contrast to the treated OTCs, the AIS length of untreated OTCs of AcD neurons and nonAcD neurons exhibited a similar length (mean AIS length AcD: 30.8 ± 11.2 µm nonAcD: 31.1 ± 11.0 µm) (P=0.9987, Sidák's multiple comparisons test, AcD n=40, nonAcD n=43).

While AIS length remained unaffected, the treatments seemed to affect the distance from the AIS to the soma (Figure 21C, **P=0.0094 for treatment, ****P<0.0001 for cell type, P=0.7661 for cell type x treatment interaction, two-way ANOVA with mixed-effects model, Tukey's multiple comparisons test). Overall, neurons treated with $MgSO_4$ displayed more proximally located AIS in AcD and nonAcD neurons (Figure 20B, median distance to soma: $MgSO_4$: 4.7 µm CTL: 7.9 µm, Bicu: 7.5 µm). In more detail, the AIS in $MgSO_4$-treated nonAcD neurons was located approximately 3.8 µm closer to the soma than CTL nonAcD neurons, however, not significantly (mean distance $MgSO_4$: 7.3 ± 3.9 µm, CTL: 11.1 ± 7.6 µm) (P=0.0644, Sidák's multiple comparisons test, $MgSO_4$ n=11, CTL n=40). Sim-

ilarly, for AcD neurons, $MgSO_4$-treated AcD neurons were approximately 2.6 µm located more proximally than CTL AcD neurons, however also not significantly (mean distance $MgSO_4$: 2.2 ± 2.8 µm, CTL: 4.8 ± 4.9 µm) (P=0.0840, Sidák's multiple comparisons test, $MgSO_4$ n=37, CTL n=43). Bicuculline treatment did not affect the distance from the AIS to the soma in AcD or nonAcD neurons. The AIS of AcD neurons in bicuculline-treated neurons exhibited a similar location of the AIS than control AcD neurons (mean distance bicuculline AcD: 10.9 ± 5.8 µm, CTL: 11.1 ± 7.6 µm) (P=0.9914, Sidák's multiple comparisons test, bicuculline n=26, CTL n=40). Similarly, in nonAcD neurons, bicuculline was not observed to affect the location of the AIS (mean distance $MgSO_4$: 4.2 ± 3.2 µm, CTL: 4.8 ± 4.9 µm) (P=0.8618, Sidák's multiple comparisons test, $MgSO_4$ n=29, CTL n=43).

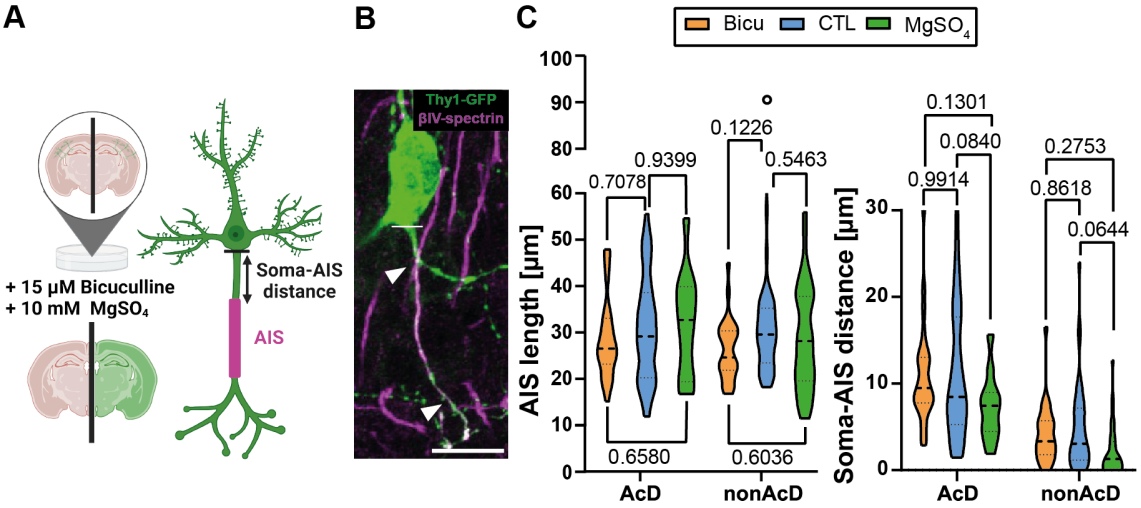

Figure 21: AIS parameters in treated OTCs. **A** Schematic overview of analysis. The AIS of neurons from $MgSO_4$- and bicuculline-treated OTCs were analyzed with regard to their AIS length and AIS location. Scale bar = 15 µm **B** Representative examples of analyzed AIS parameters in a Thy1-GFP positive neuron. Immunostaining of βIV-spectrin for labeling the AIS (magenta). Arrows indicate the origin of the axons. **C** AIS length was not significantly different between AcD and nonAcD cells treated with one of the reagents compared to the control group. In addition, the soma-AIS distance did not differ significantly between treatments or between cell types within the same treatment (two-way ANOVA with mixed-effects model (REML), Tukey's multiple comparisons test, Bicu: AcD n=26, nonAcD n=29; CTL AcD n=40, nonAcD n=43; $MgSO_4$ AcD n=11, nonAcD n=37). Violine plots indicate medians with 25–75% intervals, and error bars indicate min. to max. values.

In summary, increasing network activity with bicuculline increased the percentage of AcD neurons, but did not affect AIS length or position. Decreasing network activity with $MgSO_4$ showed an opposing trend by decreasing the percentage of AcD cells. However, it did not significantly affect AIS length or location.

4.4 A pilot study: electrophysiological profiling of cortical OTCs

The electrophysiological profiling serves as a preliminary study, which is not yet reliable with respect to the parameters to be evaluated and the results. Measurement methods for different parameters, such as AP parameters and EPSC recordings were used as described for acute slices in Jamann, Dannehl, et al. (2021). The establishment of electrophysiological recordings in OTCs was part of this thesis and serves as an important prerequisite for a thorough analysis of functional development and activity-dependent plasticity of AcD neurons.

4.4.1 Excitatory postsynaptic activity in treated OTCs

Morphological transformation in response to the administered treatments in cortical OTCs revealed that the number of AcD neurons was affected by bicuculline or $MgSO_4$ treatment. While bicuculline is known to increase the network activity (Samoilova et al. 2003), its treatment increased the number of AcD neurons (see section 4.3.3). $MgSO_4$ treatment is a well-described treatment that is known to decrease network activity (Dodge and Rahamimoff 1967), and its application resulted in an opposing trend in the number of AcD neurons by increasing the percentage of nonAcD neurons. However, it is unknown whether prolonged administration of these treatments in the OTC system sufficiently changed network activity in this study. Therefore, in a pilot study, I investigated whether excitatory currents were affected by bicuculline or $MgSO_4$. Similarly to the above-mentioned experiment, OTCs were treated with either bicuculline or $MgSO_4$ for seven consecutive days from DIV3 to DIV10. Based on live-cell imaging observations, which revealed that most transformations occurred from DIV6 onward, whole-cell patch-clamp experiments were performed from DIV6 to DIV10. During electrophysiological measurements, the administered drug was added to the artificial cerebrospinal fluid at the same concentration to avoid withdrawal effects. To improve the recording quality of excitatory postsynaptic currents (EPSCs), a cesium-based intracellular solution was used to block potassium channels. EPSC recordings in treated and control OTCs were initially investigated with respect to their frequency, amplitude, and rise-time and over the entire time course of the experiment (DIV6 to DIV10). However, those EPSC recordings in treated and control OTCs showed a strong heterogeneity in their kinetics (number of patched cells: Bicu: 24, CTL: 27, $MgSO_4$: 27). Therefore, EPSC kinetics were not further examined. Reasons for

this observation are unknown but it might depict an artifact. Therefore, I did not perform statistical analysis. However, I observed that bicuculline and $MgSO_4$ displayed a similar median frequency of 3.4 Hz and 3.2 Hz, respectively, and control cells of 3.1 Hz (Figure 22). This indicates that prolonged treatment seems not to influence the frequency of EPSCs. Notably, these observations need to be taken with caution as indicated above and were not statistically analyzed.

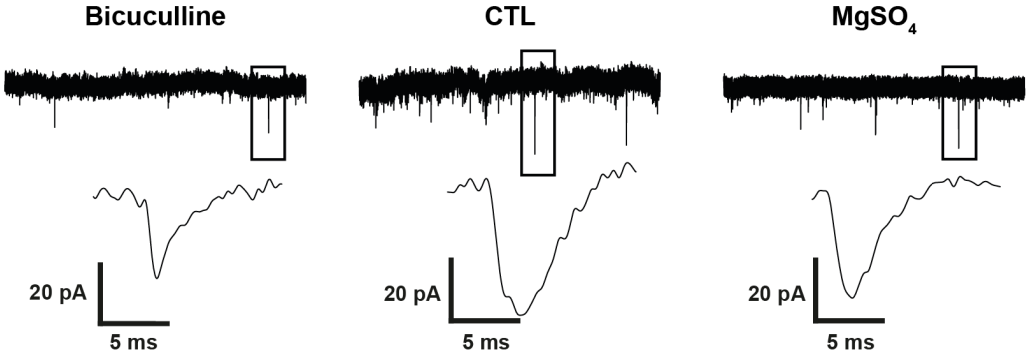

Figure 22: EPSCs in treated OTCs. Representative traces of EPSCs in treated OTCs. EPSCs were recorded at -70 mV.

4.4.2 Intrinsic cell properties in treated OTCs

Passive parameters

Further profiling of intrinsic cell parameters remains valuable for understanding the overall functional state of treated neurons. Therefore, this pilot study aimed to uncover potential compensatory mechanisms or alterations in response to treatments with regard to intrinsic cell parameters. Thus, whole-cell patch clamp recordings were performed with a potassium gluconate-based intracellular solution, and the passive and active properties of neurons treated with bicuculline or $MgSO_4$ were compared to those of control neurons. Patch-clamp recordings were performed in treated and control OTCs from DIV6 to DIV10. These days were selected based on the observation in the live-cell imaging study that most transformations started to appear from DIV6 onward. Pyramidal neurons were identified under the microscope by their triangular shape and characteristic AP firing pattern evoked by 500 ms current injection pulses into the soma. Treatment of OTCs with $MgSO_4$ or bicuculline did not affect the passive properties of pyramidal neurons, such as resting membrane potential (RMP), membrane resistance (R_{mem}), membrane capacitance (C_{mem}), or membrane time constant (τ) (Figure 23, P=0.2408 for treatment, ordinary one-way ANOVA, Tukey's multi-

ple comparisons test, $MgSO_4$ n=21, CTL n=20, Bicu n=23). RMP of the treated and untreated groups was very similar, with a median of -67.6 mV in $MgSO_4$-treated cells, -70.3 mV in control cells, and -69.8 mV in bicuculline-treated cells. Similarly, R_{mem} was not significantly different between the groups, but showed a tendency toward higher median values in $MgSO_4$-treated cells (183.0 MΩ) and bicuculline-treated cells (169.6 MΩ) compared to control cells (147.5 MΩ) (Figure 23, P=0.5742 for treatment, Kruskal-Wallis test, Dunn's multiple comparisons test). C_{mem} was observed in all treatment groups at approximately the same median value ($MgSO_4$: 85.2 pF, CTL: 84.4 pF, Bicu: 86.7 pF). Hence, C_{mem} remained largely unaffected by the treatment, and no significant differences were observed between the treatment groups (P=0.9424 for treatment, Kruskal-Wallis test, Dunn's multiple comparisons test). Furthermore, τ, which describes the time constant of the cell membrane, remained largely unaffected by the treatments (P=0.3988 for treatment, Kruskal-Wallis test, Dunn's multiple comparisons test). However, τ was observed to be slightly longer in $MgSO_4$-treated cells compared to control or bicuculline-treated cells, however not significantly ($MgSO_4$: 15.0 ms, CTL: 13.2 ms, Bicu: 14.4 ms) (Figure 23, Dunn's multiple comparisons test). Despite observing no changes in the passive cell properties of the treated cells, active parameters were investigated to explore the potential effects of the treatments on neuronal excitability. Specifically, AP characteristics and voltage-gated conductance were examined to shed light on any modulatory effects induced by the treatments.

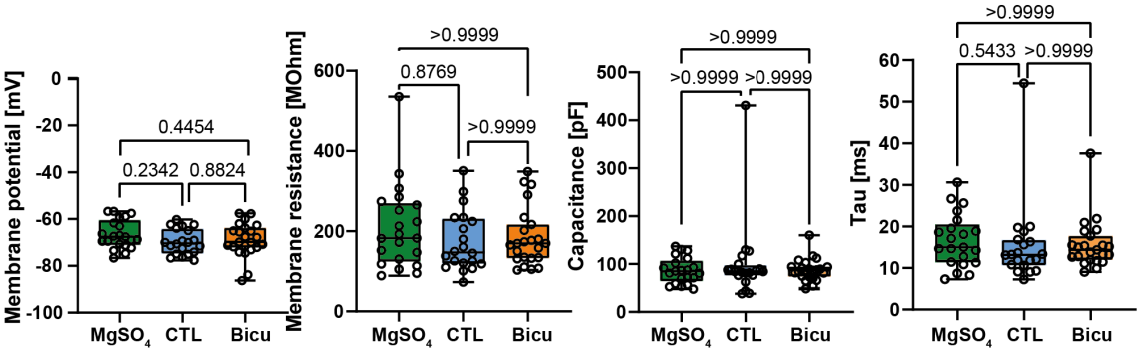

Figure 23: Passive properties remained unchanged in treated cells. RMP remained unaffected by the treatments (P=0.2408 for treatment, ordinary one-way ANOVA, Tukey's multiple comparisons test). R_{mem} was not affected by the treatments as well (P=0.5742 for treatment, Kruskal-Wallis test, Dunn's multiple comparisons test). C_{mem} remained largely unaffected by the treatment (P=0.9424 for treatment, Kruskal-Wallis test, Dunn's multiple comparisons test). τ remained largely unaffected (P=0.3988 for treatment, Kruskal-Wallis test, Dunn's multiple comparisons test) For all graphs: $MgSO_4$ n=21, CTL n=20, bicuculline n=23. Each dot represents a single cell.

Active parameters - action potential parameters

The amplitude of the first AP, elicited by injecting stepwise increasing current pulses of 20 ms duration, was affected by the treatments. $MgSO_4$- and bicuculline-treated cells exhibited a significantly smaller AP amplitude compared to that in control cells in median ($MgSO_4$: 79.5 pA, CTL: 85.9 pA, Bicu: 79.1 pA) (Figure 24B, *P=0.0104 for treatment, ordinary one-way ANOVA, Tukey's multiple comparisons test, $MgSO_4$ n=23, CTL: n=21, Bicu: n=20). In contrast, the AP half-width, which was defined as the time interval between de- and repolarizing voltage at halfway between threshold and peak, remained largely unaffected by the treatments (Figure 24C, P=0.6871 for treatment, Kruskal-Wallis, Dunn's multiple comparisons test). The median current threshold needed to elicit the first AP was slightly higher in bicuculline-treated cells, however, no significant differences between the treatment groups were observed (Bicu: 152.1 pA, CTL: 142.0 pA, $MgSO_4$: 142.0 pA) (Figure 24E, P=0.6511 for treatment, ordinary one-way ANOVA, Tukey's multiple comparisons test). Interestingly, cells treated with $MgSO_4$ showed a significantly lower voltage threshold in the first elicited AP than bicuculline-treated or control cells (Figure 24D, P<0.0001 for treatment, ordinary one-way ANOVA, Tukey's multiple comparisons test). Furthermore, upstroke and peak-related AP parameters were explored in treated and control cells. Therefore, phase plots (dV/dt vs. V) of the first elicited AP, generated by a current injection of 20 ms duration, were initially examined. However, the maximal voltage showed strong heterogeneity within groups and exhibited values that likely display artifacts during the recordings. For this reason, phase plots were not further investigated and not statistically analyzed. Additionally, to further investigate putative effects of the treatments, this investigation explored possible alterations in voltage-gated conductance by analyzing the behavior of sodium and potassium ion channels, which play a crucial role in AP generation and propagation. However, owing to the high complexity and branching morphology of pyramidal neurons, the voltage across the entire neuron is difficult to control and results in a space-clamp problem. Therefore, applying a specific voltage to neurons will not instantaneously and uniformly transmit across the entire neuron. Another confounding factor is the uneven distribution of channels across the membrane, which further complicates how voltage changes propagate through the cell. For these reasons, inward and outward currents were not further statistically analyzed. However, while $MgSO_4$-treated cells exhibited lower maximal inward current (generated by voltage pulses) at voltage levels of -30 mV to -10 mV, bicuculline-treated cells showed decreased

inward currents at higher voltage clamping levels (+10 mV and +30 mV) compared to control neurons. The outward current was examined at the step +30 mV, with regard to fast and delayed rectifier potassium currents. The fast rectifier current was measured using the maximal outward current peak directly after the repolarization phase. The delayed-rectifier potassium current was quantified by averaging the final third of the cell response to the voltage pulse. Treated and control cells exhibited a similar fast outward current (median: $MgSO_4$: 1430 pA, CTL: 1545 pA, Bicu: 1520 pA), but the delayed current was decreased in $MgSO_4$-treated cells (median $MgSO_4$: 1218 pA, CTL: 1520 pA, Bicu: 1508 pA). As mentioned above, these results do not depict the voltage-gated conductance accurately and need to be taken with caution.

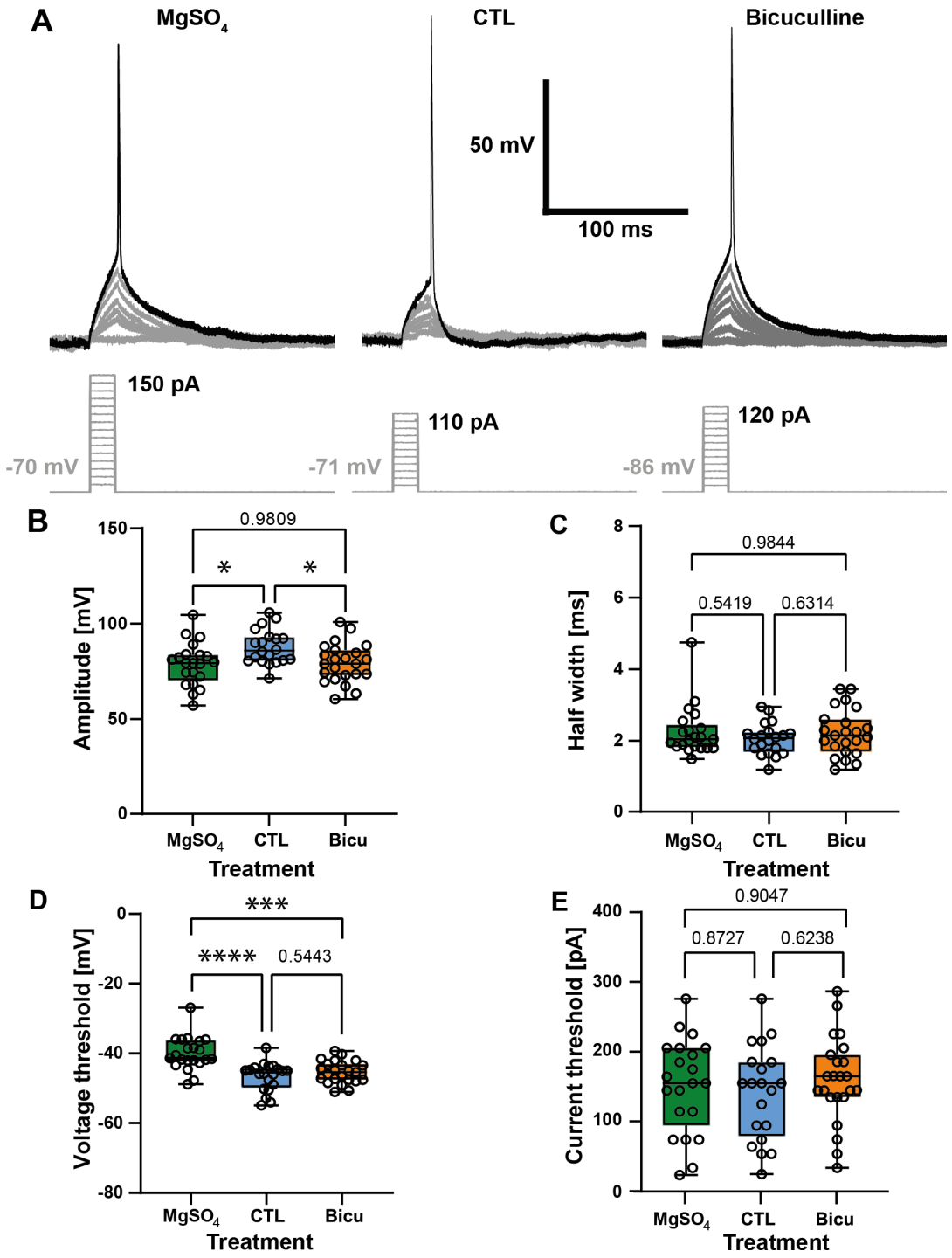

Figure 24: Changes in AP properties in cells treated with $MgSO_4$ and bicuculline. **A** Representative trace of the first AP elicited by 20 ms current injection from one cell in each treatment.

Figure 24 continued:

B-E Data from the analysis of AP properties and their thresholds. **B** Data on AP amplitude for each treatment. The amplitude of cells treated with $MgSO_4$ and bicuculline decreased significantly compared to that of cells in the control group (ordinary one-way ANOVA, Tukey's multiple comparisons tests). **C** Half-width of the AP amplitude was unchanged (P=0.6871 for treatment, Kruskal-Wallis, Dunn's multiple comparisons test). **D** Voltage threshold increased significantly in cells treated with $MgSO_4$ compared to the control and bicuculline group (P<0.0001 for treatment, ordinary one-way ANOVA, Tukey's multiple comparisons test). **E** Current threshold was unchanged (P=0.6511 for treatment, ordinary one-way ANOVA, Tukey's multiple comparisons test), for all tests: $MgSO_4$ n=21, CTL n=20, bicuculline n=23. Each dot represents a single cell.

4.4.2.1 Active parameters – input-output relationship

The input-output relationship of treated neurons was investigated by injecting current stepwise for 500 ms into the soma. The input-output curve showed that $MgSO_4$-treated cells elicited significantly fewer APs when 200 pA to 650 pA current was injected, whereas bicuculline-treated cells remained largely unaffected (Figure 25, **P=0.0020 for treatment, ****P<0.0001 for current pulses, ****P<0.0001 for treatment × current pulse interaction, ordinary two-way ANOVA, Tukey's multiple comparisons test). The maximal number of fired APs in response to current injection pulses was observed in $MgSO_4$-treated cells at a current injection pulse of 200 pA, but was significantly lower than that in bicuculline-treated and control cells (mean number of elicited APs $MgSO_4$ 14.8 ± 6.9, CTL: 20.4 ± 7.4, Bicu: 17.2 ± 9.7). However, the maximal number of APs in control cells was observed at a current injection of 250 pA for control and bicuculline-treated cells (mean number of APs CTL: 22.6 ± 9.1, Bicu:18.9 ± 12.8, $MgSO_4$: 13.6 ± 8.7). Notably, the protocol used a long injection pulse which led to prolonged depolarization. This possibly caused inactivation of voltage-gated ion channels making the cells unable to fire AP trains.

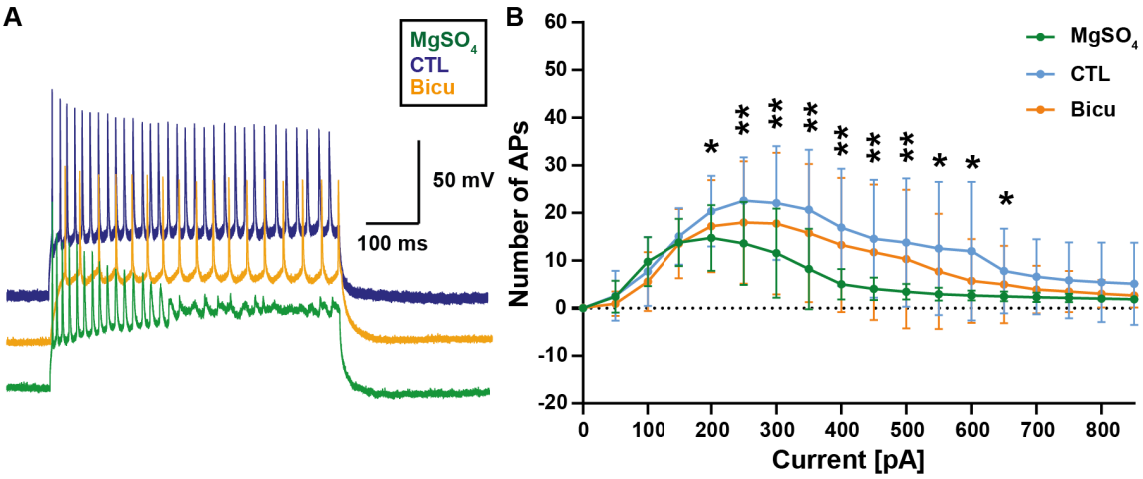

Figure 25: Neuronal firing frequency is reduced in $MgSO_4$ treated cells. **A** Representative traces of AP trains elicited by 500 ms current injection at 250 pA. **B** Firing frequency determined by 500 ms current injection with increased intensity. The firing frequency was significantly reduced in $MgSO_4$ treated cells from 200 to 650 pA current injection (P=0.0020 for treatment, P<0.0001 for current pulses, P<0.0001 for treatment × current pulse interaction, ordinary two-way ANOVA, Tukey's multiple comparisons test, $MgSO_4$ n=21, CTL n=20, bicuculline n=23, * P<0.05, ** P<0.01). All results of multiple comparisons are shown in Supplementary Table 18.

In conclusion, this pilot study indicated that bicuculline- and $MgSO_4$-treated cells exhibited significantly lower AP amplitudes. In addition, $MgSO_4$-treated cells showed an effect on the input-output relationship and exhibited a decreased voltage threshold in AP initiation.

4.4.3 Intrinsic cell properties in treated OTCs during development

Following the investigation of the overall effect of the treatments on intrinsic cell parameters, further exploration was undertaken to examine the developmental dynamics of these parameters. A previous study highlighted changes in cell properties during early cortical development, such as increased AP frequencies, maximal voltage velocity, and decreased AP voltage threshold and half-width (Benedetti et al. 2020). However, little is known about the electrophysiological developmental profile of cortical OTCs. Additionally, the impact of bicuculline, the treatment that significantly affected the number of AcD neurons in OTCs (see Section 4.3.3), remained largely unexplored in terms of its influence on these intrinsic parameters during development. This pilot study specifically focused on bicuculline treatment because of its significant morphological effects on AcD neurons in OTCs. Furthermore, previous findings have indicated that bicuculline affects the amplitude of APs (Section 4.4.2). To understand the intrinsic electrophysiological parameters that may underlie the observed increase in AcD neurons in bicuculline-treated OTCs compared to control OTCs, whole-cell patch clamp data obtained from Section 4.4.2 were divided according to the recording dates which spanned from DIV6 to DIV10.

Passive parameters

To investigate the passive properties, RMP, R_{mem}, C_{mem}, and τ were selected. While R_{mem}, C_{mem}, and τ remained largely unaffected during development, RMP exhibited alterations during development (**P=0.0070 for age, P=0.4357 for treatment, *P=0.0399 for age x treatment interaction, two-way ANOVA with mixed-effects model (REML), Tukey's multiple comparisons test for age, Sidák's multiple comparisons test for treatment; details in Supplementary Table 19 for age and 20 for treatment). Specifically, the RMP of bicuculline-treated and control cells depolarized in the course of the development and hyperpolarized again (Figure 26, DIV6: Bicu: -79.9 ± 6.5 mV, CTL: - 72.3 ± 4.5 mV, DIV 8: Bicu: -65.6 ± 7.4 mV, CTL: -69.7 ± 8.2 mV, Bicu: -74.1 ± 10.1 mV, CTL: -74.3 ± 10.2 mV). However, no significant effects were observed between the treatments or between any specific time point during development (Tukey's multiple comparisons test for age, see Supplementary Table 19, Sidák's multiple comparisons test for treatment; details in Supplementary Table 20).

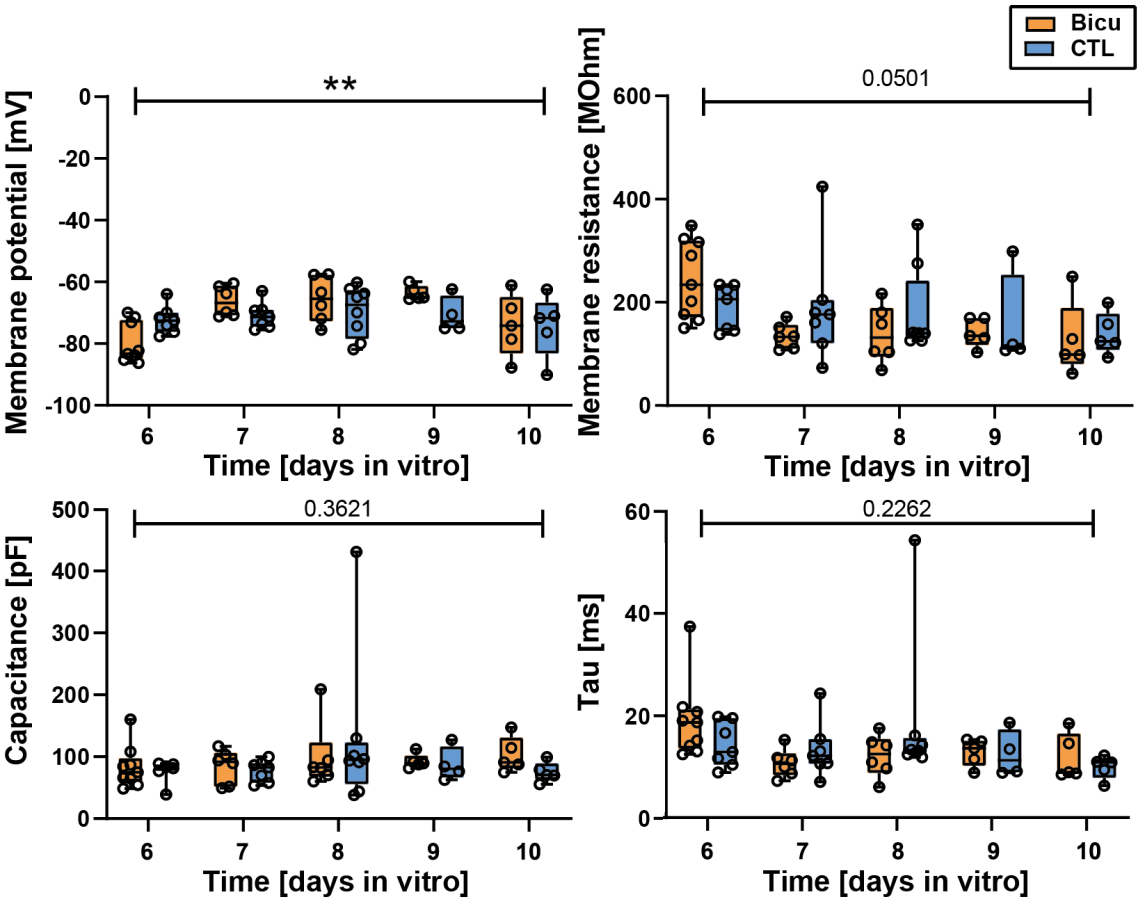

Figure 26: Resting membrane potential changes during development. R_{mem}, C_{mem}, and time-constant τ remained unchanged during development and between treatments. However, the RMP of bicuculline-treated and control cells depolarized in the course of the development and hyperpolarized again (P=0.0070 for age, P=0.4357 for treatment, P=0.0399 for age x treatment interaction). For all graphs: Two-way ANOVA with mixed-effects model (REML), Tukey's multiple comparisons test, Bicu DIV6 n=9, DIV7 n=6, DIV8 n=6, DIV 9 n=5, DIV 10 n=5; CTL DIV6 n=7, DIV7 n=7, DIV8 n=8, DIV9 n=4, DIV10 n=5. Each dot represents a single cell. Significant bars at the top of each graph represent the p-value of the ANOVA for age. All results of multiple comparisons are shown in Supplementary Table for Tukey's multiple comparisons test 19 and for Sidák's multiple comparisons test 20.

Active parameters - action potential parameters

Active intrinsic properties were tested using stepwise current injections. The amplitude of the first elicited AP increased continuously with increasing age (Figure 27B, ***P=0.0010 for age, *P=0.0395 for treatment, P=0.3276 for age × treatment interaction, two-way ANOVA with mixed-effects model (REML), Tukey's multiple comparisons test for age, Sidák's multiple comparisons test for treatment; all details can be found in Supplementary Tables 21 and 22). In more detail, the amplitude increased continuously with significant effects from DIV6 to DIV8 and to DIV10, regardless of the treatment (mean values for AP amplitude Bicu: 72.9 ± 7.0 mV, CTL: 79.9 ± 4.5 mV, DIV 8: Bicu: 78.9 ± 10.4 mV, CTL: 96.4 ± 9.5 mV, Bicu: 106.0 ± 22.2 mV, CTL: 103.4 ± 16.1 mV). However, at DIV8, the AP amplitude was significantly greater in the control cells than in the bicuculline-treated cells (*P=0.0404, Sidák's multiple comparisons test for treatment; details in Supplementary Table 22). Moreover, the half-width of the first elicited AP decreased in both treatments during development (Figure 27C, **P=0.0033 for age, P=0.2587 for treatment, *P=0.0420 for age x treatment interaction, two-way ANOVA with mixed effects model (REML), details in Supplementary Tables 21 and 22). In particular, the AP half-width decreased significantly from DIV6 to DIV7 regardless of the treatment group (**P=0.0056, Tukey's multiple comparisons test for age, DIV6: Bicu: 2.6 ± 0.6 ms, CTL: 2.3 ± 0.4 ms, DIV7 Bicu: 1.9 ± 0.4 ms, CTL: 1.6 ± 0.2 ms, details in Supplementary Table 21). In addition, while bicuculline-treated and control cells did not exhibit significant differences in the half-width, at DIV9, the AP half-width was significantly lower in bicuculline-treated cells than in control cells (**P=0.0083, Sidák's multiple comparisons test for treatment, details in Supplementary Table 22). Interestingly, the voltage threshold decreased continuously during development in both treatment groups, however, no significant differences between treatment groups or between any time point during development was observed (Figure 27D, **P=0.0032 for age, P=0.8782 for treatment, P=0.1068 for age × treatment interaction, two-way ANOVA with mixed-effects model (REML), Tukey's multiple comparisons test for age, Sidák's multiple comparisons test for treatment). In contrast to the other active parameters that were investigated, the current threshold of the AP remained remarkably unchanged (Figure 27E, P=0.8832 for age, P=0.7819 for treatment, P=0.3183 for age × treatment interaction, two-way ANOVA with mixed-effects model (REML), all details to Tukey's (for age) and Sidák's (for treatment) multiple comparisons test can be found in Supplementary Tables 21 and 22).

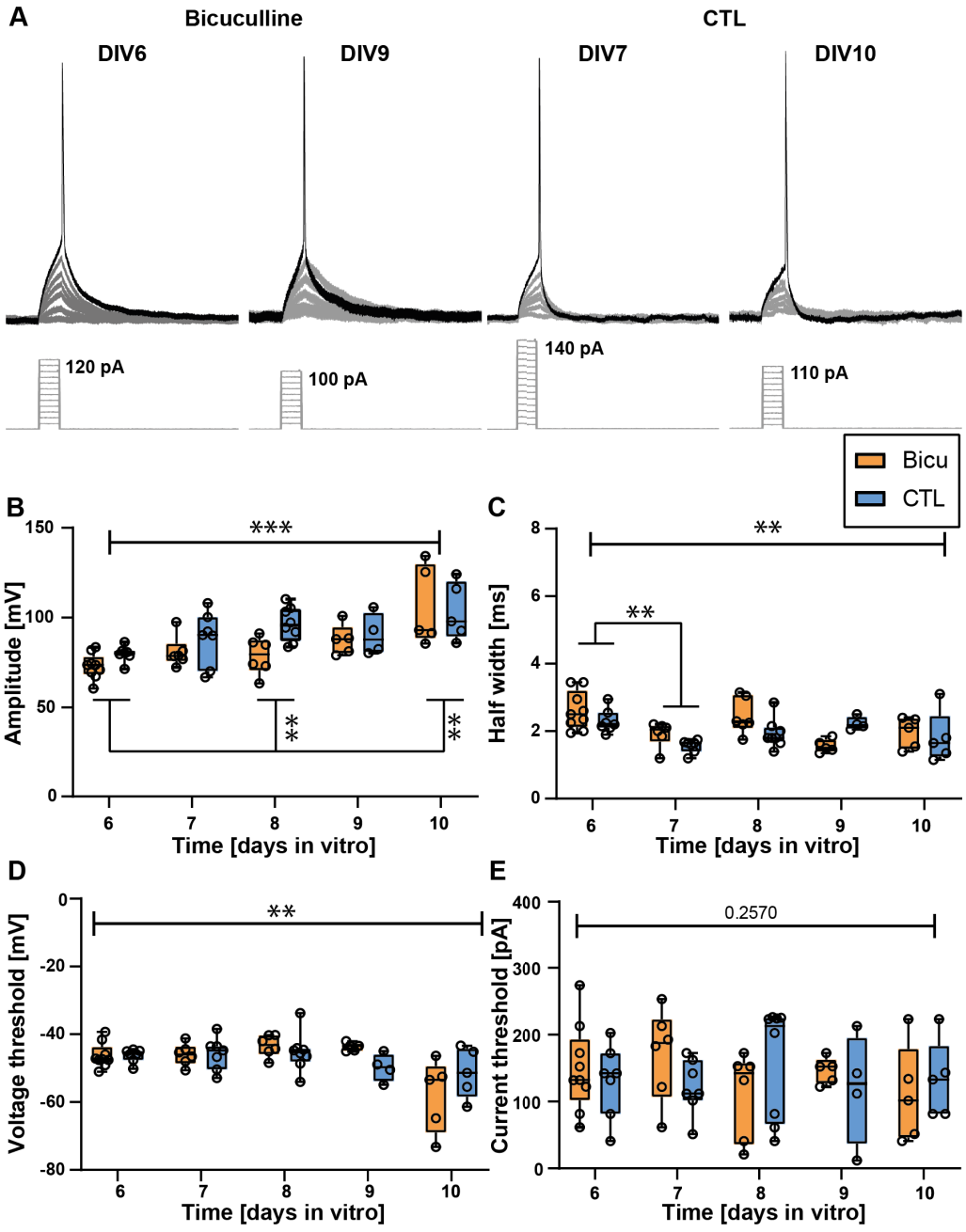

Figure 27: Changes in AP properties during development. **A** Representative traces of the first AP elicited by 20 ms current injection in bicuculline-treated and control cells during development. **B** Data on the development of the amplitude of the first elicited AP in bicuculline and control cells. During development, the amplitude increased significantly between DIV6, DIV8, and DIV10 (P=0.0010 for age, P=0.0395 for treatment, P=0.3276 for age × treatment interaction). **C** The half-width of the AP amplitude decreased significantly between DIV6 and DIV7 (P=0.0033 for age, P=0.2587 for treatment, P=0.0420 for age x treatment interaction). **D** Voltage threshold decreased significantly during development (P=0.0032 for age, P=0.8782 for treatment, P=0.1068 for age × treatment interaction).

Figure 27 continued:

E The current threshold was unchanged during development in cortical OTCs (P=0.8832 for age, P=0.7819 for treatment, P=0.3183 for age × treatment interaction). For all graphs: Bicu DIV6 n=9, DIV7 n=6, DIV8 n=6, DIV 9 n=5, DIV 10 n=5; CTL DIV6 n=7, DIV7 n=7, DIV8 n=8, DIV9 n=4, DIV10 n=5, two-way ANOVA with mixed-effects model (REML), Tukey's multiple comparisons test for age, Sidák's multiple comparisons test for treatment). Each dot represents a single cell. Significant bars at the top of each graph represent the p-value of the ANOVA for age. All results of multiple comparisons are shown in Supplementary Table for Tukey's multiple comparisons test 21 and for Sidák's multiple comparisons test 22 .

Active parameters - input-output relationship

The relationship between firing frequency and current injection revealed that control neurons were able to fire more APs during development than bicuculline-treated cells (Figure 28, ***P=0.0006 for treatment, ****P<0.0001 for current steps, ****P<0.0001 for treatment x current step interaction, ****P<0.0001 for subject variability, two-way ANOVA, Tukey's multiple comparisons test; more statistical results are shown in the Supplementary Tables for bicuculline-treated cells 25 and for control cells 24). However, control cells reached the maximal frequency at the current injection step of 500 pA at DIV10 (on average 34.8 ± 14.3 fired APs), while in bicuculline-treated cells, the maximal number of fired APs was reached at 250 pA at DIV7 (on average 32.2 ± 18.1). Additionally, the highest AP frequency in bicuculline-treated cells was observed in cells at DIV7 and DIV9, whereas it was observed in control cells at DIV10. Notably, the protocol used a long injection pulse which led to prolonged depolarization. This possibly caused inactivation of voltage-gated ion channels making the cells unable to fire AP trains.

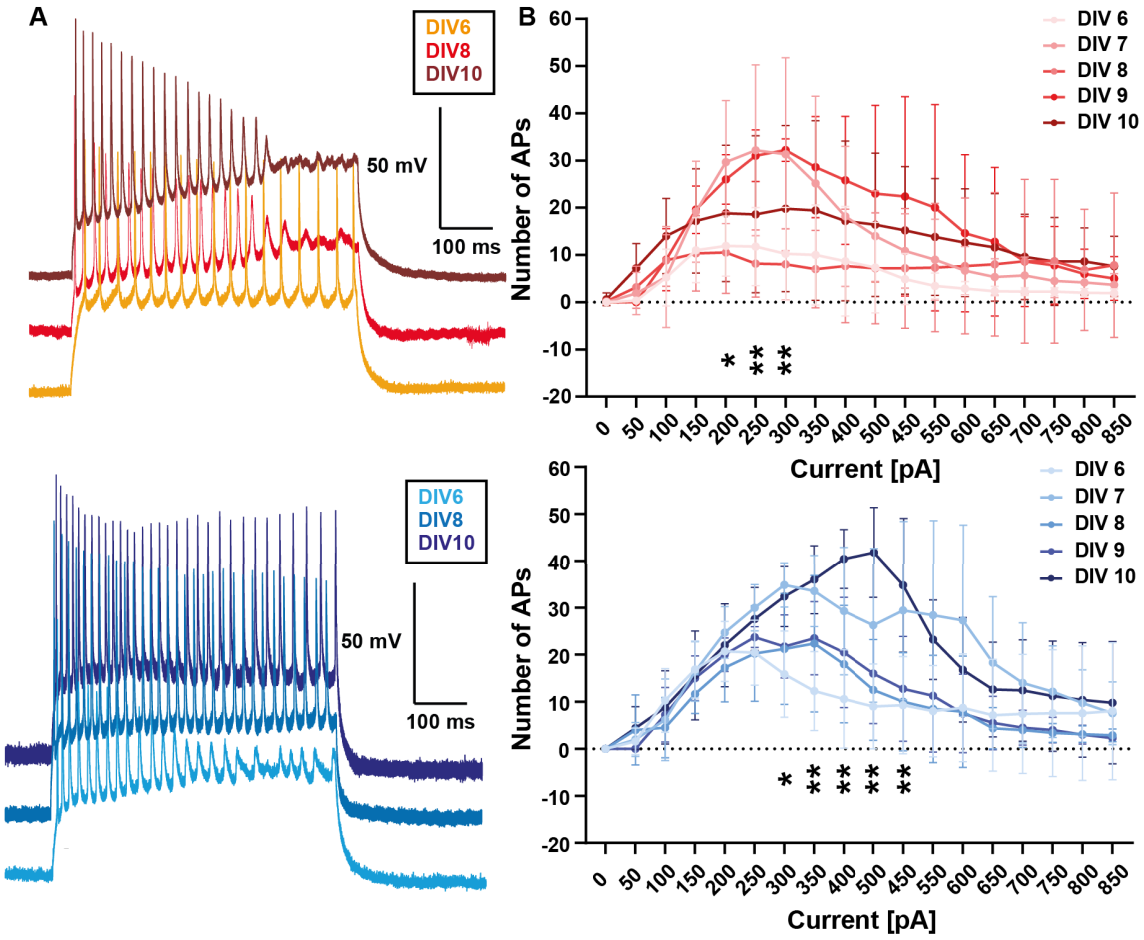

Figure 28: Neuronal firing frequency changes during development. A Representative firing traces of bicuculline-treated cells (top) and control cells (bottom) at different time points. **B** (top) Maximal number of fired APs peaked in neurons at DIV7 and DIV8, but decreased at DIV10. In general, neuronal firing peaked at current injections of 250 pA and 300 pA. **B** (bottom) Number of fired APs increased steadily during maturation. The highest frequency occurred at a current injection of 450 pA (P=0.0006 for treatment, P<0.0001 for current steps, P<0.0001 for treatment x current step interaction, P<0.0001 for subject variability, two-way ANOVA, Tukey's multiple comparisons test), for both graphs: Bicu DIV6 n=9, DIV7 n=6, DIV8 n=6, DIV 9 n=5, DIV 10 n=5; CTL DIV6 n=7, DIV7 n=7, DIV8 n=8, DIV9 n=4, DIV10 n=5). All results of multiple comparisons are shown in the Supplementary Table for bicuculline-treated cells 25 and for control cells 24.

Together, these findings reflect the maturation of active intrinsic properties within the period of observation (DIV 6-10). Cells exhibited a larger AP amplitude, and maximal voltage, whereas the AP half-width and voltage threshold decreased with increasing age in both treatment groups. Notably, in some of these active intrinsic properties, bicuculline-treated cells showed maximal values earlier than control cells.

Conclusion on activity-dependent AcD development *in vitro*

Live-cell imaging of cortical OTCs revealed that the axon onset is a highly dynamic feature, with cells changing from an initial classification of nonAcD to AcD neurons and *vice versa*. Furthermore, after moving the axon onset, the neuron was still able to revert this change. These transformations appeared within two to three days *in vitro*.

Blocking GABAergic synapses in cortical OTCs with bicuculline increased the number of AcD neurons compared to the contralateral, untreated hemisphere.

Bicuculline-treated cells exhibited decreased AP amplitudes compared to control cells. However, during development bicuculline-treated cells exhibited earlier maturation of several intrinsic active properties than control neurons. Hence, it can be hypothesized that bicuculline does not significantly interfere but might accelerate the neuronal maturation process.

4.5 Activity-dependent AcD development *in vivo*

4.5.1 The number of AcD neurons increases with enhanced sensory activity *in vivo*

Parts of the text of the following section have been taken and adapted from Lehmann et al. 2023 and were originally written by myself.

Live-cell imaging data *in vitro* demonstrated that the axon onset in cortical neurons is principally a dynamic feature, transitioning between somatic and dendritic locations. This type of plasticity can be regulated by pharmacologically induced changes in network activity. However, it remains unknown whether these remarkable morphological remodeling events can occur in living animals. Several critical periods (CP) occur during barrel cortex development and are essential for normal cortical development and sensory information processing (reviewed in (Erzurumlu and Gaspar 2012; Yang et al. 2018)). During these CPs, the barrel cortex undergoes substantial changes in neuronal excitability, synaptogenesis, and balance between excitation and inhibition (reviewed in (Yang et al. 2018)). Consequently, I hypothesized that an increase or reduction in sensory input during these CPs modulates the preferred axon onset in neurons of the sensory cortex. Several studies have found that early whisker-specific sensory experiences significantly affect the subcellular anatomy, such as dendritic spines and the AIS of neurons in the barrel cortex during development (Lee, Chen, et al. 2009; Jamann, Dannehl, et al. 2021). Sensory deprivation through whisker trimming significantly reduces neuronal connections in the deprived cortex (Cheetham et al. 2007), whereas sensory enrichment increases excitatory activity (Alwis and Rajan 2013). To study the effects of sensory deprivation and activation on axonal onset morphology, I unilaterally clipped whiskers and compared the deprived hemisphere to the intact/stimulated hemisphere in the same mouse, thereby minimizing inter-mouse variability. Notably, as mentioned in the Material and Method section, in this study Thy1-GFP positive neurons were analyzed, which mostly occur in layer V of S1BF. The lengths and onsets of the experiments were adapted to capture certain critical windows during the development (Figure 29A). Enriched environments (EE) with novel objects introduced daily were incorporated to boost exploration, thus facilitating an imbalance between cut and intact whisker fields. For AcD percentage analysis, approximately 100 Thy1-GFP neurons in the barrel field per brain and hemisphere were analyzed.

In the long-deprivation paradigm, whiskers were unilaterally clipped daily from the day of birth (P0) to P16 (Figure 29A). This approach aimed to examine the effects of sensory deprivation on axonal onset morphology. The assumption was that a prolonged period of sensory deprivation might lead to a significant change in the number of AcD neurons. However, long-term unilateral whisker deprivation had no significant impact on the number of AcD neurons in the deprived and intact S1BF (Figure 29C; intact: 12.2 ± 3.8%, deprived: 9.9 ± 3.4%, P=0.2679, paired *t*-test, n=5).

Long-term changes in sensory input might led to rapid network adaptation that could mask the initial plasticity of axon onsets. Thus, the duration of whisker deprivation was reduced to five days. The whisker deprivation window was selected from P12 (start of exploration and whisker movement, (reviewed in (Erzurumlu and Gaspar 2012)) to P16 (Figure 29A). Short deprivation caused no change in the number of AcD cells either (Figure 29C, intact: 11.5 ± 5.3%, deprived: 14.4 ± 5.4%, P=0.5130, paired *t*-test, n=6).

Although it is assumed that removing whiskers from one side would increase the use of the contralateral/intact site (Vees et al. 1998), the potential for exploration is generally limited in standard housing cages. Therefore, exploration and the use of intact whiskers were boosted by exposing the mice to EE for 6h daily from P12 to P16. Every day, novel objects with a variety of textures were introduced that could be explored, allowing the uncut whiskers to explore them. After five days of exploration, cells in the stimulated hemisphere showed an increased number of AcD neurons, whereas the deprived hemisphere exhibited a decreased number of AcD neurons (Figure 29D, 10.5% vs. 17.7% of all Thy1-GFP positive neurons, ***P=0.0006, paired *t*-test, n=6).

The plasticity of AcD morphology may be limited to specific developmental windows. Therefore, I added an older cohort of mice (>P100) that underwent five days of unilateral whisker removal paired with EE. Overall, the percentage of AcD neurons in mature mice was lower than that in juvenile mice. However, there was no discernible difference in the proportion of AcD neurons between the stimulated and deprived hemispheres (Figure 29D, enriched: 9.7 ± 2.2%, deprived: 9.9 ± 0.7%, n=5, P=0.8729, paired *t*-test, n=5).

To determine if the behavioral paradigms in conjunction with whisker trimming influenced the number of AcD cells, I examined the abundance of AcD neurons in

control mice that were kept in their home cage until P16 without any experimental manipulation. Notably, the number of AcD neurons is affected by the different paradigms, but no significant differences were observed between any group (CTL, stimulated, or deprived hemispheres in juvenile and mature mice) (*P=0.0407, ordinary one-way ANOVA, Tukey's multiple comparisons test). It is worth noting that the variation in the number of AcD neurons between animals decreased when they explored the EE in both deprived and enriched hemispheres as well as in old and young mice (Bartelett's test: P=0.0006, Supplementary Figure 31 and Supplementary Table 11).

In conclusion, a significant imbalance in barrel cortex inputs, resulting from unilateral whisker cutting and EE, caused an uneven distribution of AcD cells between both hemispheres in juvenile mice.

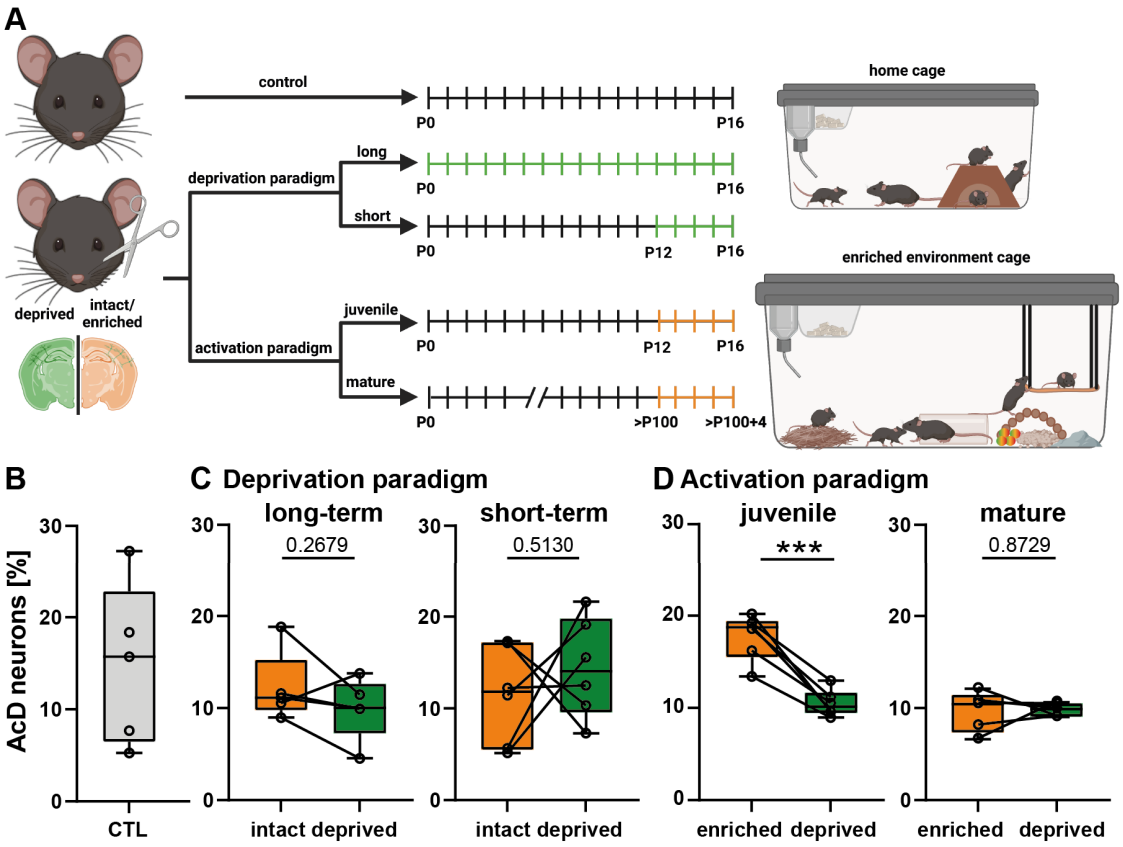

Figure 29: Unilateral whisker deprivation and stimulation of intact whiskers changed the number of AcD neurons. **A** Experimental design of the activation paradigm. Time scales indicate the different time periods of unilateral whisker trimming. Deprivation paradigms are indicated by green lines and hemisphere, whereas activation paradigms are indicated by orange lines and hemisphere. The whisker of control mice remained bilaterally unaffected. While in the deprivation paradigm, mice stayed in their home cage, in the activation paradigm mice were placed in an enriched environment cage (EE). Mice were placed in EE cage for 5 consecutive days for 6h daily. The floor space of the EE cage was significantly larger than the home cage (EE cage: 1500 cm^3, home cage: 542 cm^3). Every day novel objects with different textures were added to EE cage, to avoid habituation. **B** Box plot of the number of AcD neurons in control mice. Notably, the variance is significantly larger than observed in EE mice (young and old), for detailed statistical results, see Supplementary Figure 31 and Table 11. **C** Data on short- and long-term deprivation paradigm. Long-term unilateral whisker deprivation had no significant impact on the number of AcD neurons in the deprived and intact S1BF (P=0.2679, paired *t*-test, n=5). Similarly, short deprivation caused no change in AcD cell number (P=0.5130, paired *t*-test, n=6). **D** Data on activation paradigm in juvenile and mature mice. After five days of exploration, cells in the deprived hemisphere contained lower numbers of AcD neurons than those in the enriched hemisphere (P=0.0006, paired *t*-test, n=6). However, no discernible difference in the proportion of AcD neurons between the stimulated and deprived hemispheres in mature mice (>P100) was observed (P=0.8729, paired *t*-test, n=5).

4.5.2 The AIS lengths remains unaffected by stimulation paradigms

In a previous study by Jamann, Dannehl, et al. (2021), sensory deprivation was observed to alter AIS length. Therefore, AIS parameters, such as length and position, were investigated in the previously classified Thy1-GFP positive neurons from the EE experiment conducted in juvenile mice. In addition, these hemispheres were compared to mice of the same age (P16), but with bilaterally unaffected whiskers. Furthermore, the treated hemispheres and cell types were compared. For AIS analysis of layer V neurons, an approximately equal number of AIS in AcD and nonAcD neurons were analyzed, despite the variations in their frequencies within the samples and experiments. Therefore, approximately 25 AIS per hemisphere and brain were analyzed.

The AIS length of the stimulated and deprived hemispheres remained unaffected compared to control mice and to each other (Figure 30C, P= 0.1359 for treatment, ordinary one-way ANOVA, Tukey's multiple comparisons test). Notably, the AIS length in neurons of the stimulated hemispheres was in median shorter (~4.5 µm) than that in the bilaterally unaffected hemispheres, but not significantly (stimulated: 37.4 µm, deprived: 39.4 µm, CTL: 41.9 µm) (Figure 30C, P=0.1157, Tukey's multiple comparisons test). Additionally, no significant differences in AIS length were observed between AcD and nonAcD neurons (Figure 30D, P=0.4471 for cell type, P=0.1359 for treatment, P=0.4274 for cell type x treatment interaction, **P=0.0019 for subject variability, ordinary two-way ANOVA, Sidák's multiple comparisons test).

Additionally, the distance from the AIS to the soma was also not significantly affected by stimulated and deprived hemispheres compared to unaffected hemispheres (Figure 30D, P=0.2424 for treatment, ordinary one-way ANOVA, Tukey's multiple comparisons test). However, the AIS of stimulated hemispheres were located more distally within the axon compared to deprived or unaffected AIS, however not significantly (median AIS distance to soma: stimulated: 6.0 µm, deprived: 5.5 µm, CTL: 4.7 µm) (Figure 30D, Tukey's multiple comparisons test). Furthermore, no significant differences in soma-AIS distance were observed between treated and untreated AcD and nonAcD neurons (Figure 30C, P=0.2424 for treatment, ****P<0.0001 for cell type, P=0.6237 for treatment x cell type interaction, P=0.1510 for subject variability, two-way ANOVA, Sidák's multiple comparisons test).

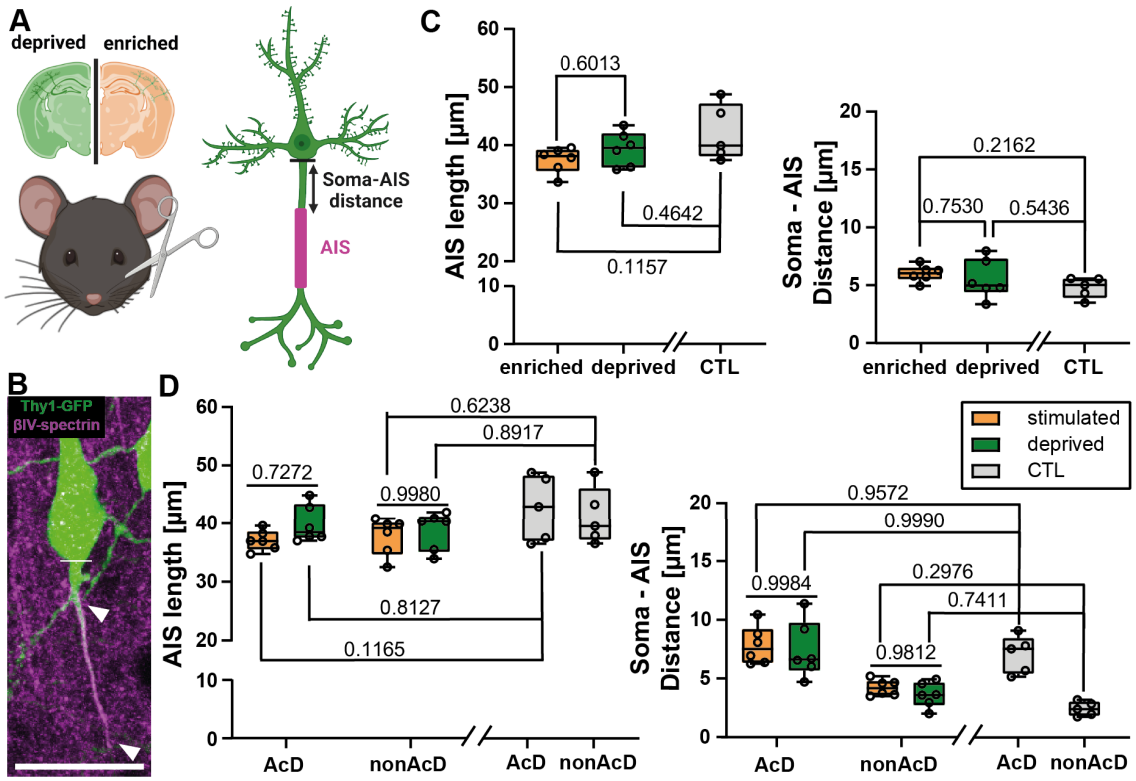

Figure 30: AIS length in Thy1-GFP positive cells of S1BF layer V neurons remained unchanged between deprived and stimulated hemispheres. A Schematic illustration of unilateral whisker deprivation and the affected hemispheres. Neurons from those hemispheres, the AIS length and their location were measured. **B** Representative illustration of AIS parameters analysis. **C** Data on AIS length and soma-AIS distance in affected (enriched and deprived) hemisphere and control hemispheres. Both AIS parameters remained unaffected by the different paradigms (AIS length: P= 0.1359 for treatment, soma-AIS distance: P=0.2424 for treatment, both ordinary one-way ANOVA). **D** Simiarly, no significant differences in AIS length were observed between AcD and nonAcD neurons (P=0.4471 for cell type, P=0.1359 for treatment, P=0.4274 for cell type x treatment interaction, P=0.0019 for subject variability, ordinary two-way ANOVA, Sidák's multiple comparisons test). Although, the soma-AIS distance is significantly more distally located in AcD and nonAcD neurons owing to the AcD branch, no effect of treated and untreated AcD and nonAcD neurons in hemispheres was observed (P=0.2424 for treatment, P<0.0001 for cell type, P=0.6237 for treatment x cell type interaction, P=0.1510 for subject variability, two-way ANOVA, Sidák's multiple comparisons test).

In conclusion, axon onset was affected by sensory deprivation or activation in juvenile mice, but AIS length and distance to the soma of layer V neurons remained largely unaffected.

Conclusions on activity-dependent AcD development *in vivo*

Unilateral whisker deprivation in combination with stimulating the remaining whiskers of the contralateral hemisphere in an EE cage revealed that the proportion of AcD neurons adapts in an activity-dependent manner. Specifically, S1BF of those hemispheres where stimulated whiskers projected showed significantly more AcD neurons than the contralateral hemisphere, which was sensory-deprived. However, this observation is unique to the early whisker-specific sensory experiences in juvenile mice (P16). Sensory deprivation alone was not sufficient to change the number of AcD neurons compared to the hemisphere with intact sensory information processing.

5 Discussion

In this study, the development of axon onset in the primary somatosensory cortex (S1) and ventral hippocampus (vHC) was investigated. Data show that (1) AcD neurons cluster $Na_v1.6$ more distally within the AIS than nonAcD neurons, (2) AcD neurons in the vHC develop differently than in S1, (3) the axon onset is a dynamic feature, and (4) the axon onset adapts in an activity-dependent manner.

5.1 Morphological differences in AcD and nonAcD neurons

$Na_v1.6$ is the main contributor to AP initiation (Royeck et al. 2008) in the AIS and clusters in the distal end of the AIS in excitatory neurons (Hu, Tian, et al. 2009; Lorincz and Nusser 2008). The starting point of this study was to investigate the differences in structural characteristics of AIS-specific features between AcD and nonAcD neurons. Therefore, AIS length, $Na_v1.6$ channel distribution along the AIS (distal vs. proximal), and expression length of $Na_v1.6$ in AcD and nonAcD neurons in S1 and vHC were investigated by performing immunofluorescence against scaffold proteins of the AIS (βIV-spectrin, ank-G) and $Na_v1.6$. Data showed that AcD neurons cluster $Na_v1.6$ channels more distally within the AIS than nonAcD neurons, while AIS length and the length of $Na_v1.6$ expression were not significantly different in AcD and nonAcD cells of S1 and vHC. A more distal location of $Na_v1.6$ within the AIS of AcD neurons might affect the excitability or timing of AP generation. Whether the distal location of $Na_v1.6$ renders the neuron more or less excitable remains unexplored. In general, the role of distally localized AIS, which occurs in AcD neurons, is under debate. Theoretically, a distally located AIS may be more excitable owing to its larger electronic isolation (Baranauskas et al. 2013; Eyal et al. 2014). Conversely, other studies have shown that a distal location of the AIS and their sodium channels reduce neuronal excitability (Grubb and Burrone 2010; Lezmy et al. 2017). However, whether a distal position of the AIS increases or decreases the excitability of a neuron is not binary but is also linked to the cell size (Goethals and Brette 2020; Gulledge and Bravo 2016). For instance, large neurons with a distally located AIS exhibited increased excitability, whereas small neurons showed the greatest excitability when the AIS was located proximally (Gulledge and Bravo 2016).

Recent findings have added a new perspective to this debate, revealing that during ripple oscillations, which are associated with high perisomatic inhibition

(Schlingloff et al. 2014), AcD neurons exhibit a 2.5-fold higher firing frequency than nonAcD neurons (Hodapp et al. 2022). However, outside these ripples, the firing frequency was similar in AcD and nonAcD neurons (Hodapp et al. 2022). Hence, the distal position of the AIS originating from a dendrite uncouples the initiation zone for APs from the perisomatic inhibition (Hodapp et al. 2022). This observation highlights the potential functional relevance of the distal AIS localization in modulating firing patterns. Further evidence from bird studies shows that neurons in the nucleus laminaris, which are tuned to high frequencies (>2kHz), have a more distal Na_v channel location than those tuned to lower frequencies (<1kHz) (Kuba, Ishii, et al. 2006; Kuba and Ohmori 2009). Hence, the location of Na_v channels may be influenced by the frequency of presynaptic inputs of a neuron (Kuba and Ohmori 2009; Kuba, Oichi, et al. 2010).

The distal shift of $Na_v1.6$ within the AIS could also affect the way a neuron integrates information from various synaptic inputs. Inputs located closer to the AP initiation site may have a greater influence on AP generation. This distant location may also affect the temporal dynamics of the synaptic integration. On the one hand, owing to the larger electronic isolation towards the soma, synapses located close to the $Na_v1.6$ channels might initiate APs faster. However, a more distal spike initiation zone may require a longer time to integrate synaptic potentials, thus generating an AP, owing to the current sink function of the soma (reviewed in (Kole and Brette 2018)). Another putative effect of the more distally localized $Na_v1.6$ isoform is the effect on the backpropagation of the AP to the somatodendritic domain. AP backpropagation is promoted by the proximally located $Na_v1.2$ isoform in the AIS (Hu, Tian, et al. 2009). It can be hypothesized that the more distal localized $Na_v1.6$ expression profile within the AIS could potentially be compensated by the $Na_v1.2$ isoform. An isoform switch of $Na_v1.2$ and $Na_v1.6$ channels was observed in retinal ganglion cells during development (Boiko, Van Wart, et al. 2003). Backpropagation is critical for various forms of synaptic plasticity, because it serves as an associative link between presynaptic excitation and postsynaptic responses (reviewed in (Stuart, Spruston, et al. 1997)). Independent of the channel distribution, the branch point from the axon and AcD might influence the probability of AP backpropagation. AP propagation into dendrites often failed at branch points in hippocampal pyramidal neurons (Spruston et al. 1995).

In the course of this study, it was initially hypothesized that there may be significant differences in the AIS length and expression length of $Na_v1.6$ between AcD

and nonAcD neurons. This expectation was based on the observation that morphological differences in neurons can have a considerable impact on their electrophysiological properties, such as AP generation and propagation (reviewed in (Goaillard et al. 2020)) and its initiation site, the AIS (Gulledge and Bravo 2016). Specifically, variations in AIS length and alterations in $Na_v1.6$ expression length could have contributed to the differential neuronal behaviors between AcD and nonAcD neurons. Contrary to these expectations, the results did not yield any significant differences in either AIS length or expression length of $Na_v1.6$ in AcD and nonAcD neurons. This result was surprising, given the substantial morphological differences between the two groups. The conservation of these key features, which are crucial to electrophysiological activity and are known to be highly adaptable, raises intriguing questions about information integration in these neurons. While the AIS length and $Na_v1.6$ expression length may not be distinguishing factors between AcD and nonAcD neurons, this lack of variation in combination with their unique morphological characteristics could still influence distinct neuronal function and behavior.

In the future, investigation regarding the expression profile of the $Na_v1.2$ isoform would elucidate whether the increased distance in AcD neurons is compensated with increased $Na_v1.2$ expression profile in the proximal part of the AIS, to ensure sufficient backpropagation. Additionally, the synaptic innervation of AcD and nonAcD neurons should be investigated by performing patch-clamp recordings in postsynaptic AcD and nonAcD neurons accompanied with low or high frequency stimulation of the inhibitory or excitatory presynaptic neuron with channelrhodopsin. This would elucidate whether the location of $Na_v1.6$ channel isoform in AcD neurons in vHC and S1 is dependent on the firing frequency of their presynaptic input.

5.2 Abundance of axo-axonic synapses

Axo-axonic synapses are highly variable in their number in pyramidal neurons compared to perisomatic synapses in pyramidal neurons of layer 2/3 in the visual cortex (Schneider-Mizell et al. 2021). Their abundance and innervation pattern from Chandelier neurons strongly depend on the AIS radius and the somatic area of pyramidal neurons (Schneider-Mizell et al. 2021). Therefore, it was initially hypothesized that the abundance of axo-axonic synapses at the AIS of AcD and nonAcD neurons might be different. In particular, axo-axonic synapses are known

to play a role in modulating the activity of postsynaptic neurons (reviewed in (Cover and Mathur 2021)). This modulation can significantly influence the information processing in neuronal networks.

The results showed no significant difference in the abundance of axo-axonic synapses at the AIS in AcD and nonAcD neurons in S1 and vHC in mature (P28) mice. A putative limitation of this study is that only axo-axonic synapses were investigated. While Chandelier neurons exclusively form axo-axonic synapses, other types of interneurons form a mix of axo-axonic and somatodendritic synapses (Schneider-Mizell et al. 2021). Therefore, other inhibitory synapses formed by different neurons located at the somatodendritic compartment of the postsynaptic neuron might also play a crucial role in information integration and lead to putative differences between AcD and nonAcD neurons. However, the AIS is the main generator of APs (reviewed in (Rasband 2010), and axo-axonic synapses at the AIS might therefore have the highest impact on AP initiation and processing. The similar abundance of axo-axonic synapses in AcD and nonAcD neurons might be governed by common molecular or cellular mechanisms that operate similarly in both types of neurons, which influence the formation and maintenance of these synapses at the AIS. These mechanisms could involve certain synaptic proteins that are involved in anchoring $GABA_A$ receptors at the postsynaptic sites such as dystrophin-gylcoprotein complex and neurolignin-2 (Panzanelli et al. 2011). However, these proteins have been specifically observed to be involved in perisomatic and dendritic innervation (Panzanelli et al. 2011), but it is not known whether this is specific to those proteins or also applies to axo-axonic innervation. Another possible mechanism could be neurotrophic factors. Brain-derived neurotrophic factor (BDNF) has been assumed to regulate the formation of inhibitory synapses (Hong et al. 2008) and may be similarly expressed in AcD and nonAcD neurons. Another aspect might be that AcD and nonAcD neurons possibly perceive similar activity levels or patterns from their presynaptic innervations. Axo-axonic synapses adapt in an activity-dependent manner, assuming that excitability is adjusted and homeostasis is maintained by altering their abundance (Wefelmeyer et al. 2015; Pan-Vazquez et al. 2020). A similar activity level would result in a similar abundance of axo-axonic synapses as part of a homeostatic response. Although the abundance of these GABAergic synapses at the AIS might not be significantly different, it remains to be elucidated whether they differ in synaptic strength. Additionally, GABAergic synapses located at the somato-dendritic compartment may lead to different signal integra-

tion in neurons. Therefore, it would be interesting to determine whether these synapses, specifically located at the stem dendrite or the AcD, are located differently in these neurons compared to nonAcD dendritic branches in AcD neurons and nonAcD neurons, thereby leading to different signal integration or propagation.

5.3 Development of AcD neurons

The underlying hypothesis of this study was that the proportion of AcD neurons changes during development. Therefore, time points during development that coincided with various critical periods of cortical development were selected (reviewed in (Erzurumlu and Gaspar 2012). Furthermore, to investigate the putative effects of brain regions, the development of AcD neurons was compared between the S1 and vHC. In addition, neurons, where the dendrites and axons branched off simultaneously (shared root cells), were considered in this study. The results showed that the proportion of AcD neurons changed during development in both brain regions. However, the effect was more prominent in the vHC. A similar observation was made for the development of shared root cells. Specifically, in vHC, the number of AcD neurons increased drastically from young pups (E18-P8) to juvenile mice (P12-P28) and decreased in mature (>P305) mice. A similar phenomenon was observed for shared root cells in vHC.

One possible reason for the difference between S1 and vHC may be related to the function of these brain regions. The hippocampus, particularly the ventral part, is known to be highly involved in functions like learning, memory, and emotional regulation (Introduction 2.3.1). Thus, AcD neurons may play a crucial role in these functions. Recently, it was discovered that AcD neurons are more likely to participate in sharp wave ripple oscillations than nonAcD neurons (Hodapp et al. 2022), which are important for memory consolidation (Girardeau et al. 2009; Fernández-Ruiz et al. 2019; Hodapp et al. 2022). During development, the brain may adapt by adjusting the number of these neurons based on the learning and memory demands. Once mice are mature and their environment and behaviors become more stable, the demand for these neurons may decrease. Another hypothesis might be that, during early development, the brain overproduces neurons and connections (reviewed in (Tierney and Nelson 2009)): the more neurons present, the greater the potential for connections. In particular, AcD neurons may have unique connectivity patterns because of this structural peculiarity. They may par-

ticipate in both receiving inputs and sending outputs in neural networks, which could enhance the complexity and efficiency of neural communication. Subsequently, neurons and connections that are not used are diminished, reflecting pruning and refinement in neural circuits based on experience as mice mature. Shared root cells show a very similar occurrence during development and might depict an intermediate state between the nonAcD and AcD states, as indicated by the live-cell imaging data of the current study (Section 4.3.2). S1 is primarily responsible for processing sensory information. The function of AcD neurons in S1 might be different from those in the hippocampus and may be less crucial for the functioning of the cortex. However, the discrepancy of the less prominent effect in the abundance of AcD neurons during development might also be caused by the specific percentages of AcD neurons in each area (vHC CA1 regions up to 50%, S1 up to 20%). The larger proportion of AcD neurons in the hippocampus might make changes more pronounced in this area. A limitation of this study was the exclusive observation of Thy1-GFP positive neurons. Thus, it remains to be elucidated whether the shift in the proportion of AcD neurons also applies to other neuronal types. For the future direction, single-cell RNA sequencing studies on AcD and nonAcD neurons could be conducted to understand their molecular and genetic profiles at different developmental stages. This could provide clues about why their numbers change with age and whether AcD neurons have a different profile than nonAcD neurons.

5.4 Development of AIS parameters

Earlier research has provided valuable insights into changes in AIS length in layers II/III and V during development in both S1BF and the primary visual cortex (Gutzmann et al. 2014; Jamann, Dannehl, et al. 2021). These studies observed activity-associated changes in AIS length, which occurred in phases from the late embryonic age to P180 in mice. Interestingly, the AIS length peaked in juvenile mice (P10-P15) and decreased significantly in P28-old mice. However, the developmental profile of the AIS in the vHC and S1, particularly in relation to AcD and nonAcD neurons, is unknown. In addition, the development of voltage-gated sodium channels, primarily responsible for AP initiation at the AIS (Royeck et al. 2008), remains largely unexplored. However, an existing patch-clamp study shed light on this topic by showing a ~10-fold increase in Na_v channel conductance relative to the membrane area in cerebral cortex pyramidal neurons between the second and third postnatal weeks (Hamill et al. 1991). However, whether this

increase in sodium conductance applies specifically to the AIS or to the entire somato-dendritic membrane is unknown. To close these knowledge gaps, this study investigated several features of the AIS with respect to AcD and nonAcD neurons in Thy1-GFP positive neurons in S1 and vHC from mice aged P12 to over P305. I specifically examined AIS length, expression length of $Na_v1.6$ within the AIS, and its distance from the starting point of the AIS. The aim was to uncover unique characteristics of AcD and nonAcD neurons during their development in S1 and vHC.

The results showed AIS length adaptation in similar profiles during development in S1 and vHC compared to those in previous studies in S1BF and the visual cortex (Gutzmann et al. 2014; Jamann, Dannehl, et al. 2021). However, AIS length did not differ between AcD and nonAcD neurons during the entire course of development. Interestingly, AIS length behaved similarly in the whole S1 and vHC, as observed in the subcortical region S1BF (longest AIS length P12-P14, shortest AIS length in mature mice (P28 and >P305). However, the decrease in AIS length from juvenile to mature mice is linked to sensory input onset and is assumed to be a homeostatic mechanism (Gutzmann et al. 2014; Jamann, Dannehl, et al. 2021). Additionally, between P12 and P18, GABAergic synapses are formed at the AIS by Chandelier neurons, and their formation peaks at the time during AIS shortening (Kobayashi et al. 2008; Zhang, Jiao, et al. 2011; Tai et al. 2019; Pan-Vazquez et al. 2020), which might also influence the adaptation of AIS length.

This phasic AIS length developmental profile was specific to sensory cortices and was not observed in non-sensory cortices in mice or monkeys (Cruz et al. 2009; Gutzmann et al. 2014; Benedetti et al. 2020). In non-sensory cortices, AIS length either increased or decreased continuously during development, depending on the cortical area (Cruz et al. 2009; Gutzmann et al. 2014; Benedetti et al. 2020). Therefore, it is interesting that the hippocampus shows the same AIS length developmental profile in the time interval between juvenile and adult mice as the sensory cortex. However, the hippocampus indirectly forms strong connections with sensory areas. The entorhinal cortex is considered the main input and output structure of the hippocampus (reviewed in (Canto et al. 2008)) and receives strong input from multimodal sensory cortices, such as the somatosensory, visual, and auditory cortex (reviewed in (Burwell 2006)). Hence, it might be assumed that those AIS length adaptations in the hippocampus are influenced by the input from sensory cortices received by their environment. Thus, fine-tuning of the

AIS length may be critical for accurately processing and integrating information for spatial navigation and memory processing.

$Na_v1.6$ channels are highly enriched in the distal end of the AIS in cortical neurons and are crucial for AP initiation (Hu, Tian, et al. 2009). However, whether and how the $Na_v1.6$ expression profile in the AIS changes during development in cortical and hippocampal neurons is unknown. Therefore, the length and location of $Na_v1.6$ expression within the AIS were investigated in AcD and nonAcD neurons during development. The results of $Na_v1.6$ expression length showed a phasic development profile similar to that of AIS length. At no time point during development, $Na_v1.6$ expression length differed between AcD and nonAcD neurons. However, fluctuations in the $Na_v1.6$ expression length profile were more prominent in vHC than in S1. The $Na_v1.6$ expression length was the highest at P18, lowest at P28, and increased slightly in >P305 mice in both brain regions. Interestingly, the maximal $Na_v1.6$ expression length was observed at a later time point than the maximal AIS length. This might indicate that the AIS length first establishes its structure, and subsequently, $Na_v1.6$ expression increases. Another hypothesis for the shifted developmental profile of $Na_v1.6$ might be that the transcription and translation in the soma of the SCN8A gene that encodes $Na_v1.6$ and then the transportation of $Na_v1.6$ channels to the AIS might cause a delay in juvenile mice. Furthermore, as shown in Figure 17, $Na_v1.6$ channels initially clustered at the soma, with a certain subpopulation temporarily trapped at the somatic membrane (Akin, Solé, Johnson, et al. 2016). From these observations, it might be hypothesized that these “trapped” $Na_v1.6$ channels may be released during later developmental stages and might migrate towards the AIS.

Interestingly, at P28, the shortest $Na_v1.6$ length was observed, which later increased in mature mice (>P305). This observation may represent a form of homeostatic plasticity in response to neuronal activity. Prior research has shown that the AIS can adjust its length and position in response to neuronal activity (Evans, Dumitrescu, et al. 2015; Grubb and Burrone 2010; Gutzmann et al. 2014; Jamann, Dannehl, et al. 2021). Typically, AIS length elongation or relocation closer to the soma tends to enhance neuronal excitability (Grubb and Burrone 2010; Jamann, Dannehl, et al. 2021). It might take some time for $Na_v1.6$ channels to adjust to these changes in the AIS, given their slow turnover rate of $Na_v1.6$ channels (Akin, Solé, Dib-Hajj, et al. 2015). The observed increase in $Na_v1.6$ length in mature mice (>P305) accompanied by a decrease in AIS length might repre-

sent a compensatory mechanism. Decreases in AIS length are associated with reduced neuronal excitability (Jamann, Dannehl, et al. 2021), however, the extension of $Na_v1.6$ channel length could counteract this by increasing sodium influx. This process could potentially lower the threshold for APs and facilitate their generation, thereby affecting their propagation. An increase in $Na_v1.6$ expression could potentially lead to a larger sodium current during APs, potentially leading to a faster AP propagation. Conversely, a decrease in AIS length may reduce the efficiency of AP initiation, potentially slowing the overall signal transmission. This intriguing dynamic likely plays a role in modulating the performance of the neuronal networks.

The site of $Na_v1.6$ concentration along the AIS can influence the AP initiation site (Royeck et al. 2008). Interestingly, during the course of development, $Na_v1.6$ expression was most distal within the AIS at P16 and most proximal in mature mice (>P305) in both brain regions. However, no significant differences in $Na_v1.6$ expression within the AIS in AcD and nonAcD neurons were observed at any specific time point during development, but $Na_v1.6$ was, in general, more distally located within the AIS in AcD neurons than in nonAcD neurons (Section 4.1.2). The effect of a more distal AP initiation site in the AIS has not been fully elucidated and is still debated, as described in more detail above (Discussion section 5.1). However, the observation of the adaptive $Na_v1.6$ location within the AIS indicates a maturation process by which the nervous system possibly develops and refines its function in response to its demands.

In the future, electrophysiological experiments recording the activity of developing neurons in combination with post-hoc staining might elucidate how the expression length and location of $Na_v1.6$ influence neuronal activity or *vice versa*. In addition, live-cell imaging *in vivo* using calcium imaging and simultaneous manipulation of $Na_v1.6$ channel with optogenetics might help to understand how changes in $Na_v1.6$ function affect the activity of neural circuits and animal behavior.

5.5 Activity-dependent remodeling of axon onset *in vitro*

The AIS adapts in length and position in an activity-dependent manner (Evans, Dumitrescu, et al. 2015; Grubb and Burrone 2010; Jamann, Dannehl, et al. 2021). Whether morphological alterations in response to altered network activity are restricted to the AIS remains unclear. To investigate the dynamics of axon onset,

cortical organotypic slice cultures (OTC) from the Thy1-GFP mouse line were prepared and intrinsically labeled cells were live-imaged for up to seven days (between DIV3 and DIV10). In a second set of experiments, established paradigms were used to either increase (bicuculline, KCl) or decrease (ifenprodil, $MgSO_4$) network activity in OTCs. Treatments were administered for seven days (DIV3 to DIV10). Subsequently, OTCs were fixed and stained against the scaffold marker (βIV-spectrin) to label the AIS.

The data provided insights into the dynamics of axon onset in Thy1-GFP positive neurons and the role of network activity in modulating this process. These neurons switched their axon onset from the AcD to the nonAcD state and *vice versa* in a matter of days. Sometimes, neurons were able to move their axon origin back to their previous position after transformation. Several pathways were observed in how the axonal onset transformation takes place, such as dendrite sprouting, axon and dendrite converging/diverging, axonal migration, and stem dendrite retraction/protrusion.

Increased network activity with bicuculline, which blocks GABAergic synapses Olsen et al. 1976, led to a significant increase in AcD neurons in treated OTCs compared to the contralateral untreated hemisphere. Decreasing network activity with $MgSO_4$ showed a tendency to increase the conversion to nonAcD neurons compared to their control hemisphere.

As mentioned above, it is known that AIS length and location adapts in an activity-dependent manner (Grubb and Burrone 2010; Evans, Dumitrescu, et al. 2015; Jamann, Dannehl, et al. 2021). Therefore, it is interesting that the axonal onset changes in response to prolonged altered network activity by increasing or decreasing it. However, the length and location of the AIS remained stable in the treated OTCs. The AIS length decrease in response to increased network activity was observed to be a short-term response, occurring within several minutes up to one hour, but diminishing afterwards (Evans, Dumitrescu, et al. 2015; Grubb and Burrone 2010; Jamann, Dannehl, et al. 2021). However, over the long term, other compensatory mechanisms, such as axonal onset changes, might take over, thereby changing the AIS onset in a more profound way and possibly compensating for the increased network activity. Additionally, reduced network activity over a prolonged period leads to the elongation of AIS in hippocampal OTCs (Thome, Janssen, et al. 2023). These apparently contradictory observations might be due

to the different neuronal cell types that were investigated. The data acquired in this study came from Thy1-GFP positive cells mainly expressed in layer V. The AIS length decrease in response to increased network activity was only observed in layer II/III and not in layer V excitatory neurons (Jamann, Dannehl, et al. 2021). These observations indicated that different types of neurons may exhibit different AIS/axonal plasticity mechanisms. In addition, even though the AIS length was not observed to change, alteration of the expression profile of voltage-gated ion channels is possible and remains to be studied.

This transformation of axon onset location in response to network activity implies a dynamic plasticity in the neuronal structure and organization of neuronal circuitry during development, which is currently not well understood. Different transition pathways were observed between nonAcD and AcD morphologies, such as dendrite sprouting, dendrite and axon converging/diverging, axonal migration with sequestration from the soma, and retraction of stem dendrites. These observations suggest that distinct subcellular processes are the driving factors. In the context of my findings on axon-onset plasticity, several activity-dependent transcription factors may potentially contribute to the observed axon-onset transformations. For example, the CREB-dependent transcription factor Wnt-2 promotes neurite growth and stimulates dendritic arborization during development, and is highly expressed between P7 and P14 in the hippocampal CA1 region in rats (Wayman et al. 2006). Wnt-2 might facilitate the transformation of nonAcD neurons to AcD neurons by promoting the formation of new dendritic branches, as observed by dendritic sprouting from stem dendrites. In addition to dendritic arborization, dendritic length, and complexity may also influence the capacity for axon-onset transformations. Calcium influx occurs in response to neuronal activity and is linked to transcriptional programs (reviewed by (Arjun McKinney et al. 2022)). Mutations in the calcium-regulated transcriptional coactivator CREST reduce dendritic length and arborization in cortical layer V neurons during development (Aizawa et al. 2004). It could be hypothesized that reduced dendritic complexity might limit the available sites for potential axon onset, thereby reducing the likelihood of dendrite sprouting from the stem dendrite, and thus axon-onset transformation.

These alterations in dendritic structure could potentially be facilitated or constrained by the underlying actomyosin skeleton of a neuron. For example, cannabinoid receptor type-1 (CB1R), which is activated by endocannabinoids and its release is driven by calcium elevation (Hashimotodani et al. 2007), has been

observed to modulate the actomyosin skeleton (Roland et al. 2014). Specifically, their activation induces the retraction of neurites and axonal growth cones, elevates neuronal rigidity, and rounds somatodendritic morphology by altering actomyosin contractility (Roland et al. 2014). Even though this might apply preferentially during pre- or early postnatal stages of development, CB1R still appears from P6 to P20 in axons with a specific laminar pattern in the somatosensory cortex and is assumed to influence the development of sensory maps (Deshmukh et al. 2007). Thus, CB1R activity could modulate the capacity for axon-onset transformation by either promoting or inhibiting changes in the neuron's dendritic structure or guiding the axon along the stem dendrite. This might be a putative mechanism that occurs when the stem dendrite is retracted, the soma sequesters a stem dendrite, or the axon migrates along the stem dendrite.

The metabolic state of the neuron and its surrounding environment may be another crucial factor influencing axon-onset plasticity. Neurite outgrowth, an energy-intensive process, requires sufficient ATP to support the increase in protein and membrane synthesis and their intracellular transportation (reviewed in (Mattson et al. 2008)). Alterations in network activity have been shown to alter nutrient availability (reviewed in (Bélanger et al. 2011)). Thus, changes in network activity could indirectly influence the metabolic status of neurons, which, in turn, could initiate axon-onset transformations. Under conditions of increased demand for nutrients to fuel the metabolic processes necessary for high network activity (Tomasi et al. 2013), ATP production could be sufficient or even elevated, thereby promoting neurite outgrowth and potentially facilitating the transformation of nonAcD neurons to the AcD state by providing the necessary energy for the establishment of dendrite sprouting, dendrite, or axonal migration, as well as sequestering a stem dendrite from the somatic membrane. Conversely, under nutrient scarcity conditions, which may occur in low network activity states, ATP production may be limited. This could restrict neurite outgrowth, favoring the retraction of AcDs, thereby increasing the conversion towards the nonAcD state. However, owing to the observation that only a subset of genetically identical neurons underwent transformations in the same environment, it can be hypothesized that this observation might be due to the variability in gene expression, often referred to as "cellular noise" (reviewed in (Eldar and Elowitz 2010)). It was already observed that members of a genetically identical group of cells in an identical environment showed variability in drug sensitivity, cellular response, and phenotype (reviewed in (Niepel et al. 2009; Eldar and Elowitz 2010)).

As this study exclusively focused on Thy1-GFP-positive neurons, several putative limitations need to be considered. First, Thy1 is primarily a promoter in pyramidal neurons. Therefore, it is important to explore how these findings might apply to other types of neurons. Because of their different morphological and functional properties, the responses of neuron types to network activity may differ significantly. Second, the expression of GFP might impact cellular processes that alter morphological and functional properties of the cell.

OTCs offer an accessible view of the brain, allowing the observation of cellular architecture and interactions in a reasonably intact environment allowing for experimental manipulations (reviewed in (Humpel 2015)). However, they have disadvantages when compared to *ex vivo* and *in vivo* systems. When compared to *in vivo* conditions, the slicing procedure disrupts connections of the neuronal network, potentially affecting the functional dynamics of brain circuits. *Ex vivo* slices, while also lacking a systemic context, may sharply imitate the *in vivo* scenario due to a lack of adaptation to culture conditions. However, *ex vivo* slices are useful for acute observations, whereas OTCs allow the study of tissues over an extended period of time.

Notably, *in vitro* manipulations may not entirely reflect physiological circumstances. For instance, KCl is known to lower the input resistance and resting membrane potential in neurons as a biophysical response due to changes in the ionic gradients (O'Leary et al. 2010), potentially affecting neuronal network dynamics and the ability to adapt their neuronal morphology. Similarly, neural network activity has been demonstrated to be critical for neuronal development (reviewed in (Luhmann et al. 2016)); thus, lowering neuronal activity with $MgSO_4$ or ifenprodil may result in neuronal deficiencies and disturb the normal dynamics of neuronal networks. However, in this study, I employed strong non-physiological experimental conditions to examine the potential of neurons for axonal onset change. The objective of this study was to explore the extent to which these cells might be capable of modifying their axonal structure under conditions that are not typical of their biological context. Despite these challenging conditions, the data did not reveal significant evidence of such transformative ability in neurons treated with one of the aforementioned treatments. However, increased $MgSO_4$ concentrations showed a tendency to increase the number of nonAcD neuron.

However, blocking GABAergic synapses with bicuculline in cortical OTCs may

more closely mimic physiological or pathophysiological conditions in the developing brain, thereby preserving the ability of neurons to interact with the network in a more physiological manner and maintain the ability to transform their axonal onset morphology in response to altered network activity.

In conclusion, these results demonstrate that axonal onset can be a highly dynamic trait that adapts in response to altered network activity. In the future, it would also be interesting to investigate the factors that contribute to changes in the axonal onset. Pharmacological reagents that are known to affect the actomyosin skeleton, such as drugs that activate or block CB1R, can be used to assess their effects on axon-onset transformation. Additionally, examining the role of genes that enable neurons to transform their axonal onset by overexpressing or downregulating viral vectors specifically linked to Wnt-2 or CREST could be applied in cultured neurons or injected into specific brain regions *in vivo*, and the changes in axon onset transformation could be monitored using imaging techniques.

5.6 Pilot study: electrophysiological profiling of treated OTCs

In this pilot study, pharmacological treatments were applied, which are widely accepted to alter the network activity. Treating cortical OTCs with bicuculline, which blocks GABAergic synapses, increases neuronal and network activity (Caeser et al. 1989). Increased $MgSO_4$ concentration increases the physiological block of NMDA receptors, thereby decreasing network activity (Dribben et al. 2010). To investigate whether prolonged treatment with these reagents alters the neuronal network or intrinsic cell properties, whole-cell patch-clamp recordings were performed from DIV6 to DIV10 in cortical OTCs from Thy1-GFP mice. OTCs were already treated from DIV3 onwards; however, electrophysiological measurements started at DIV6 since most axonal onset transformations occurred from this time point onwards.

Neuronal signal transmission The observation indicated that prolonged administration of bicuculline and $MgSO_4$ had no impact on the frequency of excitatory postsynaptic currents (EPSC). EPSCs reflect the postsynaptic response to glutamate release from presynaptic neurons. The frequency of EPSC usually reflects the presynaptic release probability, including the sensitivity of postsynaptic glutamate receptors (reviewed in (Scheefhals and MacGillavry 2018). However, neither treatment affected EPSC frequency in cortical OTCs, which might indicate

a homeostatic response or an ineffective treatment at fully blocking GABAergic synapses or diminishing NMDA receptor activity. It is plausible that the network adapted to these treatments prior to the patch-clamp experiments in order to maintain homeostasis. Homeostatic plasticity enables neurons to regulate their own excitability in order to maintain stability of neuronal firing rates. Therefore, compensatory mechanisms might have decreased the sensitivity to these pharmacological treatments by downregulating excitatory receptors in bicuculline-treated OTCs or increasing excitatory receptors in $MgSO_4$-treated OTCs, thereby counteracting the altered network activity and resulting in no change in postsynaptic currents. In fact, bicuculline administration has been reported to restore firing rates and mEPSC amplitudes to control levels after 48h of treatment (Turrigiano et al. 1998). Alternatively, long-term $MgSO_4$ administration to hippocampal OTCs has been associated with elongation of the AIS (Thome, Janssen, et al. 2023), which is assumed to increase neuronal excitability (Jamann, Dannehl, et al. 2021).

However, it is important to note that $MgSO_4$ treatment is a critical treatment with significant implications. While it can reduce neuronal network activity, potentially interfering with neuronal development, it can also affect cell survival rate (Dribben et al. 2010). Prolonged $MgSO_4$ administration may be more likely to induce apoptosis or induce changes in pathophysiological cell properties, warranting further investigation.

In conclusion, this observation suggests that neurons adapt their postsynaptic receptors to maintain homeostasis in response to pharmacological treatment. In the future, multi-electrode array (MEA) recordings could be used to elucidate whether these indicated results are responses as a homeostatic mechanism and whether earlier electrophysiological measurements showed alterations in network activity in response to those treatments. The advantage of MEAs over whole-cell patch-clamp recordings is that they are less invasive and allow simultaneous monitoring of multiple neurons, which enables the global measurement of network alterations.

Intrinsic neuronal properties Despite the lack of reliable effects of bicuculline and $MgSO_4$ on neuronal signal transmission, these treatments resulted in substantial changes in intrinsic neuronal cell properties. Both treatment groups showed a decreased amplitude of their first elicited AP in response to stepwise current injection. Notably, the $MgSO_4$-treated cells exhibited significant alterations in their firing properties. They demonstrated reduced firing frequency in response

to current injection pulses.

In the face of prolonged bicuculline exposure, neurons may attempt to maintain homeostasis and prevent hyperactivity by adapting their intrinsic properties, such as reducing the AP amplitude to prevent excitotoxicity. $MgSO_4$-treated cells showed a less negative voltage threshold, which suggests that these cells require less depolarization to initiate an AP, which could be a compensatory mechanism to the suppressive effects of $MgSO_4$ on neuronal excitability. Whole-cell patch-clamp recordings, the method employed in this study, may also have limitations in measuring various cellular properties. The process of obtaining whole-cell access for patch-clamp recordings can potentially damage the cells, potentially affecting their physiological properties, thereby influencing the accuracy of the recordings. Moreover, in these current-clamp recordings, the neurons were assumed to be isopotential, meaning that the voltage was the same at all points in the neurons. However, this is rarely the case for neurons. Therefore, the measured currents may not accurately represent those at other points in the neuron. Nevertheless, this study's primary focus was on the comparative effects of the treatments against the control, and all the samples were treated consistently.

These findings raise questions for future studies. In particular, it would be valuable to explore the intrinsic properties of treated cells at earlier time points of the treatment series to better understand how bicuculline and $MgSO_4$ alter intrinsic cell properties and how they alter neuronal activity. Additionally, calcium imaging could be utilized to visualize real-time changes in the time course of treatment administration to observe alterations in intracellular calcium concentrations, thereby providing evidence on how bicuculline and $MgSO_4$ influence neuronal network activity.

Development of intrinsic neuronal properties in control and bicuculline-treated OTCs The expression and function of various ion channels evolve during neuronal maturation. This maturation process can influence the properties of the AP, including its amplitude, half-width, and threshold, as well as the amplitude of sodium currents, which has also been observed in developing *ex vivo* slices from the motor cortex (Benedetti et al. 2020). However, the electrophysiological profile of developing cortical OTCs remains largely unexplored, particularly regarding the potential interference of bicuculline treatment on their maturation process. In this pilot study, whole-cell patch clamp recordings were

performed in cortical OTCs from DIV6 to DIV10, treated with control medium or bicuculline. The findings demonstrated an increase in AP amplitude in the course of the development. However, the amplitude was consistently greater in control cells than in bicuculline-treated cells. Additionally, the AP half-width decreased and the voltage threshold became more negative during the course of the study in both groups, with no significant differences between the treatment groups. Furthermore, the firing frequency increased with age. However, bicuculline-treated cells responded with their highest frequency earlier than control cells during development.

Intriguingly, the results suggest an accelerated maturation process in bicuculline-treated OTCs, as demonstrated by an earlier increase in firing frequency. It can be hypothesized that the blockade of GABAergic synapses by bicuculline enhances neuronal excitability, thereby driving this accelerated maturation. However, control cells eventually surpassed bicuculline-treated cells in firing frequency in response to current injections. This could be due to the slower but more sustained maturation process in control cells, leading to more robust functional capabilities in the long term.

This pilot study provides insight into the electrophysiological evolution of cortical OTCs. The data described here do not permit any binding conclusions, but nevertheless do not exclude the possibility that the treatments may result in plastic effects on individual parameters. Future studies should aim to provide more accurate recordings of control and bicuculline-treated cells, considering the possible temporal heterogeneity in these cultures. It is particularly important to correlate these alterations in cellular properties with changes in neuronal morphology. A detailed morphological reconstruction of the recorded neurons, examining structures such as the AIS and the dendritic tree, will be instrumental in uncovering how these physical changes interact with the observed electrophysiological changes. This approach could shed light on the interdependent relationship between neuronal structure and function, ultimately enhancing the understanding of neuronal development and the impact of pharmacological interventions that increase or decrease network activity.

5.7 Sensory activity changes number of AcD neurons *in vivo*

Alterations in sensory activity through whisker trimming have a profound effect on neuronal connectivity and subcellular compartments within the deprived cortex (Zuo et al. 2005; Cheetham et al. 2007; Jamann, Dannehl, et al. 2021). Reduced neuronal connections are countered by increased strength in the remaining excitatory connections, which is potentially a compensatory mechanism (Cheetham et al. 2007). At the morphological level, a reduction in the dendritic spine turnover rate and facilitation of AIS length elongation have also been observed (Zuo et al. 2005; Jamann, Dannehl, et al. 2021). In contrast, sensory enrichment increases excitatory activity (Alwis and Rajan 2013). Morphological alterations, such as increased dendritic density, accelerated dendritic spine turnover rate (Jung and Herms 2014), and rapid shortening of the AIS in barrel cortex neurons, have been observed (Jamann, Dannehl, et al. 2021). To investigate axonal onset transformation in response to altered network activity *in vivo*, the same Thy1-GFP mouse line was used, which intrinsically labels layer V neurons in S1BF. Sensory input was manipulated through unilateral whisker clipping, with additional stimulation of the remaining whiskers. The results demonstrated that increased whisker stimulation enhanced the percentage of AcD neurons, whereas whisker deprivation showed the tendency to increase the percentage of the nonAcD state. These changes were age-dependent, specifically observed in young animals, and diminished under weak whisker stimulation. The AIS can change its length and position in response to changes in network activity, both *in vitro* and in *in vivo*, thereby altering the intrinsic responsiveness of neurons (Grubb and Burrone 2010; Evans, Dumitrescu, et al. 2015; Jamann, Dannehl, et al. 2021). While the subcellular compartments of the axon change intrinsic parameters, the onset of the axon might influence its participation in neural networks by potentially altering the propagation of information and the neuron's role in network dynamics. Similar to the *in vitro* results presented in this study, AIS length remained stable in the analyzed Thy1-GFP positive neurons in layer V, as previously observed in wild-type mice (Jamann, Dannehl, et al. 2021). This observation indicates that layer V neurons have different AIS/axonal plasticity mechanisms than layer II/III neurons, in which AIS plasticity following whisker stimulation and deprivation has been observed (Jamann, Dannehl, et al. 2021).

In the hippocampus, AcD neurons significantly influence neural signaling and network integration. The strategic position of the AcD circumvents somatic inhibition,

boosting network participation and enhancing dendritic spike generation, which are crucial for signal integration (Hodapp et al. 2022; Thome, Kelly, et al. 2014). They also participate in sharp wave-ripple oscillations, which are key to memory consolidation, thereby demonstrating their pivotal role at the network level (Hodapp et al. 2022; Girardeau et al. 2009; Fernández-Ruiz et al. 2019). Similar to the hippocampus, the precise timing of neuronal responses is critical for sensory information processing in S1 (reviewed by (Lestienne 2001; Andrade-Talavera et al. 2023)). Strong, synchronous thalamocortical inputs can generate ultrafast oscillations, which may increase the bandwidth for encoding and transmitting sensory information (Hu, Hostetler, et al. 2023). In this context, AcD neurons could play a role similar to that in the hippocampus by being able to participate during these ultrafast oscillations by circumventing somatic inhibition (Hodapp et al. 2022). To date, the role of AcD neurons in sensory information processing is not well understood and is assumed to ensure the strength and timing of back-propagating action potentials as they travel from the axon to the soma and dendritic branches (Hamada et al. 2016). The plasticity of axon onset may optimize the processing of whisker-related inputs and enhance the precision and efficiency of sensory encoding. Through plasticity, neurons that are responsible for processing the inputs of certain whiskers can change their firing rates or timing to respond more quickly or accurately to their signals. The alteration of axon origin could also potentially change the responsiveness to different sensory inputs, for example, enhancing the precision of sensory encoding for certain textures that are perceived by whiskers. Unilateral whisker deprivation may have introduced confounding factors into this *in vivo* study, such as compensation from the contralateral non-deprived site. However, insufficient cross-hemispheric activation through contralateral projecting neurons was observed until the third postnatal week (Petreanu, Huber, et al. 2007). Unilateral whisker trimming also promotes intact whisker projection pathways (Simons and Land 1994; Vees et al. 1998) by amplifying the intended stimulation difference between hemispheres. Furthermore, unilateral whisker-deprived mice may face challenges in navigating in an enriched environment because of the decreased sensory input on one side, which could potentially affect their behavior and thereby possibly overuse intact whiskers. In conclusion, the findings show that increased sensory activity influences the transformation of axon onset in neurons, potentially affecting their role in neural networks and sensory information processing. In the future, research could be undertaken to explore the implications of this shift in neuronal function and behavior and to determine what drives neurons to change their axon onset.

The experiment can be conducted by performing calcium live-cell imaging of the barrel cortex *in vivo*, in combination with a transgenic mouse line where excitatory cells (e.g., under the Thy1 or Rbp4 promoter) and the AIS (Thome, Janssen, et al. 2023) are intrinsically labeled, whereas the whiskers of the animal are either stimulated with different frequencies or objects with different textures are presented. This experiment might elucidate two important aspects of AcD neurons: whether the AcD conversion is a compensatory mechanism for activity, indicated by active cells turning into AcD neurons or *vice versa*, and the putative role they might play in sensory information processing.

6 Summary

Axon-carrying dendrite (AcD) neurons are characterized by an axon that originates from a dendrite. These cells have been rarely investigated since Ramón y Cajal first described them in 1937. However, in 2014, it was shown that AcD neurons occur in a large portion of cortical pyramidal cells and have a privileged function for synaptic input integration (Thome, Kelly, et al. 2014). Thus, they might play an important role in network function. This assumption was recently underlined, as it enables cells to generate neuronal output even during strong perisomatic inhibition (Hodapp et al. 2022). These intriguing studies raised the question of how AcD neurons develop and what structural differences they have compared to nonAcD neurons. Thus, in the present study, I investigated the development of AcD neurons and the factors that may drive their emergence. Additionally, structural differences between AcD and nonAcD neurons were investigated in two brain regions: the primary somatosensory cortex (S1) and ventral hippocampus (vHC). The structural characteristics of AcD and nonAcD neurons with regard to specific features of their axon initial segment (AIS) were largely similar in S1 and vHC. Their AIS features, such as length and $Na_v1.6$ channel clustering, exhibited substantial similarities. Furthermore, both neuron types seem to have comparable numbers of putative GABAergic synapses clustered at the AIS. However, a notable difference was observed in the positioning of the $Na_v1.6$ channel cluster within the AIS. $Na_v1.6$ channels clustered more distally in AcD neurons than in nonAcD neurons across both brain regions. This distinctive location may affect the likelihood of AP generation by inputs to the axon-carrying or to the other dendrites. During development, the population of AcD neurons significantly changed, particularly in the vHC group. A noticeable increase in the proportion of AcD neurons was observed in juvenile mice (P12 to P28), surpassing the numbers observed in both younger (E18 to P3) and adult mice (>P305). Moreover, the AIS underwent adaptive modifications in its length during development, with a similar profile across both brain regions. Similar trends were also identified in the $Na_v1.6$ channel clustering length and its positioning within the AIS. However, while developmental changes in the $Na_v1.6$ channel expression length were more apparent in the vHC, the S1 region showed a more pronounced shift in the positioning of the $Na_v1.6$ channels within the AIS. Live-cell imaging of cortical organotypic slice cultures (OTCs) revealed that the axon onset is a highly dynamic feature, with cells changing from an initial classification as nonAcD neuron to AcD neuron and *vice versa* within a matter of days. Furthermore, after moving the axon onset,

the neuron was still able to revert this change. To investigate potential effects of neuronal activity on the emergence or properties of AcD neurons, pharmaceutical treatments were applied to OTCs which increase or decrease network activity, respectively. Increasing network activity with bicuculline increased the proportion of AcD neurons but did not affect the AIS length or its position. Decreasing network activity with $MgSO_4$ showed an opposing trend towards the nonAcD state. Again, this treatment did not significantly affect the AIS length or location. In an exploratory series of electrophysiological recordings using the whole-cell patch-clamp technique, I investigated the effectiveness of the treatment and its putative influence on the maturation process in cortical OTCs. In summary, these preliminary experiments did not show major functional alterations following pharmacological alteration of network activity. Subtle changes, e.g. in action potential properties or spontaneous postsynaptic current frequency, cannot be excluded at this state and warrant further experiments. Unilateral whisker deprivation in combination with stimulation of the remaining whiskers of the contralateral hemisphere in an enriched environment cage revealed that the number of AcD neurons adapted in an activity-dependent manner. Specifically, the somatosensory cortex of those hemispheres where stimulated whiskers projected showed significantly more AcD neurons than the contralateral hemisphere, which was sensory-deprived. However, this observation is unique to the early whisker-specific sensory experiences in juvenile mice. Sensory deprivation, on the other hand, was not sufficient to change the number of AcD neurons compared to the hemisphere with intact sensory information processing. In summary, this study revealed remarkable dynamics and plasticity of axon onset in cortical neurons. Notably, the axon onset showed bi-directional transitions between somatic and dendritic origins over the course of several days. Additionally, the study revealed that changes in network activity had a profound impact on the abundance of AcD cells. These findings provide insights into a hitherto unexplored mode of morphological plasticity and suggest the importance of axon origin as a new morpho-functional parameter for neuronal adaptability and its role in network activity.

7 Supplementary

7.1 Supplmentary material and methods

Equipment	Product name	Source
Amplifier	EPC 10 USB	HEKA electronics GmbH, Lambrecht, Germany
Amplifier Software	PatchMaster 2x90	HEKA electronics GmbH, Lambrecht, Germany
Bath chamber	RC-27, rectangular open bath chamber	Warner Instruments, Hamden, USA
Heated perfusion cube	Heated Perfusion Cube G (HPC-G)	ALA Scientific Instruments, New York, USA
Temperature control system	TC-20	npi electronic GmbH, Tamm, Germany
Camera	OrcaFlash 4.0 LT Scientific CMOS Microscopy Camera FL400-Sensor with 4.0 megapixels	Hamamatsu, Photonics, Hamamatsu City, Japan
Light Source	Photofluor-LM75	89 North, Williston, USA
Microscope	ECLIPSE FN1, upright microscope, IR-DIC, 10x objective water immersion NA 0.10, WD 3.5 mm, 40x objective, water immersion, NA 0.80, WD 3.5 mm	Nikon Instruments Europe, Düsseldorf, Germany
Micromanipulator	Sensapex piezo-driven micromanipulator, SMX series	Sensapex, Oulu, Finland
XY Microscope Stage	MT-1000	Sutter Instruments, Novato, USA
Peristaltic pump	Reglo analog	Ismatec, Wertheim, Germany
Pipette Puller	P-97 Flaming/Brown micropipette puller	Sutter Instruments, Novato, USA

Equipment	Product name	Source
Glass capillaries	GB150F-10, 0.86x1.5x100mm, Borosilicate glass with filament	Science products, Hofheim, Germany
Harp	HSG-5f harp slice grid	ALA Scientific Instruments, New York, USA

Table 10: Equipment electrophysiology.

7.2 Supplementary statistical results and figures

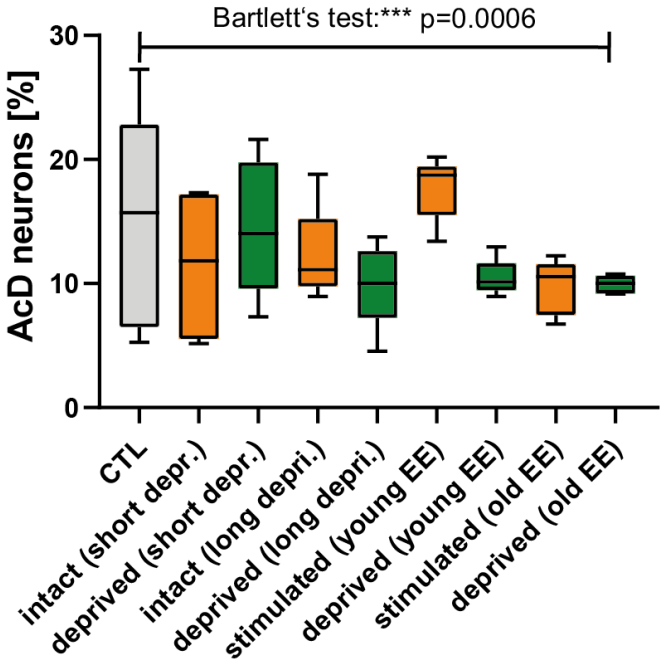

Supplementary figure 31: Variance in AcD percentage *in vivo*. Statistical results of Bartlett's test in ordinary one-way ANOVA. Data indicate that the variance in the number of AcD neurons is lower in stimulated and deprived hemispheres of mice placed in enriched environment compared to bilaterally unaffected mice (in juvenile (young) and mature (old) mice).

Age	AcD neurons	Shared root cells	n1	n2
P8 vs. P12	0.9976	>0.9999	5	5
P8 vs. P14	0.4506	0.9993	5	5
P8 vs. P16	>0.9999	>0.9999	5	6
P8 vs. P18	0.9978	0.9983	5	5

Age	AcD neurons	Shared root cells	n1	n2
P8 vs. P21	0.8162	0.9977	5	8
P8 vs. P28	0.9997	0.4850	5	6
P8 vs. >P305	0.1440	0.9727	5	6
P12 vs. P14	0.1450	0.9994	5	5
P12 vs. P16	0.9990	>0.9999	5	6
P12 vs. P18	0.8897	0.9981	5	5
P12 vs. P21	0.3725	0.9975	5	8
P12 vs. P28	0.9357	0.4799	5	6
P12 vs. >P305	*	0.9739	5	6
P14 vs. P16	0.3332	0.9985	5	6
P14 vs. P18	0.8424	0.9359	5	5
P14 vs. P21	0.9906	0.9093	5	8
P14 vs. P28	0.6988	0.1938	5	6
P14 vs. >P305	0.9991	0.9999	5	6
P16 vs. P18	0.9926	0.9986	6	5
P16 vs. P21	0.6992	0.9981	6	8
P16 vs. P28	0.9983	0.4550	6	6
P16 vs. >P305	0.0840	0.9547	6	6
P18 vs. P21	0.9946	>0.9999	5	8
P18 vs. P28	>0.9999	0.8683	5	6
P18 vs. >P305	0.4625	0.7195	5	6
P21 vs. P28	0.9693	0.7640	8	6
P21 vs. >P305	0.7982	0.6219	8	6
P28 vs. >P305	0.2896	0.0563	6	6

Supplementary table 12: P-values of Sidák's multiple comparisons test of AcD and shared root percentage in S1 during development.

Treatment	P-value t-test	P-value F-test
intact (short depriv.) vs. CTL	0.4520	0.2940
deprived (short depriv.) vs. CTL	0.9197	0.3131
intact (long depriv.) vs. CTL	0.5532	0.1347
deprived (long depriv.) vs. CTL	0.2766	0.0910
stimulated (EE young) vs. CTL	0.4598	*
deprived (EE young) vs. CTL	0.2587	**
stimulated (EE old) vs. CTL	0.2423	*
deprived (EE old) vs. CTL	0.2476	***

Supplementary table 11: Variance in AcD percentage *in vivo*. Table results depict the P-values of unpaired t-test and F-test. As indicated in Figure 31, the variance of the proportion of AcD neurons is significantly lower in treated hemispheres of young and old mice, which were placed in EE cage compared to control hemispheres.

Age	AcD neurons	Shared root cells	n1	n2
E18 vs. P3	>0.9999	>0.9999	6	5
E18 vs. P8	0.9996	0.8005	6	6
E18 vs. P12	*	0.6276	6	5
E18 vs. P14	0.2304	0.9928	6	5
E18 vs. P16	**	***	6	5
E18 vs. P18	**	*	6	6
E18 vs. P21	**	*	6	6
E18 vs. P28	****	****	6	6
E18 vs. >P305	0.9100	0.9930	6	6
P3 vs. P8	0.9966	0.9715	6	6
P3 vs. P12	0.0838	0.8983	5	5
P3 vs. P14	0.4128	>0.9999	5	5
P3 vs. P16	*	**	5	5
P3 vs. P18	*	0.1659	5	6
P3 vs. P21	*	0.0913	5	6
P3 vs. P28	***	***	5	6
P3 vs. >P305	0.9794	>0.9999	5	6
P8 vs. P12	**	>0.9999	6	5
P8 vs. P14	0.0574	0.9997	6	5
P8 vs. P16	***	0.0549	6	5
P8 vs. P18	***	0.7901	6	6

Age	AcD neurons	Shared root cells	n1	n2
P8 vs. P21	***	0.6138	6	6
P8 vs. P28	****	**	6	6
P8 vs. >P305	0.5396	0.9993	6	6
P12 vs. P14	0.9979	0.9935	5	5
P12 vs. P16	0.9990	0.1668	5	5
P12 vs. P18	>0.9999	0.9577	5	6
P12 vs. P21	>0.9999	0.8727	5	6
P12 vs. P28	0.7634	*	5	6
P12 vs. >P305	0.5206	0.9874	5	6
P14 vs. P16	0.8567	*	5	5
P14 vs. P18	0.9425	0.4362	5	6
P14 vs. P21	0.9202	0.2819	5	6
P14 vs. P28	0.2464	***	5	6
P14 vs. >P305	0.9554	>0.9999	5	6
P16 vs. P18	>0.9999	0.8082	5	6
P16 vs. P21	>0.9999	0.9229	5	6
P16 vs. P28	0.9929	0.9984	5	6
P16 vs. >P305	0.1331	**	5	6
P18 vs. P21	>0.9999	>0.9999	6	6
P18 vs. P28	0.9389	0.2570	6	6
P18 vs. >P305	0.1955	0.3398	6	6
P21 vs. P28	0.9581	0.4126	6	6
P21 vs. >P305	0.1657	0.2031	6	6
P28 vs. >P305	**	***	6	6

Supplementary table 13: P-values of Tukey's multiple comparisons test of AcD and shared root percentage in vHC during development.

Age	AIS length	$Na_v1.6$ length	AIS - $Na_v1.6$ distance	n1	n2
P12 vs. P14	>0.9999	0.9898	0.9996	5	5
P12 vs. P16	0.9132	0.8226	0.9974	5	5
P12 vs. P18	0.3079	0.9908	**	5	5
P12 vs. P21	*	>0.9999	*	5	6
P12 vs. P28	***	0.0574	0.3142	5	6
P12 vs. >P305	****	0.4948	***	5	4
P14 vs. P16	0.9833	0.9975	0.9998	5	5
P14 vs. P18	0.5034	0.9170	*	5	5
P14 vs. P21	0.0820	0.9934	**	5	6
P14 vs. P28	***	0.4443	0.0612	5	6
P14 vs. >P305	****	0.4363	***	5	4
P16 vs. P18	0.9171	0.5097	0.0760	5	5
P16 vs. P21	0.3346	0.7023	0.0557	5	6
P16 vs. P28	**	0.7365	0.4443	5	6
P16 vs. >P305	****	0.7025	***	5	4
P18 vs. P21	0.9436	0.8718	>0.9999	5	6
P18 vs. P28	0.0698	**	0.8232	5	6
P18 vs. >P305	****	0.2170	0.2643	5	4
P21 vs. P28	0.4916	0.0779	0.9000	6	6
P21 vs. >P305	***	0.2282	*	6	4
P28 vs. >P305	0.0677	>0.9999	*	6	4

Supplementary table 14: P-values of Tukey's multiple comparisons test of AIS length, $Na_v1.6$ length, and AIS - $Na_v1.6$ distance in S1 during development.

Age	AIS length	$Na_v1.6$ length	AIS - $Na_v1.6$ distance	n
P12	0.7430	0.9783	>0.9999	5
P14	0.5591	0.9925	0.7790	6
P16	>0.9999	0.7689	0.8332	6
P18	09982	>0.9999	0.8973	6
P21	0.9988	>0.9999	0.9953	6
P28	>0.9999	0.6812	0.9541	6
>P305	0.6898	>0.9999	0.9694	4

Supplementary table 15: P-values of Sidák's multiple comparisons test of AIS length, $Na_v1.6$ length, and AIS - $Na_v1.6$ distance in S1 between AcD and nonAcD neurons during development.

Age	AIS length	$Na_v1.6$ length	AIS - $Na_v1.6$ distance	n
P12	>0.9999	>0.9999	0.9998	5
P14	0.9899	>0.9999	0.9784	5
P16	>0.9999	0.9988	0.7573	5
P18	>0.9999	0.9966	0.9872	5
P21	0.9990	0.9797	0.9979	5
P28	0.9273	0.9973	0.2381	6
>P305	0.9938	0.9864	>0.9999	4

Supplementary table 16: P-values of Sidák's multiple comparisons test of AIS length, $Na_v1.6$ length, and AIS - $Na_v1.6$ distance in vHC between AcD and nonAcD neurons during development.

Age	AIS length	$Na_v1.6$ length	AIS - $Na_v1.6$ distance	n1	n2
P12 vs. P14	>0.9999	0.9993	0.8493	5	5
P12 vs. P16	0.9930	>0.9999	0.1547	5	5
P12 vs. P18	0.8044	0.9183	0.6191	5	5
P12 vs. P21	0.4449	0.9868	>0.9999	5	5
P12 vs. P28	**	**	0.1730	5	6
P12 vs. >P305	*	*	0.9172	5	4
P14 vs. P16	0.9986	0.9999	0.9602	5	5
P14 vs. P18	0.9320	0.3767	0.2487	5	5
P14 vs. P21	0.4274	0.9923	0.9952	5	5
P14 vs. P28	****	****	0.9706	5	6
P14 vs. >P305	****	**	0.2972	5	4
P16 vs. P18	0.5601	0.9556	**	5	5
P16 vs. P21	0.3820	0.9980	0.9262	5	5
P16 vs. P28	**	0.0798	>0.9999	5	6
P16 vs. >P305	**	0.1286	0.0932	5	4
P18 vs. P21	0.3177	0.7096	0.9417	5	5
P18 vs. P28	****	***	0.0861	5	6
P18 vs. >P305	***	***	0.9984	5	4
P21 vs. P28	***	***	0.6892	5	6
P21 vs. >P305	**	0.2035	0.9760	5	4
P28 vs. >P305	0.6001	0.5576	0.1324	6	4

Supplementary table 17: P-values of Tukey's multiple comparisons test of AIS length, $Na_v1.6$ length, and AIS - $Na_v1.6$ distance in vHC during development.

Current injection [pA]	$MgSO_4$ vs. CTL	$MgSO_4$ vs. Bicu	Bicu vs. CTL
0	0.000	0.5846	0.5846
50	0.9916	0.2306	0.4036
100	0.5698	0.0508	0.5619
150	0.7361	0.9910	0.7328
200	*	0.6105	0.4530
250	**	0.3780	0.3758
300	**	0.2293	0.5487
350	**	0.0979	0.4670
400	**	*	0.6415
450	**	*	0.7692
500	**	0.0849	0.7025
550	*	0.1653	0.4636
600	*	0.2428	0.2321
650	*	0.3321	0.5281
700	0.0620	0.2986	0.4003
750	0.1229	0.3325	0.4698
800	0.1938	0.2653	0.4543
850	0.2381	0.3301	0.4507

Supplementary table 18: P-values of Tukey's multiple comparisons test of the input-frequency relationship curve between treatments.

Days in vitro	RMP	Rmem	Cmem	τ	n1	n2
6 vs. 7	0.0932	0.4008	>0.9999	0.3851	16	13
6 vs. 8	0.0689	0.4402	0.7251	0.9972	16	14
6 vs. 9	0.0871	0.3039	0.9112	0.4814	16	9
6 vs. 10	0.9419	0.0688	0.9322	0.0950	16	10
7 vs. 8	0.9966	>0.9999	0.7371	0.8306	13	14
7 vs. 9	0.7709	0.9907	0.8729	0.9974	13	9
7 vs. 10	0.5334	0.7497	0.9467	0.9349	13	10
8 vs. 9	0.9577	0.9769	0.5216	0.5128	14	9
8 vs. 10	0.4822	0.6748	0.9042	0.7527	14	10
9 vs. 10	0.3566	0.9741	>0.9999	0.6937	9	10

Supplementary table 19: P-values of Tukey's multiple comparisons test of passive cell properties during development.

Days in vitro	RMP	Rmem	Cmem	τ	Bicu n	CTL n
6	0.0697	0.3789	0.9954	0.5055	9	7
7	0.4104	0.7364	0.9903	0.8238	6	7
8	0.8874	0.8272	0.9872	0.7937	6	8
9	0.3920	0.9990	0.9994	>0.9999	5	4
10	>0.9999	0.9992	0.4102	0.9389	5	5

Supplementary table 20: P-values of Sidák's multiple comparisons test of the passive cell properties between treatments during development.

Days in vitro	Amplitude	Half width	Voltage threshold	Current threshold	n1	n2
6 vs. 7	0.1428	**	0.9991	0.9997	16	13
6 vs. 8	**	0.2706	0.6421	>0.9999	16	14
6 vs. 9	0.0612	0.2498	>0.9999	0.9989	16	9
6 vs. 10	**	0.1331	0.1549	0.9563	16	10
7 vs. 8	0.9397	0.2187	0.9409	0.9999	13	14
7 vs. 9	0.9517	0.9406	0.9968	0.9876	13	9
7 vs. 10	0.2531	0.9333	0.1177	0.8874	13	10
8 vs. 9	>0.9999	0.8282	0.6695	0.9998	14	9
8 vs. 10	0.1725	0.5594	0.0589	0.9654	14	10
9 vs. 10	0.1753	>0.9999	0.2066	0.9894	9	10

Supplementary table 21: P-values of Tukey's multiple comparisons test of AP parameters during development.

Days in vitro	Amplitude	Half width	Voltage threshold	Current threshold	Bicu n	CTL n
6	0.1377	0.6657	>0.9999	0.9807	9	7
7	0.8283	0.3187	>0.9999	0.5963	6	7
8	*	0.3560	0.9494	0.7476	6	8
9	0.9975	**	0.2469	0.9858	5	4
10	0.9999	0.9982	0.8198	0.9913	5	5

Supplementary table 22: P-values of Sidák's multiple comparisons test of AP parameters between treatments during development.

Days in vitro / Current[pA]	6 vs. 7	6 vs. 8	6 vs. 9	6 vs. 10	7 vs. 8	7 vs. 9	7 vs. 10	8 vs. 9	8 vs. 10	9 vs. 10
0										
50	0.9942	0.8316	0.8923	0.3157	0.9999	0.9785	0.7186	0.7469	0.9089	0.2814
100	>0.9999	0.9568	0.9761	0.5520	0.9983	0.9987	0.8489	>0.9999	0.9432	0.9733
150	0.7926	>0.9999	0.2890	0.9591	0.8116	>0.9999	>0.9999	0.4491	0.9587	>0.9999
200	0.2106	>0.9999	*	0.9760	0.2056	0.9992	0.9290	0.0919	0.9627	0.9721
250	0.3659	0.9932	**	0.9914	0.2310	>0.9999	0.9314	**	0.9161	0.8155
300	0.4575	>0.9999	**	0.9608	0.3547	>0.9999	0.9839	**	0.8878	0.8211
350	0.7114	0.9996	0.1813	0.9769	0.5241	>0.9999	0.9999	0.0987	0.9015	0.9869
400	0.9242	>0.9999	0.4382	0.9804	0.9184	0.9927	>0.9999	0.4579	0.9754	0.9921
450	0.9295	>0.9999	0.7438	0.9447	0.9726	0.9829	>0.9999	0.7950	0.9682	0.9995
500	0.8143	>0.9999	0.7127	0.7934	0.9996	0.9518	0.9991	0.8868	0.9830	0.9991
550	0.8383	0.9981	0.7701	0.7019	>0.9999	0.9703	0.9978	0.9631	0.9957	0.9997
600	0.7410	0.9942	0.8179	0.6803	>0.9999	0.9740	0.9685	0.9980	0.9994	>0.9999
650	0.6862	0.9876	0.8497	0.7143	>0.9999	0.9717	0.9471	0.9999	>0.9999	>0.9999
700	0.5647	0.9876	0.8468	0.7137	>0.9999	0.9988	0.9884	>0.9999	>0.9999	>0.9999
750	0.8269	0.9876	0.8402	0.8341	0.9995	0.9930	0.9858	>0.9999	>0.9999	>0.9999
800	0.5368	0.9868	0.7613	0.6059	0.9998	0.9972	0.9038	>0.9999	>0.9999	0.9990
850	0.7356	0.9839	0.8513	0.6363	0.9986	0.9995	0.9128	>0.9999	>0.9999	0.9977

Supplementary table 23: P-values of Tukey's multiple comparisons test of input-output curve during development in bicuculline-treated cells.

Days in vitro / Current[pA]	6 vs. 7	6 vs. 8	6 vs. 9	6 vs. 10	7 vs. 8	7 vs. 9	7 vs. 10	8 vs. 9	8 vs. 10	9 vs. 10
0										
50	>0.9999	0.9945	0.8639	0.9410	0.9991	0.8664	0.9850	0.8483	>0.9999	0.5718
100	0.9863	0.7808	0.9964	>0.9999	>0.9999	>0.9999	0.9998	0.9974	0.9789	>0.9999
150	>0.9999	0.6554	0.9997	>0.9999	0.7662	>0.9999	>0.9999	0.9421	ß.9892	>0.9999
200	0.9458	0.9883	>0.9999	>0.9999	0.4685	0.7623	0.9994	0.9937	0.9817	>0.9999
250	0.1896	>0.9999	0.9580	0.7204	0.4018	0.2385	0.9987	0.9896	0.8360	0.9420
300	*	0.9873	0.9478	0.0738	0.1997	0.1868	0.9979	>0.9999	0.5036	0.4330
350	**	0.7907	0.5084	**	0.6677	0.5829	0.9998	>0.9999	0.4835	0.4127
400	0.2138	0.9481	0.8882	**	0.7945	0.9651	0.6715	>0.9999	*	0.2752
450	0.3934	0.9991	0.9636	**	0.6703	0.9398	0.5833	0.9998	*	0.1074
500	0.3842	>0.9999	0.9998	0.1457	0.4110	0.7030	0.9998	>0.9999	0.1570	0.3519
550	0.4131	>0.9999	>0.9999	0.2312	0.4573	0.7372	0.9995	>0.9999	0.2977	0.7722
600	0.5618	>0.9999	>0.9999	0.9486	0.5039	0.4860	0.9660	>0.9999	0.9091	0.8830
650	0.8243	0.9996	>0.9999	0.9946	0.3863	0.5548	0.9963	>0.9999	0.7541	0.9137
700	0.9891	0.9985	0.9997	0.9982	0.6231	0.7036	>0.9999	>0.9999	0.7726	0.8376
750	0.9985	0.9948	0.9987	>0.9999	0.4642	0.5811	>0.9999	>0.9999	0.8523	0.9054
800	>0.9999	0.9947	0.9943	>0.9999	0.4358	0.4492	>0.9999	>0.9999	0.9036	0.9020
850	>0.9999	0.9881	0.9756	>0.9999	0.7090	0.5790	>0.9999	0.9641	0.9413	0.9122

Supplementary table 24: P-values of Tukey's multiple comparisons test of input/frequency curve during development in control cells.

Days in vitro / Current[pA]	6	7	8	9	10
50	0.9623	>0.9999	>0.9999	NA	0.9913
100	0.8431	>0.9999	0.9171	>0.9999	0.9787
150	0.7236	0.9998	>0.9999	0.8918	>0.9999
200	0.2463	0.9925	0.8458	0.6041	>0.9999
250	0.4521	>0.9999	0.3026	0.3454	0.9603
300	0.9635	>0.9999	0.3302	0.3225	0.8475
350	>0.9999	0.9762	0.3539	0.9948	0.7111
400	>0.9999	0.9028	0.8402	0.9993	0.3007
450	>0.9999	0.7865	0.9941	0.9982	0.1953
500	0.9819	0.4369	>0.9999	0.9915	0.5029
550	0.9483	0.4604	>0.9999	0.9968	0.894
600	0.9109	0.3615	>0.9999	0.994	0.9996
650	0.9719	0.4599	0.9996	0.9833	>0.9999
700	0.9689	0.7987	0.9988	0.9904	>0.9999
750	0.9745	0.6525	0.9967	0.9821	>0.9999
800	0.9772	0.6427	0.9978	0.948	>0,9999
850	0.9658	0.88	0.995	0.907	>0.9999
Bicu n	9	6	6	5	5
CTL n	7	7	8	4	5

Supplementary table 25: P-values of Tukey's multiple comparisons test of the input-output curve in bicuculline-treated and control cells during development.

8 Acknowledgment

I wish to express my sincere gratitude to my supervisor Prof. Maren Engelhardt for giving me the opportunity to conduct this project and setting its course. Without her pivotal role in defining the project's trajectory, this work would not have been possible.

I am profoundly grateful to Prof. Andreas Draguhn for his unfailing support throughout the writing process of this dissertation. His understanding, patience, and constructive criticism played a crucial role in shaping this research work.

I extend my deepest gratitude to Dr. Christian Thome for his contribution to this dissertation. Throughout this journey, Christian has been an irreplaceable discussion partner and source of mental support. Our spirited debates helped me refine my arguments in the dissertation and paper writing process. I am immensely grateful for his intellect, patience, and companionship.

Thank you to Prof. Christian Schultz for giving me the opportunity to conduct the project in his lab. Furthermore, I want to thank Corinna Thielemann who supported me in the lab at the beginning of my journey and even after she left the lab, her support did not stop.

I would like to express my deepest gratitude to my family for their boundless love, patience, and unwavering support throughout this journey. My parents have always encouraged my curiosity and fostered my love of learning, setting the foundation for this achievement.

Foremost, I would like to express my deepest appreciation to my boyfriend, Thorsten Rätscher, whose unconditional support has been my rock throughout this journey. His unwavering belief in me, even during the most challenging times, provided me with a comfort zone where I could regroup and regain my focus. In addition to his emotional support, Thorsten has provided me with constructive and instrumental feedback in the programming aspect of this project. I am more grateful for your love and support than words can express.

This dissertation, a milestone in my academic journey, is a testament to the power of love and family support and I am beyond grateful to have these people in my life.

9 Disclosure

Parts of this work have been published or are in preparation for publication.

Lehmann, Nadja, Stefan Markovic, Christian Thome, and Maren Engelhardt (2023). “Axon onset remodeling in response to network activity in mouse cortical neurons”. preprint. DOI: 10.1101/2023.07.31.551236. URL: https://www.biorxiv.org/content/10. 1101/2023.07.31.551236v1.

Wahle, Petra, Eric Sobierajski, Ina Gasterstädt, Nadja Lehmann, Susanna Weber, Joachim HR Lübke, Maren Engelhardt, Claudia Distler, and Gundela Meyer (2022). “Neocortical pyramidal neurons with axons emerging from dendrites are frequent in non-primates, but rare in monkey and human”. en. In: eLife 11, e76101. ISSN: 2050- 084X. DOI: 10.7554/eLife.76101. URL: https://elifesciences.org/articles/ 76101.

10 References

Aizawa, Hiroyuki, Shu-Ching Hu, Kathryn Bobb, Karthik Balakrishnan, Gulayse Ince, Inga Gurevich, Mitra Cowan, and Anirvan Ghosh (2004). “Dendrite Development Regulated by CREST, a Calcium-Regulated Transcriptional Activator”. en. In: *Science* 303.5655, pp. 197–202. ISSN: 0036-8075, 1095-9203. DOI: 10.1126/science.1089845. URL: https://www.science.org/doi/10.1126/science.1089845.

Akin, Elizabeth J., Laura Solé, Sulayman D. Dib-Hajj, Stephen G. Waxman, and Michael M. Tamkun (2015). “Preferential Targeting of Nav1.6 Voltage-Gated Na+ Channels to the Axon Initial Segment during Development”. en. In: *PLOS ONE* 10.4. Ed. by Bernard Attali, e0124397. ISSN: 1932-6203. DOI: 10.1371/journal.pone.0124397. URL: https://dx.plos.org/10.1371/journal.pone.0124397.

Akin, Elizabeth J., Laura Solé, Ben Johnson, Mohamed el Beheiry, Jean-Baptiste Masson, Diego Krapf, and Michael M. Tamkun (2016). “Single-Molecule Imaging of Na v 1.6 on the Surface of Hippocampal Neurons Reveals Somatic Nanoclusters”. en. In: *Biophysical Journal* 111.6, pp. 1235–1247. ISSN: 00063495. DOI: 10.1016/j.bpj.2016.08.016. URL: https://linkinghub.elsevier.com/retrieve/pii/S0006349516307044.

Alwis, Dasuni S. and Ramesh Rajan (2013). “Environmental enrichment causes a global potentiation of neuronal responses across stimulus complexity and lamina of sensory cortex”. In: *Frontiers in Cellular Neuroscience* 7. ISSN: 1662-5102. DOI: 10.3389/fncel.2013.00124. URL: http://journal.frontiersin.org/article/10.3389/fncel.2013.00124/abstract.

Andrade-Talavera, Yuniesky, André Fisahn, and Antonio Rodríguez-Moreno (2023). “Timing to be precise? An overview of spike timing-dependent plasticity, brain rhythmicity, and glial cells interplay within neuronal circuits”. en. In: *Molecular Psychiatry*. ISSN: 1359-4184, 1476-5578. DOI: 10.1038/s41380-023-02027-w. URL: https://www.nature.com/articles/s41380-023-02027-w.

Ango, Fabrice, Graziella di Cristo, Hiroyuki Higashiyama, Vann Bennett, Priscilla Wu, and Z.Josh Huang (2004). “Ankyrin-Based Subcellular Gradient of Neurofascin, an Immunoglobulin Family Protein, Directs GABAergic Innervation at Purkinje Axon Initial Segment”. en. In: *Cell* 119.2, pp. 257–272. ISSN: 00928674. DOI: 10.1016/j.cell.2004.10.004. URL: https://linkinghub.elsevier.com/retrieve/pii/S009286740400947X.

Arjun McKinney, Arpana, Ralitsa Petrova, and Georgia Panagiotakos (2022). “Calcium and activity-dependent signaling in the developing cerebral cortex”. en. In: *Development* 149.17, dev198853. ISSN: 0950-1991, 1477-9129. DOI: 10.1242/dev.198853. URL: https://journals.biologists.com/dev/article/149/17/dev198853/276624/Calcium-and-activity-dependent-signaling-in-the.

Baranauskas, G., Y. David, and I. A. Fleidervish (2013). “Spatial mismatch between the Na+ flux and spike initiation in axon initial segment”. en. In: *Proceedings of the National Academy of Sciences* 110.10, pp. 4051–4056. ISSN: 0027-8424, 1091-6490. DOI: 10.1073/pnas.1215125110. URL: http://www.pnas.org/cgi/doi/10.1073/pnas.1215125110.

Bartsch, T. and P. Wulff (2015). “The hippocampus in aging and disease: From plasticity to vulnerability”. en. In: *Neuroscience* 309, pp. 1–16. ISSN: 03064522. DOI: 10.1016/j.neuroscience.2015.07.084. URL: https://linkinghub.elsevier.com/retrieve/pii/S0306452215007113.

Battefeld, Arne, Baouyen T. Tran, Jason Gavrilis, Edward C. Cooper, and Maarten H. P. Kole (2014). “Heteromeric Kv7.2/7.3 Channels Differentially Regulate Action Potential Initiation and Conduction in Neocortical Myelinated Axons”. en. In: *Journal of Neuroscience* 34.10, pp. 3719–3732. ISSN: 0270-6474, 1529-2401. DOI: 10.1523/JNEUROSCI.4206-13.2014. URL: https://www.jneurosci.org/content/34/10/3719.

Bekkers, John M. (2011). “Pyramidal neurons”. In: *Current biology* 21.24. Publisher: Elsevier, R975.

Bélanger, Mireille, Igor Allaman, and Pierre J. Magistretti (2011). “Brain Energy Metabolism: Focus on Astrocyte-Neuron Metabolic Cooperation”. en. In: *Cell Metabolism* 14.6, pp. 724–738. ISSN: 15504131. DOI: 10.1016/j.cmet.2011.08.016. URL: https://linkinghub.elsevier.com/retrieve/pii/S1550413111004207.

Belford, Gary R. and Herbert P. Killackey (1980). “The sensitive period in the development of the trigeminal system of the neonatal rat”. en. In: *The Journal of Comparative Neurology* 193.2, pp. 335–350. ISSN: 0021-9967, 1096-9861. DOI: 10.1002/cne.901930203. URL: https://onlinelibrary.wiley.com/doi/10.1002/cne.901930203.

Benavides-Piccione, Ruth, Mamen Regalado-Reyes, Isabel Fernaud-Espinosa, Asta Kastanauskaite, Silvia Tapia-González, Gonzalo León-Espinosa, Concepcion Rojo, Ricardo Insausti, Idan Segev, and Javier DeFelipe (2020). “Differential Structure of Hippocampal CA1 Pyramidal Neurons in the Human and Mouse”. In: *Cerebral Cortex* 30.2, pp. 730–752. ISSN: 1047-3211. DOI: 10.1093/cercor/bhz122. URL: https://doi.org/10.1093/cercor/bhz122.

Bender, Kevin J. and Laurence O. Trussell (2009). “Axon Initial Segment Ca2+ Channels Influence Action Potential Generation and Timing”. en. In: *Neuron* 61.2, pp. 259–271. ISSN: 08966273. DOI: 10.1016/j.neuron.2008.12.004. URL: https://linkinghub.elsevier.com/retrieve/pii/S0896627308010519.

Benedeczky, Istvan, Elek Molnár, and Péter Somogyi (1994). “The cisternal organelle as a Ca2+-storing compartment associated with GABAergic synapses in the axon initial segment of hippocampal pyramidal neurones”. en. In: *Experimental Brain Research* 101.2, pp. 216–230. ISSN: 0014-4819, 1432-1106. DOI: 10.1007/BF00228742. URL: http://link.springer.com/10.1007/BF00228742.

Benedetti, Bruno, Dominik Dannehl, Jan Maximilian Janssen, Corinna Corcelli, Sébastien Couillard-Després, and Maren Engelhardt (2020). “Structural and Functional Maturation of Rat Primary Motor Cortex Layer V Neurons”. en. In: *International Journal of Molecular Sciences* 21.17, p. 6101. ISSN: 1422-0067. DOI: 10.3390/ijms21176101. URL: https://www.mdpi.com/1422-0067/21/17/6101.

Benned-Jensen, Tau, Rasmus Kordt Christensen, Federico Denti, Jean-Francois Perrier, Hanne Borger Rasmussen, and Søren-Peter Olesen (2016). “Live Imaging of Kv7.2/7.3 Cell Surface Dynamics at the Axon Initial Segment: High Steady-State Stability and Calpain-Dependent Excitotoxic Downregulation Revealed”. en. In: *The Journal of Neuroscience* 36.7, pp. 2261–2266. ISSN: 0270-6474, 1529-2401. DOI: 10.1523/JNEUROSCI.2631-15.2016. URL: http://www.jneurosci.org/lookup/doi/10.1523/JNEUROSCI.2631-15.2016.

Benshalom, Gadi and Edward L. White (1986). “Quantification of thalamocortical synapses with spiny stellate neurons in layer IV of mouse somatosensory cortex”. en. In: *The Journal of Comparative Neurology* 253.3, pp. 303–314. ISSN: 0021-9967, 1096-9861. DOI: 10.1002/cne.902530303. URL: https://onlinelibrary.wiley.com/doi/10.1002/cne.902530303.

Berger, Stephen L., Alejandra Leo-Macias, Stephanie Yuen, Latika Khatri, Sylvia Pfennig, Yanqing Zhang, Esperanza Agullo-Pascual, Ghislaine Caillol, Min-Sheng Zhu, Eli Rothenberg, Carmen V. Melendez-Vasquez, Mario Delmar, Christophe Leterrier, and James L. Salzer (2018). "Localized Myosin II Activity Regulates Assembly and Plasticity of the Axon Initial Segment". en. In: *Neuron* 97.3, 555–570.e6. ISSN: 08966273. DOI: 10.1016/j.neuron.2017.12.039. URL: https://linkinghub.elsevier.com/retrieve/pii/S089662731731187X.

Boiko, Tatiana, Max Vakulenko, Helge Ewers, Chan Choo Yap, Caren Norden, and Bettina Winckler (2007). "Ankyrin-Dependent and -Independent Mechanisms Orchestrate Axonal Compartmentalization of L1 Family Members Neurofascin and L1/Neuron–Glia Cell Adhesion Molecule". en. In: *The Journal of Neuroscience* 27.3, pp. 590–603. ISSN: 0270-6474, 1529-2401. DOI: 10.1523/JNEUROSCI.4302-06.2007. URL: https://www.jneurosci.org/lookup/doi/10.1523/JNEUROSCI.4302-06.2007.

Boiko, Tatiana, Audra Van Wart, John H. Caldwell, S. Rock Levinson, James S. Trimmer, and Gary Matthews (2003). "Functional Specialization of the Axon Initial Segment by Isoform-Specific Sodium Channel Targeting". en. In: *The Journal of Neuroscience* 23.6, pp. 2306–2313. ISSN: 0270-6474, 1529-2401. DOI: 10.1523/JNEUROSCI.23-06-02306.2003. URL: http://www.jneurosci.org/lookup/doi/10.1523/JNEUROSCI.23-06-02306.2003.

El-Boustani, Sami, B. Semihcan Sermet, Georgios Foustoukos, Tess B. Oram, Ofer Yizhar, and Carl C. H. Petersen (2020). "Anatomically and functionally distinct thalamocortical inputs to primary and secondary mouse whisker somatosensory cortices". en. In: *Nature Communications* 11.1, p. 3342. ISSN: 2041-1723. DOI: 10.1038/s41467-020-17087-7. URL: https://www.nature.com/articles/s41467-020-17087-7.

Bouvier, G., C. Bidoret, M. Casado, and P. Paoletti (2015). "Presynaptic NMDA receptors: Roles and rules". en. In: *Neuroscience* 311, pp. 322–340. ISSN: 03064522. DOI: 10.1016/j.neuroscience.2015.10.033. URL: https://linkinghub.elsevier.com/retrieve/pii/S0306452215009525.

Bréchet, Aline, Marie-Pierre Fache, Anna Brachet, Géraldine Ferracci, Agnés Baude, Marie Irondelle, Sandrine Pereira, Christophe Leterrier, and Bénédicte Dargent (2008). "Protein kinase CK2 contributes to the organization of sodium channels in axonal membranes by regulating their interactions with ankyrin G". en. In: *Journal of Cell Biology* 183.6, pp. 1101–1114. ISSN: 1540-8140, 0021-9525. DOI: 10.1083/jcb.200805169. URL: https://rupress.org/jcb/article/183/6/1101/35366/Protein-kinase-CK2-contributes-to-the-organization.

Brette, Romain (2013). "Sharpness of Spike Initiation in Neurons Explained by Compartmentalization". en. In: *PLoS Computational Biology* 9.12. Ed. by Nicolas Brunel, e1003338. ISSN: 1553-7358. DOI: 10.1371/journal.pcbi.1003338. URL: https://dx.plos.org/10.1371/journal.pcbi.1003338.

Burwell, Rebecca D. (2006). "The Parahippocampal Region: Corticocortical Connectivity". en. In: *Annals of the New York Academy of Sciences* 911.1, pp. 25–42. ISSN: 00778923, 17496632. DOI: 10.1111/j.1749-6632.2000.tb06717.x. URL: https://onlinelibrary.wiley.com/doi/10.1111/j.1749-6632.2000.tb06717.x.

Caeser, M., T. Bonhoeffer, and J. Bolz (1989). "Cellular organization and development of slice cultures from rat visual cortex". en. In: *Experimental Brain Research* 77.2, pp. 234–244. ISSN: 0014-4819, 1432-1106. DOI: 10.1007/BF00274981. URL: http://link.springer.com/10.1007/BF00274981.

Canto, Cathrin B., Floris G. Wouterlood, and Menno P. Witter (2008). "What Does the Anatomical Organization of the Entorhinal Cortex Tell Us?" en. In: *Neural Plasticity*

2008, pp. 1–18. ISSN: 2090-5904, 1687-5443. DOI: 10.1155/2008/381243. URL: http://www.hindawi.com/journals/np/2008/381243/.

Cembrowski, Mark S. and Nelson Spruston (2019). "Heterogeneity within classical cell types is the rule: lessons from hippocampal pyramidal neurons". en. In: *Nature Reviews Neuroscience* 20.4, pp. 193–204. ISSN: 1471-003X, 1471-0048. DOI: 10.1038/s41583-019-0125-5. URL: http://www.nature.com/articles/s41583-019-0125-5.

Cheetham, Claire E. J., Martin S. L. Hammond, Clarissa E. J. Edwards, and Gerald T. Finnerty (2007). "Sensory Experience Alters Cortical Connectivity and Synaptic Function Site Specifically". en. In: *The Journal of Neuroscience* 27.13, pp. 3456–3465. ISSN: 0270-6474, 1529-2401. DOI: 10.1523/JNEUROSCI.5143-06.2007. URL: https://www.jneurosci.org/lookup/doi/10.1523/JNEUROSCI.5143-06.2007.

Cherubini, Enrico and Richard Miles (2015). "The CA3 region of the hippocampus: how is it? What is it for? How does it do it?" In: *Frontiers in Cellular Neuroscience* 9. ISSN: 1662-5102. DOI: 10.3389/fncel.2015.00019. URL: http://journal.frontiersin.org/Article/10.3389/fncel.2015.00019/abstract.

Connor, J. A. and C. F. Stevens (1971). "Voltage clamp studies of a transient outward membrane current in gastropod neural somata". en. In: *The Journal of Physiology* 213.1, pp. 21–30. ISSN: 00223751. DOI: 10.1113/jphysiol.1971.sp009365. URL: https://onlinelibrary.wiley.com/doi/10.1113/jphysiol.1971.sp009365.

Coombs, J. S., D. R. Curtis, and J. C. Eccles (1957). "The generation of impulses in motoneurones". en. In: *The Journal of Physiology* 139.2, pp. 232–249. ISSN: 00223751. DOI: 10.1113/jphysiol.1957.sp005888. URL: http://doi.wiley.com/10.1113/jphysiol.1957.sp005888.

Cover, Kara K. and Brian N. Mathur (2021). "Axo□axonic synapses: Diversity in neural circuit function". en. In: *Journal of Comparative Neurology* 529.9, pp. 2391–2401. ISSN: 0021-9967, 1096-9861. DOI: 10.1002/cne.25087. URL: https://onlinelibrary.wiley.com/doi/10.1002/cne.25087.

Cruz, Dianne A., Emily M. Lovallo, Steven Stockton, Matthew Rasband, and David A. Lewis (2009). "Postnatal development of synaptic structure proteins in pyramidal neuron axon initial segments in monkey prefrontal cortex". en. In: *The Journal of Comparative Neurology* 514.4, pp. 353–367. ISSN: 00219967, 10969861. DOI: 10.1002/cne.22006. URL: http://doi.wiley.com/10.1002/cne.22006.

Danielson, Nathan B., Jeffrey D. Zaremba, Patrick Kaifosh, John Bowler, Max Ladow, and Attila Losonczy (2016). "Sublayer-Specific Coding Dynamics during Spatial Navigation and Learning in Hippocampal Area CA1". en. In: *Neuron* 91.3, pp. 652–665. ISSN: 08966273. DOI: 10.1016/j.neuron.2016.06.020. URL: https://linkinghub.elsevier.com/retrieve/pii/S0896627316302987.

Davis, J Q, S Lambert, and V Bennett (1996). "Molecular composition of the node of Ranvier: identification of ankyrin-binding cell adhesion molecules neurofascin (mucin+/third FNIII domain-) and NrCAM at nodal axon segments." en. In: *Journal of Cell Biology* 135.5, pp. 1355–1367. ISSN: 0021-9525, 1540-8140. DOI: 10.1083/jcb.135.5.1355. URL: https://rupress.org/jcb/article/135/5/1355/56565/Molecular-composition-of-the-node-of-Ranvier.

De Kock, C. P. J., R. M. Bruno, H. Spors, and B. Sakmann (2007). "Layer- and cell-type-specific suprathreshold stimulus representation in rat primary somatosensory cortex: Sensory responses throughout barrel cortex". en. In: *The Journal of Physiology* 581.1, pp. 139–154. ISSN: 00223751. DOI: 10.1113/jphysiol.2006.124321. URL: https://onlinelibrary.wiley.com/doi/10.1113/jphysiol.2006.124321.

De Kock, Christiaan P. J. and Bert Sakmann (2009). “Spiking in primary somatosensory cortex during natural whisking in awake head-restrained rats is cell-type specific”. en. In: *Proceedings of the National Academy of Sciences* 106.38, pp. 16446–16450. ISSN: 0027-8424, 1091-6490. DOI: 10.1073/pnas.0904143106. URL: https://pnas.org/doi/full/10.1073/pnas.0904143106.

DeFelipe, Javier and Isabel Fariñas (1992). “The pyramidal neuron of the cerebral cortex: Morphological and chemical characteristics of the synaptic inputs”. en. In: *Progress in Neurobiology* 39.6, pp. 563–607. ISSN: 03010082. DOI: 10.1016/0301-0082(92)90015-7. URL: https://linkinghub.elsevier.com/retrieve/pii/0301008292900157.

Deshmukh, S., K. Onozuka, K.J. Bender, V.A. Bender, B. Lutz, K. Mackie, and D.E. Feldman (2007). “Postnatal development of cannabinoid receptor type 1 expression in rodent somatosensory cortex”. en. In: *Neuroscience* 145.1, pp. 279–287. ISSN: 03064522. DOI: 10.1016/j.neuroscience.2006.11.033. URL: https://linkinghub.elsevier.com/retrieve/pii/S0306452206016423.

Dodge, F. A. and R. Rahamimoff (1967). “Co-operative action of calcium ions in transmitter release at the neuromuscular junction”. en. In: *The Journal of Physiology* 193.2, pp. 419–432. ISSN: 00223751. DOI: 10.1113/jphysiol.1967.sp008367. URL: https://onlinelibrary.wiley.com/doi/10.1113/jphysiol.1967.sp008367.

Dodson, Paul D., Matthew C. Barker, and Ian D. Forsythe (2002). “Two Heteromeric Kv1 Potassium Channels Differentially Regulate Action Potential Firing”. en. In: *The Journal of Neuroscience* 22.16, pp. 6953–6961. ISSN: 0270-6474, 1529-2401. DOI: 10.1523/JNEUROSCI.22-16-06953.2002. URL: https://www.jneurosci.org/lookup/doi/10.1523/JNEUROSCI.22-16-06953.2002.

Dougherty, Kelly A., Tasnim Islam, and Daniel Johnston (2012). “Intrinsic excitability of CA1 pyramidal neurones from the rat dorsal and ventral hippocampus: Intrinsic excitability of the dorsal and ventral hippocampus”. en. In: *The Journal of Physiology* 590.22, pp. 5707–5722. ISSN: 00223751. DOI: 10.1113/jphysiol.2012.242693. URL: http://doi.wiley.com/10.1113/jphysiol.2012.242693.

Draguhn, Andreas, Roger D. Traub, Andrea Bibbig, and Dietmar Schmitz (2000). “Ripple (□200-Hz) Oscillations in Temporal Structures”. en-US. In: *Journal of Clinical Neurophysiology* 17.4, p. 361. ISSN: 0736-0258. URL: https://journals.lww.com/clinicalneurophys/Fulltext/2000/07000/Ripple___200_Hz__Oscillations_in_Temporal.3.aspx#R44-3.

Dribben, W H, L N Eisenman, and S Mennerick (2010). “Magnesium induces neuronal apoptosis by suppressing excitability”. en. In: *Cell Death & Disease* 1.8, e63–e63. ISSN: 2041-4889. DOI: 10.1038/cddis.2010.39. URL: https://www.nature.com/articles/cddis201039.

Du, Jing, Laurel L. Haak, Emily Phillips□Tansey, James T. Russell, and Chris J. McBain (2000). “Frequency□dependent regulation of rat hippocampal somato□dendritic excitability by the K^+ channel subunit Kv2.1”. en. In: *The Journal of Physiology* 522.1, pp. 19–31. ISSN: 0022-3751, 1469-7793. DOI: 10.1111/j.1469-7793.2000.t01-2-00019.xm. URL: https://onlinelibrary.wiley.com/doi/10.1111/j.1469-7793.2000.t01-2-00019.xm.

Dubey, Sushil, Nishita Bhembre, Shivani Bodas, Sukh Veer, Aurnab Ghose, Andrew Callan-Jones, and Pramod Pullarkat (2020). “The axonal actin-spectrin lattice acts as a tension buffering shock absorber”. en. In: *eLife* 9, e51772. ISSN: 2050-084X. DOI: 10.7554/eLife.51772. URL: https://elifesciences.org/articles/51772.

Duflocq, Amandine, Barbara Le Bras, Erika Bullier, François Couraud, and Marc Davenne (2008). “Nav1.1 is predominantly expressed in nodes of Ranvier and axon initial segments”. en. In: *Molecular and Cellular Neuroscience* 39.2, pp. 180–192. ISSN: 10447431. DOI: 10.1016/j.mcn.2008.06.008. URL: https://linkinghub.elsevier.com/retrieve/pii/S1044743108001619.

Egger, Robert, Rajeevan T. Narayanan, Jason M. Guest, Arco Bast, Daniel Udvary, Luis F. Messore, Suman Das, Christiaan P.J. De Kock, and Marcel Oberlaender (2020). “Cortical Output Is Gated by Horizontally Projecting Neurons in the Deep Layers”. en. In: *Neuron* 105.1, 122–137.e8. ISSN: 08966273. DOI: 10.1016/j.neuron.2019.10.011. URL: https://linkinghub.elsevier.com/retrieve/pii/S0896627319308840.

Eldar, Avigdor and Michael B. Elowitz (2010). “Functional roles for noise in genetic circuits”. en. In: *Nature* 467.7312, pp. 167–173. ISSN: 0028-0836, 1476-4687. DOI: 10.1038/nature09326. URL: https://www.nature.com/articles/nature09326.

Engelhardt, Maren, Nora Jamann, and Winnie Wefelmeyer (2019). “Small domain, large consequences: the axon initial segment as a key player in neuronal excitability”. In: Neuroforum 25.1, pp. 49–60. DOI: 10.1515/nf-2018-0023. URL: https://doi.org/10.1515/nf-2018-0023.

Erzurumlu, Reha S. and Patricia Gaspar (2012). “Development and critical period plasticity of the barrel cortex: Barrel cortex plasticity”. en. In: *European Journal of Neuroscience* 35.10, pp. 1540–1553. ISSN: 0953816X. DOI: 10.1111/j.1460-9568.2012.08075.x. URL: http://doi.wiley.com/10.1111/j.1460-9568.2012.08075.x.

Evans, Mark D., Adna S. Dumitrescu, Dennis L.H. Kruijssen, Samuel E. Taylor, and Matthew S. Grubb (2015). “Rapid Modulation of Axon Initial Segment Length Influences Repetitive Spike Firing”. en. In: *Cell Reports* 13.6, pp. 1233–1245. ISSN: 22111247. DOI: 10.1016/j.celrep.2015.09.066. URL: https://linkinghub.elsevier.com/retrieve/pii/S2211124715011080.

Evans, Mark D., Rosanna P. Sammons, Sabrina Lebron, Adna S. Dumitrescu, Thomas B. K. Watkins, Victor N. Uebele, John J. Renger, and Matthew S. Grubb (2013). “Calcineurin Signaling Mediates Activity-Dependent Relocation of the Axon Initial Segment”. en. In: *The Journal of Neuroscience* 33.16, pp. 6950–6963. ISSN: 0270-6474, 1529-2401. DOI: 10.1523/JNEUROSCI.0277-13.2013. URL: https://www.jneurosci.org/lookup/doi/10.1523/JNEUROSCI.0277-13.2013.

Eyal, G., H. D. Mansvelder, C. P. J. de Kock, and I. Segev (2014). “Dendrites Impact the Encoding Capabilities of the Axon”. en. In: *Journal of Neuroscience* 34.24, pp. 8063–8071. ISSN: 0270-6474, 1529-2401. DOI: 10.1523/JNEUROSCI.5431-13.2014. URL: http://www.jneurosci.org/cgi/doi/10.1523/JNEUROSCI.5431-13.2014.

Feng, Guoping, Rebecca H. Mellor, Michael Bernstein, Cynthia Keller-Peck, Quyen T. Nguyen, Mia Wallace, Jeanne M. Nerbonne, Jeff W. Lichtman, and Joshua R. Sanes (2000). “Imaging Neuronal Subsets in Transgenic Mice Expressing Multiple Spectral Variants of GFP”. en. In: *Neuron* 28.1, pp. 41–51. ISSN: 08966273. DOI: 10.1016/S0896-6273(00)00084-2. URL: https://linkinghub.elsevier.com/retrieve/pii/S0896627300000842.

Fernández-Ruiz, Antonio, Azahara Oliva, Eliezyer Fermino De Oliveira, Florbela Rocha-Almeida, David Tingley, and György Buzsáki (2019). “Long-duration hippocampal sharp wave ripples improve memory”. en. In: *Science* 364.6445, pp. 1082–1086. ISSN: 0036-8075, 1095-9203. DOI: 10.1126/science.aax0758. URL: https://www.science.org/doi/10.1126/science.aax0758.

Ferreira, Tiago, Cameron Arshadi, and Kyle I S Harrington (2021). *morphonets/SNTmanuscript: Prebuilt Packages (2020-12-07)*. DOI: 10.5281/ZENODO.4568540. URL: https://zenodo.org/record/4568540.

Fleidervish, Ilya A, Nechama Lasser-Ross, Michael J Gutnick, and William N Ross (2010). "Na+ imaging reveals little difference in action potential–evoked Na+ influx between axon and soma". en. In: *Nature Neuroscience* 13.7, pp. 852–860. ISSN: 1097-6256, 1546-1726. DOI: 10.1038/nn.2574. URL: https://www.nature.com/articles/nn.2574.

Geiller, Tristan, Sebastien Royer, and June-Seek Choi (2017). "Segregated Cell Populations Enable Distinct Parallel Encoding within the Radial Axis of the CA1 Pyramidal Layer". en. In: *Experimental Neurobiology* 26.1, pp. 1–10. ISSN: 1226-2560, 2093-8144. DOI: 10.5607/en.2017.26.1.1. URL: http://www.en-journal.org/journal/view.html?doi=10.5607/en.2017.26.1.1.

Girardeau, Gabrielle, Karim Benchenane, Sidney I Wiener, György Buzsáki, and Michaël B Zugaro (2009). "Selective suppression of hippocampal ripples impairs spatial memory". en. In: *Nature Neuroscience* 12.10, pp. 1222–1223. ISSN: 1097-6256, 1546-1726. DOI: 10.1038/nn.2384. URL: https://www.nature.com/articles/nn.2384.

Goaillard, Jean-Marc, Estelle Moubarak, Mónica Tapia, and Fabien Tell (2020). "Diversity of Axonal and Dendritic Contributions to Neuronal Output". In: *Frontiers in Cellular Neuroscience* 13, p. 570. ISSN: 1662-5102. DOI: 10.3389/fncel.2019.00570. URL: https://www.frontiersin.org/article/10.3389/fncel.2019.00570/full.

Goethals, Sarah and Romain Brette (2020). "Theoretical relation between axon initial segment geometry and excitability". en. In: *eLife* 9, e53432. ISSN: 2050-084X. DOI: 10.7554/eLife.53432. URL: https://elifesciences.org/articles/53432.

Gogolla, Nadine, Ivan Galimberti, Vincenzo DePaola, and Pico Caroni (2006). "Long-term live imaging of neuronal circuits in organotypic hippocampal slice cultures". en. In: *Nature Protocols* 1.3, pp. 1223–1226. ISSN: 1754-2189, 1750-2799. DOI: 10.1038/nprot.2006.169. URL: http://www.nature.com/articles/nprot.2006.169.

Golbs, A., B. Nimmervoll, J.-J. Sun, I. E. Sava, and H. J. Luhmann (2011). "Control of Programmed Cell Death by Distinct Electrical Activity Patterns". en. In: *Cerebral Cortex* 21.5, pp. 1192–1202. ISSN: 1047-3211, 1460-2199. DOI: 10.1093/cercor/bhq200. URL: https://academic.oup.com/cercor/article-lookup/doi/10.1093/cercor/bhq200.

Green, John D. and Arnaldo A. Arduini (1954). "HIPPOCAMPAL ELECTRICAL ACTIVITY IN AROUSAL". en. In: *Journal of Neurophysiology* 17.6, pp. 533–557. ISSN: 0022-3077, 1522-1598. DOI: 10.1152/jn.1954.17.6.533. URL: https://www.physiology.org/doi/10.1152/jn.1954.17.6.533.

Groh, Alexander, Christiaan P. J. De Kock, Verena C. Wimmer, Bert Sakmann, and Thomas Kuner (2008). "Driver or Coincidence Detector: Modal Switch of a Corticothalamic Giant Synapse Controlled by Spontaneous Activity and Short-Term Depression". en. In: *The Journal of Neuroscience* 28.39, pp. 9652–9663. ISSN: 0270-6474, 1529-2401. DOI: 10.1523/JNEUROSCI.1554-08.2008. URL: https://www.jneurosci.org/lookup/doi/10.1523/JNEUROSCI.1554-08.2008.

Grubb, Matthew S. and Juan Burrone (2010). "Activity-dependent relocation of the axon initial segment fine-tunes neuronal excitability". en. In: *Nature* 465.7301, pp. 1070–1074. ISSN: 0028-0836, 1476-4687. DOI: 10.1038/nature09160. URL: http://www.nature.com/articles/nature09160.

Gulledge, A. T. and J. J. Bravo (2016). “Neuron Morphology Influences Axon Initial Segment Plasticity”. en. In: *eNeuro* 3.1. ISSN: 2373-2822. DOI: 10.1523/ENEURO.0085-15.2016. URL: http://eneuro.org/cgi/doi/10.1523/ENEURO.0085-15.2016.

Guo, Yu, Zi-jun Su, Yi-kun Chen, and Zhen Chai (2017). “Brain-derived neurotrophic factor/neurotrophin 3 regulate axon initial segment location and affect neuronal excitability in cultured hippocampal neurons”. en. In: *Journal of Neurochemistry* 142.2, pp. 260–271. ISSN: 00223042. DOI: 10.1111/jnc.14050. URL: https://onlinelibrary.wiley.com/doi/10.1111/jnc.14050.

Gutzmann, Annika, Nursah ErgÃ¼l, Rebecca Grossmann, Christian Schultz, Petra Wahle, and Maren Engelhardt (2014). “A period of structural plasticity at the axon initial segment in developing visual cortex”. In: *Frontiers in Neuroanatomy* 8. ISSN: 1662-5129. DOI: 10.3389/fnana.2014.00011. URL: http://journal.frontiersin.org/article/10.3389/fnana.2014.00011/abstract.

Hallak, Mordechai, Robert F. Berman, Susan M. Irtenkauf, Cynthia A. Janusz, and David B. Cotton (1994). “Magnesium Sulfate Treatment Decreases N-Methyl-D-Aspartate Receptor Binding in the Rat Brain: An Autoradiographic Study”. en. In: *Journal of the Society for Gynecologic Investigation* 1.1, pp. 25–30. ISSN: 1071-5576. DOI: 10.1177/107155769400100106. URL: http://journals.sagepub.com/doi/10.1177/107155769400100106.

Hamada, Mustafa S., Sarah Goethals, Sharon I. de Vries, Romain Brette, and Maarten H. P. Kole (2016). “Covariation of axon initial segment location and dendritic tree normalizes the somatic action potential”. en. In: *Proceedings of the National Academy of Sciences* 113.51, pp. 14841–14846. ISSN: 0027-8424, 1091-6490. DOI: 10.1073/pnas.1607548113. URL: http://www.pnas.org/lookup/doi/10.1073/pnas.1607548113.

Hamill, O. P., J. R. Huguenard, and D. A. Prince (1991). “Patch-Clamp Studies of Voltage-Gated Currents in Identified Neurons of the Rat Cerebral Cortex”. en. In: *Cerebral Cortex* 1.1, pp. 48–61. ISSN: 1047-3211, 1460-2199. DOI: 10.1093/cercor/1.1.48. URL: https://academic.oup.com/cercor/article-lookup/doi/10.1093/cercor/1.1.48.

Hanemaaijer, Naomi AK, Marko A Popovic, Xante Wilders, Sara Grasman, Oriol Pavón Arocas, and Maarten HP Kole (2020). “Ca2+ entry through NaV channels generates submillisecond axonal Ca2+ signaling”. en. In: *eLife* 9, e54566. ISSN: 2050-084X. DOI: 10.7554/eLife.54566. URL: https://elifesciences.org/articles/54566.

Hashimotodani, Yuki, Takako Ohno-Shosaku, Masahiko Watanabe, and Masanobu Kano (2007). “Roles of phospholipase Cβ and NMDA receptor in activity-dependent endocannabinoid release: Phospholipase Cβ and NMDA receptor in endocannabinoid release”. en. In: *The Journal of Physiology* 584.2, pp. 373–380. ISSN: 00223751. DOI: 10.1113/jphysiol.2007.137497. URL: http://doi.wiley.com/10.1113/jphysiol.2007.137497.

Häusser, Michael, Greg Stuart, Claudia Racca, and Bert Sakmann (1995). “Axonal initiation and active dendritic propagation of action potentials in substantia nigra neurons”. en. In: *Neuron* 15.3, pp. 637–647. ISSN: 08966273. DOI: 10.1016/0896-6273(95)90152-3. URL: https://linkinghub.elsevier.com/retrieve/pii/0896627395901523.

Hayashi, Kanehiro, Ken-ichiro Kubo, Ayako Kitazawa, and Kazunori Nakajima (2015). “Cellular dynamics of neuronal migration in the hippocampus”. In: *Frontiers in Neuroscience* 9. ISSN: 1662-453X. DOI: 10.3389/fnins.2015.00135. URL: http://journal.frontiersin.org/article/10.3389/fnins.2015.00135/abstract.

Hedstrom, Kristian L., Xiaorong Xu, Yasuhiro Ogawa, Renato Frischknecht, Constanze I. Seidenbecher, Peter Shrager, and Matthew N. Rasband (2007). “Neurofascin assembles a specialized extracellular matrix at the axon initial segment”. en. In: *The Journal of Cell Biology* 178.5, pp. 875–886. ISSN: 0021-9525, 1540-8140. DOI: 10.1083/jcb.200705119. URL: http://www.jcb.org/lookup/doi/10.1083/jcb.200705119.

Hensch, Takao K. (2005). “Critical period plasticity in local cortical circuits”. en. In: *Nature Reviews Neuroscience* 6.11, pp. 877–888. ISSN: 1471-003X, 1471-0048. DOI: 10.1038/nrn1787. URL: https://www.nature.com/articles/nrn1787.

Hermann, L (1905). “Beiträge zur physiologie und physik des nerven”. In: *Archiv für die Gesamte Physiologie des Menschen und der Tiere* 109.3-4. Publisher: Springer-Verlag Berlin/Heidelberg, pp. 95–144. ISSN: 0365-267X.

Hodapp, Alexander, Martin E. Kaiser, Christian Thome, Lingjun Ding, Andrei Rozov, Matthias Klumpp, Nikolas Stevens, Moritz Stingl, Tina Sackmann, Nadja Lehmann, Andreas Draguhn, Andrea Burgalossi, Maren Engelhardt, and Martin Both (2022). “Dendritic axon origin enables information gating by perisomatic inhibition in pyramidal neurons”. en. In: *Science* 377.6613, pp. 1448–1452. ISSN: 0036-8075, 1095-9203. DOI: 10.1126/science.abj1861. URL: https://www.science.org/doi/10.1126/science.abj1861.

Hodgkin, A. L. and A. F. Huxley (1952). “A quantitative description of membrane current and its application to conduction and excitation in nerve”. en. In: *The Journal of Physiology* 117.4, pp. 500–544. ISSN: 0022-3751, 1469-7793. DOI: 10.1113/jphysiol.1952.sp004764. URL: https://onlinelibrary.wiley.com/doi/10.1113/jphysiol.1952.sp004764.

Hodgkin, Alan Lloyd and William Albert Hugh Rushton (1946). “The electrical constants of a crustacean nerve fibre”. en. In: *Proceedings of the Royal Society of London. Series B - Biological Sciences* 133.873, pp. 444–479. ISSN: 2053-9193. DOI: 10.1098/rspb.1946.0024. URL: https://royalsocietypublishing.org/doi/10.1098/rspb.1946.0024.

Höfflin, Felix, Alexander Jack, Christian Riedel, Julia Mack-Bucher, Johannes Roos, Corinna Corcelli, Christian Schultz, Petra Wahle, and Maren Engelhardt (2017). “Heterogeneity of the Axon Initial Segment in Interneurons and Pyramidal Cells of Rodent Visual Cortex”. In: *Frontiers in Cellular Neuroscience* 11. ISSN: 1662-5102. DOI: 10.3389/fncel.2017.00332. URL: https://www.ncbi.nlm.nih.gov/pmc/articles/PMC5684645/.

Holmes, J. E. and W. R. Adey (1960). “Electrical activity of the entorhinal cortex during conditioned behavior”. en. In: *American Journal of Physiology-Legacy Content* 199.5, pp. 741–744. ISSN: 0002-9513. DOI: 10.1152/ajplegacy.1960.199.5.741. URL: https://www.physiology.org/doi/10.1152/ajplegacy.1960.199.5.741.

Hong, Elizabeth J., Alejandra E. McCord, and Michael E. Greenberg (2008). “A Biological Function for the Neuronal Activity-Dependent Component of Bdnf Transcription in the Development of Cortical Inhibition”. en. In: *Neuron* 60.4, pp. 610–624. ISSN: 08966273. DOI: 10.1016/j.neuron.2008.09.024. URL: https://linkinghub.elsevier.com/retrieve/pii/S0896627308008027.

Hu, Hang, Rachel E Hostetler, and Ariel Agmon (2023). “Ultrafast (400 Hz) network oscillations induced in mouse barrel cortex by optogenetic activation of thalamocortical axons”. en. In: *eLife* 12, e82412. ISSN: 2050-084X. DOI: 10.7554/eLife.82412. URL: https://elifesciences.org/articles/82412.

Hu, Ming and Xiaolong Jiang (2022). “PatchView: A Python Package for Patch-clamp DataAnalysis and Visualization”. In: *Journal of Open Source Software* 7.78, p. 4706.

ISSN: 2475-9066. DOI: 10.21105/joss.04706. URL: https://joss.theoj.org/papers/10.21105/joss.04706.

Hu, Wenqin, Cuiping Tian, Tun Li, Mingpo Yang, Han Hou, and Yousheng Shu (2009). "Distinct contributions of Na v 1.6 and Na v 1.2 in action potential initiation and backpropagation". en. In: *Nature Neuroscience* 12.8, pp. 996–1002. ISSN: 1546-1726. DOI: 10.1038/nn.2359. URL: https://www.nature.com/articles/nn.2359.

Huang, Claire Yu-Mei, Chuansheng Zhang, Tammy Szu-Yu Ho, Juan Oses-Prieto, Alma L. Burlingame, Joshua Lalonde, Jeffrey L. Noebels, Christophe Leterrier, and Matthew N. Rasband (2017). "αII Spectrin Forms a Periodic Cytoskeleton at the Axon Initial Segment and Is Required for Nervous System Function". en. In: *The Journal of Neuroscience* 37.47, pp. 11311–11322. ISSN: 0270-6474, 1529-2401. DOI: 10.1523/JNEUROSCI.2112-17.2017. URL: http://www.jneurosci.org/lookup/doi/10.1523/JNEUROSCI.2112-17.2017.

Humpel, C. (2015). "Organotypic brain slice cultures: A review". en. In: *Neuroscience* 305, pp. 86–98. ISSN: 03064522. DOI: 10.1016/j.neuroscience.2015.07.086. URL: https://linkinghub.elsevier.com/retrieve/pii/S0306452215007162.

Huszár, Roman, Yunchang Zhang, Heike Blockus, and György Buzsáki (2022). "Preconfigured dynamics in the hippocampus are guided by embryonic birthdate and rate of neurogenesis". en. In: *Nature Neuroscience* 25.9, pp. 1201–1212. ISSN: 1097-6256, 1546-1726. DOI: 10.1038/s41593-022-01138-x. URL: https://www.nature.com/articles/s41593-022-01138-x.

Igarashi, Kei M., Hiroshi T. Ito, Edvard I. Moser, and May-Britt Moser (2014). "Functional diversity along the transverse axis of hippocampal area CA1". en. In: *FEBS Letters* 588.15, pp. 2470–2476. ISSN: 00145793. DOI: 10.1016/j.febslet.2014.06.004. URL: http://doi.wiley.com/10.1016/j.febslet.2014.06.004.

Inan, Melis and Stewart A. Anderson (2014). "The chandelier cell, form and function". en. In: *Current Opinion in Neurobiology* 26, pp. 142–148. ISSN: 09594388. DOI: 10.1016/j.conb.2014.01.009. URL: https://linkinghub.elsevier.com/retrieve/pii/S0959438814000245.

Inda, Maria Carmen, Javier DeFelipe, and Alberto Muñoz (2006). "Voltage-gated ion channels in the axon initial segment of human cortical pyramidal cells and their relationship with chandelier cells". en. In: *Proceedings of the National Academy of Sciences* 103.8, pp. 2920–2925. ISSN: 0027-8424, 1091-6490. DOI: 10.1073/pnas.0511197103. URL: https://www.pnas.org/content/103/8/2920.

Jamann, Nora, Dominik Dannehl, Nadja Lehmann, Robin Wagener, Corinna Thielemann, Christian Schultz, Jochen Staiger, Maarten H. P. Kole, and Maren Engelhardt (2021). "Sensory input drives rapid homeostatic scaling of the axon initial segment in mouse barrel cortex". en. In: *Nature Communications* 12.1, p. 23. ISSN: 2041-1723. DOI: 10.1038/s41467-020-20232-x. URL: http://www.nature.com/articles/s41467-020-20232-x.

Jamann, Nora, Merryn Jordan, and Maren Engelhardt (2018). "Activity-Dependent Axonal Plasticity in Sensory Systems". en. In: *Neuroscience* 368, pp. 268–282. ISSN: 03064522. DOI: 10.1016/j.neuroscience.2017.07.035. URL: https://linkinghub.elsevier.com/retrieve/pii/S0306452217305055.

Jenkins, Scott M. and Vann Bennett (2001). "Ankyrin-G coordinates assembly of the spectrin-based membrane skeleton, voltage-gated sodium channels, and L1 CAMs at Purkinje neuron initial segments". en. In: *Journal of Cell Biology* 155.5, pp. 739–746. ISSN: 1540-8140, 0021-9525. DOI: 10.1083/jcb.200109026. URL: https://

rupress.org/jcb/article/155/5/739/32409/AnkyrinG-coordinates-assembly-of-the-spectrinbased.

Jensen, Kf and Hp Killackey (1987). “Terminal arbors of axons projecting to the somatosensory cortex of the adult rat. II. The altered morphology of thalamocortical afferents following neonatal infraorbital nerve cut”. en. In: *The Journal of Neuroscience* 7.11, pp. 3544–3553. ISSN: 0270-6474, 1529-2401. DOI: 10.1523/JNEUROSCI.07-11-03544.1987. URL: https://www.jneurosci.org/lookup/doi/10.1523/JNEUROSCI.07-11-03544.1987.

Johnson, Steven W and Vincent Seutin (1997). “Bicuculline methiodide potentiates NMDA-dependent burst firing in rat dopamine neurons by blocking apamin-sensitive Ca2+-activated K+ currents”. en. In: *Neuroscience Letters* 231.1, pp. 13–16. ISSN: 03043940. DOI: 10.1016/S0304-3940(97)00508-9. URL: https://linkinghub.elsevier.com/retrieve/pii/S0304394097005089.

Johnston, Jamie, Sarah J. Griffin, Claire Baker, Anna Skrzypiec, Tatanya Chernova, and Ian D. Forsythe (2008). “Initial segment Kv2.2 channels mediate a slow delayed rectifier and maintain high frequency action potential firing in medial nucleus of the trapezoid body neurons: Kv2.2 conductance in MNTB”. en. In: *The Journal of Physiology* 586.14, pp. 3493–3509. ISSN: 00223751. DOI: 10.1113/jphysiol.2008.153734. URL: http://doi.wiley.com/10.1113/jphysiol.2008.153734.

Jung, Christian K.E. and Jochen Herms (2014). “Structural Dynamics of Dendritic Spines are Influenced by an Environmental Enrichment: An In Vivo Imaging Study”. en. In: *Cerebral Cortex* 24.2, pp. 377–384. ISSN: 1460-2199, 1047-3211. DOI: 10.1093/cercor/bhs317. URL: https://academic.oup.com/cercor/article-lookup/doi/10.1093/cercor/bhs317.

Kaas, J H, M M Merzenich, and H P Killackey (1983). “The Reorganization of Somatosensory Cortex Following Peripheral Nerve Damage in Adult and Developing Mammals”. en. In: *Annual Review of Neuroscience* 6.1, pp. 325–356. ISSN: 0147-006X, 1545-4126. DOI: 10.1146/annurev.ne.06.030183.001545. URL: https://www.annualreviews.org/doi/10.1146/annurev.ne.06.030183.001545.

Kapitein, Lukas C. and Casper C. Hoogenraad (2011). “Which way to go? Cytoskeletal organization and polarized transport in neurons”. en. In: *Molecular and Cellular Neuroscience* 46.1, pp. 9–20. ISSN: 1044-7431. DOI: 10.1016/j.mcn.2010.08.015. URL: http://www.sciencedirect.com/science/article/pii/S104474311000206X.

Kim, J., C. J. Matney, A. Blankenship, S. Hestrin, and S. P. Brown (2014). “Layer 6 Corticothalamic Neurons Activate a Cortical Output Layer, Layer 5a”. en. In: *Journal of Neuroscience* 34.29, pp. 9656–9664. ISSN: 0270-6474, 1529-2401. DOI: 10.1523/JNEUROSCI.1325-14.2014. URL: https://www.jneurosci.org/lookup/doi/10.1523/JNEUROSCI.1325-14.2014.

King, Anna N., Colleen F. Manning, and James S. Trimmer (2014). “A unique ion channel clustering domain on the axon initial segment of mammalian neurons: Ion channel clustering on the axon initial segment”. en. In: *Journal of Comparative Neurology* 522.11, pp. 2594–2608. ISSN: 00219967. DOI: 10.1002/cne.23551. URL: http://doi.wiley.com/10.1002/cne.23551.

Kobayashi, Masayuki, Tomohiro Hamada, Mikihiko Kogo, Yuchio Yanagawa, Kunihiko Obata, and Youngnam Kang (2008). “Developmental profile of GABA $_{A}$ -mediated synaptic transmission in pyramidal cells of the somatosensory cortex”. en. In: *European Journal of Neuroscience* 28.5, pp. 849–861. ISSN: 0953816X, 14609568. DOI: 10.1111/j.1460-9568.2008.06401.x. URL: https://onlinelibrary.wiley.com/doi/10.1111/j.1460-9568.2008.06401.x.

Kole, Maarten H P, Susanne U Ilschner, Björn M Kampa, Stephen R Williams, Peter C Ruben, and Greg J Stuart (2008). “Action potential generation requires a high sodium channel density in the axon initial segment”. en. In: *Nature Neuroscience* 11.2, pp. 178–186. ISSN: 1097-6256, 1546-1726. DOI: 10.1038/nn2040. URL: http://www.nature.com/articles/nn2040.

Kole, Maarten H. P., Johannes J. Letzkus, and Greg J. Stuart (2007). “Axon Initial Segment Kv1 Channels Control Axonal Action Potential Waveform and Synaptic Efficacy”. en. In: *Neuron* 55.4, pp. 633–647. ISSN: 0896-6273. DOI: 10.1016/j.neuron.2007.07.031. URL: http://www.sciencedirect.com/science/article/pii/S0896627307005764.

Kole, Maarten H. P. and Greg J. Stuart (2012). “Signal Processing in the Axon Initial Segment”. en. In: *Neuron* 73.2, pp. 235–247. ISSN: 0896-6273. DOI: 10.1016/j.neuron.2012.01.007. URL: http://www.sciencedirect.com/science/article/pii/S0896627312000505.

Kole, Maarten HP and Romain Brette (2018). “The electrical significance of axon location diversity”. en. In: *Current Opinion in Neurobiology* 51, pp. 52–59. ISSN: 09594388. DOI: 10.1016/j.conb.2018.02.016. URL: https://linkinghub.elsevier.com/retrieve/pii/S095943881730288X.

Komada, Masayuki and Philippe Soriano (2002). “βIV-spectrin regulates sodium channel clustering through ankyrin-G at axon initial segments and nodes of Ranvier”. en. In: *The Journal of Cell Biology* 156.2, pp. 337–348. ISSN: 0021-9525, 1540-8140. DOI: 10.1083/jcb.200110003. URL: http://jcb.rupress.org/content/156/2/337.

Kuba, H., R. Adachi, and H. Ohmori (2014). “Activity-Dependent and Activity-Independent Development of the Axon Initial Segment”. en. In: *Journal of Neuroscience* 34.9, pp. 3443–3453. ISSN: 0270-6474, 1529-2401. DOI: 10.1523/JNEUROSCI.4357-13.2014. URL: http://www.jneurosci.org/cgi/doi/10.1523/JNEUROSCI.4357-13.2014.

Kuba, Hiroshi, Takahiro M. Ishii, and Harunori Ohmori (2006). “Axonal site of spike initiation enhances auditory coincidence detection”. en. In: *Nature* 444.7122, pp. 1069–1072. ISSN: 0028-0836, 1476-4687. DOI: 10.1038/nature05347. URL: http://www.nature.com/articles/nature05347.

Kuba, Hiroshi and Harunori Ohmori (2009). “Roles of axonal sodium channels in precise auditory time coding at nucleus magnocellularis of the chick: Axonal Na $^{+}$ channels for precise temporal coding”. en. In: *The Journal of Physiology* 587.1, pp. 87–100. ISSN: 00223751. DOI: 10.1113/jphysiol.2008.162651. URL: http://doi.wiley.com/10.1113/jphysiol.2008.162651.

Kuba, Hiroshi, Yuki Oichi, and Harunori Ohmori (2010). “Presynaptic activity regulates Na + channel distribution at the axon initial segment”. en. In: *Nature* 465.7301, pp. 1075–1078. ISSN: 1476-4687. DOI: 10.1038/nature09087. URL: https://www.nature.com/articles/nature09087.

Kumar, Pratap and Ora Ohana (2008). “Inter- and Intralaminar Subcircuits of Excitatory and Inhibitory Neurons in Layer 6a of the Rat Barrel Cortex”. en. In: *Journal of Neurophysiology* 100.4, pp. 1909–1922. ISSN: 0022-3077, 1522-1598. DOI: 10.1152/jn.90684.2008. URL: https://www.physiology.org/doi/10.1152/jn.90684.2008.

Lam, Y.-W. and S. M. Sherman (2010). “Functional Organization of the Somatosensory Cortical Layer 6 Feedback to the Thalamus”. en. In: *Cerebral Cortex* 20.1, pp. 13–24. ISSN: 1047-3211, 1460-2199. DOI: 10.1093/cercor/bhp077. URL: https://academic.oup.com/cercor/article-lookup/doi/10.1093/cercor/bhp077.

Le Bras, Barbara, Amélie Fréal, Antonny Czarnecki, Pascal Legendre, Erika Bullier, Masayuki Komada, Peter J. Brophy, Marc Davenne, and François Couraud (2014). “In

vivo assembly of the axon initial segment in motor neurons". en. In: *Brain Structure and Function* 219.4, pp. 1433–1450. ISSN: 1863-2653, 1863-2661. DOI: 10.1007/s00429-013-0578-7. URL: http://link.springer.com/10.1007/s00429-013-0578-7.

Lee, Inah, D. Yoganarasimha, Geeta Rao, and James J. Knierim (2004). "Comparison of population coherence of place cells in hippocampal subfields CA1 and CA3". en. In: *Nature* 430.6998, pp. 456–459. ISSN: 0028-0836, 1476-4687. DOI: 10.1038/nature02739. URL: http://www.nature.com/articles/nature02739.

Lee, Li-Jen, Wan-Jung Chen, Ya-Wen Chuang, and Yu-Chun Wang (2009). "Neonatal whisker trimming causes long-lasting changes in structure and function of the somatosensory system". en. In: *Experimental Neurology* 219.2, pp. 524–532. ISSN: 00144886. DOI: 10.1016/j.expneurol.2009.07.012. URL: https://linkinghub.elsevier.com/retrieve/pii/S0014488609002775.

Lehmann, Nadja, Stefan Markovic, Christian Thome, and Maren Engelhardt (2023). *Axon onset remodeling in response to network activity in mouse cortical neurons*. preprint. DOI: 10.1101/2023.07.31.551236. URL: https://www.biorxiv.org/content/10.1101/2023.07.31.551236v1.

Lestienne, Rémy (2001). "Spike timing, synchronization and information processing on the sensory side of the central nervous system". en. In: *Progress in Neurobiology* 65.6, pp. 545–591. ISSN: 03010082. DOI: 10.1016/S0301-0082(01)00019-3. URL: https://linkinghub.elsevier.com/retrieve/pii/S0301008201000193.

Leterrier (2021). "Putting the axonal periodic scaffold in order". en. In: *Current Opinion in Neurobiology* 69, pp. 33–40. ISSN: 09594388. DOI: 10.1016/j.conb.2020.12.015. URL: https://linkinghub.elsevier.com/retrieve/pii/S0959438820302063.

Leterrier, C., H. Vacher, M.-P. Fache, S. A. d'Ortoli, F. Castets, A. Autillo-Touati, and B. Dargent (2011). "End-binding proteins EB3 and EB1 link microtubules to ankyrin G in the axon initial segment". en. In: *Proceedings of the National Academy of Sciences* 108.21, pp. 8826–8831. ISSN: 0027-8424, 1091-6490. DOI: 10.1073/pnas.1018671108. URL: http://www.pnas.org/cgi/doi/10.1073/pnas.1018671108.

Leterrier, Christophe (2018). "The Axon Initial Segment: An Updated Viewpoint". en. In: *The Journal of Neuroscience* 38.9, pp. 2135–2145. ISSN: 0270-6474, 1529-2401. DOI: 10.1523/JNEUROSCI.1922-17.2018. URL: http://www.jneurosci.org/lookup/doi/10.1523/JNEUROSCI.1922-17.2018.

Leterrier, Christophe, Nadine Clerc, Fanny Rueda-Boroni, Audrey Montersino, Bénédicte Dargent, and Francis Castets (2017). "Ankyrin G Membrane Partners Drive the Establishment and Maintenance of the Axon Initial Segment". In: *Frontiers in Cellular Neuroscience* 11. ISSN: 1662-5102. DOI: 10.3389/fncel.2017.00006. URL: http://journal.frontiersin.org/article/10.3389/fncel.2017.00006/full.

Leterrier, Christophe and Bénédicte Dargent (2014). "No Pasaran! Role of the axon initial segment in the regulation of protein transport and the maintenance of axonal identity". en. In: *Seminars in Cell & Developmental Biology* 27, pp. 44–51. ISSN: 10849521. DOI: 10.1016/j.semcdb.2013.11.001. URL: https://linkinghub.elsevier.com/retrieve/pii/S1084952113001201.

Leterrier, Christophe, Pankaj Dubey, and Subhojit Roy (2017). "The nano-architecture of the axonal cytoskeleton". en. In: *Nature Reviews Neuroscience* 18.12, pp. 713–726. ISSN: 1471-003X, 1471-0048. DOI: 10.1038/nrn.2017.129. URL: http://www.nature.com/articles/nrn.2017.129.

Leterrier, Christophe, Jean Potier, Ghislaine Caillol, Claire Debarnot, Fanny Rueda Boroni, and Bénédicte Dargent (2015). "Nanoscale Architecture of the Axon Initial Segment Reveals an Organized and Robust Scaffold". en. In: *Cell Reports* 13.12, pp. 2781–

2793. ISSN: 22111247. DOI: 10.1016/j.celrep.2015.11.051. URL: https://linkinghub.elsevier.com/retrieve/pii/S2211124715013820.

Leutgeb, Stefan, Jill K. Leutgeb, Alessandro Treves, May-Britt Moser, and Edvard I. Moser (2004). "Distinct Ensemble Codes in Hippocampal Areas CA3 and CA1". en. In: *Science* 305.5688, pp. 1295–1298. ISSN: 0036-8075, 1095-9203. DOI: 10.1126/science.1100265. URL: https://www.science.org/doi/10.1126/science.1100265.

Lezmy, Jonathan, Maya Lipinsky, Yana Khrapunsky, Eti Patrich, Lia Shalom, Asher Peretz, Ilya A. Fleidervish, and Bernard Attali (2017). "M-current inhibition rapidly induces a unique CK2-dependent plasticity of the axon initial segment". en. In: *Proceedings of the National Academy of Sciences* 114.47, E10234–E10243. ISSN: 0027-8424, 1091-6490. DOI: 10.1073/pnas.1708700114. URL: http://www.pnas.org/lookup/doi/10.1073/pnas.1708700114.

Lipkin, Anna M., Margaret M. Cunniff, Perry W. E. Spratt, Stefan M. Lemke, and Kevin J. Bender (2021). "Functional Microstructure of Ca $_V$ -Mediated Calcium Signaling in the Axon Initial Segment". en. In: *The Journal of Neuroscience* 41.17, pp. 3764–3776. ISSN: 0270-6474, 1529-2401. DOI: 10.1523/JNEUROSCI.2843-20.2021. URL: https://www.jneurosci.org/lookup/doi/10.1523/JNEUROSCI.2843-20.2021.

Liu, Wenjing and Jérôme J. Devaux (2014). "Calmodulin orchestrates the heteromeric assembly and the trafficking of KCNQ2/3 (Kv7.2/3) channels in neurons". en. In: *Molecular and Cellular Neuroscience* 58, pp. 40–52. ISSN: 1044-7431. DOI: 10.1016/j.mcn.2013.12.005. URL: http://www.sciencedirect.com/science/article/pii/S104474311300119X.

Lorincz, A. and Z. Nusser (2008). "Cell-Type-Dependent Molecular Composition of the Axon Initial Segment". en. In: *Journal of Neuroscience* 28.53, pp. 14329–14340. ISSN: 0270-6474, 1529-2401. DOI: 10.1523/JNEUROSCI.4833-08.2008. URL: http://www.jneurosci.org/cgi/doi/10.1523/JNEUROSCI.4833-08.2008.

Lorincz, Andrea and Zoltan Nusser (2010). "Molecular Identity of Dendritic Voltage-Gated Sodium Channels". en. In: *Science* 328.5980, pp. 906–909. ISSN: 0036-8075, 1095-9203. DOI: 10.1126/science.1187958. URL: https://science.sciencemag.org/content/328/5980/906.

Luhmann, Heiko J., Anne Sinning, Jenq-Wei Yang, Vicente Reyes-Puerta, Maik C. Stüttgen, Sergei Kirischuk, and Werner Kilb (2016). "Spontaneous Neuronal Activity in Developing Neocortical Networks: From Single Cells to Large-Scale Interactions". In: *Frontiers in Neural Circuits* 10. ISSN: 1662-5110. DOI: 10.3389/fncir.2016.00040. URL: http://journal.frontiersin.org/Article/10.3389/fncir.2016.00040/abstract.

Ma, Pokay M. (1991). "The barrelettes?architectonic vibrissal representations in the brainstem trigeminal complex of the mouse. Normal structural organization". en. In: *The Journal of Comparative Neurology* 309.2, pp. 161–199. ISSN: 0021-9967, 1096-9861. DOI: 10.1002/cne.903090202. URL: https://onlinelibrary.wiley.com/doi/10.1002/cne.903090202.

Mainen, Zachary F., Jasdan Joerges, John R. Huguenard, and Terrence J. Sejnowski (1995). "A model of spike initiation in neocortical pyramidal neurons". en. In: *Neuron* 15.6, pp. 1427–1439. ISSN: 08966273. DOI: 10.1016/0896-6273(95)90020-9. URL: https://linkinghub.elsevier.com/retrieve/pii/0896627395900209.

Malik, Ruchi, Kelly Ann Dougherty, Komal Parikh, Connor Byrne, and Daniel Johnston (2016). "Mapping the electrophysiological and morphological properties of CA1 pyramidal neurons along the longitudinal hippocampal axis: DORSOVENTRAL GRADIENT IN EXCITABILITY OF CA1 NEURONS". en. In: *Hippocampus* 26.3, pp. 341–361. ISSN:

10509631. DOI: 10.1002/hipo.22526. URL: https://onlinelibrary.wiley.com/doi/10.1002/hipo.22526.

Mancini, Jayme D. and William D. Atchison (2007). “The NR2B subunit in NMDA receptors is functionally important during cerebellar granule cell migration”. en. In: *Neuroscience Letters* 429.2-3, pp. 87–90. ISSN: 03043940. DOI: 10.1016/j.neulet.2007.09.079. URL: https://linkinghub.elsevier.com/retrieve/pii/S0304394007010749.

Maravall, M. (2004). “Experience-dependent Changes in Basal Dendritic Branching of Layer 2/3 Pyramidal Neurons During a Critical Period for Developmental Plasticity in Rat Barrel Cortex”. en. In: *Cerebral Cortex* 14.6, pp. 655–664. ISSN: 1460-2199. DOI: 10.1093/cercor/bhh026. URL: https://academic.oup.com/cercor/article-lookup/doi/10.1093/cercor/bhh026.

Maravall, Miguel, Edward A. Stern, and Karel Svoboda (2004). “Development of Intrinsic Properties and Excitability of Layer 2/3 Pyramidal Neurons During a Critical Period for Sensory Maps in Rat Barrel Cortex”. en. In: *Journal of Neurophysiology* 92.1, pp. 144–156. ISSN: 0022-3077, 1522-1598. DOI: 10.1152/jn.00598.2003. URL: https://www.physiology.org/doi/10.1152/jn.00598.2003.

Martina, M. (2000). “Distal Initiation and Active Propagation of Action Potentials in Interneuron Dendrites”. en. In: *Science* 287.5451, pp. 295–300. ISSN: 00368075, 10959203. DOI: 10.1126/science.287.5451.295. URL: https://www.sciencemag.org/lookup/doi/10.1126/science.287.5451.295.

Mattson, Mark P., Marc Gleichmann, and Aiwu Cheng (2008). “Mitochondria in Neuroplasticity and Neurological Disorders”. en. In: *Neuron* 60.5, pp. 748–766. ISSN: 08966273. DOI: 10.1016/j.neuron.2008.10.010. URL: https://linkinghub.elsevier.com/retrieve/pii/S0896627308008532.

McCormick, David A., Yousheng Shu, and Yuguo Yu (2007). “Hodgkin and Huxley model — still standing?” en. In: *Nature* 445.7123, E1–E2. ISSN: 0028-0836, 1476-4687. DOI: 10.1038/nature05523. URL: http://www.nature.com/articles/nature05523.

McGaugh, J. L. (2000). “Memory–a Century of Consolidation”. In: *Science* 287.5451, pp. 248–251. ISSN: 00368075, 10959203. DOI: 10.1126/science.287.5451.248. URL: http://www.sciencemag.org/cgi/doi/10.1126/science.287.5451.248.

Mercer, Audrey, David C. West, Oliver T. Morris, Sarah Kirchhecker, Jane E. Kerkhoff, and Alex M. Thomson (2005). “Excitatory Connections Made by Presynaptic Cortico-Cortical Pyramidal Cells in Layer 6 of the Neocortex”. en. In: *Cerebral Cortex* 15.10, pp. 1485–1496. ISSN: 1460-2199, 1047-3211. DOI: 10.1093/cercor/bhi027. URL: http://academic.oup.com/cercor/article/15/10/1485/396548/Excitatory-Connections-Made-by-Presynaptic.

Moore, J W, N Stockbridge, and M Westerfield (1983). “On the site of impulse initiation in a neurone.” en. In: *The Journal of Physiology* 336.1, pp. 301–311. ISSN: 00223751. DOI: 10.1113/jphysiol.1983.sp014582. URL: https://onlinelibrary.wiley.com/doi/10.1113/jphysiol.1983.sp014582.

Nakada, Chieko, Kenneth Ritchie, Yuichi Oba, Mitsuhiro Nakamura, Yoko Hotta, Ryota Iino, Rinshi S. Kasai, Kazuhiko Yamaguchi, Takahiro Fujiwara, and Akihiro Kusumi (2003). “Accumulation of anchored proteins forms membrane diffusion barriers during neuronal polarization”. en. In: *Nature Cell Biology* 5.7, pp. 626–632. ISSN: 1465-7392, 1476-4679. DOI: 10.1038/ncb1009. URL: http://www.nature.com/articles/ncb1009.

Niepel, Mario, Sabrina L Spencer, and Peter K Sorger (2009). “Non-genetic cell-to-cell variability and the consequences for pharmacology”. en. In: *Current Opinion in Chem-*

ical Biology 13.5-6, pp. 556–561. ISSN: 13675931. DOI: 10.1016/j.cbpa.2009.09.015. URL: https://linkinghub.elsevier.com/retrieve/pii/S1367593109001379.

Nowak, L., P. Bregestovski, P. Ascher, A. Herbet, and A. Prochiantz (1984). "Magnesium gates glutamate-activated channels in mouse central neurones". en. In: *Nature* 307.5950, pp. 462–465. ISSN: 0028-0836, 1476-4687. DOI: 10.1038/307462a0. URL: http://www.nature.com/articles/307462a0.

O'Keefe, J. and J. Dostrovsky (1971). "The hippocampus as a spatial map. Preliminary evidence from unit activity in the freely-moving rat". en. In: *Brain Research* 34.1, pp. 171–175. ISSN: 00068993. DOI: 10.1016/0006-8993(71)90358-1. URL: https://linkinghub.elsevier.com/retrieve/pii/0006899371903581.

O'Leary, Timothy, Mark C. W. van Rossum, and David J. A. Wyllie (2010). "Homeostasis of intrinsic excitability in hippocampal neurones: dynamics and mechanism of the response to chronic depolarization". en. In: *The Journal of Physiology* 588.1, pp. 157–170. ISSN: 1469-7793. DOI: 10.1113/jphysiol.2009.181024. URL: https://physoc.onlinelibrary.wiley.com/doi/abs/10.1113/jphysiol.2009.181024.

Oberlaender, Marcel, Zimbo S. R. M. Boudewijns, Tatjana Kleele, Huibert D. Mansvelder, Bert Sakmann, and Christiaan P. J. De Kock (2011). "Three-dimensional axon morphologies of individual layer 5 neurons indicate cell type-specific intracortical pathways for whisker motion and touch". en. In: *Proceedings of the National Academy of Sciences* 108.10, pp. 4188–4193. ISSN: 0027-8424, 1091-6490. DOI: 10.1073/pnas.1100647108. URL: https://pnas.org/doi/full/10.1073/pnas.1100647108.

Oberlaender, Marcel, Christiaan P. J. De Kock, Randy M. Bruno, Alejandro Ramirez, Hanno S. Meyer, Vincent J. Dercksen, Moritz Helmstaedter, and Bert Sakmann (2012). "Cell Type–Specific Three-Dimensional Structure of Thalamocortical Circuits in a Column of Rat Vibrissal Cortex". en. In: *Cerebral Cortex* 22.10, pp. 2375–2391. ISSN: 1460-2199, 1047-3211. DOI: 10.1093/cercor/bhr317. URL: https://academic.oup.com/cercor/article-lookup/doi/10.1093/cercor/bhr317.

Ogawa, Yasuhiro, Ido Horresh, James S. Trimmer, David S. Bredt, Elior Peles, and Matthew N. Rasband (2008). "Postsynaptic Density-93 Clusters Kv1 Channels at Axon Initial Segments Independently of Caspr2". en. In: *The Journal of Neuroscience* 28.22, pp. 5731–5739. ISSN: 0270-6474, 1529-2401. DOI: 10.1523/JNEUROSCI.4431-07.2008. URL: https://www.jneurosci.org/lookup/doi/10.1523/JNEUROSCI.4431-07.2008.

Ogiwara, I., H. Miyamoto, N. Morita, N. Atapour, E. Mazaki, I. Inoue, T. Takeuchi, S. Itohara, Y. Yanagawa, K. Obata, T. Furuichi, T. K. Hensch, and K. Yamakawa (2007). "Nav1.1 Localizes to Axons of Parvalbumin-Positive Inhibitory Interneurons: A Circuit Basis for Epileptic Seizures in Mice Carrying an Scn1a Gene Mutation". en. In: *Journal of Neuroscience* 27.22, pp. 5903–5914. ISSN: 0270-6474, 1529-2401. DOI: 10.1523/JNEUROSCI.5270-06.2007. URL: http://www.jneurosci.org/cgi/doi/10.1523/JNEUROSCI.5270-06.2007.

Olsen, Richard W., Matt Ban, and Thomas Miller (1976). "Studies on the neuropharmacological activity of bicuculline and related compounds". en. In: *Brain Research* 102.2, pp. 283–299. ISSN: 00068993. DOI: 10.1016/0006-8993(76)90883-0. URL: https://linkinghub.elsevier.com/retrieve/pii/0006899376908830.

Owens, David F., Leslie H. Boyce, Marion B. E. Davis, and Arnold R. Kriegstein (1996). "Excitatory GABA Responses in Embryonic and Neonatal Cortical Slices Demonstrated by Gramicidin Perforated-Patch Recordings and Calcium Imaging". en. In: *The Journal of Neuroscience* 16.20, pp. 6414–6423. ISSN: 0270-6474, 1529-2401. DOI: 10.1523/

JNEUROSCI.16-20-06414.1996. URL: https://www.jneurosci.org/lookup/doi/10.1523/JNEUROSCI.16-20-06414.1996.

Padilla-Coreano, Nancy, Scott S. Bolkan, Georgia M. Pierce, Dakota R. Blackman, William D. Hardin, Alvaro L. Garcia-Garcia, Timothy J. Spellman, and Joshua A. Gordon (2016). "Direct Ventral Hippocampal-Prefrontal Input Is Required for Anxiety-Related Neural Activity and Behavior". en. In: *Neuron* 89.4, pp. 857–866. ISSN: 08966273. DOI: 10.1016/j.neuron.2016.01.011. URL: https://linkinghub.elsevier.com/retrieve/pii/S089662731600012X.

Palay, Sanford L., Constantino Sotelo, Alan Peters, and Paula M. Orkand (1968). "THE AXON HILLOCK AND THE INITIAL SEGMENT". en. In: *Journal of Cell Biology* 38.1, pp. 193–201. ISSN: 1540-8140, 0021-9525. DOI: 10.1083/jcb.38.1.193. URL: https://rupress.org/jcb/article/38/1/193/48066/THE-AXON-HILLOCK-AND-THE-INITIAL-SEGMENT.

Pan, Z. (2006). "A Common Ankyrin-G-Based Mechanism Retains KCNQ and NaV Channels at Electrically Active Domains of the Axon". en. In: *Journal of Neuroscience* 26.10, pp. 2599–2613. ISSN: 0270-6474, 1529-2401. DOI: 10.1523/JNEUROSCI.4314-05.2006. URL: http://www.jneurosci.org/cgi/doi/10.1523/JNEUROSCI.4314-05.2006.

Pan-Vazquez, Alejandro, Winnie Wefelmeyer, Victoria Gonzalez Sabater, Guilherme Neves, and Juan Burrone (2020). "Activity-Dependent Plasticity of Axo-axonic Synapses at the Axon Initial Segment". en. In: *Neuron* 106.2, 265–276.e6. ISSN: 08966273. DOI: 10.1016/j.neuron.2020.01.037. URL: https://linkinghub.elsevier.com/retrieve/pii/S0896627320300647.

Panzanelli, Patrizia, Benjamin G. Gunn, Monika C. Schlatter, Dietmar Benke, Shiva K. Tyagarajan, Peter Scheiffele, Delia Belelli, Jeremy J. Lambert, Uwe Rudolph, and Jean-Marc Fritschy (2011). "Distinct mechanisms regulate GABA $_A$ receptor and gephyrin clustering at perisomatic and axo-axonic synapses on CA1 pyramidal cells: GABA $_A$ receptors in perisomatic synapses". en. In: *The Journal of Physiology* 589.20, pp. 4959–4980. ISSN: 00223751. DOI: 10.1113/jphysiol.2011.216028. URL: http://doi.wiley.com/10.1113/jphysiol.2011.216028.

Peerboom, Carlijn and Corette J. Wierenga (2021). "The postnatal GABA shift: A developmental perspective". en. In: *Neuroscience & Biobehavioral Reviews* 124, pp. 179–192. ISSN: 01497634. DOI: 10.1016/j.neubiorev.2021.01.024. URL: https://linkinghub.elsevier.com/retrieve/pii/S0149763421000506.

Peters, Alan, Charmian C. Proskauer, and Ita R. Kaiserman-Abramof (1968). "THE SMALL PYRAMIDAL NEURON OF THE RAT CEREBRAL CORTEX". en. In: *Journal of Cell Biology* 39.3, pp. 604–619. ISSN: 1540-8140, 0021-9525. DOI: 10.1083/jcb.39.3.604. URL: https://rupress.org/jcb/article/39/3/604/17275/THE-SMALL-PYRAMIDAL-NEURON-OF-THE-RAT-CEREBRAL.

Peters, Alan, Charmian C. Proskauer, and Charles E. Ribak (1982). "Chandelier cells in rat visual cortex". en. In: *The Journal of Comparative Neurology* 206.4, pp. 397–416. ISSN: 0021-9967, 1096-9861. DOI: 10.1002/cne.902060408. URL: https://onlinelibrary.wiley.com/doi/10.1002/cne.902060408.

Petersen, Anders Victor, Florence Cotel, and Jean-François Perrier (2017). "Plasticity of the Axon Initial Segment: Fast and Slow Processes with Multiple Functional Roles". en. In: *The Neuroscientist* 23.4, pp. 364–373. ISSN: 1073-8584, 1089-4098. DOI: 10.1177/1073858416648311. URL: http://journals.sagepub.com/doi/10.1177/1073858416648311.

Petreanu, Leopoldo, Daniel Huber, Aleksander Sobczyk, and Karel Svoboda (2007). "Channelrhodopsin-2–assisted circuit mapping of long-range callosal projections". en. In: *Nature Neuroscience* 10.5, pp. 663–668. ISSN: 1097-6256, 1546-1726. DOI: 10.1038/nn1891. URL: http://www.nature.com/articles/nn1891.

Petreanu, Leopoldo, Tianyi Mao, Scott M. Sternson, and Karel Svoboda (2009). "The subcellular organization of neocortical excitatory connections". en. In: *Nature* 457.7233, pp. 1142–1145. ISSN: 0028-0836, 1476-4687. DOI: 10.1038/nature07709. URL: http://www.nature.com/articles/nature07709.

Petrof, Iraklis, Angela N. Viaene, and S. Murray Sherman (2012). "Two populations of corticothalamic and interareal corticocortical cells in the subgranular layers of the mouse primary sensory cortices". en. In: *The Journal of Comparative Neurology* 520.8, pp. 1678–1686. ISSN: 00219967. DOI: 10.1002/cne.23006. URL: https://onlinelibrary.wiley.com/doi/10.1002/cne.23006.

Petrovich, Gorica D, Newton S Canteras, and Larry W Swanson (2001). "Combinatorial amygdalar inputs to hippocampal domains and hypothalamic behavior systems". en. In: *Brain Research Reviews* 38.1-2, pp. 247–289. ISSN: 01650173. DOI: 10.1016/S0165-0173(01)00080-7. URL: https://linkinghub.elsevier.com/retrieve/pii/S0165017301000807.

Pichon, Fabien, Irina Nikonenko, Rudolf Kraftsik, and Egbert Welker (2012). "Intracortical connectivity of layer VI pyramidal neurons in the somatosensory cortex of normal and barrelless mice: Layer VI pyramidal neurons in mouse barrel cortex". en. In: *European Journal of Neuroscience* 35.6, pp. 855–869. ISSN: 0953816X. DOI: 10.1111/j.1460-9568.2012.08011.x. URL: https://onlinelibrary.wiley.com/doi/10.1111/j.1460-9568.2012.08011.x.

Ramón y Cajal, S (1937). "Recollections of My Life□Santiago Ramón y Cajal". In: Publisher: The MIT Press Cambridge.

Rasband, Matthew N. (2010). "The axon initial segment and the maintenance of neuronal polarity". en. In: *Nature Reviews Neuroscience* 11.8, pp. 552–562. ISSN: 1471-0048. DOI: 10.1038/nrn2852. URL: jamann.

Reh, Rebecca K., Brian G. Dias, Charles A. Nelson, Daniela Kaufer, Janet F. Werker, Bryan Kolb, Joel D. Levine, and Takao K. Hensch (2020). "Critical period regulation across multiple timescales". en. In: *Proceedings of the National Academy of Sciences* 117.38, pp. 23242–23251. ISSN: 0027-8424, 1091-6490. DOI: 10.1073/pnas.1820836117. URL: https://pnas.org/doi/full/10.1073/pnas.1820836117.

Rienecker, Kira D. A., Robert G. Poston, and Ramendra N. Saha (2020). "Merits and Limitations of Studying Neuronal Depolarization-Dependent Processes Using Elevated External Potassium". en. In: *ASN Neuro* 12, p. 175909142097480. ISSN: 1759-0914, 1759-0914. DOI: 10.1177/1759091420974807. URL: http://journals.sagepub.com/doi/10.1177/1759091420974807.

Rivera, Claudio, Juha Voipio, John A. Payne, Eva Ruusuvuori, Hannele Lahtinen, Karri Lamsa, Ulla Pirvola, Mart Saarma, and Kai Kaila (1999). "The K+/Cl− co-transporter KCC2 renders GABA hyperpolarizing during neuronal maturation". en. In: *Nature* 397.6716, pp. 251–255. ISSN: 0028-0836, 1476-4687. DOI: 10.1038/16697. URL: https://www.nature.com/articles/16697.

Rockland, Kathleen S (2022). "Looking for the origins of axons". en. In: *eLife* 11, e79839. ISSN: 2050-084X. DOI: 10.7554/eLife.79839. URL: https://elifesciences.org/articles/79839.

Rojo, Concepción, Ignacio Leguey, Asta Kastanauskaite, Concha Bielza, Pedro Larrañaga, Javier DeFelipe, and Ruth Benavides-Piccione (2016). "Laminar Differences

in Dendritic Structure of Pyramidal Neurons in the Juvenile Rat Somatosensory Cortex". en. In: *Cerebral Cortex* 26.6, pp. 2811–2822. ISSN: 1047-3211, 1460-2199. DOI: 10.1093/cercor/bhv316. URL: https://academic.oup.com/cercor/article-lookup/doi/10.1093/cercor/bhv316.

Roland, Alexandre B, Ana Ricobaraza, Damien Carrel, Benjamin M Jordan, Felix Rico, Anne Simon, Marie Humbert-Claude, Jeremy Ferrier, Maureen H McFadden, Simon Scheuring, and Zsolt Lenkei (2014). "Cannabinoid-induced actomyosin contractility shapes neuronal morphology and growth". en. In: *eLife* 3, e03159. ISSN: 2050-084X. DOI: 10.7554/eLife.03159. URL: https://elifesciences.org/articles/03159.

Romo-Parra, Héctor, Mario Treviño, Uwe Heinemann, and Rafael Gutiérrez (2008). "GABA Actions in Hippocampal Area CA3 During Postnatal Development: Differential Shift From Depolarizing to Hyperpolarizing in Somatic and Dendritic Compartments". en. In: *Journal of Neurophysiology* 99.3, pp. 1523–1534. ISSN: 0022-3077, 1522-1598. DOI: 10.1152/jn.01074.2007. URL: https://www.physiology.org/doi/10.1152/jn.01074.2007.

Royeck, Michel, Marie-Therese Horstmann, Stefan Remy, Margit Reitze, Yoel Yaari, and Heinz Beck (2008). "Role of Axonal NaV1.6 Sodium Channels in Action Potential Initiation of CA1 Pyramidal Neurons". In: *Journal of Neurophysiology* 100.4, pp. 2361–2380. ISSN: 0022-3077. DOI: 10.1152/jn.90332.2008. URL: https://www.physiology.org/doi/full/10.1152/jn.90332.2008.

Samoilova, Marina, Jianxue Li, Marc R. Pelletier, Kirsten Wentlandt, Yana Adamchik, Christian C. Naus, and Peter L. Carlen (2003). "Epileptiform activity in hippocampal slice cultures exposed chronically to bicuculline: increased gap junctional function and expression: Chronic bicuculline exposure in slice cultures". en. In: *Journal of Neurochemistry* 86.3, pp. 687–699. ISSN: 00223042, 14714159. DOI: 10.1046/j.1471-4159.2003.01893.x. URL: http://doi.wiley.com/10.1046/j.1471-4159.2003.01893.x.

Sarmiere, Patrick D, Cecile M Weigle, and Michael M Tamkun (2008). "The Kv2.1 K+ channel targets to the axon initial segment of hippocampal and cortical neurons in culture and in situ". en. In: *BMC Neuroscience* 9.1, p. 112. ISSN: 1471-2202. DOI: 10.1186/1471-2202-9-112. URL: http://bmcneurosci.biomedcentral.com/articles/10.1186/1471-2202-9-112.

Scannevin, R H, H Murakoshi, K J Rhodes, and J S Trimmer (1996). "Identification of a cytoplasmic domain important in the polarized expression and clustering of the Kv2.1 K+ channel." en. In: *Journal of Cell Biology* 135.6, pp. 1619–1632. ISSN: 0021-9525, 1540-8140. DOI: 10.1083/jcb.135.6.1619. URL: https://rupress.org/jcb/article/135/6/1619/29326/Identification-of-a-cytoplasmic-domain-important.

Schafer, D. P., S. Jha, F. Liu, T. Akella, L. D. McCullough, and M. N. Rasband (2009). "Disruption of the Axon Initial Segment Cytoskeleton Is a New Mechanism for Neuronal Injury". en. In: *Journal of Neuroscience* 29.42, pp. 13242–13254. ISSN: 0270-6474, 1529-2401. DOI: 10.1523/JNEUROSCI.3376-09.2009. URL: http://www.jneurosci.org/cgi/doi/10.1523/JNEUROSCI.3376-09.2009.

Scheefhals, Nicky and Harold D. MacGillavry (2018). "Functional organization of postsynaptic glutamate receptors". en. In: *Molecular and Cellular Neuroscience* 91, pp. 82–94. ISSN: 10447431. DOI: 10.1016/j.mcn.2018.05.002. URL: https://linkinghub.elsevier.com/retrieve/pii/S1044743117304050.

Schindelin, Johannes, Ignacio Arganda-Carreras, Erwin Frise, Verena Kaynig, Mark Longair, Tobias Pietzsch, Stephan Preibisch, Curtis Rueden, Stephan Saalfeld, Benjamin Schmid, Jean-Yves Tinevez, Daniel James White, Volker Hartenstein, Kevin Eli-

ceiri, Pavel Tomancak, and Albert Cardona (2012). “Fiji: an open-source platform for biological-image analysis”. en. In: *Nature Methods* 9.7, pp. 676–682. ISSN: 1548-7091, 1548-7105. DOI: 10.1038/nmeth.2019. URL: http://www.nature.com/articles/nmeth.2019.

Schlingloff, Dániel, Szabolcs Káli, Tamás F. Freund, Norbert Hájos, and Attila I. Gulyás (2014). “Mechanisms of Sharp Wave Initiation and Ripple Generation”. en. In: *The Journal of Neuroscience* 34.34, pp. 11385–11398. ISSN: 0270-6474, 1529-2401. DOI: 10.1523/JNEUROSCI.0867-14.2014. URL: https://www.jneurosci.org/lookup/doi/10.1523/JNEUROSCI.0867-14.2014.

Schneider-Mizell, Casey M, Agnes L Bodor, Forrest Collman, Derrick Brittain, Adam Bleckert, Sven Dorkenwald, Nicholas L Turner, Thomas Macrina, Kisuk Lee, Ran Lu, Jingpeng Wu, Jun Zhuang, Anirban Nandi, Brian Hu, JoAnn Buchanan, Marc M Takeno, Russel Torres, Gayathri Mahalingam, Daniel J Bumbarger, Yang Li, Thomas Chartrand, Nico Kemnitz, William M Silversmith, Dodam Ih, Jonathan Zung, Aleksandar Zlateski, Ignacio Tartavull, Sergiy Popovych, William Wong, Manuel Castro, Chris S Jordan, Emmanouil Froudarakis, Lynne Becker, Shelby Suckow, Jacob Reimer, Andreas S Tolias, Costas A Anastassiou, H Sebastian Seung, R Clay Reid, and Nuno Maçarico Da Costa (2021). “Structure and function of axo-axonic inhibition”. en. In: *eLife* 10, e73783. ISSN: 2050-084X. DOI: 10.7554/eLife.73783. URL: https://elifesciences.org/articles/73783.

Scoville, W. B. and B. Milner (1957). “LOSS OF RECENT MEMORY AFTER BILATERAL HIPPOCAMPAL LESIONS”. en. In: *Journal of Neurology, Neurosurgery & Psychiatry* 20.1, pp. 11–21. ISSN: 0022-3050. DOI: 10.1136/jnnp.20.1.11. URL: http://jnnp.bmj.com/cgi/doi/10.1136/jnnp.20.1.11.

Simons, D. J. and P. W. Land (1994). “Neonatal whisker trimming produces greater effects in nondeprived than deprived thalamic barreloids”. en. In: *Journal of Neurophysiology* 72.3, pp. 1434–1437. ISSN: 0022-3077, 1522-1598. DOI: 10.1152/jn.1994.72.3.1434. URL: https://www.physiology.org/doi/10.1152/jn.1994.72.3.1434.

Somogyi, P., T.F. Freund, and A. Cowey (1982). “The axo-axonic interneuron in the cerebral cortex of the rat, cat and monkey”. en. In: *Neuroscience* 7.11, pp. 2577–2607. ISSN: 03064522. DOI: 10.1016/0306-4522(82)90086-0. URL: https://linkinghub.elsevier.com/retrieve/pii/0306452282900860.

Somogyi, Péter, M.G. Nunzi, A. Gorio, and A.D. Smith (1983). “A new type of specific interneuron in the monkey hippocampus forming synapses exclusively with the axon initial segments of pyramidal cells”. en. In: *Brain Research* 259.1, pp. 137–142. ISSN: 00068993. DOI: 10.1016/0006-8993(83)91076-4. URL: https://linkinghub.elsevier.com/retrieve/pii/0006899383910764.

Spruston, Nelson, Yitzhak Schiller, Greg Stuart, and Bert Sakmann (1995). “Activity-Dependent Action Potential Invasion and Calcium Influx into Hippocampal CA1 Dendrites”. en. In: *Science* 268.5208, pp. 297–300. ISSN: 0036-8075, 1095-9203. DOI: 10.1126/science.7716524. URL: https://www.science.org/doi/10.1126/science.7716524.

Staiger, Jochen F. and Carl C. H. Petersen (2021). “Neuronal Circuits in Barrel Cortex for Whisker Sensory Perception”. en. In: *Physiological Reviews* 101.1, pp. 353–415. ISSN: 0031-9333, 1522-1210. DOI: 10.1152/physrev.00019.2019. URL: https://journals.physiology.org/doi/10.1152/physrev.00019.2019.

Stuart, Greg, Nelson Spruston, Bert Sakmann, and Michael Häusser (1997). “Action potential initiation and backpropagation in neurons of the mammalian CNS”. en. In: *Trends in Neurosciences* 20.3, pp. 125–131. ISSN: 01662236. DOI: 10.1016/S0166-

2236(96)10075-8. URL: https://linkinghub.elsevier.com/retrieve/pii/S0166223696100758.

Stuart, Greg J and Nelson Spruston (2015). "Dendritic integration: 60 years of progress". en. In: *Nature Neuroscience* 18.12, pp. 1713–1721. ISSN: 1097-6256, 1546-1726. DOI: 10.1038/nn.4157. URL: http://www.nature.com/articles/nn.4157.

Sugitani, M., J. Yano, T. Sugai, and H. Ooyama (1990). "Somatotopic organization and columnar structure of vibrissae representation in the rat ventrobasal complex". en. In: *Experimental Brain Research* 81.2. ISSN: 0014-4819, 1432-1106. DOI: 10.1007/BF00228125. URL: http://link.springer.com/10.1007/BF00228125.

Sun, Qian, Alaba Sotayo, Alejandro S. Cazzulino, Anna M. Snyder, Christine A. Denny, and Steven A. Siegelbaum (2017). "Proximodistal Heterogeneity of Hippocampal CA3 Pyramidal Neuron Intrinsic Properties, Connectivity, and Reactivation during Memory Recall". en. In: *Neuron* 95.3, 656–672.e3. ISSN: 08966273. DOI: 10.1016/j.neuron.2017.07.012. URL: https://linkinghub.elsevier.com/retrieve/pii/S0896627317306347.

Tai, Yilin, Nicholas B. Gallo, Minghui Wang, Jia-Ray Yu, and Linda Van Aelst (2019). "Axo-axonic Innervation of Neocortical Pyramidal Neurons by GABAergic Chandelier Cells Requires AnkyrinG-Associated L1CAM". en. In: *Neuron* 102.2, 358–372.e9. ISSN: 08966273. DOI: 10.1016/j.neuron.2019.02.009. URL: https://linkinghub.elsevier.com/retrieve/pii/S0896627319301187.

Tamamaki, Nobuaki, Koutarou Abe, and Yoshiaki Nojyo (1987). "Columnar organization in the subiculum formed by axon branches originating from single CA1 pyramidal neurons in the rat hippocampus". en. In: *Brain Research* 412.1, pp. 156–160. ISSN: 00068993. DOI: 10.1016/0006-8993(87)91452-1. URL: https://linkinghub.elsevier.com/retrieve/pii/0006899387914521.

Telenczuk, Maria, Bertrand Fontaine, and Romain Brette (2017). "The basis of sharp spike onset in standard biophysical models". en. In: *PLOS ONE* 12.4. Ed. by Maurice J. Chacron, e0175362. ISSN: 1932-6203. DOI: 10.1371/journal.pone.0175362. URL: https://dx.plos.org/10.1371/journal.pone.0175362.

Theyel, Brian B, Daniel A Llano, and S Murray Sherman (2010). "The corticothalamocortical circuit drives higher-order cortex in the mouse". en. In: *Nature Neuroscience* 13.1, pp. 84–88. ISSN: 1097-6256, 1546-1726. DOI: 10.1038/nn.2449. URL: http://www.nature.com/articles/nn.2449.

Thome, Christian, Jan Maximilian Janssen, Seda Karabulut, Claudio Acuna, Elisa D'Este, Stella J. Soyka, Konrad Baum, Michael Bock, Nadja Lehmann, Masashi Hasegawa, Dan Alin Ganea, Chloé Maëlle Benoit, Jan Gründemann, Christian Schultz, Vann Bennett, Paul M. Jenkins, and Maren Engelhardt (2023). *Live imaging of excitable axonal microdomains in ankyrin-G-GFP mice*. preprint. elife. DOI: 10.7554/eLife.87078.1. URL: https://elifesciences.org/reviewed-preprints/87078v1.

Thome, Christian, Tony Kelly, Antonio Yanez, Christian Schultz, Maren Engelhardt, Sidney B. Cambridge, Martin Both, Andreas Draguhn, Heinz Beck, and Alexei V. Egorov (2014). "Axon-Carrying Dendrites Convey Privileged Synaptic Input in Hippocampal Neurons". en. In: *Neuron* 83.6, pp. 1418–1430. ISSN: 08966273. DOI: 10.1016/j.neuron.2014.08.013. URL: https://linkinghub.elsevier.com/retrieve/pii/S0896627314006886.

Thomson, A.M and A.P Bannister (1998). "Postsynaptic pyramidal target selection by descending layer III pyramidal axons: dual intracellular recordings and biocytin filling in slices of rat neocortex". en. In: *Neuroscience* 84.3, pp. 669–683. ISSN: 03064522. DOI:

10.1016/S0306-4522(97)00557-5. URL: https://linkinghub.elsevier.com/retrieve/pii/S0306452297005575.

Thomson, Alex M. (2007). "Functional maps of neocortical local circuitry". In: *Frontiers in Neuroscience* 1.1, pp. 19–42. ISSN: 16624548. DOI: 10.3389/neuro.01.1.1.002.2007. URL: http://journal.frontiersin.org/article/10.3389/neuro.01.1.1.002.2007/abstract.

Tierney, Adrienne L. and Charles A. Nelson (2009). "Brain Development and the Role of Experience in the Early Years". eng. In: *Zero to Three* 30.2, pp. 9–13. ISSN: 0736-8038.

Tomasi, Dardo, Gene-Jack Wang, and Nora D. Volkow (2013). "Energetic cost of brain functional connectivity". en. In: *Proceedings of the National Academy of Sciences* 110.33, pp. 13642–13647. ISSN: 0027-8424, 1091-6490. DOI: 10.1073/pnas.1303346110. URL: https://pnas.org/doi/full/10.1073/pnas.1303346110.

Tozzi, Arturo (2015). "Information processing in the CNS: a supramolecular chemistry?" en. In: *Cognitive Neurodynamics* 9.5, pp. 463–477. ISSN: 1871-4080, 1871-4099. DOI: 10.1007/s11571-015-9337-1. URL: http://link.springer.com/10.1007/s11571-015-9337-1.

Triarhou, Lazaros C. (2014). "Axons emanating from dendrites: phylogenetic repercussions with Cajalian hues". en. In: *Frontiers in Neuroanatomy* 8. ISSN: 1662-5129. DOI: 10.3389/fnana.2014.00133. URL: http://journal.frontiersin.org/article/10.3389/fnana.2014.00133/abstract.

Turrigiano, Gina G., Kenneth R. Leslie, Niraj S. Desai, Lana C. Rutherford, and Sacha B. Nelson (1998). "Activity-dependent scaling of quantal amplitude in neocortical neurons". en. In: *Nature* 391.6670, pp. 892–896. ISSN: 1476-4687. DOI: 10.1038/36103. URL: https://www.nature.com/articles/36103.

Vacher, Hélène, Jae-Won Yang, Oscar Cerda, Amapola Autillo-Touati, Bénédicte Dargent, and James S. Trimmer (2011). "Cdk-mediated phosphorylation of the Kvβ2 auxiliary subunit regulates Kv1 channel axonal targeting". en. In: *The Journal of Cell Biology* 192.5, pp. 813–824. ISSN: 0021-9525, 1540-8140. DOI: 10.1083/jcb.201007113. URL: http://jcb.rupress.org/content/192/5/813.

Van Der Loos, Hendrik (1976). "Barreloids in mouse somatosensory thalamus". en. In: *Neuroscience Letters* 2.1, pp. 1–6. ISSN: 03043940. DOI: 10.1016/0304-3940(76)90036-7. URL: https://linkinghub.elsevier.com/retrieve/pii/0304394076900367.

Van Der Loos, Hendrik and Thomas A. Woolsey (1973). "Somatosensory Cortex: Structural Alterations following Early Injury to Sense Organs". en. In: *Science* 179.4071, pp. 395–398. ISSN: 0036-8075, 1095-9203. DOI: 10.1126/science.179.4071.395. URL: https://www.science.org/doi/10.1126/science.179.4071.395.

Van Wart, Audra, James S. Trimmer, and Gary Matthews (2007). "Polarized distribution of ion channels within microdomains of the axon initial segment". en. In: *The Journal of Comparative Neurology* 500.2, pp. 339–352. ISSN: 00219967, 10969861. DOI: 10.1002/cne.21173. URL: http://doi.wiley.com/10.1002/cne.21173.

Vees, Aretha M., Kristina D. Micheva, Clermont Beaulieu, and Laurent Descarries (1998). "Increased number and size of dendritic spines in ipsilateral barrel field cortex following unilateral whisker trimming in postnatal rat". en. In: *The Journal of Comparative Neurology* 400.1, pp. 110–124. ISSN: 0021-9967, 1096-9861. DOI: 10.1002/(SICI)1096-9861(19981012)400:1<110::AID-CNE8>3.0.CO;2-C. URL: https://onlinelibrary.wiley.com/doi/10.1002/(SICI)1096-9861(19981012)400:1%3C110::AID-CNE8%3E3.0.CO;2-C.

Wahle, Petra, Eric Sobierajski, Ina Gasterstädt, Nadja Lehmann, Susanna Weber, Joachim HR Lübke, Maren Engelhardt, Claudia Distler, and Gundela Meyer (2022). "Neocortical pyramidal neurons with axons emerging from dendrites are frequent in non-primates, but rare in monkey and human". en. In: *eLife* 11, e76101. ISSN: 2050-084X. DOI: 10.7554/eLife.76101. URL: https://elifesciences.org/articles/76101.

Wang, P. Y., R. S. Petralia, Y.-X. Wang, R. J. Wenthold, and S. D. Brenowitz (2011). "Functional NMDA Receptors at Axonal Growth Cones of Young Hippocampal Neurons". en. In: *Journal of Neuroscience* 31.25, pp. 9289–9297. ISSN: 0270-6474, 1529-2401. DOI: 10.1523/JNEUROSCI.5639-10.2011. URL: https://www.jneurosci.org/lookup/doi/10.1523/JNEUROSCI.5639-10.2011.

Wayman, Gary A., Soren Impey, Daniel Marks, Takeo Saneyoshi, Wilmon F. Grant, Victor Derkach, and Thomas R. Soderling (2006). "Activity-Dependent Dendritic Arborization Mediated by CaM-Kinase I Activation and Enhanced CREB-Dependent Transcription of Wnt-2". en. In: *Neuron* 50.6, pp. 897–909. ISSN: 08966273. DOI: 10.1016/j.neuron.2006.05.008. URL: https://linkinghub.elsevier.com/retrieve/pii/S0896627306003746.

Wefelmeyer, Winnie, Daniel Cattaert, and Juan Burrone (2015). "Activity-dependent mismatch between axo-axonic synapses and the axon initial segment controls neuronal output". en. In: *Proceedings of the National Academy of Sciences* 112.31, pp. 9757–9762. ISSN: 0027-8424, 1091-6490. DOI: 10.1073/pnas.1502902112. URL: http://www.pnas.org/lookup/doi/10.1073/pnas.1502902112.

Wen, J. A. and A. L. Barth (2011). "Input-Specific Critical Periods for Experience-Dependent Plasticity in Layer 2/3 Pyramidal Neurons". en. In: *Journal of Neuroscience* 31.12, pp. 4456–4465. ISSN: 0270-6474, 1529-2401. DOI: 10.1523/JNEUROSCI.6042-10.2011. URL: http://www.jneurosci.org/cgi/doi/10.1523/JNEUROSCI.6042-10.2011.

Williams, K. (1993). "Ifenprodil discriminates subtypes of the N-methyl-D-aspartate receptor: selectivity and mechanisms at recombinant heteromeric receptors." en. In: *Molecular Pharmacology* 44.4. Publisher: American Society for Pharmacology and Experimental Therapeutics, pp. 851–859. ISSN: 0026-895X, 1521-0111. URL: https://molpharm.aspetjournals.org/content/44/4/851.

Winckler, Bettina, Paul Forscher, and Ira Mellman (1999). "A diffusion barrier maintains distribution of membrane proteins in polarized neurons". en. In: *Nature* 397.6721, pp. 698–701. ISSN: 0028-0836, 1476-4687. DOI: 10.1038/17806. URL: http://www.nature.com/articles/17806.

Woodhall, Gavin, D. Ieuan Evans, Mark O. Cunningham, and Roland S. G. Jones (2001). "NR2B-Containing NMDA Autoreceptors at Synapses on Entorhinal Cortical Neurons". en. In: *Journal of Neurophysiology* 86.4, pp. 1644–1651. ISSN: 0022-3077, 1522-1598. DOI: 10.1152/jn.2001.86.4.1644. URL: https://www.physiology.org/doi/10.1152/jn.2001.86.4.1644.

Woodruff, Alan R., Laura M. McGarry, Tim P. Vogels, Melis Inan, Stewart A. Anderson, and Rafael Yuste (2011). "State-Dependent Function of Neocortical Chandelier Cells". en. In: *The Journal of Neuroscience* 31.49, pp. 17872–17886. ISSN: 0270-6474, 1529-2401. DOI: 10.1523/JNEUROSCI.3894-11.2011. URL: https://www.jneurosci.org/lookup/doi/10.1523/JNEUROSCI.3894-11.2011.

Woolsey, Thomas A. and Hendrik Van der Loos (1970). "The structural organization of layer IV in the somatosensory region (S I) of mouse cerebral cortex". en. In: *Brain*

Research 17.2, pp. 205–242. ISSN: 00068993. DOI: 10.1016/0006-8993(70)90079-X. URL: https://linkinghub.elsevier.com/retrieve/pii/000689937090079X.

Xu, Ke, Guisheng Zhong, and Xiaowei Zhuang (2013). "Actin, Spectrin, and Associated Proteins Form a Periodic Cytoskeletal Structure in Axons". en. In: *Science* 339.6118, pp. 452–456. ISSN: 0036-8075, 1095-9203. DOI: 10.1126/science.1232251. URL: https://www.science.org/doi/10.1126/science.1232251.

Xu, Mingxuan and Edward C. Cooper (2015). "An Ankyrin-G N-terminal Gate and Protein Kinase CK2 Dually Regulate Binding of Voltage-gated Sodium and KCNQ2/3 Potassium Channels". en. In: *Journal of Biological Chemistry* 290.27, pp. 16619–16632. ISSN: 0021-9258, 1083-351X. DOI: 10.1074/jbc.M115.638932. URL: http://www.jbc.org/lookup/doi/10.1074/jbc.M115.638932.

Yamada, Rei and Hiroshi Kuba (2016). "Structural and Functional Plasticity at the Axon Initial Segment". In: *Frontiers in Cellular Neuroscience* 10. ISSN: 1662-5102. DOI: 10.3389/fncel.2016.00250. URL: http://journal.frontiersin.org/article/10.3389/fncel.2016.00250/full.

Yamashita, Takayuki, Angeliki Vavladeli, Aurélie Pala, Katia Galan, Sylvain Crochet, Sara S. A. Petersen, and Carl C. H. Petersen (2018). "Diverse Long-Range Axonal Projections of Excitatory Layer 2/3 Neurons in Mouse Barrel Cortex". In: *Frontiers in Neuroanatomy* 12, p. 33. ISSN: 1662-5129. DOI: 10.3389/fnana.2018.00033. URL: http://journal.frontiersin.org/article/10.3389/fnana.2018.00033/full.

Yang, Jenq-Wei, Werner Kilb, Sergei Kirischuk, Petr Unichenko, Maik C Stüttgen, and Heiko J Luhmann (2018). "Development of the whisker-to-barrel cortex system". en. In: *Current Opinion in Neurobiology* 53, pp. 29–34. ISSN: 09594388. DOI: 10.1016/j.conb.2018.04.023. URL: https://linkinghub.elsevier.com/retrieve/pii/S0959438818300394.

Yu, Yuguo, Carlos Maureira, Xiuxin Liu, and David McCormick (2010). "P/Q and N Channels Control Baseline and Spike-Triggered Calcium Levels in Neocortical Axons and Synaptic Boutons". en. In: *The Journal of Neuroscience* 30.35, pp. 11858–11869. ISSN: 0270-6474, 1529-2401. DOI: 10.1523/JNEUROSCI.2651-10.2010. URL: https://www.jneurosci.org/lookup/doi/10.1523/JNEUROSCI.2651-10.2010.

Zhang, Z., Y.-Y. Jiao, and Q.-Q. Sun (2011). "Developmental maturation of excitation and inhibition balance in principal neurons across four layers of somatosensory cortex". en. In: *Neuroscience* 174, pp. 10–25. ISSN: 03064522. DOI: 10.1016/j.neuroscience.2010.11.045. URL: https://linkinghub.elsevier.com/retrieve/pii/S0306452210015368.

Zhang, Zhong-Wei and Martin Deschênes (1997). "Intracortical Axonal Projections of Lamina VI Cells of the Primary Somatosensory Cortex in the Rat: A Single-Cell Labeling Study". en. In: *The Journal of Neuroscience* 17.16, pp. 6365–6379. ISSN: 0270-6474, 1529-2401. DOI: 10.1523/JNEUROSCI.17-16-06365.1997. URL: https://www.jneurosci.org/lookup/doi/10.1523/JNEUROSCI.17-16-06365.1997.

Zhou, Daixing, Stephen Lambert, Peter L. Malen, Scott Carpenter, Linda M. Boland, and Vann Bennett (1998). "Ankyrin $_G$ Is Required for Clustering of Voltage-gated Na Channels at Axon Initial Segments and for Normal Action Potential Firing". en. In: *The Journal of Cell Biology* 143.5, pp. 1295–1304. ISSN: 0021-9525, 1540-8140. DOI: 10.1083/jcb.143.5.1295. URL: http://www.jcb.org/lookup/doi/10.1083/jcb.143.5.1295.

Zuo, Yi, Guang Yang, Elaine Kwon, and Wen-Biao Gan (2005). "Long-term sensory deprivation prevents dendritic spine loss in primary somatosensory cortex". en. In: *Nature* 436.7048, pp. 261–265. ISSN: 0028-0836, 1476-4687. DOI: 10.1038/nature03715. URL: https://www.nature.com/articles/nature03715.